

UC Berkeley

UC Berkeley Electronic Theses and Dissertations

Title

Effects of climate, physical erosion, parent mineralogy, and dust on chemical erosion rates in mountainous terrain

Permalink

<https://escholarship.org/uc/item/20d1v3p2>

Author

Ferrier, Ken

Publication Date

2009

Peer reviewed|Thesis/dissertation

**Effects of climate, physical erosion, parent mineralogy, and dust on chemical
erosion rates in mountainous terrain**

by

Kenneth Leslie Ferrier

A dissertation submitted in partial satisfaction
of the requirements for the degree of

Doctor of Philosophy

in

Earth & Planetary Science

in the

Graduate Division

of the

University of California, Berkeley

Committee in charge:

Professor James W. Kirchner, Chair
Professor William E. Dietrich
Professor Ronald Amundson

Fall 2009

Effects of climate, physical erosion, parent mineralogy, and dust on chemical erosion rates
in mountainous terrain

Copyright © 2009

by

Kenneth Leslie Ferrier

Abstract

Effects of climate, physical erosion, parent mineralogy, and dust on chemical erosion rates
in mountainous terrain

by

Kenneth Leslie Ferrier

Doctor of Philosophy in Earth & Planetary Science

University of California, Berkeley

Professor James W. Kirchner, Chair

Chemical weathering influences many components of the Earth system, from nutrient supply to landscape evolution to long-term climate. Despite considerable advances in understanding what controls chemical weathering in theoretical models and laboratory experiments, there is still much uncertainty surrounding the controls of chemical weathering in nature. Here I present several studies on chemical erosion rates in steep, eroding terrain. In Chapter 2, I present a 1-D numerical model for the evolution of soil mineralogy on an eroding hillslope, to quantify how much fluctuations in physical erosion rates should affect soil composition and thus estimates of chemical erosion rates inferred from soil composition. In Chapter 3, I combine new measurements of mineral abundances in soil, saprolite, and bedrock with prior measurements of soil production rates, dust deposition rates, and chemical composition in soil, saprolite, bedrock, and dust at an intensely weathered site in Puerto Rico. These data suggest this suite of measurements can – for abundant, soluble mineral phases – produce estimates of long-term mineral-specific weathering rates with uncertainties smaller than 20% of the mean. Lastly, I discuss new measurements of soil production rates and rock and soil composition along two steep altitudinal (and hence climatic) transects in the Idaho Batholith. In Chapter 4, I show how these data may be combined with measurements of dust composition to quantify long-term dust deposition rates. Under the assumption that mafic-rich dust from the nearby Palouse loess has been mixed into the otherwise granitic Idaho soils, I calculate dust deposition rates of 3-13 t km⁻² yr⁻¹ at our field sites, consistent with modern dust deposition rates measured elsewhere in the western United States. In Chapter 5, I show that mean annual soil temperature exerts no discernible effect on chemical erosion rates or on the degree of chemical weathering across these Idaho field sites. These measurements also show that the degree of chemical weathering, but not the rate of chemical erosion, increases with (a) the annual duration of wet conditions in the soil, and (b) soil residence time. Contrary to many prior measurements in similar terrain, these measurements are consistent with kinetic-limited weathering, rather than supply-limited weathering.

There is nothing like looking, if you want to find something (or so Thorin said to the young dwarves). You certainly usually find something, if you look, but it is not always quite the something you were after. So it proved on this occasion.

– J.R.R. Tolkien, *The Hobbit*, p. 68

Contents

Acknowledgements	v
1 Introduction	1
2 Effects of physical erosion on chemical denudation rates: a numerical modeling study of soil-mantled hillslopes	5
2.1 Abstract	5
2.2 Introduction	6
2.3 Theory	7
2.4 Model Results	11
2.5 Generalization of model	12
2.6 Nondimensional model results	13
2.7 Discussion	16
2.8 Acknowledgments	18
3 Mineral-specific chemical weathering rates over millennial timescales: Measurements at Rio Icacos, Puerto Rico	26
3.1 Abstract	26
3.2 Introduction	27
3.3 A steady-state framework for measuring mineral-specific chemical weathering rates in saprolite and soil	28
3.4 Field sites: Rio Icacos, Puerto Rico	31
3.5 Methods	32
3.6 Results and discussion	37
3.7 Conclusions	46

4	A geochemical method for estimating millennial-scale dust deposition rates on soil-mantled hillslopes, and an application of the method in the Idaho Batholith	59
4.1	Abstract	59
4.2	Introduction	60
4.3	A hillslope mass balance framework for estimating dust deposition rates . . .	61
4.4	Field application in the Idaho Batholith	63
4.5	Conclusions	66
5	Effects of climate, physical erosion rates, and dust on long-term chemical erosion rates: Measurements along two altitudinal transects in the Idaho Batholith	71
5.1	Abstract	71
5.2	Introduction	72
5.3	Measuring chemical and physical erosion rates with cosmogenic nuclides and elemental abundances in soil, rock, and dust	75
5.4	Study area: Pilot Peak and Tailholt Mountain in the Idaho Batholith	78
5.5	Methods	80
5.6	Data	82
5.7	Chemical evidence for atmospheric deposition at Pilot Peak and Tailholt Mountain	88
5.8	Chemical erosion rates and CDFs	90
5.9	Supply-limited vs. kinetically-limited weathering	93
5.10	Conclusions	95
	Bibliography	123
A	Supplementary information for the numerical model in Chapter 2	137
A.1	Derivation of model equations	137
A.2	Derivation of nondimensional model equations	141
A.3	Tables of parameter values used in model runs	143
B	Mineral abundances in rock, soil, and saprolite samples at Rio Icacos, Puerto Rico	146

C	Chemical composition of soil profile samples at Pilot Peak and Tailholt Mountain, Idaho	149
D	Soil climate records at Pilot Peak and Tailholt Mountain, Idaho	167
E	Photographs of field sites at Pilot Peak and Tailholt Mountain, Idaho	186
F	Chemical composition of rock and soil samples at Pilot Peak and Tailholt Mountain, Idaho	204

Acknowledgements

This dissertation could not have existed without the help of many people, most importantly Jim Kirchner, who guided and funded this work from the first day I arrived on campus. I have benefited a tremendous amount from Jim's guidance and example. His enthusiasm and acuity in research, teaching, and writing are all things I strive to mimic, and his breadth of expertise is something I would love to match someday. When I started grad school, someone told me that grad students spend the first few years learning from their advisors and the last few years teaching them. Eight and a half years later, I still look forward to reaching that second stage with Jim.

My second and third thesis committee members deserve thanks too, and not just for reading and signing my thesis. I have greatly enjoyed all my discussions about landscape evolution with Bill Dietrich, whose catlike curiosity is a continuous source of inspiration, and who is always generous in sharing his knowledge of how the world works and his speculations about how it might work. Those fortunate enough to catch Bill, like a leprechaun, are likely to leave his office with a pot full of rich scientific ideas. Ron Amundson provided frequent advice on sampling soils and interpreting their chemical characteristics at many stages of this work, and his insights were always useful and his encouragement greatly appreciated.

Cliff Riebe has practically been a second advisor in many stages of this work, and has advised me enthusiastically on everything from preparing cosmogenic nuclide samples to writing papers. Cliff is at the University of Wyoming now, which unfortunately has made our multi-hour discussions about chemical erosion less frequent. Thankfully, the distance is mitigated by Cliff's new habit of showing up when he's least expected and most needed, like Gandalf. It is always a good day when Cliff appears in town.

The work presented in this dissertation was made possible by the financial and logistical support of a number of individuals and organizations. National Science Foundation grants written by Jim and Cliff funded the collection and analysis of samples from Idaho and Puerto Rico. Without that support, this dissertation would have contained much less new data. Lawrence Livermore National Laboratory funded my salary through the Lawrence Scholar Program for the past three years, and I thank everyone at LLNL's Center for Accelerator Mass Spectrometry for welcoming me as a visiting student, especially Bob Finkel for running our cosmogenic ^{10}Be samples, and Graham Bench, Tom Guilderson, and Nanette Sorensen for support. I have learned a lot at CAMS, and I hope to continue our collaboration in the future. The US National Forest Service office in McCall, Idaho graciously allowed me to collect one thousand rock and soil samples and install soil monitoring devices at a number of sites in Payette National Forest. They also provided invaluable information on conditions in my field area, which was much needed; winter snows and summer forest fires prevented access to my field sites for over 80% of the three years we monitored those sites.

Our work in Idaho was possible only with the huge help of field assistants Michael Ferrier, Marisa Palucis, Leslie Hsu, and Jim Kirchner. They endured strenuous hikes,

rattlesnakes, backpacks full of rocks, and temperatures that sometimes varied by as much as 40 °C in less than 24 hours. On top of this they uncomplainingly shouldered the hardest work, digging soil pits and sampling granite outcrops. They had little more than a dip in the chilly South Fork of the Salmon River at the end of each day, but they were always cheerful, and their persistent good humor was always much appreciated and never unsurprising. Many of my favorite memories from grad school are from these trips.

Back in Berkeley, Tim Teague provided continuous and patient advice on XRF and XRD sample preparation. I am grateful for the help of undergraduate lab assistants Ajay Limaye, Shreya Ramesh, Greg Nishiimura, and Evan Kha, who together prepared hundreds of XRF samples and saved me hundreds of hours of lab work.

Beyond the research itself, I would not have been able to complete this Ph.D. without many faculty who provided inspiration and many friends who provided commiseration. Together they kept me sane. A few classes left particularly strong impressions. Jim Kirchner's class on analysis of environmental data was a model of a supremely well-organized pedagogy, and I am grateful to have had the opportunity to be a GSI for that class. Bill Dietrich's undergraduate and graduate geomorphology classes were models for tackling difficult field-based problems, and Bill's example as a lecturer reassured me that making frequent reference to characters in fantasy novels is entirely appropriate. The Geography department's Geomorphology of California class, led by the immensely quotable Kurt Cuffey, stands as the precise template for the field class I'd like to teach someday, and was so enjoyable that I took it a second time. It remains the only class I have ever voluntarily taken twice. Michael Manga's geodynamics and fluid mechanics classes were models of clarity and simplicity, and Michael himself stands as evidence that even nerdy Canadians can, with hard work and good grooming, grow up to be featured in *People Magazine's Sexiest Men* issue*. He too is an inspiration.

Almost lastly, I want to thank the geomorphology research group here at UC Berkeley. It is filled with remarkably bright people who are also remarkably fun to be around, and they made every research group meeting a real pleasure. They will be what I miss most when I leave Berkeley. Joel Rowland and Taylor Perron were officemates, sounding boards, and friends for many years, and I look forward to working with Taylor again soon as a postdoc at MIT. Leslie Hsu, Johnny Sanders, Peter Nelson, and Christian Braudrick are all good friends and uncommonly good human beings and I wish they were all moving to MIT with me. Others who have passed through the geomorphology group or who are still here – Marisa Palucis, Justine Owen, Sarah Godsey, Kathleen Swanson, Vicky Lee, Mike Lamb, Dino Bellugi, Noah Finnegan, Elowyn Yager, Tim Creyts, George Hilley, John Stock, Douglas Allen, Leonard Sklar, Roland Kaitna, Daniella Rempe, and Jasper Oshun – all provided support, criticism, sympathy, and camaraderie at various times and in various measures over the years, and without them my time at Berkeley would have been much poorer. I feel lucky to have spent time with all of them.

Lastly, a big thanks to my family, who knew when to stop asking when I was going to finish.

* *People Magazine*, 28 November 2005, p. 152. Look for me there in 2019.

Chapter 1

Introduction

As far as we humans know, grizzly bears spend little time thinking about chemical weathering. Our knowledge of bear behavior suggests that the average *Ursus arctos horribilis* spends most of his time hunting salmon in mountain streams, eating berries on the neighboring hillslopes, and hibernating. However, bears would do well to put aside their presumed indifference to chemical weathering, for it affects them and their surroundings in many ways. Chemical weathering breaks down minerals and releases solutes to soils and streams, thus providing the nutritional foundation for life, including the salmon that nourish the bears. On the hillslopes around them, berry bushes grow in soils that developed in part through chemical weathering of the underlying rock. Because chemical weathering accelerates landscape evolution by weakening bedrock and promoting physical erosion, it helps shape the bears' habitat, including the dens where they choose to hibernate. And, as Earth's primary long-term sink for atmospheric carbon dioxide, chemical weathering modulates Earth's temperature via the greenhouse effect. For hundreds of millions of years, chemical weathering has played a central role in keeping Earth's climate habitable. It is in no small way responsible for making modern mountain ranges like the Canadian Rockies a textbook place for bears.

The influence of chemical weathering, of course, is not limited to bears; chemical weathering exerts a widespread influence on life and landscapes. As such, quantifying the dependence of chemical weathering rates on various factors (e.g., climate, lithology, tectonics, and land use) is important for understanding the past evolution of Earth's topography and its inhabitants, and in predicting how changes in climate and human activity will affect them in the future. Although there has been considerable progress in understanding the controls on chemical weathering rates in the lab and in theoretical models (e.g., Brady and Carroll, 1994; Blum and Stillings, 1995; Chen and Brantley, 1997; White et al., 1999a; Brantley, 2008), there remains considerable uncertainty about the dependence of chemical weathering rates on climate, lithology, tectonics, and human activity in natural settings. Predicting the responses of natural chemical weathering rates to current and future changes in these factors remains a challenge.

In this dissertation I use lab measurements, field observations, and numerical models

to examine the effects of climate, physical erosion, and mineralogy on chemical weathering. Much of this work centers around using a solid-phase mass balance method to measure chemical erosion rates in eroding terrain. As conventionally applied, this method requires measurements of soil production rates and rock-to-soil enrichments of chemically immobile elements, under the assumption that soil thickness and composition are steady in time (White et al., 1998; Riebe et al., 2001b, 2003, 2004b,a; Green et al., 2006; Yoo et al., 2007; Burke et al., 2007, 2009; Dixon et al., 2009). This technique has grown more popular over the past decade thanks to advances in cosmogenic nuclide geochemistry, which now permit routine determination of long-term soil production rates. This approach has great value because of its wide applicability – unlike prior methods, it is not restricted to non-eroding soils of known age, and thus can be applied to eroding terrain – and because it provides a long-term view of chemical erosion. Rates calculated with this method are averaged over the soil residence time (typically 10^3 - 10^5 years on most eroding hillslopes), and thus can provide a baseline against which modern chemical erosion rates can be compared.

In chapter 2 (previously published as Ferrier and Kirchner, 2008) I present a numerical model that simulates chemical erosion rates in a hillslope soil under time-varying physical erosion. This work was motivated by the desire to determine how deviations from steady state should affect chemical erosion rates in nature, and how much those deviations from steady state should affect estimates of chemical erosion rates inferred with the solid-phase mass balance technique (W_{inf}). Our modeling results suggest that W_{inf} should closely resemble actual chemical erosion rates averaged over the timescale of cosmogenic nuclide accumulation, even during large-amplitude and long-period oscillations in physical erosion rates. For example, this model predicts that when physical erosion rates fluctuate sinusoidally by 50% of their mean over any period in time, W_{inf} should differ from actual chemical erosion rates by less than 15%. Unexpectedly, modeled chemical erosion rates in soil do not increase monotonically with physical erosion rates; instead, modeled soil chemical erosion rates reach a maximum at an intermediate physical erosion rate, and approach zero as physical erosion rates approach either zero or the maximum possible soil production rate. This is contrary to the expectation that rapid physical erosion (e.g., in response to rapid rock uplift) should produce proportionally rapid chemical weathering and thus rapid drawdown of atmospheric CO_2 (Raymo et al., 1988). In other words, the weathering-modulated negative feedback between climate and tectonics may be weaker than expected; indeed, if physical erosion rates are close to the maximum soil production rate, it may even be a positive feedback. As noted by von Blanckenburg (2009), these model results suggest that a full understanding of the global linkages between silicate weathering and climate may require turning our attention toward chemical weathering on other parts of the Earth’s surface (e.g., floodplains).

In chapter 3, I show how the solid-phase mass-balance method may be used to measure mineral-specific chemical weathering rates in saprolite and soil. This method requires measurements of soil production rates and dust deposition rates as well as concentrations of minerals and an immobile element in the soil, saprolite, parent rock, and dust. The primary purpose of this study is to show that quantitative analysis of powder X-ray diffraction (XRD) patterns can – at least in samples with relatively simple

mineralogies – yield mineral abundances that are accurate enough to be profitably used in this mass balance method for estimating mineral weathering rates. To demonstrate that uncertainties in calculated mineral weathering rates are not so large that they negate the utility of this approach, we applied this technique to two intensely weathered regoliths in the rainforests of Puerto Rico. We combined XRD-based mineral abundances in soil, saprolite, and rock samples with prior measurements of soil production rates (from cosmogenic ^{10}Be), immobile element concentrations (from X-ray fluorescence), and published estimates of dust deposition rate and dust composition. Our results suggest this suite of measurements can, for highly soluble and highly abundant minerals, yield mineral weathering rates with uncertainties that are lower than 20% of the mean. This implies that this approach indeed can be useful in measuring long-term mineral weathering rates, and thus can help clarify how factors such as temperature, precipitation, vegetation, and physical erosion rates influence mineral weathering.

In chapters 4 and 5 I present measurements at a series of field sites along two altitudinal (and hence climatic) transects in the Idaho Batholith, where we measured soil production rates and soil and rock compositions to infer long-term chemical and physical erosion rates. At these sites, soils are richer in several mafic elements (Ti, Fe, Mg) than would be expected from simple weathering of the underlying granite, suggesting that mafic-rich dust has been incorporated into the otherwise granitic soils. This necessitates the inclusion of dust deposition in the solid-phase mass balance method for measuring long-term chemical and physical erosion rates. Unfortunately, direct physical measurements of dust deposition rates or dust composition near these field sites are unavailable. To address this problem, in chapter 4 I develop a new method for estimating long-term dust deposition rates in actively eroding terrain. Unlike previous applications of the solid-phase mass balance framework for estimating chemical and physical erosion rates, it makes use of two immobile elements rather than one. The existence of multiple immobile elements provides an additional constraint on the chemical evolution of an eroding soil, which permits determination of the fraction of the soil's parent material that is derived from dust (f_d). When combined with measurements of soil production rates inferred from cosmogenic nuclide concentrations in soil-borne quartz, f_d permits determination of dust deposition rates. I suggest that the most plausible dust source to the Idaho Batholith field sites is the glacial outburst flood sediments in Eureka Flat in southeastern Washington State, which is considered the primary source of the nearby mafic-rich Palouse loess (Sweeney et al., 2007). Under the assumption that the composition of the dust that fell on the Idaho soils is the same as that of the Eureka Flat sediments, I estimate dust deposition rates of 3-13 t km $^{-2}$ yr $^{-1}$, similar to modern dust deposition rates measured elsewhere in the western United States. These calculations demonstrate the power of dust to affect soil composition (and hence chemical erosion rates inferred from soil composition), even in places where dust deposition rates are only a few percent of the soil production rates from the underlying bedrock.

In chapter 5, I present measurements of chemical and physical erosion rates at the same field sites in the Idaho Batholith, and discuss how these rates appear to be affected (or unaffected) by climate and the length of time soils undergo weathering. The chemical

and physical erosion rates are inferred from measurements of soil production rates (derived from cosmogenic ^{10}Be in soil-borne quartz), dust deposition rates calculated in chapter 4, and enrichments of chemically immobile elements in soil relative to its parent material. Time series measurements from soil moisture and temperature probes at these sites permit direct comparison of the soil climates between sites. Our measurements suggest that mean annual soil temperature exerts a negligible influence on both chemical erosion rates and the extent to which soils are chemically weathered. These data also suggest that the annual duration of high soil moisture conditions (which at these sites depends primarily on the annual duration of snow cover) strongly influences the degree of chemical weathering, and may influence chemical erosion rates. Our measurements also show that soils at these sites tend to grow more chemically weathered with increasing soil residence time, implying that weathering at these sites is primarily limited by the kinetics of mineral dissolution rather than by the supply rate of fresh minerals to the soil. Finally, these data suggest that influxes of mafic-rich dust are a significant source of minor and trace elements to the Idaho Batholith, and hence are an important supplier of nutrients to this terrain.

Each of the studies in this dissertation is focused on a different aspect of chemical erosion in steep terrain, and, accordingly, each study has different conclusions. However, these studies are tied together by two common goals: to better understand what controls chemical erosion rates in nature, and to better understand the strengths and limitations of the solid-phase mass balance method for quantifying chemical erosion rates. I submit that these studies have taken modest steps toward these goals.

Chapter 2

Effects of physical erosion on chemical denudation rates: a numerical modeling study of soil-mantled hillslopes

2.1 Abstract

Many biogeochemical and Earth surface processes depend critically on chemical weathering. The immediate products of chemical weathering are present as solutes and secondary minerals in groundwater, soils, and streams, and form the nutritional foundation for terrestrial biogeochemistry. Chemical weathering also contributes to physical erosion by weakening bedrock and producing easily erodible regolith, and as the primary long-term sink for atmospheric CO₂ it modulates Earth's long-term climate via the greenhouse effect. Long-term chemical denudation rates on soil-mantled hillslopes can be estimated from cosmogenic radionuclide (CRN) concentrations in soil-borne quartz and the enrichment of a chemically inert tracer in soil relative to its parent bedrock, a technique that inherently assumes steady physical erosion over the timescale of CRN accumulation. We present a numerical model that computes changes in soil mineralogy and CRN concentrations under time-varying physical erosion rates, and we use this model to assess the accuracy of the CRN-based technique for estimating chemical denudation rates in non-steady conditions.

Our modeling results suggest that CRN-based estimates of chemical denudation rates closely resemble actual chemical denudation rates averaged over the timescale of CRN accumulation, even during large-amplitude and long-period oscillations in physical erosion rates. For example, this model predicts that when physical erosion rates fluctuate sinusoidally by 50% of their mean over any period in time, CRN-based estimates of chemical denudation rates should differ from actual chemical denudation rates by less than 15%. Our model also implies that chemical denudation rates should approach zero both

when physical erosion rates approach zero (because soluble minerals become depleted in the soil) and when physical erosion rates approach the maximum soil production rate (because soil thickness approaches zero). Modeled chemical denudation rates thus reach a maximum at intermediate physical erosion rates. If this relationship holds in nature, it implies that in rapidly eroding regions, further increases in physical erosion rates (e.g., due to increases in tectonic uplift rates) may not necessarily lead to faster chemical denudation on soil-mantled hillslopes.

2.2 Introduction

Consider a scientist standing on a ridge overlooking a catchment. Under her feet the soil hosts a diverse biotic community, and the landscape below her is furrowed by ridges and valleys with streams flowing down the valley axes. All of these features of the catchment, both living and inanimate, depend on chemical weathering. Dissolved mineral constituents (the immediate products of chemical weathering) are present as cations and anions in ground and surface waters, and provide mineral-derived nutrients for organisms living in the soil and streams. Chemical weathering thus contributes to the nutritional foundation for terrestrial biogeochemistry. The geomorphic processes that sculpt the landscape also depend on chemical weathering, which converts bedrock to erodible regolith and thus accelerates landscape evolution. Chemical weathering of silicate minerals is the dominant sink for atmospheric CO₂ over geologic time (Walker et al., 1981; Berner et al., 1983), so to the degree that silicate weathering rates increase with temperature, they create a feedback loop that regulates Earth's long-term surface temperature via the greenhouse effect. Chemical weathering thus plays a critical role in many Earth surface processes across a wide range of timescales. In order to understand how these processes respond to various environmental factors (e.g., temperature, precipitation, pH), it is necessary to measure how these factors influence chemical weathering rates. This in turn requires the ability to measure chemical weathering rates accurately.

Several different approaches have been used to measure chemical weathering rates. Mineral dissolution rates have often been measured in laboratory experiments (e.g., Busenberg and Clemency, 1976; Chou and Wollast, 1984; White et al., 1999a; White, 2003), an approach that allows tight control over the weathering environment, and thus has the ability to isolate specific weathering mechanisms. Laboratory weathering experiments, however, are conducted over timescales much shorter than the natural timescales of mineral weathering, and the rates derived from these short-term studies are often several orders of magnitude faster than those those derived from longer-term field studies (e.g., White, 2003). This suggests that laboratory-derived rates cannot be applied directly to natural weathering environments, and highlights the need for field-based measurements of chemical weathering rates. At the catchment scale, field-derived chemical weathering rates were first determined by Garrels and Mackenzie (1967), based on the assumption that chemical weathering accounts for the difference in solute fluxes into and out of a catchment. Two decades later, Brimhall and Dietrich (1987) showed that measurements of mobile and

immobile element concentrations in regolith and parent bedrock could be combined to yield chemical weathering rates averaged over the age of the soil. This technique requires sampling datable soils that have undergone negligible physical erosion (e.g., marine terraces (Brimhall et al., 1991) or river terraces (White et al., 1996)), and thus is difficult to apply to actively eroding landscapes that lack such soils. In 1997, Kirchner et al. proposed that chemical denudation rates can be determined in actively eroding landscapes using measurements of denudation rates, inferred from concentrations of in-situ produced cosmogenic radionuclides (CRN) in quartz, combined with measurements of immobile element enrichment in regolith relative to its parent bedrock. Subsequent studies (Riebe et al., 2001b, 2003, 2004b,a) demonstrated the accuracy of this technique and applied it to landscapes spanning a wide range of climates. This technique has two major strengths: (1) it can be applied to a wide range of landscapes because it does not require a datable non-eroding soil, and (2) it gives insight into soil formation and landscape evolution processes, because it is intrinsically averaged over the long timescales of soil formation and denudation. This method assumes that: (1) the soil mineralogy is derived solely from the bedrock beneath it (i.e., that any contamination of the soil by minerals from external sources such as windblown volcanic ash is negligible); (2) the soil has been representatively sampled; (3) the rock and soil contain an immobile tracer (element or mineral) that is so resistant to chemical dissolution that it is effectively lost from the soil only through physical erosion; and (4) the soil maintains a steady-state mass per unit area over the timescale of CRN accumulation (typically > 1000 years on eroding hillslopes).

In this paper, we examine the degree to which deviations from this steady-state assumption affect chemical denudation rates inferred from the technique of Kirchner et al. (1997) and Riebe et al. (2001b, 2003, 2004b,a). We approach this problem by modeling how mineral abundances and cosmogenic radionuclide concentrations in the soil evolve through time, imposing time-varying physical erosion rates on the model, and calculating the resulting variations in inferred chemical denudation rates.

2.3 Theory

2.3.1 Chemical denudation rates inferred from concentrations of cosmogenic radionuclides and immobile elements

Consider a hillslope soil which undergoes steady-state formation and denudation such that it maintains a constant mass per unit area over time (Figure 2.1). On such a steady-state hillslope, the soil production rate ϵ_b equals the denudation rate D , which itself equals the sum of the physical erosion rate E and chemical denudation rate W :

$$\epsilon_b = D = E + W. \quad (2.1)$$

Here ϵ_b , D , E , and W all have dimensions of mass per unit area of hillslope per time. We describe W as a chemical denudation rate and not a chemical weathering rate to emphasize

that W connotes transport of dissolved mineral constituents out of the soil, and not merely chemical alteration of minerals. If secondary minerals precipitate in the soil, then the chemical denudation rate W is the difference between the sum of all primary mineral dissolution rates and all secondary mineral precipitation rates. Conservation of mass for an individual mineral or element X dictates that

$$D \cdot [X]_r = E \cdot [X]_s + W_X, \quad (2.2)$$

where $[X]_r$ and $[X]_s$ are the average concentrations [mol M⁻¹] of X in rock and soil, respectively, and W_X is the chemical denudation rate of X [mol L⁻² T⁻¹] per unit area of hillslope, not unit mineral surface area. In using this equation, we assume that changes in the soil composition by aeolian deposition and convergence or divergence of soil from upslope (e.g., Mudd and Furbish, 2006) are negligible. If X is an element or mineral that is so resistant to dissolution that its chemical denudation rate W_X is negligible, it is termed "immobile" and Equation 2.2 yields an expression for E in terms of the denudation rate and the average immobile element concentrations in the rock and soil.

$$E = D \frac{[Zr]_r}{[Zr]_s} \quad (2.3)$$

Here we have chosen zirconium as an example of a commonly-used immobile element. This expression can be substituted into Equation 2.1 to yield the following expression for chemical denudation rate W .

$$W = D \left(1 - \frac{[Zr]_r}{[Zr]_s} \right) \quad (2.4)$$

Equation 2.3 can similarly be substituted into Equation 2.2 to yield an expression for the chemical denudation rate of an individual element or mineral X .

$$W_X = D \left([X]_r - [X]_s \frac{[Zr]_r}{[Zr]_s} \right) \quad (2.5)$$

At this point it is necessary to distinguish between instantaneous rates and inferred rates. We define the instantaneous denudation rate D_{inst} as the denudation rate at any moment in time. It is distinct from the inferred denudation rate D_{inf} , which in practice may be calculated from measurements of cosmogenic radionuclide concentrations in soil-borne quartz, as described below. Similarly, the instantaneous chemical denudation rate W_{inst} is the chemical denudation rate at any moment in time, while the inferred chemical denudation rate W_{inf} is that calculated with Equation 2.4, as described above. To emphasize that the chemical denudation rate in Equation 2.4 is an inferred rate, we rewrite Equation 2.4 with the inferred variables D_{inf} and W_{inf} .

$$W_{inf} = D_{inf} \left(1 - \frac{[Zr]_r}{[Zr]_s} \right) \quad (2.6)$$

In practice, CRN concentrations may be used to infer the denudation rate D_{inf} , as in Equation 2.7 (Lal, 1991):

$$D_{inf} = \frac{P_0 \Lambda}{N_s}. \quad (2.7)$$

Here D_{inf} is the inferred denudation rate [$\text{M L}^{-2} \text{T}^{-1}$], P_0 is the surface production rate of CRN in quartz [$\text{atoms M}^{-1} \text{T}^{-1}$], N_s is the measured concentration of CRN in quartz [atoms M^{-1}], and Λ [M L^{-2}] is the so-called penetration depth of cosmic ray neutrons, an exponential scaling constant that describes how quickly the cosmic ray neutron flux is attenuated as it passes through matter. Note that in Equations 2.2-2.7, $[Zr]_s$, $[X]_s$, and N_s are the average concentrations of Zr, X, and N_s in the soil, which means that from a practical standpoint the entire soil column must be sampled to obtain representative average concentrations. This equation assumes that muogenic production of CRN and radioactive decay of CRN are both negligible contributors to the overall CRN budget in the soil. For the shallow and continually-eroding soils we are modeling these are justifiable assumptions; in the upper meter below the Earth’s surface, muogenic production of CRN accounts for less than 3% of the total (Stone et al., 1998), and the residence time of quartz grains within the penetration depth of CRN-producing nucleons is, for our model conditions, <2% of the 1.5 Myr half-life of the commonly-used CRN ^{10}Be . For CRN with much shorter half-lives, such as ^{14}C , losses to radioactive decay are significant and Equation 2.7 is inaccurate; for this reason our analysis is restricted to CRN that have long half-lives or are stable (e.g., ^{10}Be , ^{26}Al , ^3He , ^{21}Ne). We note that muogenic production of CRN is significant in rapidly eroding sites at low elevations (see Balco et al., 2008 for discussion), and we ignore it because muogenic corrections to CRN-derived denudation rates are small for the high-elevation sites where this technique has most often been applied (e.g., Riebe et al., 2001b), and because there is only a minor benefit in adding muogenic production to a model that is intended for exploring general patterns in chemical denudation rates, rather than comparing modeled CRN concentrations to measured CRN concentrations. Equation 2.7 also ignores the effects of selective enrichment of quartz in the soil, which increases the exposure time of quartz to cosmic radiation and so artificially lowers inferred denudation rates (Small et al., 1999; Riebe et al., 2001a). Except in cases of extreme chemical weathering, this effect is small; Riebe et al. (2001a) showed that this process biases denudation rates by an average of only 6% for granitic soils in the Sierra Nevada under conditions similar to those that we model in this paper.

Inherent in the approach of Equation 2.7 for measuring denudation rates – and hence in the approach of Equation 2.6 for measuring chemical denudation rates – is an assumption of steady state; that is, it is assumed that denudation rates are constant over the timescale of CRN accumulation in quartz. In this paper, we are primarily concerned with quantifying the accuracy of this approach if denudation rates vary through time, making the assumption of steady state invalid. With this goal in mind, we created a numerical model that tracks the variables in Equation 2.6 under time-varying physical erosion rates.

2.3.2 A model of chemical denudation rates in soil

In order to model the effects of non-steady physical erosion on chemical denudation rates inferred from Equation 2.6, it is necessary to calculate the effects of non-steady physical erosion on immobile element concentrations in the soil and on inferred denudation

rates over time. This requires tracking the time-varying concentrations of all minerals in the soil and cosmogenic radionuclide (CRN) concentrations in soil-borne quartz. Here we give a brief outline of the equations used to track these variables over time and list the assumptions upon which these equations rest. Full derivations of these equations are presented in Appendix A.

The model rests on several fundamental assumptions. First, we assume that the soil production rate ϵ_b depends exponentially on soil thickness H as in the formulation of Heimsath et al. (1997, 1999, 2000, 2001, 2005).

$$\epsilon_b = \epsilon_0 e^{-\alpha H} \quad (2.8)$$

Here ϵ_0 represents the soil production rate at zero soil thickness, and α [L^{-1}] is a constant that describes the exponential dependence of soil production rate on soil thickness. Second, we follow the approach of Chamberlain et al. (2005) in assuming that the dissolution rate of mineral phase X is a linear function of its specific surface area A_X [$\text{L}^2 \text{mol}^{-1}$] and its concentration in the soil $[X]_s$ [mol M^{-1}].

$$\frac{d[X]_s}{dt} (\text{mineral dissolution}) = -k_X A_X [X]_s \quad (2.9)$$

Here k_X is the dissolution rate constant [$\text{mol L}^{-2} \text{T}^{-1}$] for mineral phase X . Third, we assume, as in Chamberlain et al. (2005), that any given secondary mineral phase X is produced at a constant rate s_X [$\text{mol L}^{-3} \text{T}^{-1}$] per unit volume of soil. Fourth, we assume that CRN production rates decrease exponentially below the Earth's surface (Lal, 1991).

$$P(z) = P_0 e^{-\rho z/\Lambda} \quad (2.10)$$

Here $P(z)$ is the CRN production rate at depth z , P_0 is the CRN production rate at the surface, ρ is the density of the material (e.g., soil, rock) through which the cosmic ray flux passes, and Λ is the penetration depth of cosmogenic gamma ray neutrons, expressed as mass per unit area. We also assume that changes in CRN concentrations due to radioactive decay, muogenic production, and downslope divergences in soil fluxes are all negligible. Lastly, we assume that mass is conserved during soil production and denudation. Given these assumptions, we derive the following differential equations for soil thickness, CRN concentrations and mineral concentrations.

Soil thickness H varies at a rate proportional to the imbalance between rates of soil production and soil denudation:

$$\frac{dH}{dt} = \frac{1}{\rho_s} (\epsilon_0 e^{-\alpha H} - E_{inst} - W_{inst}). \quad (2.11)$$

Here ρ_s is the density of soil and E_{inst} and W_{inst} are the instantaneous rates of physical erosion and chemical denudation. We impose a time-varying E_{inst} on the model, and allow all other variables to respond to it. E_{inst} drives the model.

Soil CRN concentrations N_s vary according to

$$\frac{dN_s}{dt} = \frac{1}{\rho_s H} \left(\epsilon_0 e^{-\alpha H} (N_{z_b} - N_s) + \Lambda P_0 (1 - e^{-\rho_s H/\Lambda}) \right), \quad (2.12)$$

where N_{z_b} is the CRN concentration in bedrock at the soil-bedrock boundary. Because soil thickness varies during non-steady denudation, N_{z_b} also varies in time:

$$\frac{dN_{z_b}}{dt} = P_0 e^{-\rho_s H/\Lambda} - \epsilon_0 e^{-\alpha H} \frac{N_{z_b}}{\Lambda}. \quad (2.13)$$

Lastly, soil mineral concentrations $[X]_s$ are given by

$$\begin{aligned} \frac{d[X]_s}{dt} = & \frac{\epsilon_0 e^{-\alpha H}}{\rho_s H} ([X]_r - [X]_s) + \frac{s_X}{\rho_s} - k_X A_X [X]_s \\ & + [X]_s \sum_{j=1}^n (k_j A_j [X_j]_s w_j - \frac{s_j w_j}{\rho_s}), \end{aligned} \quad (2.14)$$

where $[X]_r$ is the concentration of mineral phase X in bedrock [mol M^{-1}], n is the number of mineral phases in the soil, $[X_j]_s$ is the concentration of the j^{th} soil mineral phase in the summation [mol M^{-1}], and k_j , A_j , s_j , and w_j are the dissolution rate constant, specific surface area, secondary mineral production rate, and molar mass, respectively, of mineral phase X_j .

These assumptions also allow us to calculate instantaneous chemical denudation rates over time. Expressed in dimensions of [$\text{M L}^{-2} \text{T}^{-1}$], instantaneous chemical denudation rates are the difference between the sum of all mineral dissolution rates and all secondary mineral production rates.

$$W_{inst} = \sum_{j=1}^n (k_j A_j [X_j]_s w_j \rho_s H - s_j w_j H) \quad (2.15)$$

We use a fourth-order Runge-Kutta routine (Press et al., 1992) to numerically integrate Equations 2.11-2.14 over time. This allows us to calculate variations in soil CRN and mineral concentrations, from which we calculate variations in chemical denudation rates inferred with Equation 2.6. Together, these equations comprise a useful tool for examining the influence of variable physical erosion rates on soils; we can impose an arbitrary temporal pattern in physical erosion rates on the soil and observe the responses in soil thickness, mineral concentrations, CRN concentrations, and chemical denudation rates.

2.4 Model Results

How do modeled soils respond to variable rates of physical erosion? Figure 2.2 shows the results of a model run in which we drive the model with a sinusoidal physical erosion rate E_{inst} whose magnitude varies by a factor of 5 over a 10,000-year period, and in which the bedrock has a granitic mineralogy consisting of 40% plagioclase feldspar, 24.99% quartz, 20% potassium feldspar, 15% biotite, and 0.01% zircon. Table A.1 lists all other parameter values used for this model run. In the top panel of Figure 2.2 is the instantaneous physical

erosion rate E_{inst} , which we impose on the model and which drives the variations in all other variables. In the lower panels are soil thickness, soil mineral concentrations, and instantaneous and inferred chemical denudation rates. Note that the resultant soil characteristics are similar to those in mountainous granitic soils: soil thickness oscillates between 21 and 37 cm, chemical denudation rates average 27% of the denudation rate, and the average soil mineralogy (34% quartz, 18% plagioclase, 26% K-feldspar, 3% biotite, and 18% kaolinite) is, as expected, depleted in soluble minerals (plagioclase and biotite) and enriched in less soluble minerals (quartz and K-feldspar) and secondary clays (kaolinite).

We can draw several conclusions from Figure 2.2. First, the fluctuations in soil thickness, soil mineral concentrations, and chemical denudation rates are less pronounced than the fluctuations in physical erosion rates. All of the response variables are damped. Second, inferred chemical denudation rates W_{inf} are less variable in time than instantaneous chemical denudation rates W_{inst} , as the bottom panel in Figure 2.2 shows. This is not surprising; W_{inf} is intrinsically a time-averaged quantity because it is inferred from quantities that are themselves time-averaged and buffered against rapid changes in physical erosion rates – namely, concentrations of CRN and an inert tracer in the soil. Thus W_{inf} ought to be less variable in time than W_{inst} , and the model verifies that it is. Third, W_{inf} lags behind physical erosion rates; because W_{inf} is inferred from quantities that are buffered against sudden changes in physical erosion rates, it responds slowly to changes in physical erosion rates.

2.5 Generalization of model

The lower panel in Figure 2.2 shows chemical denudation rates responding to one particular set of conditions governing rates of physical erosion and mineral dissolution, and it provokes several questions about the general behavior of W_{inf} . How does the amplitude of W_{inf} depend on the amplitude and period of the physical erosion rate driver E_{inst} ? How does the response of W_{inf} depend on the values of rate constants for mineral dissolution and clay production? In order to answer these questions, we simplify and generalize the model by nondimensionalizing Equations 2.6-2.15, and in so doing we eliminate the model’s dependence on particular values for soil production parameters ϵ_0 and α and CRN production parameters P_0 and Λ . We leave the full derivation of the nondimensional equations to Appendix A, and here simply point out two important elements of the nondimensionalization. First, physical erosion rates and chemical denudation rates are scaled by the soil production coefficient ϵ_0 , such that, e.g., the nondimensional physical erosion rate \hat{E}_{inst} is zero at $E_{inst} = 0$ and \hat{E}_{inst} is 1 at $E_{inst} = \epsilon_0$. Throughout this paper nondimensional variables are denoted with a carat. Second, we scale time by a soil production timescale $T_P = \Lambda\epsilon_0^{-1}$, such that nondimensional time \hat{t} is given by

$$\hat{t} = \frac{t}{T_P} = \frac{t\epsilon_0}{\Lambda}. \quad (2.16)$$

Note that for the range of published values for ϵ_0 , one unit of nondimensional time \hat{t} translates to a range of 4,267-25,157 years in real time, for the Oregon Coast Range (Heimsath et al., 2001) and southeastern Australia (Heimsath et al., 2000), respectively.

2.6 Nondimensional model results

2.6.1 How do the amplitude and period of fluctuations in physical erosion rates affect the stability of inferred chemical denudation rates?

The extent to which inferred chemical denudation rates deviate from their long-term mean should depend on the amplitude and period of the physical erosion rates that perturb them. In Figure 2.3 we show two snapshots of the behavior of \hat{W}_{inf} in response to two physical erosion rate patterns which share the same amplitude but have different frequencies. In each of these model runs, \hat{W}_{inf} oscillates about its long-term mean with a characteristic amplitude. In the "high frequency" model run in Figure 2.3, for example, where \hat{E}_{inst} deviates from its mean by 67% and the nondimensional period of \hat{E}_{inst} is 1.5 (equivalent to 6400 years given the value for ϵ_0 used in Figure 2.2), the amplitude of \hat{W}_{inf} is 6% of the mean \hat{W}_{inf} . This is the maximum deviation of \hat{W}_{inf} ; at most moments during the model run, the deviation of \hat{W}_{inf} is less than 6% of its mean. The model runs in Figure 2.3 suggest that increasing the period of \hat{E}_{inst} increases the amplitude of deviations in \hat{W}_{inf} .

We can create a more complete picture of the stability of inferred chemical denudation rates by plotting the amplitude of \hat{W}_{inf} as a function of the amplitude and period in the physical erosion rate driver. The results are shown in Figure 2.4. These show the amplitude of \hat{W}_{inf} , defined as the maximum deviation of \hat{W}_{inf} from its mean over the course of the model run. Figures 2.4(a)-(b) show that, as expected, chemical denudation rates fluctuate to a greater degree at large amplitude oscillations in \hat{E}_{inst} and at long period oscillations in \hat{E}_{inst} . The fact that higher amplitude oscillations in \hat{E}_{inst} cause higher amplitude oscillations in \hat{W}_{inf} is not surprising; stronger forcing ought to induce a stronger response, and Figure 2.4(a) shows that it does. Longer-period oscillations in physical erosion rates, on the other hand, produce larger oscillations in chemical denudation rates because \hat{W}_{inf} takes time to respond to changes in \hat{E}_{inst} . During short-period oscillations in \hat{E}_{inst} , \hat{W}_{inf} has little time to respond to changes in \hat{E}_{inst} , and so always remains close to its mean, whereas during long-period oscillations in \hat{E}_{inst} , \hat{W}_{inf} has more time to adjust to swings in physical erosion rate, and thus deviates farther from its mean. All of this implies that \hat{W}_{inf} is more stable at physical erosion rates that oscillate at shorter periods and smaller amplitudes.

2.6.2 How do inferred chemical erosion rates compare to actual chemical erosion rates?

The analysis in section 2.6.1 show how far inferred chemical denudation rates deviate from their long-term mean. When physical erosion rates oscillate with periods much longer than the timescale of CRN accumulation (e.g., in the "low frequency" example in Figure 2.3), inferred chemical denudation rates stray far from their mean averaged over many oscillations, but do not stray as far from the mean chemical denudation rate averaged over the timescale of CRN accumulation – which is what we are trying to measure. How accurately do inferred chemical denudation rates mimic actual chemical denudation rates averaged over the CRN accumulation timescale?

We answer this question by defining a new variable, W_{avg} , as the mean chemical denudation rate averaged over the CRN accumulation timescale T_{CRN} . On a steadily eroding hillslope, T_{CRN} can be calculated as the penetration depth of cosmic-ray neutrons divided by the inferred denudation rate.

$$T_{CRN} = \frac{\Lambda}{D_{inf}} \quad (2.17)$$

This timescale depends on the value of D_{inf} , which itself changes as CRN concentrations fluctuate in response to fluctuations in physical erosion rates. In the model run in Figure 2.2, for example, T_{CRN} oscillates between 9,185 and 10,840 years. At each moment during a model run, we calculate W_{avg} as the average of all instantaneous chemical denudation rates W_{inst} stretching back over the previous T_{CRN} years. In this manner we can compare inferred chemical denudation rates (W_{inf}) to actual chemical denudation rates averaged over the timescale of CRN accumulation (W_{avg}), as Figure 2.5 shows. A comparison of Figure 2.5 with Figure 2.4 shows that inferred chemical denudation rates mimic W_{avg} more accurately than they mimic the mean chemical denudation rate averaged over many oscillations in physical erosion rate. During the largest possible swings in physical erosion rates – i.e., 100% of the mean – W_{inf} may deviate from W_{avg} by as much as 57% (Figure 2.5), but this deviation drops off quickly at smaller oscillations in physical erosion rates. When physical erosion rates oscillate by 50% of their mean, for example, W_{inf} deviates from W_{avg} by no more than 15%. These errors are not negligible, but they are small for field-derived measurements of chemical denudation rates averaged over millennial timescales.

2.6.3 How do mineral dissolution rates and clay mineral production rates affect the stability of inferred chemical denudation rates?

The literature records a wide range of published rate constants for mineral dissolution and clay production (see, e.g., reviews by White, 2003 and Price et al., 2005). How does the choice of rate constants affect the degree to which \hat{W}_{inf} deviates from its mean? In

Figure 2.6 we show the maximum amplitude of \hat{W}_{inf} – defined as in section 2.6.2 as the maximum deviation of \hat{W}_{inf} from \hat{W}_{avg} – as a function of the nondimensional rate constants for mineral dissolution and clay production. To generate a range of rate constants, in each model run we multiplied the rate constants k_X and s_X listed in Table A.1 by a single coefficient, which ranged from 0.01-1 between model runs. This approach ensured that the rate constants k_X and s_X remained within the limits of published values for mineral dissolution and clay production, and maintained the same relative magnitudes between model runs. The results in Figure 2.6 imply that the stability of \hat{W}_{inf} is not strongly affected by the choice of rate constants for mineral dissolution and clay production, and suggests that chemical denudation rates calculated with Equation 2.6 are likely to be accurate over a wide range of mineral dissolution rates and clay production rates.

What does it mean to change the nondimensional rate constants? The concentration of soluble minerals in the soil is primarily a function of two competing rates: the rate of mineral dissolution (a function of kA) and the rate of fresh mineral supply (a function of α and ϵ_0). Soluble minerals are depleted in the soil more quickly at faster dissolution rates (i.e., at higher values of k) and are replenished more quickly at faster soil production rates (i.e., at higher values of ϵ_0). Soil mineral concentrations thus reflect the balance between mineral dissolution and mineral supply. This suggests that the most important factor controlling soil mineral concentrations is not the absolute values of the mineral dissolution rates, but rather the values of the dissolution rates relative to the soil production rate. A useful means of comparing these rates is by examining the timescales associated with each rate. We define a mineral dissolution timescale $T_k = k^{-1}A^{-1}$ such that the nondimensional dissolution rate constant $\hat{k}\hat{A}$ is the ratio between the soil production timescale $T_P = \Lambda\epsilon_0^{-1}$ and the mineral dissolution timescale.

$$\hat{k}\hat{A} = \frac{kA\Lambda}{\epsilon_0} = \frac{T_P}{T_k} \quad (2.18)$$

When the soil production timescale T_P is much shorter than the dissolution timescale T_k , fresh soil is produced faster than soluble minerals are depleted in the soil; in this situation, soil mineral concentrations vary little over time and remain close to the mineral concentrations of the parent rock. By contrast, when T_P is much longer than T_k , soluble minerals are depleted from the soil more quickly than soil production can replenish them; in this situation, soil mineral concentrations vary more widely and depend strongly on the rate of soil production.

2.6.4 Chemical denudation rates at steady physical erosion rates

Up to this point, we have only examined the transient response of inferred chemical denudation rates to non-steady physical erosion rates. Now we consider chemical denudation rates under steady physical erosion rates. This steady-state behavior sheds light on the transient model results, because the response of chemical denudation rates to a shift in physical erosion rates can be understood as a transition from one steady-state chemical denudation rate to another.

According to the model, at any steady physical erosion rate there is a corresponding steady chemical denudation rate. We can calculate steady-state chemical denudation rates by setting the time derivatives in Equations 2.11-2.14 to zero, solving for steady-state soil thickness, CRN and mineral concentrations, and substituting these values into Equation 2.15. The results indicate a nonlinear dependence of chemical denudation rates on physical erosion rates. As Figure 2.7(c) shows, modeled chemical denudation rates approach zero at both $\hat{E} = 0$ and $\hat{E} = 1$ (i.e., at $E = 0$ and $E = \epsilon_0$), and reach a maximum at an intermediate physical erosion rate. Why does the model predict this relationship?

The nonlinear dependence of chemical denudation rates on physical erosion rates can be understood from the variations in soil thickness and soil mineral concentrations in Figures 2.7(a) and (b). As physical erosion rates approach the maximum soil production rate (i.e., as $E \rightarrow \epsilon_0$), soil thickness shrinks towards zero and soil mineral concentrations approach the concentrations of the parent rock. Conversely, as $E \rightarrow 0$, soil thickness increases and the soil residence time increases as well, with the consequence that the more soluble minerals (here plagioclase and biotite) are depleted to a greater extent because they have more time to dissolve. Thus, as physical erosion rates decrease, concentrations of the more soluble minerals decrease too. Our numerical model assumes that the chemical denudation rate of a single mineral phase scales linearly with the mass of that phase in the soil, and that the total chemical denudation rate is the sum of the chemical denudation rates of all the mineral phases. This can be simplified by recognizing that some mineral phases are several orders of magnitude more soluble than others (see the relative solubilities listed in Table A.1), so to first order total chemical denudation rates depend only on the mass of the most soluble mineral phases in the soil. Thus to first order, chemical denudation rates are proportional to the product of the soil mass and the concentration of those soluble minerals in the soil. As concentrations of soluble minerals in the soil approach zero (which occurs as $E \rightarrow 0$), chemical denudation rates also approach zero. Similarly, as soil thickness approaches zero (which occurs as $E \rightarrow \epsilon_0$), chemical denudation rates also approach zero. In short, the model predicts that chemical denudation rates approach zero at both $E = 0$ and at $E = \epsilon_0$ because soluble minerals disappear as $E \rightarrow 0$ and the soil itself disappears as $E \rightarrow \epsilon_0$.

2.7 Discussion

The model presented in this paper simulates how soil bulk mineralogy and cosmogenic radionuclide concentrations evolve under forcing by an arbitrary temporal pattern in physical erosion rates. It then compares the "actual" (simulated) chemical denudation rates with those that would be inferred from the concentrations of cosmogenic nuclides and immobile elements. We have primarily used this model to estimate how much inferred rates deviate from actual rates when physical erosion rates vary over time. The model results show that even when physical erosion rates are not steady in time, chemical denudation rates inferred with Equation 2.6 should closely approximate actual chemical denudation rates averaged over the timescale of cosmogenic radionuclide accumulation, especially

during short-period oscillations in physical erosion rates. When physical erosion rates vary over short timescales (i.e., those on the order of the CRN accumulation time or shorter), the inferred chemical denudation rate W_{inf} is an averager – it smooths out fluctuations in instantaneous chemical denudation rates, and closely resembles the long-term mean. Over long timescales (i.e., those on the order of ten CRN accumulation times or longer), W_{inf} is a follower – it mirrors fluctuations in physical erosion rates. We find that W_{inf} is an accurate recorder of actual chemical denudation rates over a wide range of amplitudes and periods in physical erosion rates and a wide range of mineral dissolution rates and secondary mineral production rates. For example, given the rate constants for mineral dissolution and soil production used in Table A.1 (which, notably, produce soils similar to those in mountainous granitic terrain), the model predicts that when physical erosion rates fluctuate by 50% of the mean, inferred chemical denudation rates deviate from the mean chemical denudation rate averaged over the CRN accumulation timescale by no more than 1% during 1,000-year oscillations in physical erosion rates, by 9% during 10,000-year oscillations, and 12% during 100,000-year oscillations. These are the maximum deviations predicted by the model; at most times during the model runs, the discrepancies between inferred and actual chemical denudation rates are smaller.

Is the numerical model outlined in this paper an accurate description of nature? As with any model, it is only as accurate as the assumptions behind it. The major assumptions in the model concern the parameterization of processes that form and erode soil. The first assumption is that soil forms strictly from the bedrock underneath it, and that this process is completely characterized by the soil production function of Heimsath et al. (1997), in which denudation rates decrease exponentially with increasing soil thickness. The second important assumption is that mineral dissolution rates depend only on soil mineral mass, specific surface area, and reactivity. Such a formulation ignores any other factors that might speed or slow dissolution, such as microbial activity, pH, temperature, mineral coatings, and the saturation state of the soil pore water relative to the surrounding minerals. These factors may influence mineral dissolution processes, but they have been left out of the model in the interest of simplicity and tractability. Furthermore, these missing factors may be subsumed in the rate constants for mineral dissolution themselves. Regardless of the influences of these factors, we submit that chemical denudation rates should still scale with the quantity of minerals available to be weathered. Thus, while the model is a highly simplified version of nature, it nonetheless should accurately mimic nature to the degree that the soil production function applies and mineral dissolution rates scale with the total mineral mass in the soil.

Our model also makes a prediction about the steady-state relationship between rates of chemical denudation and physical erosion, a topic of interest in the study of Earth’s long-term geomorphic and climatic evolution. Some have theorized that periods of rapid tectonic uplift (and hence rapid physical erosion) might also be marked by rapid chemical weathering because fresh minerals are brought more rapidly to the Earth’s surface where weathering occurs (e.g., Raymo et al. 1988). This assumes that chemical weathering rates increase with increasing physical erosion rates. The model outlined in this paper predicts a different relationship; it predicts that chemical denudation rates increase with physical

erosion rates, but only up to a point, beyond which chemical denudation rates decrease with further increases in physical erosion rates, a prediction consistent with the hypothesis of Anderson et al. (2002) and the predictions of a landslide model by Gabet (2007). If we drive the model with steady erosion, weathering rates can decline to zero at sufficiently high erosion rates. If instead we drive the model with episodic erosion to mimic the periodic growth and removal of soil under intermittent landsliding, chemical denudation rates can still be greater than zero at very high physical erosion rates because the average soil residence time can be greater than zero. This model prediction also hinges on the assumption that all chemical denudation on hillslopes occurs within the soil; hence as soil thickness approaches zero (in response to very high physical erosion rates), so too chemical denudation rates approach zero. This assumption is not strictly valid because some chemical denudation occurs within the bedrock as groundwater percolates through fractures and dissolves minerals that are highly susceptible to chemical weathering, such as calcite (e.g., White et al., 1999b). However, as long as chemical denudation rates in bedrock are much smaller than chemical denudation rates in soil – as is likely to be the case in granites, which typically contain about 0.1% calcite by mass (White et al., 1999b) – total chemical denudation rates should decrease as physical erosion rates approach soil production rates, as may occur in steep catchments with thin soils. This is a testable prediction, and the degree to which it matches field measurements could indicate how well this model reflects soil formation, denudation, and mineral dissolution under field conditions.

2.8 Acknowledgments

We thank two anonymous reviewers and editor R. Carlson for insightful and constructive comments that significantly improved this manuscript. Our work was supported by a SEGRF fellowship from Lawrence Livermore National Laboratory to K.L.F. and NSF grant EAR-0643129 to J.W.K. K.L.F. thanks Elsevier for permission to reprint this previously published paper (Ferrier and Kirchner, 2008, *Earth and Planetary Science Letters*, v. 272, p. 591-599) in this dissertation.

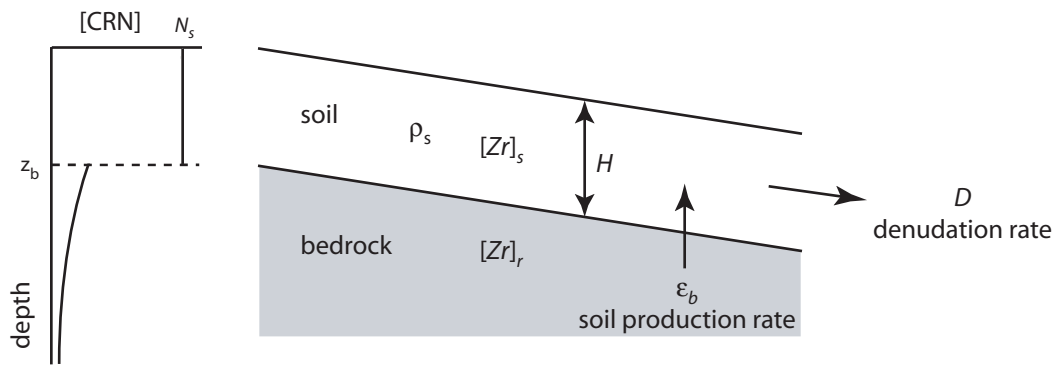


Figure 2.1. In the idealized soil-mantled hillslope pictured here, soil is produced at the soil-bedrock boundary at a rate ϵ_b and is lost downslope at a denudation rate D . In steady state, soil production rates match denudation rates, and the mass of soil per unit area (given by soil density ρ_s times soil thickness H) is constant in time. For a steady-state hillslope such as this, it is possible to infer chemical denudation rates by combining measurements of cosmogenic radionuclide (CRN) concentrations in the soil with measurements of the average immobile element concentrations in soil and its parent bedrock ($[Zr]_s$ and $[Zr]_r$, respectively).

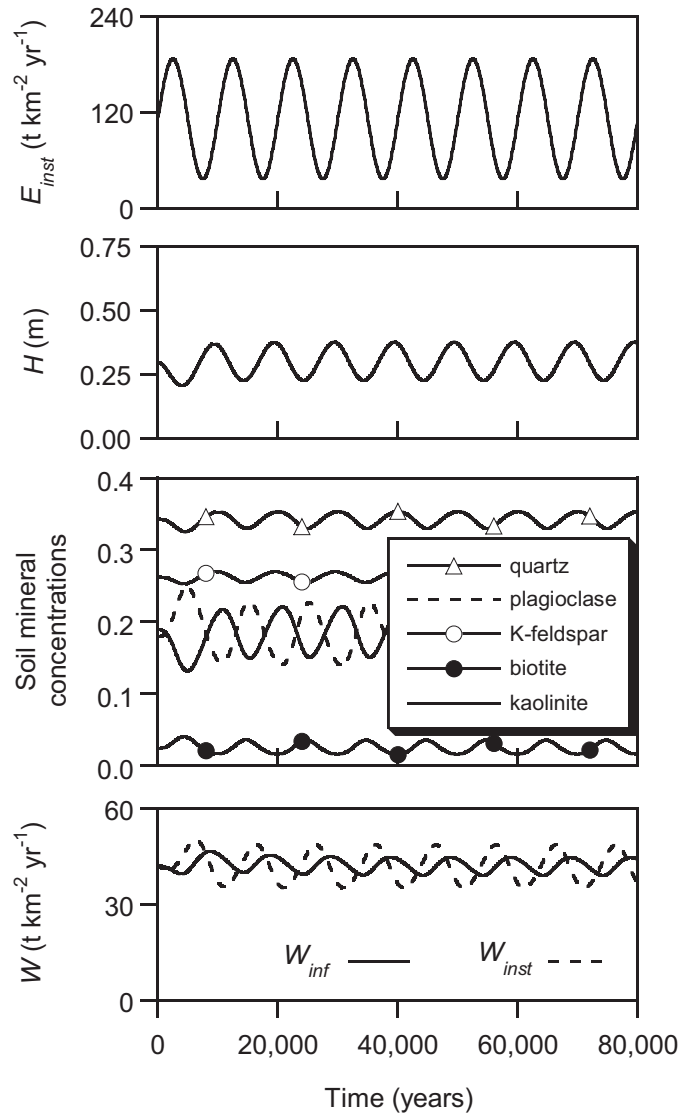


Figure 2.2. Results of one model run. In the top panel is the instantaneous physical erosion rate E_{inst} , which we impose on the model and which drives variations in all other variables. In the lower panels are soil thickness H , soil mineral concentrations (in kg mineral/kg soil), and instantaneous and inferred chemical denudation rates W_{inst} and W_{inf} , calculated with Equations 2.15 and 2.6, respectively. In this model run we have set soil production constants to $\epsilon_0 = 375 \text{ t km}^{-2} \text{ yr}^{-1}$ and $\alpha = 3 \text{ m}^{-1}$ (Heimsath et al., 2001). Values for all other rate constants used in this model run are listed in Table A.1.

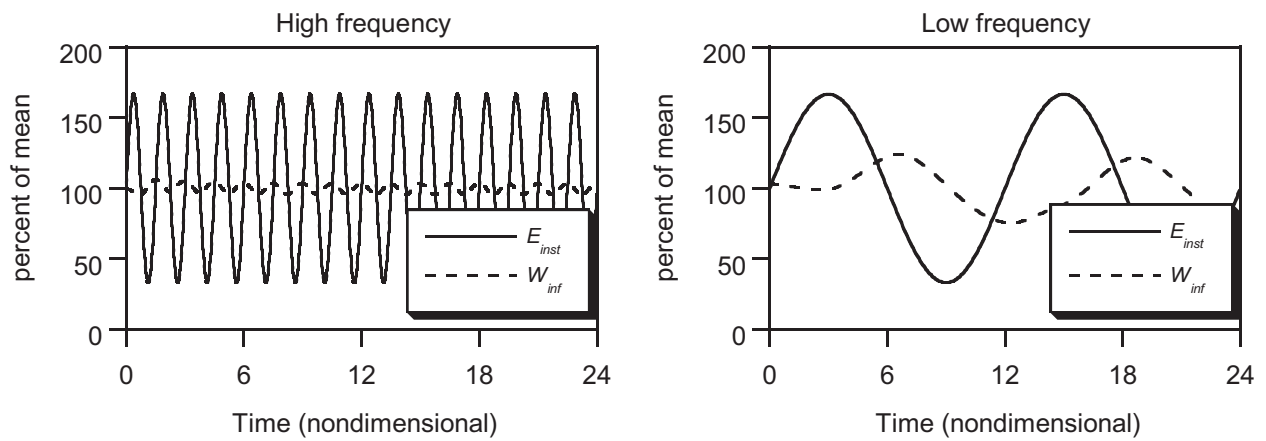


Figure 2.3. Responses of inferred chemical denudation rates to two physical erosion rate patterns of the same amplitude and different periods. Each plot shows instantaneous physical erosion rates E_{inst} (imposed upon the model) and inferred chemical denudation rates W_{inf} (responding to E_{inst}) as percentages of their means over the course of a model run. Nondimensional parameter values used in these runs are listed in Table A.2. These figures suggest that inferred chemical denudation rates vary more widely under longer period oscillations in physical erosion rate.

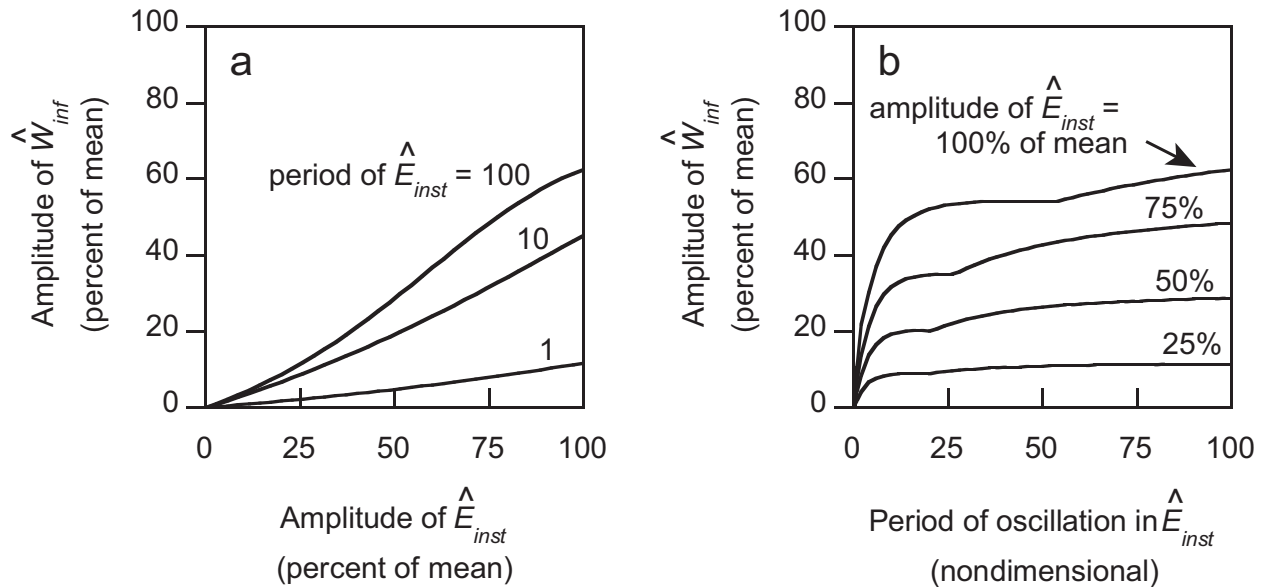


Figure 2.4. Figures 2.4(a) and (b) depict the amplitude of \hat{W}_{inf} – defined as the maximum deviation of chemical denudation rates from their long-term mean – as a function of the amplitude and period of imposed oscillations in physical erosion rate \hat{E}_{inst} . (By way of example, in the "high frequency" panel of Figure 2.3, in which \hat{E}_{inst} has a nondimensional period of 1.5 and an amplitude of 67% of the mean, the amplitude of \hat{W}_{inf} is 6% of its mean.) Here, in Figure 2.4, physical erosion rates oscillated around a mean \hat{E}_{inst} of 0.35. Nondimensional parameter values used in these runs are listed in Table A.2. These figures indicate that inferred chemical denudation rates fluctuate to a greater degree under high-amplitude and long-period oscillations in physical erosion rate. Even under very high amplitude and very long period oscillations in \hat{E}_{inst} , however, \hat{W}_{inf} is less variable than \hat{E}_{inst} .

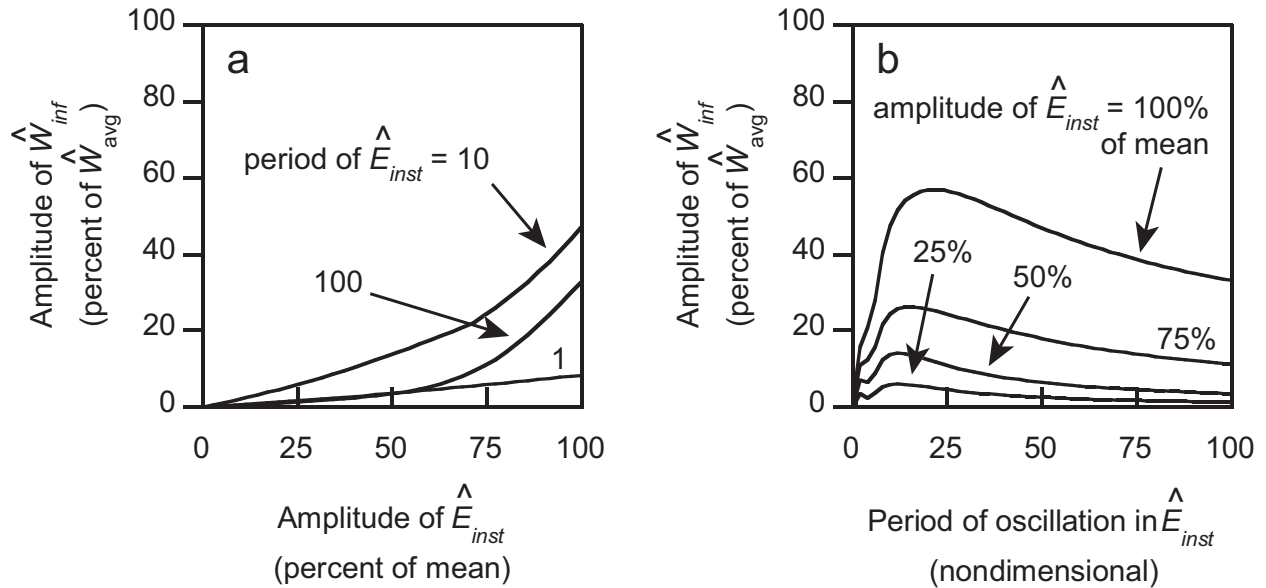


Figure 2.5. These show the degree to which inferred chemical denudation rates \hat{W}_{inf} deviate from \hat{W}_{avg} , where \hat{W}_{avg} is the mean chemical denudation rate averaged over the CRN accumulation timescale. Nondimensional parameter values used in these runs are listed in Table A.2. Note that the amplitudes of \hat{W}_{inf} in Figure 2.5 are smaller than in Figure 2.4; this indicates that deviations of \hat{W}_{inf} from \hat{W}_{avg} are smaller than deviations of \hat{W}_{inf} from the mean chemical denudation rate averaged over many oscillations in physical erosion rates. \hat{W}_{inf} is thus a more accurate estimate of chemical denudation rates averaged over the CRN accumulation timescale than over the period of oscillation in physical erosion rates.

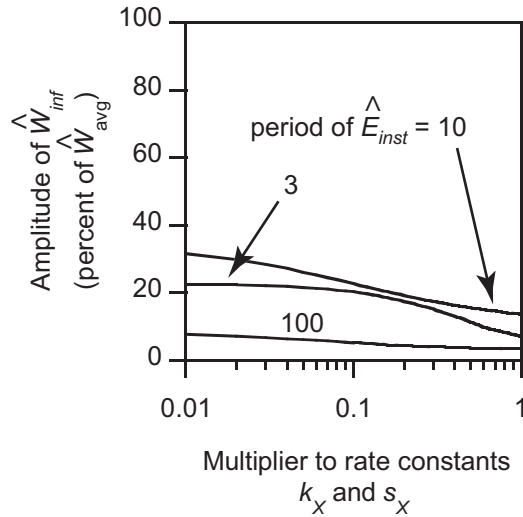


Figure 2.6. This depicts the amplitude of \hat{W}_{inf} – defined as the maximum deviation of \hat{W}_{inf} from \hat{W}_{avg} – as a function of the magnitude of the rate constants for mineral dissolution \hat{k}_X and clay production \hat{s}_X , relative to their magnitudes in Table A.1. To generate a range of rate constants, in each model run we multiplied the rate constants \hat{k}_X and \hat{s}_X in Table A.1 by a single coefficient that ranged from 0.01-1 between model runs. This approach ensured that \hat{k}_X and \hat{s}_X maintained the same relative magnitudes between model runs and remained within the range of published values for mineral dissolution and clay production rate constants. During these model runs, we held the amplitude of \hat{E}_{inst} constant at 50% of its mean. This figure suggests that the magnitude of the rate constants for mineral dissolution and clay production have only a small effect on the degree to which inferred chemical denudation rates deviate from average chemical denudation rates during non-steady physical erosion.

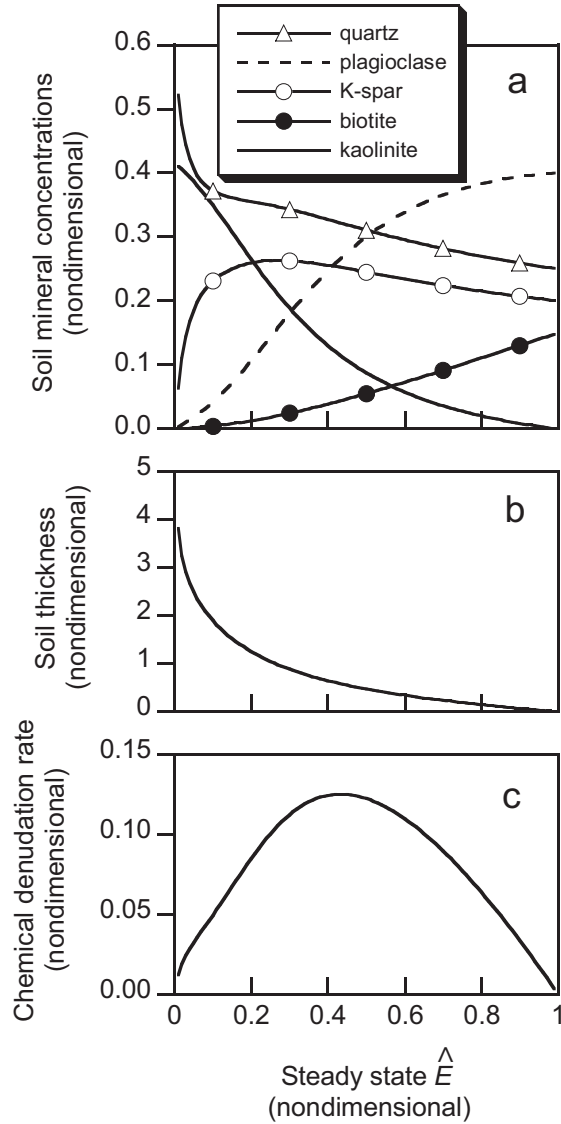


Figure 2.7. Soil mineral concentrations, soil thickness, and chemical denudation rates as a function of steady-state physical erosion rate \hat{E} . Nondimensional parameter values used in these runs are listed in Table A.2. Chemical denudation rates approach zero at both $\hat{E} \rightarrow 0$ and $\hat{E} \rightarrow 1$ (i.e., as $E \rightarrow 0$ and $E \rightarrow \epsilon_0$) because soluble minerals become depleted in the soil as $E \rightarrow 0$ and because soil thickness approaches zero as $E \rightarrow \epsilon_0$.

Chapter 3

Mineral-specific chemical weathering rates over millennial timescales: Measurements at Rio Icacos, Puerto Rico

3.1 Abstract

Mineral weathering plays a prominent role in many biogeochemical and geomorphological processes. It supplies nutrients to soils and streams, accelerates physical erosion by weakening bedrock and producing easily erodible soil, and modulates Earth's long-term climate by drawing down atmospheric carbon dioxide. We calculate mineral-specific chemical weathering rates at two field sites in the Rio Icacos catchment, Puerto Rico, by combining new mineral abundance measurements from quantitative powder X-ray diffraction (XRD) with existing measurements of (i) soil production rates from cosmogenic nuclides, (ii) chemical alteration of the regolith from X-ray fluorescence (XRF), and (iii) dust deposition rates. Our results suggest that combining measurements of cosmogenic nuclides with XRF-based geochemistry and XRD-based mineralogy can, in favorable cases, provide weathering rates of abundant, soluble mineral phases in actively eroding terrain to an accuracy of better than 20% of the mean. Mineral weathering at our two field sites is dominated by plagioclase, at rates of $3285 \pm 573 \text{ mol ha}^{-1} \text{ yr}^{-1}$ and $3085 \pm 538 \text{ mol ha}^{-1} \text{ yr}^{-1}$, followed by hornblende, at $188 \pm 69 \text{ mol ha}^{-1} \text{ yr}^{-1}$ and $309 \pm 92 \text{ mol ha}^{-1} \text{ yr}^{-1}$. Within the uncertainty of our data, all weathering of these primary minerals occurs below the saprolite-soil interface. Our measurements imply that kaolinite production in saprolite is roughly 1.3 times faster than kaolinite weathering in the soil. Our results show that this geochemical mass balance approach can be useful in quantifying long-term rates of mineral weathering and secondary mineral production in both saprolite and soil on actively eroding hillslopes, implying that it can be a valuable tool for

quantifying the effects of climate, vegetation, tectonics, and other factors on weathering rates of individual mineral phases.

3.2 Introduction

Plants, animals, and landforms are all influenced by mineral weathering. As primary minerals dissolve, they provide the nutritional foundation for terrestrial biogeochemistry by releasing solutes to natural waters and promoting secondary mineral precipitation. As bedrock is weathered to soil, it loses much of its shear strength and thus its resistance to physical erosion, leading to important differences in rates and processes of erosion in soil-mantled and bedrock landscapes. To the extent that silicate dissolution rates increase with temperature, silicate weathering regulates Earth's long-term surface temperature via the greenhouse effect, because silicate chemical weathering is the dominant sink for atmospheric CO₂ over million-year timescales (Walker et al., 1981; Berner et al., 1983). Thus, predicting the responses of landscapes, biota, and atmospheric CO₂ concentrations to changes in environmental factors such as temperature, precipitation, and pH requires measuring how these factors influence mineral weathering rates over the long timescales of mineral weathering in the field.

A number of techniques have been used to measure mineral weathering rates. Dissolution rates have often been measured in laboratory experiments (e.g., Chou and Wollast, 1984; Swoboda-Colberg and Drever, 1993; Anbeek et al., 1994), but these lab-derived rates are typically several orders of magnitude faster than field-derived rates (White and Brantley, 2003, and references therein), reflecting differences between the lab and the field in both the weathering environment (e.g., in deviations of the pore fluid from thermodynamic saturation) and in the mineral surfaces themselves (e.g., in mineral surface area, density of structural heterogeneities, and leached layers and clay coatings that build up over time). In field settings, chemical erosion rates of individual mineral phases were first inferred by ascribing solute fluxes of particular elements (e.g., sodium) to dissolution of particular minerals (e.g., albite). This approach, pioneered in Garrels and Mackenzie (1967), has since been extended to rationalize a suite of solute fluxes in terms of a suite of mineral weathering rates, and has been applied at a number of catchments (e.g., Cleaves et al., 1970; Paces, 1983; Velbel, 1985; Clayton, 1986; Taylor and Velbel, 1991; Swoboda-Colberg and Drever, 1993; Clow and Drever, 1996; Price et al., 2005). Inferring mineral weathering rates with this catchment-scale solute mass-balance method requires measuring the export of solutes from the catchment in streamwater, the import of solutes by atmospheric deposition, and any changes in solute storage within the catchment. These additional sources and sinks of solutes can be significant fractions of the outgoing solute fluxes and can have large uncertainties, which may confound interpretations of catchment-scale mineral dissolution rates (e.g., Taylor and Velbel, 1991). At the finer scale of a weathering profile, mineral weathering rates may also be inferred from gradients in vertical solute fluxes within the soil and saprolite (Murphy et al., 1998; White, 2002, 2003; White et al., 2005, 2008).

In this paper we measure field-derived mineral weathering rates by combining concentrations of minerals and immobile elements in the bedrock and the regolith – where the regolith is defined as the entirety of weathered material overlying bedrock – with measurements of the soil production rate, under the assumption that the composition and mass per unit area of the regolith are in steady state. Classified as a solid-phase mass-balance method because it relies on measurements of the bulk chemistry and mineralogy of regolith and bedrock, this approach has appeared in several different formulations in the literature; we refer the reader to Riebe et al. (in review) for a quantitative review of several of these methods. Here we use an extension of the mass balance formulation in Stallard (1985) to calculate mineral weathering rates. After presenting the mathematical framework for this approach in section 3.3, we use this method to infer mineral weathering rates in section 3.6 at two sites in the Rio Icacos catchment, Puerto Rico.

3.3 A steady-state framework for measuring mineral-specific chemical weathering rates in saprolite and soil

Chemical weathering rates can be determined by combining measurements of chemical mass loss (inferred from immobile element enrichment in regolith relative to bedrock) with an appropriate rate constant derived from, e.g., the age of the soil in non-eroding landscapes (Merritts et al., 1991), or the overall flux of material from the regolith (Stallard, 1985) measured with cosmogenic nuclides (White et al., 1998; Riebe et al., 2001a). Here we review the theoretical underpinnings for this technique. The mathematical framework is an extension of a formulation proposed by Stallard (1985), and it follows Owen et al. (2008) in its inclusion of dust deposition in the mass balance and it follows Dixon et al. (2009) in its application to both saprolite and soil. Unlike some studies (Mudd and Furbish, 2004; Green et al., 2006; Yoo et al., 2007; Owen et al., 2008), the framework presented here assumes that downslope gradients in soil composition are negligible. However, it extends the model by explicitly demonstrating how mineral-specific weathering rates may be calculated in saprolite and soil.

We begin by considering an actively eroding hillslope (Figure 3.1) in which both soil and saprolite maintain a constant mass per unit area of hillslope per time. Saprolite is defined here as chemically weathered bedrock, susceptible to mass loss by chemical dissolution but not by physical erosion. We distinguish soil from saprolite by defining soil as the portion of the weathered profile that is physically mobile, and thus is susceptible to mass losses by both chemical dissolution and physical erosion. In steady state, the rate at which mass is added to the soil – i.e., the soil production rate P_{soil} plus the dust deposition rate P_d – is balanced by the rate at which mass is lost from the soil.

$$P_{soil} + P_d = E + W_{soil} \quad (3.1)$$

Here E and W_{soil} are the physical erosion rate and chemical erosion rate in soil, and, like P_{soil} and P_d , have dimensions of mass per unit area of hillslope per time. The flux of an individual mineral or element X into the soil is the sum of the influxes of X from the saprolite and dust, and in steady state this rate is matched by the rate at which X is lost from the soil by physical erosion and chemical erosion.

$$P_{soil}X_{sap} + P_dX_d = EX_{soil} + W_{soil,X}. \quad (3.2)$$

Here X_{sap} , X_{soil} , and X_d are the concentrations (mol M⁻¹) of X in saprolite, soil, and dust, respectively, and $W_{soil,X}$ is the chemical erosion rate of X in the soil (mol L⁻² T⁻¹). If X is a chemically "immobile" element or mineral – that is, if X is so resistant to dissolution that its chemical erosion rate $W_{soil,X}$ is negligible – then Equation 3.2 yields the following expression for the physical erosion rate:

$$E = P_{soil} \frac{Zr_{sap}}{Zr_{soil}} + P_d \frac{Zr_d}{Zr_{soil}}. \quad (3.3)$$

Here we have substituted zirconium, which occurs predominantly in zircons and which is frequently assumed to be immobile, for X . Equation 3.3 can be combined with Equation 3.1 to yield an expression for the soil chemical erosion rate W_{soil} .

$$W_{soil} = P_{soil} \left(1 - \frac{Zr_{sap}}{Zr_{soil}}\right) + P_d \left(1 - \frac{Zr_d}{Zr_{soil}}\right) \quad (3.4)$$

Similarly, substituting Equation 3.3 into Equation 3.2 yields an expression for the chemical weathering rate of mineral phase X in the soil.

$$W_{soil,X} = P_{soil} \left(X_{sap} - X_{soil} \frac{Zr_{sap}}{Zr_{soil}}\right) + P_d \left(X_d - X_{soil} \frac{Zr_d}{Zr_{soil}}\right) \quad (3.5)$$

A similar analysis to Equations 3.1-3.5 provides expressions for the same rates in saprolite. If the combined mass of saprolite and soil stays constant over time and if dust deposition does not affect saprolite composition, then the rate at which bedrock is converted to saprolite – i.e., the saprolite production rate P_{sap} – is balanced by the rate at which mass is lost from the soil and saprolite, commonly called the denudation rate.

$$P_{sap} = P_{soil} + W_{sap} \quad (3.6)$$

In steady state, conservation of mass for a mineral or element X implies that

$$P_{sap}X_{rock} = P_{soil}X_{sap} + W_{sap,X}. \quad (3.7)$$

For an immobile element like zirconium, $W_{sap,Zr}$ is negligible and Equation 3.7 then yields an expression for the saprolite production rate in terms of the soil production rate and the concentrations of zirconium in saprolite and bedrock.

$$P_{sap} = P_{soil} \frac{Zr_{sap}}{Zr_{rock}} \quad (3.8)$$

Substituting Equation 3.8 into Equation 3.6 yields the bulk chemical erosion rate in saprolite W_{sap} ,

$$W_{sap} = P_{soil} \left(\frac{Zr_{sap}}{Zr_{rock}} - 1 \right), \quad (3.9)$$

and substituting Equation 3.8 into Equation 3.7 yields the mineral-specific chemical weathering rate in saprolite $W_{sap,X}$.

$$W_{sap,X} = P_{soil} \left(X_{rock} \frac{Zr_{sap}}{Zr_{rock}} - X_{sap} \right) \quad (3.10)$$

If we again use the term "regolith" to mean the soil and saprolite together, then the bulk chemical erosion rate and the mineral-specific chemical weathering rates in the regolith are

$$\begin{aligned} W_{regolith} &= W_{soil} + W_{sap} \\ &= P_{soil} Zr_{sap} \left(\frac{1}{Zr_{rock}} - \frac{1}{Zr_{soil}} \right) + P_d \left(1 - \frac{Zr_d}{Zr_{soil}} \right) \end{aligned} \quad (3.11)$$

and

$$\begin{aligned} W_{regolith,X} &= W_{soil,X} + W_{sap,X} \\ &= P_{soil} Zr_{sap} \left(\frac{X_{rock}}{Zr_{rock}} - \frac{X_{soil}}{Zr_{soil}} \right) + P_d \left(X_d - X_{soil} \frac{Zr_d}{Zr_{soil}} \right), \end{aligned} \quad (3.12)$$

respectively.

At field sites that have soil and bedrock but no saprolite (or saprolite that is not substantially depleted by chemical losses), W_{sap} and $W_{sap,X}$ are zero and Equations 3.11 and 3.12 simplify to

$$\begin{aligned} W_{regolith} &= W_{soil} \\ &= P_{soil} \left(1 - \frac{Zr_{rock}}{Zr_{soil}} \right) + P_d \left(1 - \frac{Zr_d}{Zr_{soil}} \right) \end{aligned} \quad (3.13)$$

and

$$\begin{aligned} W_{regolith,X} &= W_{soil,X} \\ &= P_{soil} \left(X_{rock} - X_{soil} \frac{Zr_{rock}}{Zr_{soil}} \right) + P_d \left(X_d - X_{soil} \frac{Zr_d}{Zr_{soil}} \right), \end{aligned} \quad (3.14)$$

respectively (Riebe et al., 2001b, 2003, 2004b,a).

Mineral-specific chemical weathering rates in soil and saprolite can thus be estimated by measuring the soil production rate and concentrations of minerals and immobile elements in soil, saprolite, dust, and bedrock. In cases where dust influxes are negligible, all terms that include P_d become insignificant and these expressions converge to the same expressions derived in Dixon et al. (2009), as they should.

Below we use this mass-balance framework to calculate mineral-specific chemical weathering rates at two sites in Rio Icacos, Puerto Rico. We do so by combining new measurements of mineral concentrations estimated with quantitative X-ray diffraction (XRD) with previous measurements of soil production rates estimated from cosmogenic ^{10}Be concentrations in soil-borne quartz (Riebe et al., 2003), immobile element concentrations in soil, saprolite, and bedrock measured with X-ray fluorescence (XRF) (Riebe et al., 2003), and dust flux and dust composition (Pett-Ridge et al., 2009; Glaccum and Prospero, 1980; Herwitz et al., 1996).

3.4 Field sites: Rio Icacos, Puerto Rico

We measured mineral-specific chemical weathering rates in two small tributary catchments of Rio Icacos in Puerto Rico's Luquillo Mountains (Figure 3.2), in a densely vegetated tropical rainforest where the climate is hot (mean annual temperature = 22°C ; White et al., 1998) and humid (mean annual precipitation = 4300 mm yr^{-1} ; McDowell and Asbury, 1994). The Rio Blanco quartz diorite that underlies the catchment is dominated by plagioclase feldspar and quartz, with lesser amounts of hornblende, biotite, and accessory potassium feldspar (Seiders, 1971; White et al., 1998). Directly above the bedrock is a narrow zone of saprock a few tens of cm thick (White et al., 1998), in which pristine rock rapidly grades to deeply weathered saprolite. Above the saprock lies an oxidized saprolite layer up to eight meters thick, and although the saprolite appears physically undisturbed its density ($1.19\text{-}1.35\text{ g cm}^{-3}$) is less than half that of its parent rock (2.70 g cm^{-3}), reflecting the near-total loss of plagioclase and hornblende (White et al., 1998). Above the saprolite is a low-density ($1.19\text{-}1.37\text{ g cm}^{-3}$), bioturbated inceptisol 50-100 cm thick, which grades from an organic-rich A horizon in the upper ten cm of the profile to a clay-rich B horizon at depths greater than 40 cm (White et al., 1998; Buss et al., 2005).

Rio Icacos has been the site of many chemical weathering studies. Measurements of solute fluxes in soils and streams at Rio Icacos have yielded bulk chemical weathering fluxes over annual to decadal timescales (McDowell and Asbury, 1994; Stonestrom et al., 1998; White et al., 1998), and long-term bulk chemical weathering rates have been calculated from the chemical and isotopic compositions of regolith relative to parent bedrock (Stonestrom et al., 1998; White et al., 1998; Riebe et al., 2003). Mineral-specific chemical weathering rates at Rio Icacos have been inferred for plagioclase feldspar (Turner et al., 2003; Buss et al., 2008), biotite (Murphy et al., 1998; White, 2002; Buss et al., 2008), hornblende (Buss et al., 2008), and quartz (Schulz and White, 1999). These studies show that silicate weathering rates at Rio Icacos are among the fastest documented on Earth.

Dust deposition plays an important role in contributing mass to the soils in Rio Icacos. A number of studies examining dust transport from northern Africa to the Caribbean have concluded that African dust is a major driver of soil development on many Caribbean islands (e.g., Prospero et al., 1970, 1981; Prospero and Lamb, 2003; Glaccum and Prospero, 1980; Muhs et al., 1990, 2007; Herwitz et al., 1996; Mahowald et al., 2006).

There have been no direct physical measurements of dust deposition rates in the Rio Icacos catchment, but a recent study has concluded, based on discrepancies between inputs and outputs in a Rio Icacos Sr isotope budget, that Saharan dust contributes $21 \pm 7 \text{ t km}^{-2} \text{ yr}^{-1}$ to the Rio Icacos catchment (Pett-Ridge et al., 2009), an estimate consistent with predictions of atmospheric dust transport models (Mahowald et al., 2006). Given that millennial-timescale soil production rates from saprolite are 113 ± 17 and $118 \pm 17 \text{ t km}^{-2} \text{ yr}^{-1}$ at our two Rio Icacos field sites (Riebe et al., 2003; discussed further in section 3.5), a dust flux of $21 \pm 7 \text{ t km}^{-2} \text{ yr}^{-1}$ represents a nontrivial contribution to Rio Icacos soils. We are unaware of any direct measurements of dust mineralogy or Zr concentrations at Rio Icacos. However, measurements in Barbados and Miami of dust mineralogy from Saharan dust outbreaks show little variation in dust mineralogy across the Caribbean (Glaccum and Prospero, 1980), consistent with homogenization of Saharan dust during transatlantic transport (e.g., Reid et al., 2003). This suggests that Saharan dust falling in Puerto Rico, which lies between Barbados and Miami, is likely to have a composition similar to Saharan dust measured at Barbados and Miami.

3.5 Methods

Equations 3.5 and 3.10 provide a framework for determining chemical weathering rates of individual mineral phases in soil and saprolite on actively eroding hillslopes, and this framework is independent of the techniques used to measure soil production rates, immobile element concentrations, and mineral abundances. Here we describe the particular techniques we used to measure each of these quantities.

3.5.1 Measuring soil production rates with cosmogenic nuclides

We inferred soil production rates from concentrations of cosmogenic ^{10}Be in soil-borne quartz. Beryllium-10 is produced in quartz only through interactions of cosmogenic high-energy neutrons and muons with atomic nuclei in the crystal lattice (e.g., Lal, 1991). Because the fluxes of these cosmogenic particles decrease exponentially below the Earth's surface, the rate of ^{10}Be production in quartz also decreases exponentially with depth. Concentrations of ^{10}Be in quartz collected from surface soils thus record the integrated exposure of quartz to cosmogenic radiation during its exhumation from depth. Several studies have shown that the steady-state soil denudation rate may be inferred from cosmogenic nuclide concentrations in the rock underlying the soil (e.g., Heimsath et al., 1997) or, if production of cosmogenic nuclides in the soil during downslope soil transport is negligible relative to the production of cosmogenic nuclides during exhumation, in the soil itself (e.g., Brown et al., 1995; Granger et al., 1996). Under the steady state assumption, the soil production rate equals the soil denudation rate. In this paper we use the ^{10}Be measurements and data analyses of Riebe et al. (2003), which should be seen for details of the ^{10}Be analyses.

For our ^{10}Be measurements at each study catchment (RI-1 and RI-4 in Figure 3.2), we collected surface soils at distributed locations, and amalgamated these soils to obtain a bulk soil sample representative of the average catchment soil (Riebe et al., 2003). ^{10}Be concentrations were measured in quartz extracted from the > 250 micron size fraction of these amalgamated soil samples, a practice that excludes dust-derived quartz, which is likely composed almost entirely of particles smaller than 20 microns, based on dust measurements elsewhere in the Caribbean (Prospero et al., 1970). In light of recent efforts by the cosmogenic isotope research community to standardize calculation of cosmogenic-based denudation rates (Balco et al., 2008), and because our new measurements of quartz abundances at Rio Icacos permit calculation of a correction factor due to quartz enrichment in the soil (Small et al., 1999; Riebe et al., 2001a), we have recalculated soil production rates with the CRONUS calculator (Balco et al., 2008) rather than using the rates previously calculated for these Rio Icacos sites by Riebe et al. (2003). The CRONUS calculator takes as inputs the relevant sample characteristics (latitude and longitude, elevation, topographic shielding, sample thickness, parent material density, and the measured ^{10}Be concentration, for which values specific to RI-1 and RI-4 are listed in Table 3.1) and computes soil production rates using several different cosmogenic nuclide production scaling schemes (see Balco et al., 2008 for details). We use the Lal and Stone constant production rate scaling scheme in our analysis (Lal, 1991; Stone, 2000); other scaling schemes yield soil production rates that are faster by 3-10%. After computing rates with the CRONUS calculator, we modified these rates following Small et al. (1999) and Riebe et al. (2001a) to account for biases in ^{10}Be concentrations due to quartz enrichment. Quartz's strong resistance to chemical dissolution can result in a longer regolith residence time – and hence a longer exposure to cosmogenic radiation – for quartz relative to the average mineral in the parent material. If chemical erosion of soluble minerals leaves quartz enriched in regolith relative to its parent material, soil production rates inferred from ^{10}Be concentrations in quartz will be biased to the extent that quartz's exposure to cosmogenic radiation is longer than that of the average mineral in the parent material. To correct for this bias, we multiplied the CRONUS-calculated rates by a quartz enrichment factor (Small et al., 1999; Riebe et al., 2001a) of 1.68 ± 0.19 derived from our measured quartz concentrations to yield soil production rates of $113 \pm 17 \text{ t km}^{-2} \text{ yr}^{-1}$ at RI-1 and $118 \pm 17 \text{ t km}^{-2} \text{ yr}^{-1}$ at RI-4.

These soil production rates are averaged over the timescale of ^{10}Be accumulation in quartz, which at these sites is approximately 14 kyr. This timescale is calculated as Λ/P_{soil} , where Λ is the so-called attenuation length for ^{10}Be production by high-energy spallation. This attenuation length is an exponential scaling constant that describes how the intensity of cosmogenic radiation is attenuated as it passes through matter, typically taken to be 160 g cm^{-2} (Gosse and Phillips, 2001), which can be converted to a true length scale by dividing by the density of the material the cosmogenic radiation is passing through. In granite of density 2.7 g cm^{-3} , for example, this translates to a depth of 59 cm. The value of the empirical constant Λ is based on calculations on an infinite horizontal surface (e.g., Gosse and Phillips, 2001). Soil production rates inferred from cosmogenic

nuclides are thus considered to be rates of mass loss in the vertical direction (i.e., per unit area in map view), not normal to the hillslope.

We consider our measured ^{10}Be concentrations in soil-borne quartz to be a proxy for soil production rates, and not saprolite production rates, because the thickness of soil plus saprolite at our field sites in Rio Icacos is much larger than the penetration depth of ^{10}Be -producing cosmogenic neutrons, implying that the great majority of cosmogenic ^{10}Be in quartz is produced above the saprolite-bedrock boundary. ^{10}Be concentrations in soil-borne quartz thus reflect the rate of mass loss above the saprolite-bedrock boundary, and do not reflect chemical weathering losses during the conversion of bedrock to saprolite. These soil production rates are calculated under the assumption of steady-state soil formation and denudation, which at Rio Icacos is likely to be a reasonable approximation (Turner et al., 2003; Fletcher et al., 2006). We then relate these P_{soil} rates to the saprolite production rate through concentrations of immobile Zr in the rock and saprolite (Equation 3.8).

3.5.2 Measuring immobile element concentrations with XRF

As described in Riebe et al. (2003), immobile element concentrations were measured by X-ray fluorescence (XRF). After drying and powdering rock, saprolite, and soil samples to a grain size of approximately 50 microns in a tungsten carbide Spex mill, we baked them at 550 °C for 12 hours to eliminate organic material. Approximately three grams of powder was then pressed into a boric acid binder, and trace element concentrations were measured from these pellets on a Phillips model PW 2400 X-ray spectrophotometer.

3.5.3 Measuring mineral abundances with powder XRD patterns

We determined mineral abundances in rock, saprolite, and soil samples through quantitative analysis of X-ray diffraction (XRD) patterns measured on powdered samples. Although the principle underlying quantitative powder XRD is straightforward – the XRD pattern of a powdered sample should be the sum of the XRD patterns of the sample’s constituent mineral phases, scaled by their relative abundances – in practice calculating mineral abundances from XRD patterns is limited by factors that affect measured XRD patterns (e.g., crystallite size, preferred orientation of crystallites during sample preparation, variation in mineral composition, and degree of structural disorder; e.g., Jenkins and Snyder, 1996). Because of these practical complications, uncertainties for mineral abundances determined from quantitative XRD are typically no better than 2-3% absolute (e.g., Hillier, 2000; Chipera and Bish, 2002; Omotoso et al., 2006; Jeong et al., 2008; Eberl and Smith, 2009), implying that powder XRD may be useful for quantifying high-abundance mineral phases but has limited utility for quantifying trace mineral phases.

In our analyses we used FULLPAT (Chipera and Bish, 2002) to determine mineral abundances in our rock, saprolite, and soil samples based on each sample’s powder XRD

pattern. FULLPAT is an inversion method that calculates mineral abundances by creating a synthetic XRD pattern from XRD patterns of standard minerals and adjusting the abundances of the standard minerals to optimize the fit between the synthetic pattern and the measured sample pattern. Unlike some earlier quantitative XRD methods (e.g., Chung, 1974), FULLPAT does not scale the sum of all mineral abundances in a sample to 100%, and thus is able to accurately quantify the abundances of known mineral phases even if other mineral phases in the sample are unquantified. Figure 3.3 shows an example of FULLPAT's approach on a test sample that we prepared from a mixture of several standard minerals.

Within FULLPAT we calculated mineral abundances in two steps. In the first step, we allowed FULLPAT to scale all mineral abundances simultaneously; this yielded a synthetic pattern that closely matched the observed sample pattern. In the second step, we refined the abundance of each mineral phase individually, allowing FULLPAT to change the abundance of only one mineral phase at a time while keeping other mineral abundances constant. This refinement step was based only on the relevant mineral's highest-intensity peak, and was carried out while ensuring that the background intensity of the synthetic pattern matched the background intensity of the sample pattern. After refining the abundance of one mineral phase in this manner, we refined the abundances of the other minerals in the same manner.

A central requirement of this approach is that the XRD patterns of the standard minerals match the XRD patterns of the minerals present in the sample. Because some mineral phases have varying crystal structures – and hence varying XRD patterns – the best minerals to use as standards are pure mineral separates from the field samples themselves. This was our approach for quartz and plagioclase. Because of difficulties separating sufficient quantities of pure hornblende and biotite from field samples at Rio Icacos, we used a synthetic hornblende pattern (ID# 01-089-7282) from the Powder Diffraction File (ICDD, 2003) for our hornblende standard, and a biotite from Ward's Scientific, sourced in Bancroft Mica Mine, for our biotite standard.

Does this XRD-based approach for measuring mineral abundances work? Before using FULLPAT to calculate mineral abundances in our samples from Rio Icacos, we tested FULLPAT's accuracy on mineral mixtures that we prepared ourselves, with one mixture designed to mimic a granitic rock and another to mimic a highly weathered soil. The results of these tests are shown in Table 3.2 and Figure 3.4. In these tests, FULLPAT determined mineral abundances to an accuracy of 3.1% absolute (i.e., 3.1% of the total sample mass) or better, similar to the results of similar tests in Chipera and Bish (2002).

We prepared samples for XRD analysis by powdering them to a median grain size of approximately 5 microns, and adding an internal standard (1-micron corundum) to each sample in a 4:1 sample:standard ratio. These mixed powders were then packed into a back-loaded mount atop a frosted glass slide, and scanned under Co-K α radiation from 4 – 90° 2 θ on a Phillips X'Pert Pro diffractometer. We found that multiple XRD patterns of the same sample differed slightly between specimens; that is, repacking and remeasuring the same sample produced slightly different XRD patterns. This variability may be merely

a consequence of the counting statistics associated with X-rays diffracted from randomly oriented crystallites (e.g., Alexander et al., 1948). To account for this variability, we measured four XRD patterns for each sample (repacked between measurements), ran FULLPAT on each of the four patterns, and report the mean calculated mineral abundance over all four runs.

3.5.4 Uncertainties in inferred mineral-specific chemical weathering rates

How accurately can mineral-specific chemical weathering rates be determined with this approach? Standard error propagation shows that uncertainties in W_X derive from four sources: uncertainties in soil production rates, uncertainties in dust deposition rates, uncertainties in Zr concentrations, and uncertainties in mineral abundances. From a practical standpoint, uncertainties in Zr concentrations and dust fluxes at our field sites are negligible compared to the other uncertainties (Tables 3.3 and 3.4), so here we focus only on the errors in soil production rate and mineral abundances.

The uncertainty in soil production rate P_{soil} stems primarily from the uncertainty in the production rate P_{Be} of cosmogenic ^{10}Be (at sea level and high latitude, $P_{Be} = 5.1 \pm 0.3$ atoms of ^{10}Be per gram of quartz per year; Stone, 2000). Other uncertainties can stem from uncertainties in the degree of shielding by snow (e.g., Schildgen et al., 2005) or vegetation (e.g., Ferrier et al., 2005), analytical uncertainties in the measurement of ^{10}Be , and uncertainties in the mass attenuation constants of gamma-ray neutrons and muons (see review in Gosse and Phillips, 2001), all of which we assume are negligible at RI-1 and RI-4. Typically, the uncertainty in the ^{10}Be production rate dwarfs other uncertainties in P_{soil} . At field sites with weathered regoliths, another source of uncertainty can arise in the correction factor that accounts for the bias in ^{10}Be concentrations due to quartz enrichment in the regolith (Small et al., 1999; Riebe et al., 2001a). At our field sites, the correction factor associated with this extended exposure is 1.68 ± 0.19 , and is the largest source of uncertainty in our P_{soil} estimates.

The uncertainties listed for all mineral abundances are a composite of two uncertainties. The first uncertainty is the standard error associated with the sample-to-sample variability in mineral abundances, which was typically small ($< 1\%$). A more conservative means of estimating uncertainties in mineral abundances is to combine the sample-to-sample uncertainty with a methodological uncertainty associated with the XRD-based method itself. Our tests of FULLPAT on self-prepared mineral mixtures (Table 3.2) suggest that the uncertainties in XRD-based abundance determinations may depend on both mineral abundance and the mineral phase itself. Although our tests are not extensive enough to conclude how these methodological uncertainties depend on abundance for each mineral phase, they did reliably reproduce mineral abundances to 3.1% absolute or better over a range of abundances and a variety of mineral phases (Table 3.2), which is similar to accuracies reported by Chipera and Bish (2002). In particular, biotite appears to be resolvable at concentrations well below 1% absolute due to its strong peak at

$10.19^\circ 2\theta$ (equivalent to a d-spacing of 10.07 \AA). To account for this methodological uncertainty, we conservatively added a 3% absolute uncertainty in quadrature to the sample-to-sample uncertainty in quartz, plagioclase, and hornblende, and a 0.4% absolute uncertainty to the uncertainty in biotite abundances. This resulted in mean bedrock mineral abundances are still easily distinguishable from zero except for biotite at site RI-1. For the most abundant and most soluble minerals (here plagioclase and hornblende), the methodological uncertainty contributes a small fraction of the total uncertainty in estimated mineral weathering rates.

3.6 Results and discussion

As Equations 3.1-3.14 demonstrate, estimated mineral weathering rates depend on measurements of soil production rates, dust deposition rates, immobile element concentrations, and mineral abundances. Because the ^{10}Be and Zr measurements are discussed in detail in Riebe et al. (2003) and the dust flux estimate is discussed in detail in Pett-Ridge et al. (2009), we focus here on the new mineral abundance data and estimates of mineral weathering rates.

3.6.1 Mineral abundances

We measured mineral abundances in six rock samples and thirteen soil samples from site RI-1, and in five rock samples, thirteen saprolite samples, and 30 soil samples from site RI-4 based on the powder XRD patterns of each sample. Qualitatively, the mineralogic differences between rock and regolith can easily be seen by eye in the XRD patterns. Figure 3.5 shows representative XRD patterns for one soil sample, one saprolite sample, and one rock sample from site RI-4, and the differences in the patterns reveal clear differences in mineralogy from sample to sample. The soil and saprolite patterns look quite similar – all of their sharp peaks come from quartz, kaolinite, and the corundum standard added to each sample – but they differ from the rock pattern in that they lack peaks between 32 and $40^\circ 2\theta$, reflecting the absence of plagioclase and hornblende. Clearly, these samples show that plagioclase and hornblende have been intensively weathered during the conversion of bedrock to saprolite, in agreement with previous studies (e.g., White et al., 1998; Turner et al., 2003; Buss et al., 2008).

FULLPAT analysis of these XRD patterns provides mineral abundance data that quantitatively confirm the large mineralogic differences between rock and regolith. As Tables 3.3 and 3.4 show, the rock samples are dominated by quartz and feldspar, have less hornblende, and include trace amounts of biotite. What little biotite exists in the rock samples is completely absent in all of the saprolite and soil samples, and plagioclase and hornblende are both greatly depleted, if not completely depleted, in the saprolite and soil samples. Only one of the thirteen saprolite samples contains any measurable plagioclase or hornblende at all, while roughly two-thirds of the soil samples contain no measurable

plagioclase, and about 40% of the soil samples contain no measurable hornblende. (See Supplementary File for mineral abundances in each of the 67 samples.) The saprolite samples do not show any mineralogic trends with depth within the range of sampling depths (95 cm to 222 cm), which is consistent with observations that weathering at Rio Icacos is concentrated in a narrow zone of saprock between bedrock and saprolite well below our deepest saprolite samples (e.g., White et al., 1998; Turner et al., 2003; Buss et al., 2008). Plagioclase and hornblende are more evenly distributed in the soil samples than in the saprolite samples, which is consistent with mixing of compositionally variable saprolite samples in the soil, and supports other observations of soil mixing at Rio Icacos by earthworms, burrowing animals, and roots (e.g., White et al., 1998).

The FULLPAT-derived mineral abundances for quartz, plagioclase, and hornblende in rock, saprolite, and soil at RI-1 and RI-4 (Tables 3.3-3.4) agree well with previous measurements of mineral abundances measured in samples collected elsewhere in the Rio Icacos catchment (Murphy, 1995, as cited in White et al., 1998). The primary difference between mineral abundances at RI-1 and RI-4 and those measured elsewhere in the Rio Icacos catchment is in biotite. This is true for both the rock samples and the regolith samples. In the rock samples at RI-1 and RI-4, abundances of biotite are much lower (9-18 mmol/kg) than in rock samples examined by Murphy (208 mmol/kg) (Murphy, 1995; White et al., 1998). Is this an indication that the FULLPAT-determined estimates of biotite abundances at sites RI-1 and RI-4 are too low by a factor of 10-20? Such a bias in calculated biotite abundances could arise if, during preparation of the standard biotite specimen, the biotite crystallites were oriented along a common crystal plane, which would artificially amplify the intensity of the dominant biotite peak relative to the corundum peaks against which the biotite peaks are normalized. Such preferred orientation can be especially strong in platy minerals like biotite, which within a powdered specimen may align themselves along basal planes rather than randomly (e.g., Jenkins and Snyder, 1996; Kleeberg et al., 2008). However, although preferred orientation can be important for biotite, our measurements suggest that preferred orientation has not dramatically skewed FULLPAT-calculated estimates of biotite concentrations. If preferred orientation did cause FULLPAT to underestimate biotite abundances by over an order of magnitude, our tests on self-prepared mineral mixtures should have shown this (Figure 3.4 and Table 3.2). The FULLPAT-determined biotite abundance in this test ($5.2 \pm 0.2\%$), however, was only slightly lower than the true biotite abundance (5.6%) – far less than an order of magnitude difference. Thus we suggest preferred orientation is unlikely to have caused FULLPAT to calculate artificially low biotite abundances. Our measurements also suggest that FULLPAT-derived biotite abundances were not strongly affected by differences between the XRD pattern of the standard biotite and the biotite present in the Rio Icacos bedrock. To verify this, we measured the powder XRD pattern of biotite isolated from Rio Icacos bedrock (courtesy of Heather Buss, USGS, October 2007), and found that its XRD pattern did not differ substantially from the XRD pattern of the standard biotite used in FULLPAT. Thus our measurements suggest that FULLPAT-calculated biotite abundances were not severely skewed by preferred orientation or by a mismatch between the standard biotite and the biotite in sampled bedrock.

The biotite XRD patterns in saprolite and soil at RI-1 and RI-4 also differ from those in previous studies of soil and saprolite at Rio Icaicos. In prior studies of biotite in regolith elsewhere in the Rio Icaicos catchment, XRD patterns display a major diffraction peak at 10.5Å, indicating the presence of substantial quantities of altered biotite (Dong et al., 1998; Murphy et al., 1998). At RI-1 and RI-4, however, none of the saprolite or soil XRD patterns have a peak at 10.5Å (equivalent to $9.77^\circ 2\theta$ in Figure 3.5). The absence of peaks at 10.5Å in the RI-1 and RI-4 regolith samples indicates that these samples do not contain biotite in the altered form found by Dong et al. (1998) and Murphy et al. (1998). Similarly, the absence of peaks at 10.07Å in the RI-1 and RI-4 saprolite and soil XRD patterns indicates that pristine biotite is not present in the RI-1 and RI-4 regolith samples. These XRD measurements suggest that biotite concentrations in rock and regolith samples at RI-1 and RI-4 are much lower than in rock and regolith samples collected elsewhere in the Rio Icaicos catchment, and that the minor quantities of biotite in bedrock at RI-1 and RI-4 are completely weathered before they reach the depth of our deepest samples in the upper saprolite.

3.6.2 Mineral-specific weathering rates

We combined the FULLPAT-derived mineral abundance measurements with prior measurements of Zr concentrations in the same samples (Riebe et al., 2003), ^{10}Be concentrations in quartz extracted from amalgamated soil samples at RI-1 and RI-4 (Riebe et al., 2003), and a published dust deposition rate of $21 \pm 7 \text{ t km}^{-2} \text{ yr}^{-1}$ (Pett-Ridge et al., 2009). Because direct measurements of dust mineralogy and chemistry are unavailable at Rio Icaicos, and because studies have found that variations in African dust composition are relatively small across the Caribbean (Glaccum and Prospero, 1980), we assume that the composition of African dust deposited at our field sites is the same as the composition of Saharan dust deposited at a long-term dust monitoring station in Barbados (Glaccum and Prospero, 1980; Herwitz et al., 1996) (Tables 3.3-3.4). From these combined sets of measurements, we used Equations 3.5, 3.10, 3.12, and 3.14 to calculate chemical weathering rates for quartz, plagioclase, hornblende, and biotite (Tables 3.3 and 3.4 and Figure 3.6).

As Figure 3.6 shows, the bulk of the primary mineral weathering at Rio Icaicos is due to plagioclase weathering, and nearly all of the remainder is accounted for by hornblende weathering. Because at RI-4 samples of saprolite, rock, and soil are available, we are able to estimate mineral weathering rates in both saprolite and soil, under the assumption that the composition and mass per unit area of both saprolite and soil remain steady over time. These data reveal major differences in weathering rates between the saprolite and the soil. Within uncertainty, all of the primary mineral weathering at RI-4 occurs between the bedrock and the upper saprolite at a depth of 222 cm (i.e., the depth of our deepest saprolite samples). This is consistent with the finding that the great majority of weathering at Rio Icaicos occurs in the narrow zone of saprock between bedrock and saprolite (White et al., 1998; Turner et al., 2003; Buss et al., 2008). Plagioclase and hornblende are weathered nearly to completion below the upper saprolite, and biotite is

completely lost; consequently, their weathering rates between the bedrock and the top of the saprolite (i.e., $W_{\text{saprolite},X}$) are high. Because the concentrations of these minerals at the top of the saprolite are so small, they are supplied to the soil in small quantities during soil production, and as a consequence their weathering rates in soil (i.e., $W_{\text{soil},X}$) are low.

These calculated weathering rates (Tables 3.3-3.4) should be considered averages over the residence times of soil, saprolite, and regolith. Based on our measured soil production rates and the ranges in density and thickness of soil and saprolite at Rio Icacos, we estimate the residence times as 7-16 kyr in soil, 20-93 kyr in saprolite, and 27-109 kyr in regolith at our field sites. We calculate the soil residence time as $\rho_{\text{soil}}H_{\text{soil}}/E$, where ρ_{soil} is the soil density (1.19-1.37 g cm⁻³; White et al., 1998), H_{soil} is the soil thickness (0.5-1 m; White et al., 1998), and E is the physical erosion rate estimated with Equation 3.3. We similarly calculate the saprolite residence time as $\rho_{\text{sap}}H_{\text{sap}}/P_{\text{soil}}$, where ρ_{sap} is the saprolite density (1.19-1.35 kg m⁻³; White et al., 1998), H_{sap} is the soil thickness (0.5-1 m; White et al., 1998), and P_{soil} is the soil production rate inferred from cosmogenic ¹⁰Be. The regolith residence time is the sum of the soil and saprolite residence times.

3.6.3 Comparison to prior measurements of mineral weathering rates

The framework we use to calculate mineral weathering rates at Rio Icacos yields rates in mineral mass per unit area of hillslope per time. These are the units of greatest interest to geomorphologists studying mass fluxes from catchments in an effort to understand how landscapes evolve. By contrast, the bulk of chemical weathering rates in the literature are reported as rates of mineral mass per unit area of mineral surface per time, which are the units of greatest interest to geochemists studying the mechanisms of mineral dissolution. Comparing rates estimated by different methods requires converting weathering rates from one set of units to the other, which requires calculating the ratio of mineral surface area to landscape surface area, which in turn requires measurements of mineral specific surface area, regolith density, and mineral abundance throughout the weathering column from the surface down to bedrock. At Rio Icacos, these measurements are particularly important in the narrow zone of saprock between bedrock and saprolite where the majority of mineral weathering occurs (White et al., 1998; Turner et al., 2003; Buss et al., 2008). We do not have these measurements at RI-1 and RI-4. Our soil samples at RI-1 are representative of the soil, not the saprolite, and at site RI-4 our deepest saprolite samples come from a depth of 222 cm, well above the saprock. It would be inappropriate to extrapolate our mineral abundance data down to the bedrock-saprolite boundary. Instead, for the sake of comparison we convert previously published weathering rates to units of moles per unit area of hillslope per year, by methods described below. These rates are compiled in Table 3.5.

Plagioclase weathering rates

As calculated with Equations 3.5, 3.10, and 3.12, plagioclase weathering rates per unit area of hillslope are $3285 \pm 573 \text{ mol ha}^{-1} \text{ yr}^{-1}$ in the regolith at RI-1, $3085 \pm 538 \text{ mol ha}^{-1} \text{ yr}^{-1}$ in the saprolite at RI-4, and $32 \pm 166 \text{ mol ha}^{-1} \text{ yr}^{-1}$ within the soil at RI-4, confirming that the great majority of plagioclase weathering occurs below our deepest saprolite samples at 222 cm. Turner et al. (2003) and Buss et al. (2008) also measured in-situ plagioclase weathering rates in the Rio Icaecos catchment, and reported these rates in moles weathered per unit volume per time. To compare our measurements with theirs, we convert the reported rates of Turner et al. (2003) and Buss et al. (2008) to moles per unit area of hillslope per year as follows.

Turner et al.'s field sites (named GN and SS) were two zones of partially weathered rock that lay above unweathered corestones and below 1-2 meters of regolith. Within these weathering zones, Turner et al. measured Na and Ti concentrations and, under the assumption that Ti is immobile, calculated volumetric weathering rates of 1.52×10^{-9} and $3.82 \times 10^{-9} \text{ mol Na m}^{-3} \text{ s}^{-1}$. Assuming that plagioclase is the sole source of Na in the parent rock and that each mole of plagioclase contains 0.6 moles of Na (Turner et al., 2003), these Na weathering rates translate to 2.53×10^{-9} and $6.37 \times 10^{-9} \text{ mol plagioclase m}^{-3} \text{ s}^{-1}$. These measurements were made over a zone 58 cm thick at site GN and 45 cm thick at site SS. Multiplying the volumetric weathering rates by these thicknesses gives rates of 464 and 904 $\text{mol ha}^{-1} \text{ yr}^{-1}$ per year. These should be considered lower bounds on the total plagioclase weathering rates per unit area of hillslope at these sites, because some plagioclase still remains at the ends of the weathered rock sequences at GN and SS, and thus some plagioclase may be weathering simultaneously in the overlying regolith. At site GN, 46% of the original Na (and by extension, 46% of the original plagioclase) still exists at the end of the measured weathering zone, and at site SS 4% of the original Na remains at the end of the measured weathering zone. If all of the remaining plagioclase at each site weathered to completion in the overlying regolith, the total plagioclase weathering rates would be $464/(1 - 0.46) = 853 \text{ mol ha}^{-1} \text{ yr}^{-1}$ at GN and $904/(1 - 0.04) = 940 \text{ mol ha}^{-1} \text{ yr}^{-1}$ at SS. This suggests that plagioclase weathering rates per unit area of hillslope are at least $464 \text{ mol ha}^{-1} \text{ yr}^{-1}$ but no faster than $853 \text{ mol ha}^{-1} \text{ yr}^{-1}$ at GN, and at least $904 \text{ mol ha}^{-1} \text{ yr}^{-1}$ but no faster than $940 \text{ mol ha}^{-1} \text{ yr}^{-1}$ at SS. These ranges of possible weathering rates are over a factor of three slower than the plagioclase weathering rates calculated in this study at sites RI-1 and RI-4 and those measured by Buss et al. (2008), discussed below.

Buss et al. (2008), like Turner et al. (2003), measured the spatial gradient in solid-phase Na and Ti concentrations in a zone of weathered rock immediately above an unweathered corestone. Assuming that Ti is immobile and Na is contained only within plagioclase, these measurements permit calculation of a volumetric plagioclase weathering rate. For comparison with the plagioclase weathering rates at RI-1 and RI-4, we converted Buss et al.'s volumetric plagioclase weathering rate to a plagioclase weathering rate per unit area of hillslope by multiplying the thickness of the zone over which Na and Ti concentrations were measured (53 cm) by the volumetric plagioclase weathering rate r_s ($516 \text{ mol m}^{-3} \text{ yr}^{-1}$). This value for the volumetric weathering rate was calculated as

$r_s = \rho_{rock}\omega/(\beta b_s)$ (White, 2002), where ρ_{rock} (kg m^{-3}) is the density of the unweathered rock, ω (m yr^{-1}) is the advance rate of the weathering front, β (mol element/mol mineral) is the stoichiometric coefficient for the measured mobile element in the mineral of interest, and b_s (m kg mol^{-1}) is the reciprocal of the gradient in Ti-normalized Na concentrations. In using ρ_{rock} rather than the density of the weathered material we deviate from the expression in (White, 2002); we do this in order to resolve a minor dimensional inconsistency and to bring this expression into agreement with other established methods for calculating weathering rates (Stallard, 1985; Brimhall and Dietrich, 1987; see discussion in Riebe et al., in review). From Buss et al.'s measurements of $\rho_{rock} = 2700 \text{ kg m}^{-3}$, $\omega = 4.3 \times 10^{-5} \text{ m/yr}$, $\beta = 0.5 \text{ mol Na/mol plagioclase}$, and $b_s = 0.45 \text{ m kg mol}^{-1}$, we calculate a plagioclase weathering rate of $2735 \text{ mol ha}^{-1} \text{ yr}^{-1}$. Four percent of the parent Na remains at the top of this 53 cm weathering zone, implying that the total plagioclase weathering rate per unit area of hillslope at this site is likely to be no faster than $2735/(1 - 0.04) = 2849 \text{ mol ha}^{-1} \text{ yr}^{-1}$. This range of possible plagioclase weathering rates agrees with our calculated plagioclase weathering rates at RI-1 and RI-4 within uncertainty.

Hornblende weathering rates

As calculated with Equations 3.5, 3.10, and 3.12, hornblende weathering rates per unit area of hillslope are $188 \pm 69 \text{ mol ha}^{-1} \text{ yr}^{-1}$ in the regolith at RI-1, $309 \pm 92 \text{ mol ha}^{-1} \text{ yr}^{-1}$ in the saprolite at RI-4, and $0 \pm 52 \text{ mol ha}^{-1} \text{ yr}^{-1}$ in the soil at RI-4 (Table 3.5). These are 1.5-2.5 times slower than hornblende weathering rates inferred from measurements of the gradient in Ti-normalized Fe(II) concentrations across a 7 cm zone of protosaprolite (Buss et al., 2008). We have normalized Buss et al.'s volumetric hornblende weathering rate to a weathering rate per unit area of hillslope by multiplying the thickness of the protosaprolite (7 cm) by the volumetric weathering rate r_s within the protosaprolite ($677 \text{ mmol m}^{-3} \text{ yr}^{-1}$; calculated as $r_s = \rho_{rock}\omega/(\beta b_s)$ using Buss et al.'s measurements of $\rho_{rock} = 2700 \text{ kg m}^{-3}$, $\omega = 4.3 \times 10^{-5} \text{ m/yr}$, $\beta = 0.063 \text{ mol Fe(II)/mol hornblende}$, and $b_s = 0.088 \text{ m kg mol}^{-1}$). The resulting hornblende weathering rate per unit area of hillslope is $474 \text{ mol ha}^{-1} \text{ yr}^{-1}$. Because, as Buss et al. noted, hornblende is completely weathered across this 7 cm zone, this represents a maximum possible hornblende weathering rate per unit area of hillslope at this site.

Biotite weathering rates

As calculated with Equations 3.10 and 3.12, biotite weathering rates per unit area of hillslope are $14 \pm 16 \text{ mol ha}^{-1} \text{ yr}^{-1}$ in the regolith at RI-1 and $28 \pm 18 \text{ mol ha}^{-1} \text{ yr}^{-1}$ in the saprolite at RI-4. These are much slower than previously reported biotite weathering rates at Rio Icaos (Murphy et al., 1998; White, 2002; Buss et al., 2008), primarily because bedrock biotite abundances are much lower at RI-1 and RI-4 than in the rock samples examined in other studies, as discussed in section 3.6.1. Murphy et al. (1998) reported biotite weathering rates in saprolite at Rio Icaos of 500 and $920 \text{ mol ha}^{-1} \text{ yr}^{-1}$ based on vertical gradients in porewater concentrations of K and Mg, respectively. In White (2002),

measurements of vertical gradients in porewater K and Mg concentrations over a 7.3 m saprolite profile permit calculation of volumetric biotite weathering rates of 6-14 mmol m⁻³ yr⁻¹, while in Buss et al. (2008), measurements of Ti-normalized Fe(II) concentrations across a 46-cm zone of weathered rock permit calculation of a volumetric biotite weathering rate of 160 mmol m⁻³ yr⁻¹ (calculated as $r_s = \rho_{rock}\omega/(\beta b_s)$) and $\rho_{rock} = 2700$ kg m⁻³, $\omega = 4.3 \times 10^{-5}$ m/yr, $\beta = 0.36$ mol Fe(II)/mol biotite, and $b_s = 2.02$ m kg mol⁻¹). Multiplying these volumetric weathering rates in White (2002) and Buss et al. (2008) by the thicknesses of the zones over which each rate was measured yields biotite weathering rates of 461-990 mol ha⁻¹ yr⁻¹ and 734 mol ha⁻¹ yr⁻¹, respectively.

Quartz weathering rates

As calculated with Equations 3.10 and 3.12, quartz weathering rates in the regolith at RI-1 and in the saprolite at RI-4 overlap zero within uncertainty (-373 ± 1355 mol ha⁻¹ yr⁻¹ and 426 ± 935 mol ha⁻¹ yr⁻¹, respectively), as expected for a mineral so resistant to dissolution. These rates are also indistinguishable from the quartz weathering rate calculated in Schulz and White (1999) (Table 3.5). Within the soil at RI-4, however, Equation 3.5 yield a quartz weathering rate that is negative beyond one standard error (-1470 ± 769 mol ha⁻¹ yr⁻¹), implying an apparent gain of quartz relative to Zr in the soil. Below we discuss several ways in which this calculated negative quartz weathering rate could arise.

One possibility, however unlikely, is that the calculated negative quartz weathering rate in RI-4 soil reflects mobility of Zr relative to quartz in the soil. Although zircon has a very low solubility and is thus unlikely to lose much mass by chemical weathering, it is not perfectly insoluble: some studies have documented chemical mobility of Zr in the lab (Hodson, 2002) and in the field (Hill et al., 2000; Kurtz et al., 2000). Quartz, like zircon, has a very low solubility. In fact, its solubility is so low that some studies have used it as an immobile tracer in soils (e.g., White et al., 1996). Thus we expect chemical losses of quartz in Rio Icaos soils to be small. However, although zircon may not be perfectly insoluble and quartz is highly resistant to dissolution, it is difficult to argue that chemical losses of quartz should be smaller than those of Zr. We expect the solubility of zircon to be at least as low as the solubility of quartz, and given prior documentation of quartz dissolution in Rio Icaos saprolite (Schulz and White, 1999), we consider it unlikely that chemical losses of quartz in Rio Icaos soils are less than those of Zr.

The calculated negative quartz weathering rate in RI-4 soil could also arise if Zr were more physically mobile than quartz in the soil. Zircons have a higher density than quartz (4.65 g cm⁻³ vs. 2.65 g cm⁻³), and previous studies have concluded that soil mixing can produce physical fractionation of heavy zircons relative to lighter minerals (e.g., Colin et al., 1993). If the strong bioturbation in Rio Icaos soils were to physically segregate zircons from quartz, it is theoretically possible that zircons could be concentrated in areas within the soil profile where physical erosion is fastest, which would lead to faster physical erosion of Zr than quartz. In other words, intense soil mixing might make Zr more

physically mobile than quartz, which could account for the measured enrichment of quartz relative to Zr in RI-4 soils. Testing this would require in-situ measurements of downslope soil velocities at a number of depths within the soil column and co-located measurements of Zr and quartz concentrations. Our limited soil samples cannot test this, but we acknowledge that preferential physical mobility of Zr is a possibility at Rio Icacos, as it is at any field site.

Differences in chemical or physical mobility between quartz and Zr are not the only possible explanations for the calculated negative quartz weathering rate. If the dust deposition rate were a factor of five smaller than that determined by Pett-Ridge et al. (2009) (e.g., $4 \pm 4 \text{ t km}^{-2} \text{ yr}^{-1}$ instead of $21 \pm 7 \text{ t km}^{-2} \text{ yr}^{-1}$) or if the average dust Zr concentration were over a factor of two smaller than that determined by Herwitz et al. (1996) (e.g., $77 \pm 12 \text{ ppm}$ instead of $167 \pm 12 \text{ ppm}$), then the chemical weathering rate of quartz in RI-4 soils would be indistinguishable from zero, as expected. However, we suggest such a low dust deposition rate is unlikely because it is incompatible with Pett-Ridge et al.'s measurements of Sr fluxes and isotopic signatures in the Rio Icacos catchment, and inconsistent with Herwitz et al.'s reported Zr concentrations.

Lastly, the calculated negative quartz weathering rate in RI-4 soil could arise if there were a minor bias in the soil sampling scheme. This possibility hinges on the idea that the soil samples (which were collected from a range of soil depths) may have a composition that systematically differs from the composition of the portion of the soil that is physically eroding (which may not include the entire soil column). Because the mass-balance framework requires as input the composition of the physically eroding portion of the soil, such a bias could throw off calculated quartz weathering rates. Such a bias would not need to be large to produce the expected similarity in enrichment between quartz and Zr. For example, if the eroding soil had a mean Zr concentration that was just 6% higher than that in the sampled soil (245 ppm rather than 232 ppm) and a mean quartz concentration that was just 6% lower than that in the sampled soil (8.96 kg/mol rather than 9.47 kg/mol), then the calculated quartz weathering rate in RI-4 soil would be indistinguishable from zero, as expected. Such a sampling bias would be most likely to occur if concentrations of quartz and Zr in RI-4 soil samples were anticorrelated with each other, such that if the eroding portion of the soil had lower quartz concentrations than the sampled soil, then it would be likely to have higher concentrations of Zr than the sampled soil. As it happens, this is not the case in RI-4 soils: concentrations of quartz and Zr in RI-4 soils are positively correlated (with a correlation coefficient of 0.60), which suggests that if concentrations of Zr were higher in the eroding portion of the soil than in the sampled soil, then concentrations of quartz likely would be higher too. A further argument against such a sampling bias is that concentrations of Zr and quartz in the RI-4 soil samples do not vary systematically with depth within the soil column. Thus if only a portion of the soil were eroding physically (e.g., the upper 5 cm), this would be unlikely to change the calculated quartz weathering rate. We note that this does not rule out the possibility that a bias in soil sampling affected calculated quartz weathering rates; it only makes it less likely.

Overall, we cannot definitively rule out any of these possible explanations for the

calculated negative quartz weathering rate in RI-4 soil. We suggest, however, that it is unlikely that Zr is more chemically mobile than quartz, or that dust deposition rates are at least five times lower than that reported in Pett-Ridge et al. (2009). We therefore suggest that it is more likely that Zr and quartz have similarly low chemical mobilities in Rio Icacos soils, and the negative calculated quartz weathering rate may be indicative of enhanced physical mobility of Zr or of minor sampling bias. As such, this dataset reinforces the importance of measuring mineral abundances as well as elemental abundances in chemical weathering studies. Because both quartz and Zr should both be approximately chemically immobile, the rock-to-soil enrichment of highly abundant and deeply insoluble minerals like quartz can serve as a check on the rock-to-soil enrichments of trace elements like Zr, whose low concentrations may be more easily skewed by secondary mass influxes into the soil, or physical segregation, or sampling biases.

Kaolinite weathering rates

In addition to weathering rates of primary minerals, this method can yield production rates of secondary minerals, provided that their abundances can be accurately quantified. At Rio Icacos, kaolinite is the most abundant secondary mineral, and it manifests itself in the soil and saprolite XRD patterns as several sharp peaks (most prominently at $14.2^\circ 2\theta$) and two broad bulges at $23 - 31^\circ$ and $40 - 46^\circ 2\theta$. Our attempts to isolate from our soil samples a pure kaolinite standard with diffraction characteristics matching those in the regolith XRD patterns were unsuccessful, and as a consequence we were unable to use measured XRD patterns to reliably estimate the absolute abundances of kaolinite in our soil and saprolite samples. However, the intensities of the kaolinite peaks in the soil XRD patterns relative to those in the saprolite XRD patterns implies that kaolinite abundances in the soil are $36 \pm 6\%$ of kaolinite abundances in the saprolite, which is similar to the findings of Murphy (1995) (as cited in White et al., 1998), who reported a $[\text{kaolinite}]_{\text{soil}}/[\text{kaolinite}]_{\text{saprolite}}$ ratio of 46%. If we assume that the measured kaolinite abundances of Murphy (1995) – i.e. $[\text{kaolinite}]_{\text{rock}} = 0\%$, $[\text{kaolinite}]_{\text{saprolite}} = 59.4\%$, and $[\text{kaolinite}]_{\text{soil}} = 27.1\%$ – are representative of site RI-4, then Equations 3.5, 3.10, and 3.12 yield weathering rates for kaolinite of $W_{\text{soil,kaolinite}} = 2012 \pm 348 \text{ mol ha}^{-1} \text{ yr}^{-1}$, $W_{\text{sap,kaolinite}} = -2717 \pm 413 \text{ mol ha}^{-1} \text{ yr}^{-1}$ (where the negative sign denotes net production, rather than weathering, of kaolinite), and $W_{\text{regolith,kaolinite}} = -706 \pm 138 \text{ mol ha}^{-1} \text{ yr}^{-1}$. This suggests that the rate of kaolinite weathering in the soil is nearly three-quarters the rate of kaolinite production in the saprolite. These inferred losses of kaolinite in the soil are consistent with documented losses of aluminum between the saprolite and the soil at site RI-4 (Riebe et al., 2003) and are also consistent with the conclusions of (White et al., 1998), who measured an increase in the median grain size of kaolinite in soil relative to saprolite, which they suggest indicates preferential dissolution of the fine-grained kaolinite particles in the soil.

3.6.4 How much does dust deposition affect estimates of chemical and physical erosion rates?

At the time of Riebe et al.'s measurements of Zr and ^{10}Be (Riebe et al., 2003), no independent estimates of dust deposition rates were available at Rio Icacos, and Riebe et al. calculated bulk chemical and physical erosion rates under the assumption of negligible dust deposition. The new Rio Icacos dust flux estimate of Pett-Ridge et al. (2009) now permits incorporation of dust fluxes into the steady-state mass balance model, and it demands a reevaluation of chemical and physical erosion rates at sites RI-1 and RI-4. These updated estimates for bulk chemical and physical erosion rates are listed in Tables 3.3 and 3.4.

The updated estimates show that although a dust deposition rate of $21 \pm 7 \text{ t km}^{-2} \text{ yr}^{-1}$ is non-negligible relative to the inferred soil production rates of $113 \pm 17 \text{ t km}^{-2} \text{ yr}^{-1}$ and $118 \pm 17 \text{ t km}^{-2} \text{ yr}^{-1}$, it has only a small effect on estimates of bulk chemical erosion rates at our field sites. Ignoring dust fluxes in Equation 3.11 (i.e., assuming $P_d \rightarrow 0$) yields mean estimates of 91 and 92 $\text{t km}^{-2} \text{ yr}^{-1}$ for $W_{regolith}$ at RI-1 and RI-4, respectively, and including dust fluxes in Equation 3.11 increases those mean estimates to 94 and 98 $\text{t km}^{-2} \text{ yr}^{-1}$ at RI-1 and RI-4, respectively. Including dust fluxes in this mass-balance model has a larger effect on estimates of physical erosion rates, which are 26% larger at each site than they would be if dust fluxes were assumed negligible in Equation 3.3. Thus our updated calculations show that dust fluxes play a secondary but non-trivial role in setting bulk chemical and physical erosion rates at Rio Icacos, in agreement with the conclusions of Pett-Ridge et al. (2009).

3.7 Conclusions

The central purpose of this paper is to show that quantitative analysis of powder XRD patterns can – at least in samples with relatively simple mineralogies – yield mineral abundances that are accurate enough to be profitably used in the solid-phase mass balance approach for estimating long-term mineral weathering rates. In addition to measurements of mineral abundances, this mass-balance approach requires measurements of soil production rates, dust deposition rates, and immobile element concentrations in the soil, saprolite, parent rock, and dust. The mathematical framework in which these measurements are used to calculate weathering rates is not new. Rather, the framework is an extension of the approach put forth by Stallard (1985), and it follows previous studies in its consideration of hillslopes where dust fluxes are significant and where saprolite weathering constitutes a major fraction of the total weathering (Owen et al., 2008; Dixon et al., 2009).

To demonstrate that uncertainties in calculated mineral weathering rates are not so large that they negate the utility of this solid-phase mass balance approach, we applied this approach to two sites in the Rio Icacos catchment of Puerto Rico. Our new XRD-based mineral abundances, when combined with prior measurements of soil production rates,

immobile element concentrations, and estimates of dust deposition rate and dust composition, suggest that field-based weathering rates of abundant, soluble mineral phases can be accurately determined on eroding hillslopes in both saprolite and soil. At these field sites chemical weathering has stripped the saprolite and the soil of nearly all of its plagioclase and hornblende, and for these minerals, these measurements yield mineral weathering rates with uncertainties that are 17% of the mean for plagioclase and 37% or less of the mean for hornblende. These rates are averaged over the residence times of saprolite and soil, which at these field sites have ranges of 20-93 kyr and 10-23 kyr, respectively.

Our measurements at Rio Icacos suggest the utility of this approach for estimating mineral weathering rates is primarily limited by uncertainties in cosmogenic-based soil production rates and XRD-based mineral abundances. Although many studies have measured soil production rates with cosmogenic nuclides (e.g., Heimsath et al., 1997; Riebe et al., 2001a; Dixon et al., 2009) and quantified mineral abundances with powder XRD (e.g., Hillier, 2000; Chipera and Bish, 2002; Omotoso et al., 2006; Andrews and Eberl, 2007; Jeong et al., 2008; Eberl and Smith, 2009), we do not mean to suggest that these measurements are trivial or universally applicable. Inferring soil production rates from cosmogenic nuclides requires assuming that the hillslope soil is in steady state (which is not true everywhere) and requires accurately assessing quartz enrichment in the soil (which can be difficult without direct measurements of quartz abundances). Quantifying mineral abundances with powder XRD patterns can be hampered by factors that confound interpretation of measured XRD patterns (e.g., preferred orientation, crystallite size, and variations in the crystallinity of a given mineral phase (Jenkins and Snyder, 1996; Kleeberg et al., 2008)). Thus powder XRD patterns are most likely to yield accurate abundances for high-abundance minerals with consistent crystallinities (e.g., quartz in granite), and are least likely to be useful for minerals that have crystal structures that vary between samples (e.g., poorly ordered clays) or that are present in trace quantities (e.g., calcite in granite). With these caveats, however, our measurements at Rio Icacos suggest that – at least at sites that are close to erosional steady state and which have relatively simple mineralogies, like Rio Icacos – cosmogenic-based soil production rates and XRD-based mineral abundances can be accurate enough to yield useful estimates of long-term mineral weathering rates. Because this mass-balance approach for estimating mineral weathering rates also depends on distinguishing the composition of the regolith from the composition of the parent material, the weathering rates it yields are most accurate in field settings where weathering has been intense and the regolith mineralogy is easily distinguishable from the parent mineralogy. Thus this approach is best suited to sites where chemical weathering is fast enough to produce a soil mineralogy that is easily distinguishable from the parent mineralogy, such as Rio Icacos, the southern Appalachians (e.g., White, 2002) or the mountains of Sri Lanka (e.g., von Blanckenburg et al., 2004). We suggest that the suite of measurements used in this paper may also be fruitfully applied at other eroding hillslopes, and that this approach can be useful in building a database of long-term mineral weathering rates that can help clarify how factors such as temperature, precipitation, vegetation, and physical erosion rates influence mineral weathering.

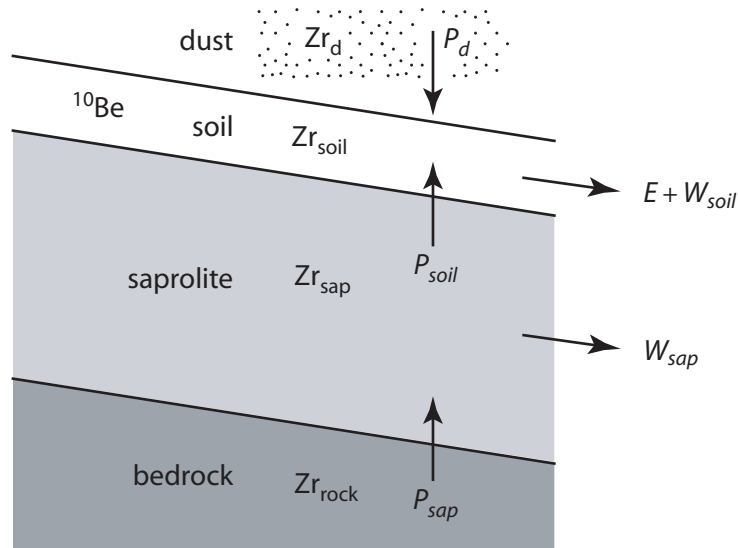


Figure 3.1. Schematic of a hillslope on which a layer of soil overlies a layer of saprolite, which itself overlies unweathered bedrock. Bedrock is converted to saprolite at a rate P_{sap} , and the saprolite loses mass through chemical erosion at a rate W_{sap} and through incorporation into the soil at a rate P_{soil} . The soil gains mass from saprolite at a rate P_{soil} and from dust deposition at a rate P_d , and loses mass by chemical erosion at a rate W_{soil} as well as by physical erosion at a rate E . As described in the text, we calculate W_{sap} , W_{soil} , and E by combining measured concentrations of cosmogenic ^{10}Be in soil-borne quartz with concentrations of an immobile element (e.g., Zr) in the soil, saprolite, bedrock, and dust.

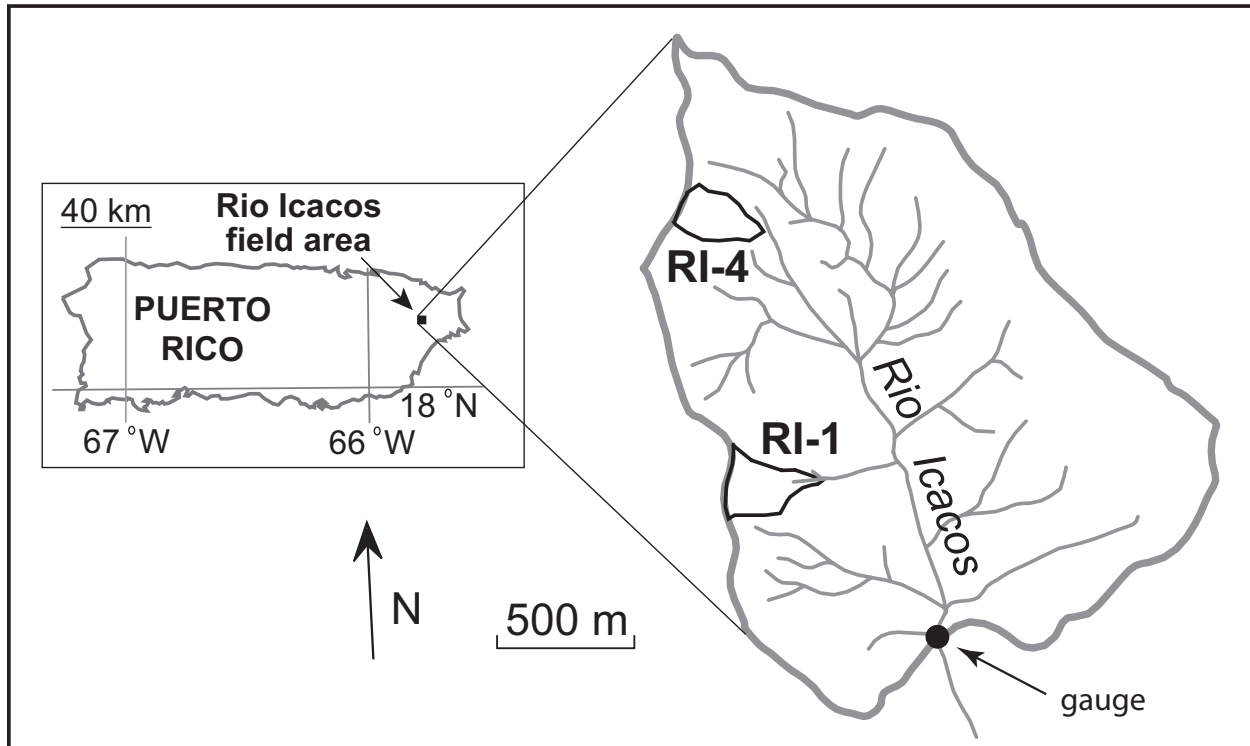


Figure 3.2. Sampling locations within the Rio Icacos catchment, Puerto Rico. Rock and soil samples were collected in subcatchment RI-1, and rock, saprolite, and soil samples were collected in subcatchment RI-4. Subcatchment RI-1 is part of the Quebrada Guaba drainage, and also encompasses the location of the lysimeter measurements of White et al. (1998). Light gray lines denote streams, and thick gray lines denote the catchment boundary. Figure adapted from Riebe et al. (2003).

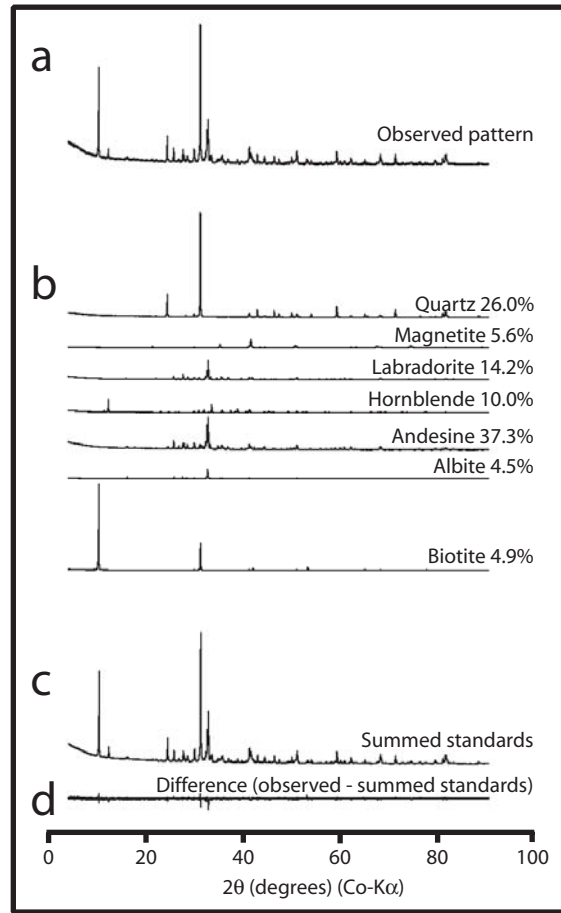


Figure 3.3. FULLPAT (Chipera and Bish, 2002) calculates mineral abundances in a sample by comparing the sample's measured XRD pattern (a) to a synthetic XRD pattern (c), which is created by summing together scaled XRD patterns of standard minerals (b). The scaling factors on the standard mineral patterns are the best-fit mineral abundances, and they are scaled to minimize the difference (d) between the measured pattern and the synthetic pattern. The observed pattern here (a) is from a test sample that we prepared in the lab by combining standard minerals in known quantities, and the synthetic pattern (c) is FULLPAT's fit to the observed pattern. Figure modeled after a similar example in Chipera and Bish (2002).

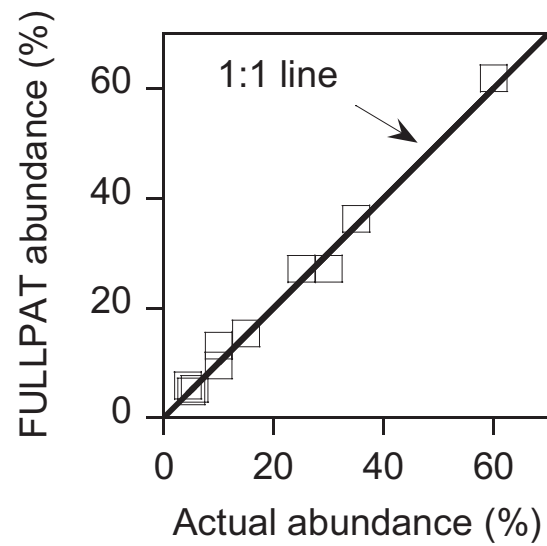


Figure 3.4. Our tests of FULLPAT (Chipera and Bish, 2002) on specially prepared mineral mixtures (Table 3.2) verify that this XRD-based method can provide close estimates of actual mineral abundances for a variety of minerals over a wide range of abundances.

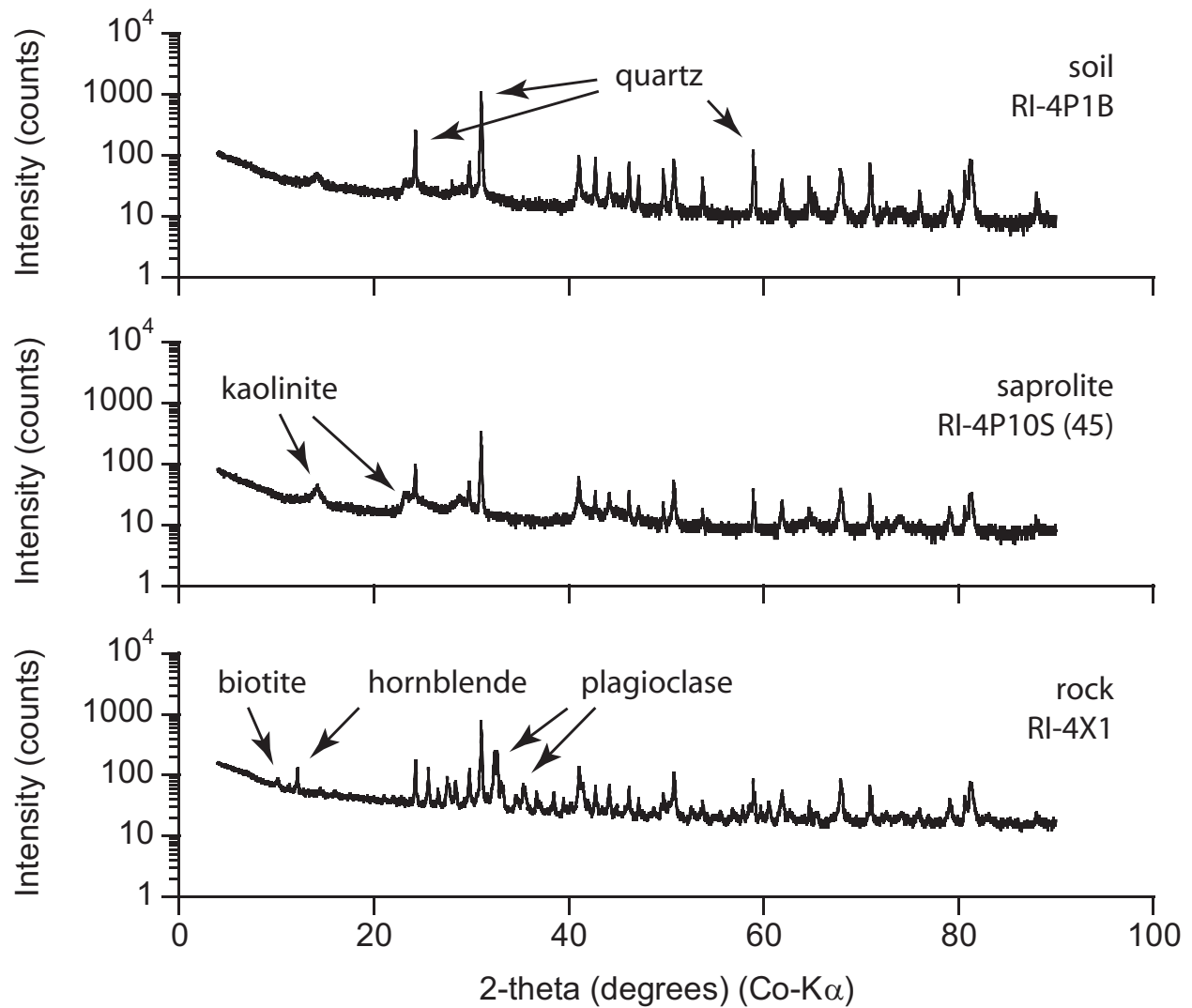


Figure 3.5. Measured XRD patterns for one rock sample, one saprolite sample, and one soil sample from site RI-4. The absence of peaks between 32 and 40° 2θ in the saprolite and soil patterns show that the plagioclase present in the rock has been completely weathered, and the absence of peaks at 10.2 and 12.2° 2θ in the saprolite and soil samples similarly show that biotite and hornblende have also been completely weathered.

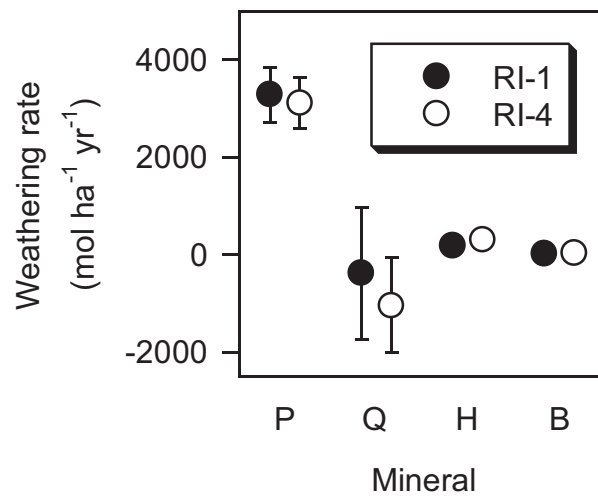


Figure 3.6. Mineral-specific chemical weathering rates in the regolith at sites RI-1 and RI-4 for P: plagioclase, Q: quartz, H: hornblende, and B: biotite, as calculated with Equation 3.12. Comparisons among these weathering rates illustrate the extent to which plagioclase weathering dominates total weathering at Rio Icacos.

Table 3.1: Inputs to CRONUS denudation rate calculator^a

	RI-1	RI-4
Latitude (°N)	18.284	18.284
Longitude (°W)	65.788	65.788
Parent material density (g cm ⁻³)	1.25	1.25
Atmospheric scaling	standard	standard
Sample thickness (cm)	2	2
[¹⁰ Be] (×10 ⁵ atoms g ⁻¹) ^b	1.83 ± 0.14	1.76 ± 0.10
Elevation (m) ^b	700	750
Topographic shielding ^b	0.937	0.902

^a Balco et al. (2008).

^b Riebe et al. (2003).

Table 3.2: Tests of FULLPAT on prepared mineral mixtures

	Actual abundance (%)	FULLPAT abundance (%) ^a	Absolute difference (%)
<i>Mixture 4</i>			
Quartz	60.0	61.9 ± 2.1	1.9 ± 2.1
Kaolinite	30.0	27.1 ± 0.5	2.9 ± 0.5
Goethite	10.0	13.1 ± 0.3	3.1 ± 0.3
Total	100.0	102.1 ± 2.2	
<i>Mixture 5</i>			
Andesine	35.0	36.2 ± 0.6	1.2 ± 0.6
Quartz	25.0	27.1 ± 0.4	2.1 ± 0.4
Labradorite	15.0	15.3 ± 0.9	0.3 ± 0.9
Hornblende	10.0	9.5 ± 0.2	0.5 ± 0.2
Biotite	5.6	5.2 ± 0.2	0.4 ± 0.2
Albite	5.0	4.7 ± 0.2	0.3 ± 0.2
Magnetite	4.4	5.8 ± 0.2	1.4 ± 0.2
Total	100.0	103.8 ± 1.2	

^a Because of small variations in XRD scans of any given sample when repacked and remeasured, we ran all samples four times on the XRD, repacking samples in the sample holder between each scan, and so generated four slightly different XRD patterns for each sample. The uncertainties listed here are the standard errors associated with the variability in FULLPAT-determined mineral abundances on the four XRD patterns.

Table 3.3: Site RI-1: Mineral abundances, mineral weathering rates, and bulk fluxes

	Mineral abundances (mol kg ⁻¹)			$W_{regolith,X}$ (mol ha ⁻¹ yr ⁻¹) ^b
	Bedrock	Soil	Dust ^a	
Quartz	3.76 ± 0.71	8.07 ± 0.68	2.30 ± 0.18	-373 ± 1355
Plagioclase	2.09 ± 0.13	0.04 ± 0.11	0.15 ± 0.01	3285 ± 573
Hornblende	0.13 ± 0.03	0.03 ± 0.04	0	188 ± 69
Biotite	0.009 ± 0.009	0.00 ± 0.01	0	14 ± 16
Zr (ppm) ^c	85 ± 9	205 ± 10	167 ± 12	
n	5 ^d or 6	13		
Bulk rates	(t km ⁻² yr ⁻¹)	Source		
P_{soil} ^e	113 ± 17	¹⁰ Be		
P_{sap} ^f	157 ± 18	Eqn. 3.8		
P_d	21 ± 7	Pett-Ridge et al. (2009)		
$W_{regolith}$	94 ± 17	Eqn. 3.11		
E	84 ± 15	Eqn. 3.3		

^a Dust mineral abundances taken from Glaccum and Prospero (1980) and dust Zr concentration from Herwitz et al. (1996).

^b $W_{regolith,X}$ rates were calculated with Equation 3.12 under the assumption that thick saprolite exists at RI-1 as it does elsewhere in the Rio Icaos catchment, and that at RI-1 the ratio Zr_{sap}/Zr_{rock} is 1.39 ± 0.07 , as was measured at the nearby RI-7 site (Riebe et al., 2003).

^c Zr concentrations in bedrock and soil from Riebe et al. (2003).

^d Because of a poor match between the measured XRD pattern of one rock sample (RI-1P4X) and standard mineral patterns for plagioclase and hornblende, we were not able to determine abundances for these minerals in that sample. The number of rock samples used for mean plagioclase and hornblende abundances is thus 5, while n for quartz and biotite is 6.

^e Soil production rate P_{soil} was calculated with the CRONUS calculator (Balco et al., 2008) from Riebe et al.'s measurements of $1.83 \pm 0.14 \times 10^5$ atoms ¹⁰Be/g quartz (Riebe et al., 2003), a topographic shielding factor of 0.937, and a quartz enrichment factor (Small et al., 1999; Riebe et al., 2001a) of 1.68 ± 0.19 .

^f Calculated with Equation 3.8 assuming that Zr_{sap}/Zr_{rock} is 1.39 ± 0.07 , as was measured at the nearby RI-7 site (Riebe et al., 2003).

Table 3.4. Site RI-4: Mineral abundances, mineral weathering rates, and bulk fluxes

	Bedrock	Mineral abundances (mol kg ⁻¹)			Weathering rates (mol ha ⁻¹ yr ⁻¹)		
		Saprolite	Soil	Dust ^a	$W_{soil,X}^b$	$W_{sap,X}^b$	$W_{regolith,X}^b$
Quartz	3.62 ± 0.53	4.25 ± 0.51	9.47 ± 0.63	2.30 ± 0.18	-1470 ± 769	426 ± 935	-1043 ± 982
Plagioclase	2.09 ± 0.14	0.04 ± 0.12	0.07 ± 0.11	0.15 ± 0.01	32 ± 166	3085 ± 538	3118 ± 527
Hornblende	0.22 ± 0.04	0.02 ± 0.04	0.03 ± 0.03	0	0 ± 52	309 ± 92	309 ± 84
Biotite	0.018 ± 0.010	0.00 ± 0.01	0.00 ± 0.01	0	0 ± 12	28 ± 18	28 ± 17
Zr (ppm) ^c	90 ± 2	115 ± 2	232 ± 8	167 ± 12			
<i>n</i>	3 ^d or 5	13	30				
Bulk fluxes (t km ⁻² yr ⁻¹)							
P_{soil}^e	118 ± 17	Source					
P_{sap}	151 ± 22	¹⁰ Be					
P_d	21 ± 7	Eqn. 3.8					
W_{soil}	65 ± 10	Pett-Ridge et al. (2009)					
W_{sap}	32 ± 12	Eqn. 3.4					
$W_{regolith}$	98 ± 16	Eqn. 3.9					
E	74 ± 11	Eqn. 3.11					
		Eqn. 3.3					

^a Dust mineral abundances taken from Glaccum and Prospero (1980) and dust Zr concentration from Herwitz et al. (1996).

^b $W_{soil,X}$, $W_{sap,X}$, and $W_{regolith,X}$ are calculated with Equations 3.5, 3.10, and 3.12, respectively.

^c Zr concentrations in bedrock, saprolite, and soil from Riebe et al. (2003).

^d Because of poor matches between the measured XRD patterns of two rock samples (RI-4X4 and RI-4X5) and standard mineral patterns for plagioclase, we were not able to determine abundances for plagioclase in those samples. The number of rock samples used for mean plagioclase abundances is thus 3, while *n* for quartz, hornblende, and biotite is 5.

^e Soil production rate was calculated with the CRONUS calculator (Balco et al., 2008) from Riebe et al.'s measurements of $1.76 \pm 0.10 \times 10^5$ atoms ¹⁰Be/g quartz (Riebe et al., 2003), a topographic shielding factor of 0.902, and a quartz enrichment factor (Small et al., 1999; Riebe et al., 2001a) of 1.68 ± 0.19 .

Table 3.5: Rio Icacos mineral weathering rates

	Weathering rate (mol ha ⁻¹ yr ⁻¹)	Source
Quartz	-373 ± 1355	RI-1 regolith, this study
	426 ± 935	RI-4 saprolite, this study
	-1470 ± 769	RI-4 soil, this study
	228	Schulz and White (1999)
Plagioclase	3285 ± 573	RI-1 regolith, this study
	3085 ± 538	RI-4 saprolite, this study
	32 ± 166	RI-4 soil, this study
	≥ 464 ^c	Turner et al. (2003), site GN
	≥ 904 ^c	Turner et al. (2003), site SS
	2735 ^c	Buss et al. (2008)
Hornblende	188 ± 69	RI-1 regolith, this study
	309 ± 92	RI-4 saprolite, this study
	0 ± 52	RI-4 soil, this study
	474 ^c	Buss et al. (2008)
Biotite	14 ± 16	RI-1 regolith, this study
	28 ± 18	RI-4 saprolite, this study
	0 ± 12	RI-4 soil, this study
	500-920	Murphy et al. (1998)
	461-990 ^c	White (2002)
	734 ^c	Buss et al. (2008)

^a Means and uncertainties are denoted with a ± symbol, e.g. 188 ± 69, and ranges are indicated with a dash, e.g. 500-920.

^b Quartz weathering rates from Schulz and White (1999) were calculated by multiplying the reported mean quartz weathering rate (1.6×10^{-15} mol m⁻² of mineral s⁻¹) by the reported total quartz surface area in a 1 m² column of saprolite (4.55×10^5 m² of mineral per m² of saprolite).

^c Calculated by multiplying the volumetric weathering rate by the thickness of the zone over which the rate measurement was made. See text for details.

Chapter 4

A geochemical method for estimating millennial-scale dust deposition rates on soil-mantled hillslopes, and an application of the method in the Idaho Batholith

4.1 Abstract

Dust fluxes are of wide interest because of their effects on climate, oceanic primary productivity, terrestrial biogeochemical cycles, and soil composition. Estimating long-term dust deposition rates, however, can be difficult, especially in steep, eroding terrain. Here we present a geochemical mass balance method for estimating long-term average dust deposition rates on steadily eroding soil-mantled hillslopes. This method requires measurements of the local soil production rate as well as the concentrations of two immobile elements in the soil, its parent rock, and dust. Dust deposition rates inferred with this method are averaged over the long timescales of soil residence on the hillslope (typically 10^3 - 10^5 years), and thus may serve as long-term averages against which modern-day dust fluxes may be compared. We apply this model to 17 field sites in the South Fork of the Salmon River in the Idaho Batholith, where rock and soil compositions imply that mafic-rich material has been added to the otherwise granitic soils. We suggest that the most likely source of this mafic material is dust sourced from the same glacial outburst flood sediments that generated the nearby Palouse loess on the Columbia Plateau, and we use the published composition of these sediments to infer dust deposition rates of 3 - $13 \text{ t km}^{-2} \text{ yr}^{-1}$ at these sites, comparable to modern-day dust fluxes elsewhere in the western United States.

4.2 Introduction

As the orange-red skies in Sydney, Australia colorfully demonstrated in September 2009, the atmosphere is capable of transporting a great deal of mineral mass. It exercises this ability regularly. Globally, the continents send about 1700 Tg of dust into the atmosphere every year, of which about 450 Tg falls to the oceans and 1250 Tg returns to land (Jickells et al., 2005). This dust flux has widespread consequences. It influences climate by affecting radiative transfer (e.g., Harrison et al., 2001), it promotes marine primary productivity by fertilizing Fe-limited regions of the oceans (e.g., Fung et al., 2000), and, where it returns to land, it affects soil composition (e.g., Rex et al., 1969). If the 1250 Tg of land-bound dust were distributed evenly over all terrestrial landmasses, it would produce a dust deposition rate of roughly $8 \text{ t km}^{-2} \text{ yr}^{-1}$. Relative to a present-day globally averaged denudation rate of roughly $140 \text{ t km}^{-2} \text{ yr}^{-1}$ (Wilkinson and McElroy, 2007) – which, in steady state, must roughly equal the soil production rate – dust deposition should be a secondary but non-trivial source of minerals and nutrients to Earth’s soils.

This is confirmed by a large number of studies that have found that dust is an important contributor to soil composition, both in arid to semi-arid soils of the western United States (e.g., Marchand, 1970; Litaor, 1987; Harden, 1988; Chadwick and Davis, 1990; Reheis, 1990; Reheis and Kihl, 1995; Reheis et al., 1995, 2009; Dahms, 1993; Reynolds et al., 2006; Goldstein et al., 2008) and elsewhere around the globe (e.g., Rex et al., 1969; Muhs et al., 1990; Brimhall et al., 1988; Chartres et al., 1988; Chadwick et al., 1999; Kurtz et al., 2001; Stiles et al., 2003; Porder et al., 2007; Pett-Ridge et al., 2009). As many of these studies have noted, dust deposition has consequences for geomorphic and geochemical studies that use the rock-to-soil enrichment of chemically immobile elements as a tool for inferring rates and processes of soil formation, chemical weathering, and physical erosion (e.g., Brimhall and Dietrich, 1987; Brimhall et al., 1991; White et al., 1998; Riebe et al., 2001b, 2003, 2004b,a; Green et al., 2006; Yoo et al., 2007; Burke et al., 2007, 2009; Dixon et al., 2009). Because the elements typically considered to be immobile are present in small quantities in most soils, their concentrations in soil can be altered by small additions of atmospheric dust, especially if the dust is rich in these elements. Quantifying the influence of dust on soil composition (and hence on chemical and physical erosion rates inferred from soil composition) thus requires estimates of the local dust deposition rate and dust composition.

It can, however, be difficult to estimate dust fluxes, especially over the long timescales relevant to soil formation and erosion. Here we present a method for estimating long-term dust fluxes averaged over the soil residence time, which on most eroding hillslopes is on the order of 10^3 - 10^5 years. This method requires estimates of soil production rates (which are now routinely inferred from cosmogenic nuclide concentrations in soils or the underlying rock) and concentrations of two immobile elements in the rock, soil, and dust (which may be measured by a variety of geochemical techniques). The approach proposed here complements other methods for quantifying long-term dust fluxes, such as measuring loess thickness over a known time interval (e.g., Busacca et al., 2004), or

attributing discrepancies in Sr isotope fluxes in and out of a catchment to dust deposition (e.g., Pett-Ridge et al., 2009).

4.3 A hillslope mass balance framework for estimating dust deposition rates

Consider a scenario in which a steady-state soil on a hillslope receives influxes of material from two sources: soil production via incorporation of the underlying rock into the soil at a rate P_r , and dust deposition from the atmosphere at a rate P_d (Figure 4.1). In many settings, the material directly underlying the soil has undergone some chemical weathering and is more accurately termed saprolite, but for simplicity in this derivation we call this underlying parent material bedrock. Central to the following derivation is the steady-state assumption, which requires that the total rate of mass addition to the soil ($P = P_r + P_d$) be balanced by the soil denudation rate D , which itself is the sum of the physical erosion rate E and the chemical erosion rate W . Similarly, for the soil to be in compositional steady state, the influx of each element X must be balanced by denudation of X . Assuming that downslope gradients in soil chemistry are negligible – a good approximation at hilltops and ridgelines (Mudd and Furbish, 2006; Yoo et al., 2007) – the steady-state mass balance equations for the bulk soil and for an element X may be written as follows.

$$P = P_r + P_d = D = E + W \quad (4.1)$$

$$P_X = P_r X_r + P_d X_d = D_X = E X_s + W_X \quad (4.2)$$

Here P_r is the soil production rate ($\text{M L}^{-2} \text{T}^{-1}$), P_d is the dust deposition rate ($\text{M L}^{-2} \text{T}^{-1}$), P is the total mass flux into the soil ($\text{M L}^{-2} \text{T}^{-1}$), P_X is the total flux of element X into the soil ($\text{M L}^{-2} \text{T}^{-1}$), E is the physical erosion rate ($\text{M L}^{-2} \text{T}^{-1}$), W_X is the chemical erosion rate of X ($\text{M L}^{-2} \text{T}^{-1}$), and X_r , X_s , and X_d are the concentrations (M/M) of X in the granite, soil, and dust, respectively.

In the case of a chemically immobile element (e.g., Zr), $W_{Zr} = 0$ and Equation 4.2 may be solved for the physical erosion rate E (Equation 4.3). This expression for E may be substituted into Equations 4.1 and 4.2 to yield expressions for the bulk chemical erosion rate W and the elemental chemical erosion rate W_X .

$$E = P_r \frac{Zr_r}{Zr_s} + P_d \frac{Zr_d}{Zr_s} \quad (4.3)$$

$$W = P_r \left(1 - \frac{Zr_r}{Zr_s}\right) + P_d \left(1 - \frac{Zr_d}{Zr_s}\right) \quad (4.4)$$

$$W_X = P_r \left(X_r - X_s \frac{Zr_r}{Zr_s}\right) + P_d \left(X_d - X_s \frac{Zr_d}{Zr_s}\right) \quad (4.5)$$

Equations 4.3-4.5 provide a straightforward framework for estimating steady-state chemical and physical erosion rates if the dust flux P_d and dust composition are known. However, measuring P_d can be difficult, especially over the long timescales of soil production and erosion which are relevant to this approach. Below we show how to estimate the magnitude of P_d by using the soil production rate P_r and the concentrations of two immobile elements in the bedrock, soil, and dust. We begin by defining a new term, f_d , as the fraction of the soil's parent material that is derived from dust.

$$\begin{aligned} f_d &\equiv \text{dust-derived fraction} = P_d/(P_r + P_d) \\ 1 - f_d &\equiv \text{bedrock-derived fraction} = P_r/(P_r + P_d) \end{aligned} \quad (4.6)$$

Under this definition, the dust deposition rate P_d may be rewritten as a function of the soil production rate P_r .

$$P_d = P_r f_d / (1 - f_d) \quad (4.7)$$

The total supply rate of an element X to the soil (Equation 4.2) may also be rewritten in terms of the total soil production rate $P_r + P_d$ and f_d .

$$P_X = (1 - f_d)(P_r + P_d)X_r + f_d(P_r + P_d)X_d \quad (4.8)$$

Next we invoke the chemical immobility of two elements (here Zr and Ti). If both Zr and Ti are immobile, then $W_{Zr} = 0$ and $W_{Ti} = 0$, which when substituted into Equation 4.2 yield Equations 4.9 and 4.10.

$$P_{Zr} = EZr_s \quad (4.9)$$

$$P_{Ti} = ETi_s. \quad (4.10)$$

Equations 4.9 and 4.10, in conjunction with Equation 4.8, yield two independent expressions for the physical erosion rate E .

$$E = (P_r + P_d) \left(\frac{(1 - f_d)Zr_r + f_dZr_d}{Zr_s} \right) \quad (4.11)$$

$$E = (P_r + P_d) \left(\frac{(1 - f_d)Ti_r + f_dTi_d}{Ti_s} \right) \quad (4.12)$$

Setting Equations 4.11 and 4.12 equal to each other permits calculation of the fraction of soil derived from dust, f_d .

$$f_d = \left(\frac{Ti_r}{Ti_s} - \frac{Zr_r}{Zr_s} \right) \left(\frac{Ti_r - Ti_d}{Ti_s} - \frac{Zr_r - Zr_d}{Zr_s} \right)^{-1} \quad (4.13)$$

Note the requirements for calculating f_d : one needs the concentrations of two immobile elements in the bedrock, soil, and dust. The value of f_d is the critical quantity in this analysis: It can be substituted into Equation 4.7 to yield the long-term dust deposition rate P_d , which can then be substituted into Equations 4.3-4.5 to yield the physical erosion rate and the bulk and elemental chemical erosion rates.

As Equation 4.13 makes clear, this approach loses its predictive power in cases where the Ti/Zr ratio in dust is indistinguishable from that in bedrock. Aside from that limiting scenario, however, this framework is useful in that it permits calculation of long-term physical and chemical erosion rates in places where dust deposition is significant without requiring direct physical measurements of long-term dust fluxes. It is also valuable because it is applicable to actively eroding hillslopes; unlike estimating dust fluxes by measuring the thickness of dust deposited over a known time interval, this approach does not require assuming that erosion of the deposited dust has been negligible. It is also valuable because the dust deposition rates it predicts are averaged over the soil residence time (10^3 - 10^5 years on most eroding hillslopes); thus it provides a means to estimate long-term dust deposition rates against which modern dust fluxes may be compared.

As stated above, this framework rests on the existence of multiple immobile elements in the system and the ability to determine their concentrations in dust. Thus it is certainly not possible to apply this framework everywhere. However, we suggest that in many environments – especially temperate climates where chemical weathering should be weak – multiple elements should be immobile, and it may be possible to use geologic considerations to constrain dust composition.

4.4 Field application in the Idaho Batholith

4.4.1 Chemical evidence for mafic dust deposition

At a series of 17 field sites along two altitudinal (and hence climatic) ridgeline transects in the canyon of the South Fork of the Salmon River in the Idaho Batholith, we collected rock and soil samples to estimate long-term chemical and physical erosion rates using Equations 4.1-4.5. The sampled ridgelines on both mountains are mantled with thin layers of soil (10-90 cm) and are dotted with large (> 1 m) granitic boulders. At each field site we collected 16 soil samples and 40 granite outcrop samples, whose compositions we assume reflect the compositions of the soil and the local granite underlying the sampled soil (Table 4.1). More extensive descriptions of the field sites, sample compositions, and the erosional history of the Idaho Batholith are reported in Chapter 5.

Several characteristics of the granite and soil compositions suggest that mafic material has been added to the otherwise granitic soils. First, the rock-to-soil enrichments of the elements most commonly assumed to be immobile (Zr and Ti) are quite different from one another, despite the fact that they should be identical if both Zr and Ti are immobile and derived entirely from the underlying rock alone. Second, the differences in Ti and Zr enrichment are systematic: At all of the field sites save one, enrichments of Ti are higher than Zr enrichments. If dust fluxes were ignored in Equation 4.4 (as is common practice (Riebe et al., 2001b, 2003, 2004b,a; Green et al., 2006; Burke et al., 2007, 2009; Dixon et al., 2009)), estimates of W would be, on average, over twice as high when estimated with Ti than with Zr (Figure 4.2). Such differences in rock-to-soil enrichments

between immobile elements are not unique to these field sites. Indeed, it is more common in the literature to find disagreements in rock-to-soil enrichments between different immobile elements (e.g., Green et al., 2006) than agreements (e.g., Anderson et al., 2002), suggesting that dust fluxes may play a significant role in setting soil composition in many places. Third, at many of our field sites rock-to-soil enrichments of several elements that are usually considered to be mobile (Mg, Fe, and Mn) are higher than those for presumably immobile Zr (Chapter 5). The high enrichments of these mafic elements suggests that mafic-rich material has been added to the otherwise granitic soil.

We suggest that the simplest explanation for these observations is deposition of mafic-rich dust. We acknowledge, however, that there are other possible explanations. For example, it is possible that the excess mafic elements could be derived from the dacite dikes rich in Ti, Fe, and Mg that intruded into the Idaho Batholith (Lund (2004); personal communication, K. Lund, March 2009)). However, we consider this unlikely. Although there are rare surface exposures of dacite on Pilot Peak and Tailholt Mountain, the sampled transects are overwhelmingly granitic, and locations for field sites were intentionally chosen near ridgelines where all of the nearby outcrops were granitic. The absence of dacite outcrops near our field sites thus makes it unlikely dacitic bedrock contributed to the sampled soils. It is also theoretically possible to explain the lower rock-to-soil enrichments of Zr relative to those of Ti, Fe, Mn, and Mg by arguing that Zr is more mobile than Ti, Fe, Mn, and Mg. This, however, is geochemically implausible. Zr in granites is found almost entirely in zircon – one of the least soluble silicates on Earth – and prior work has shown that Zr should not be more mobile than any of these elements (e.g., Hodson (2002)). Thus, rather than suggest that Ti, Fe, Mn, and Mg happen to be less mobile than Zr at our field sites, we instead favor the hypothesis that dust rich in these elements has been added to the sampled soils.

4.4.2 Eureka Flat: a proposed dust source to the canyon of the South Fork of the Salmon River

There are, to our knowledge, no direct measurements of dust fluxes or dust composition in the South Fork of the Salmon River canyon. This precludes the definitive calculation of long-term chemical and physical erosion rates at these field sites with Equations 4.3-4.5. However, it is possible to constrain probable dust compositions using published values from the literature, and to use those compositions to estimate long-term dust fluxes at our field sites using Equation 4.7.

We consider the most probable source of mafic dust to the Idaho Batholith to be the same material that generated the enormous Palouse loess fields on the Columbia Plateau. The Palouse loess extends over $> 50,000$ km² of southeastern Washington, northeastern Oregon, and northwestern Idaho (e.g., (Bryan, 1927; Busacca et al., 1992, 2004; Sweeney et al., 2007)), and the upper unit of the Palouse loess, which has been deposited over the past 15 kyr, is as much as 4.5 meters thick. Eureka Flat, an 80-km long deflationary plain 275 km WNW of our field sites in the South Fork of the Salmon River, has been proposed

as the primary source of the Palouse loess on the basis of chemical and textural similarities between the loess and the glacial outburst flood sediments blanketing Eureka Flat (Sweeney et al., 2007). The sediments in Eureka Flat are of mixed grain size (primarily silt, sand, and clay), and XRF measurements show that they are rich in Mg, Ti, and Fe (Sweeney et al., 2007), containing abundant material eroded from the Columbia Plateau basalt during repeated glacial outburst floods over the last ice age. Mean paleowind directions at Eureka Flat are reported to be primarily northeast, not southeast toward our field sites. We suggest, however, that normal variations from the mean wind direction could easily have transported a small amount of dust to our field sites in the South Fork Salmon River canyon. As we show below, only a small amount of dust from Eureka Flat must be mixed with the otherwise granitic soil at Pilot Peak and Tailholt Mountain to produce the observed soil compositions at our field sites.

The Palouse loess, of course, is not the only possible atmospheric source of minerals to our field sites. Central Idaho lies downwind of the Oregon Cascades, which have intermittently ejected large quantities of material into the atmosphere. During the Holocene, the largest Cascadia eruption was at Mt. Mazama, where 50 km^3 of material was thrown into the atmosphere roughly 7.7 ka (Bacon and Lanphere, 2006). Mt. Mazama, however, cannot be the source of mafic-rich elements at our field sites, for two reasons. First, many of our field sites have soil residence times shorter than the time since the Mazama eruption (Chapter 5); whatever Mazama ash fell on these soils would have eroded thousands of years ago. Further, the Mazama tephra has a Ti/Zr ratio of 16.6 ± 0.4 (Bacon and Druitt, 1988), similar to the sampled granite, which has Ti/Zr ratios that range from 16.3 ± 0.8 to 19.7 ± 0.7 . Deposition of Mazama tephra thus could not have produced the observed differences between rock-to-soil enrichments of Ti and Zr at our field sites.

4.4.3 Estimated dust deposition rates

Operating under the assumption that the same material that formed the Palouse loess also supplied the dust that fell on our field sites, we calculate the dust-derived fraction of the soil's parent material, f_d , and the long-term dust deposition rate P_d . These data show that the soils are dominantly derived from the underlying granite (the average f_d is $5.9 \pm 1.1\%$ on Pilot Peak and $3.3 \pm 0.5\%$ on Tailholt Mountain), and imply long-term mean dust fluxes P_d of $8 \pm 1 \text{ t km}^{-2} \text{ yr}^{-1}$ on both mountains. At all of our 17 field sites save one (discussed below), estimates of dust fluxes are in the range $3\text{-}13 \text{ t km}^{-2} \text{ yr}^{-1}$. These are comparable to dust fluxes of $4.3\text{-}15.7 \text{ t km}^{-2} \text{ yr}^{-1}$ measured elsewhere in the western United States (Reheis and Kihl, 1995; Reheis et al., 1995), which is consistent with the hypothesis that dust similar in composition to the Eureka Flat sediments has been mixed into the sampled soils. We note that even if Eureka Flat is not the source of mafic material to our field sites, these calculations demonstrate the power of relatively small dust fluxes to affect soil composition.

As Figure 4.3 shows, Equation 4.13 yields an impossible result for one site on Pilot Peak (P8, at 1277 m). This is the only site on either transect where the rock-to-soil

enrichment of Ti is smaller than that of Zr, and which therefore does not fit the Ti-rich dust hypothesis. Applying the dust model to site P8 with the proposed dust source yields the impossible result that less than 0% of the soil is derived from dust ($f_d = -2.7 \pm 0.9\%$), which itself produces a negative calculated dust flux ($P_d = -5 \pm 1 \text{ t km}^{-2} \text{ yr}^{-1}$). Thus site P8, alone among our seventeen field sites, does not fit the proposed dust model with the proposed dust source. It is not immediately clear why P8 differs from all the other sites in this respect. However, it is notable that although the rock sample composition at this site is not unusual for rocks from Pilot Peak, the P8 soil samples are on one end of the compositional spectrum for Pilot Peak soils, with more Si and less Al, Fe, Ti, Mg, Nb, and Rb than all other Pilot Peak soils. This suggests that the rock samples collected on the ridgeline above site P8 may be a poor reflection of the parent granite of the P8 soils.

4.5 Conclusions

The primary purpose of this paper is to present a simple model for estimating long-term dust fluxes to actively eroding terrain. We show that it may be used to infer long-term rates of dust deposition from measurements of soil production rates and concentrations of two immobile elements (e.g., Zr and Ti) in the soil, parent bedrock, and dust. This is, at its core, a steady-state model. Although it cannot capture any short-term variability in dust fluxes, the first-order estimates of dust deposition rate it yields may be considered long-term average rates, which can be compared with contemporary measurements of dust deposition to estimate the effects of climate change and human activity on dust production and deposition. This is a complementary approach to other methods for estimating long-term dust fluxes (e.g., measuring the thickness and ages of loess deposits (Busacca et al., 2004), or attributing imbalances in Sr isotope fluxes into and out of catchments to dust deposition (Pett-Ridge et al., 2009)).

We emphasize that our application of this method in the South Fork of the Salmon River canyon is not a definitive test of the method nor of the proposed dust source. A definitive test would require accurate direct measurements of dust flux and composition, which are unavailable over the long timescales intrinsic to the approach outlined here. However, given that Eureka Flat has been a persistent source of massive amounts of mafic dust to nearby sites (Sweeney et al., 2007), and that the magnitude of dust fluxes we estimate below are consistent with those measured elsewhere in the western United States (Reheis and Kihl, 1995; Reheis et al., 1995), we suggest that Eureka Flat is a plausible source of dust and that this is a reasonable approach to estimating long-term dust fluxes at our field sites. We suggest this approach may provide a practical tool for estimating long-term dust deposition rates in actively eroding environments, and thus help in quantifying aeolian inputs to biogeochemical cycles in a variety of field settings.

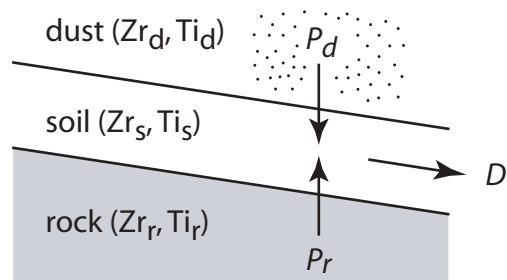


Figure 4.1. Schematic of a steadily eroding soil. In steady state the soil denudation rate D is balanced by the sum of the soil production rate P_r and the dust deposition rate P_d . Similarly, the concentrations of chemically immobile elements in the soil Zr_s and Ti_s remain constant over time.

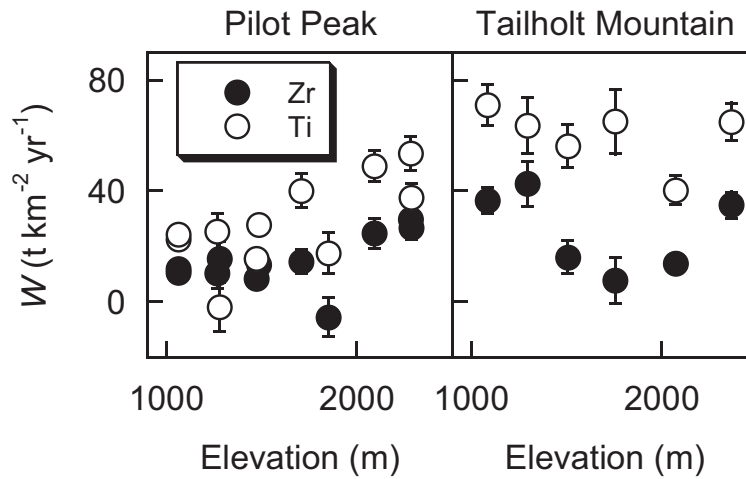


Figure 4.2. If dust fluxes were assumed to be negligible in Equation 4.4 (as is frequently done), then estimates of the chemical erosion rate W based on the rock-to-soil enrichment of a single immobile element would differ greatly depending on which element was selected as the truly immobile element. For example, if one were to assume $P_d = 0$ at our field sites in the Idaho Batholith, estimates of W calculated assuming Ti is immobile (open circles) would be, on average, more than twice as high as estimates of W calculated assuming Zr is immobile (black diamonds).

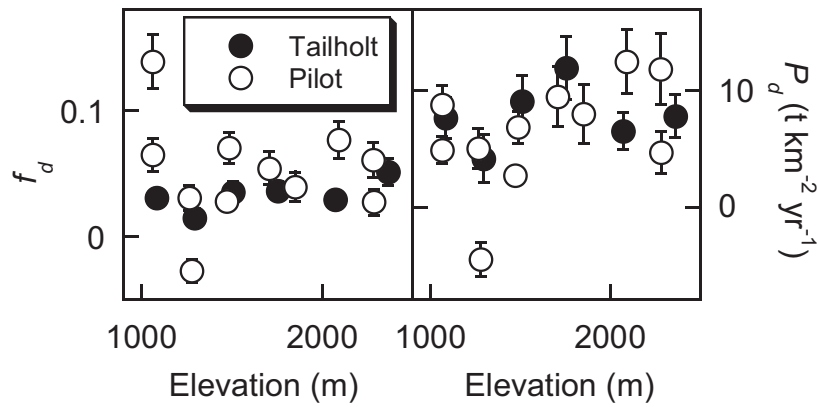


Figure 4.3. Under the assumption that the sampled soils are a weathering product of a mixture of the local granite and mafic dust derived from Columbia Plateau paleoflood sediments (Sweeney et al., 2007), we estimate the fraction of the soil’s parent material that is derived from dust, f_d (Equation 4.13), and the long-term dust deposition rate P_d (Equation 4.7).

Table 4.1: Immobile element concentrations, soil production rates, and estimated dust deposition rates

Site	Zr (ppm)		Ti (%)		P_r t km ⁻² yr ⁻¹	P_d
	rock	soil	rock	soil		
<i>Pilot Peak</i>						
P2283S	117±3	139±1	0.23±0.006	0.30±0.005	167±14	5±2
P2281N	117±3	140±1	0.23±0.006	0.33±0.006	183±15	12±3
P090	115±4	137±1	0.22±0.008	0.33±0.005	150±12	13±3
P1471S	127±3	139±1	0.22±0.006	0.27±0.004	94±7	3±1
P1485N	127±3	149±1	0.22±0.006	0.32±0.005	91±7	7±1
P1277S	119±4	131±2	0.20±0.009	0.20±0.005	171±13	-5±1
P1264N	119±4	127±1	0.20±0.009	0.24±0.006	159±12	5±2
P1062S	130±2	156±3	0.22±0.003	0.32±0.013	71±5	5±1
P1062N	130±2	161±1	0.22±0.003	0.40±0.007	55±4	9±2
P1850	123±3	120±3	0.22±0.006	0.24±0.008	194±15	8±3
P1706	123±3	134±1	0.20±0.008	0.26±0.005	166±13	10±3
<i>Tailholt Mt.</i>						
T2073	83±1	88±1	0.14±0.002	0.18±0.003	217±17	7±2
T2364	48±1	64±2	0.09±0.003	0.16±0.006	145±12	8±2
T1084	61±1	72±1	0.11±0.002	0.15±0.004	243±18	8±2
T1755	75±2	77±1	0.12±0.004	0.15±0.004	320±24	12±3
T1294	58±2	69±1	0.11±0.003	0.14±0.004	275±21	4±2
T1508	70±2	75±1	0.12±0.003	0.16±0.004	248±19	9±2

^a Zr and Ti concentrations in the proposed dust source are 166 ± 14 ppm and $1.04 \pm 0.14\%$, respectively (Sweeney et al., 2007).

^b Soil production rates from bedrock, P_r , are inferred from ¹⁰Be concentrations in soil-borne quartz using the CRONUS calculator (Balco et al., 2008), and discussed in detail in Chapter 5.

^c Dust deposition rates P_d are calculated with Equation 4.7.

Chapter 5

Effects of climate, physical erosion rates, and dust on long-term chemical erosion rates: Measurements along two altitudinal transects in the Idaho Batholith

5.1 Abstract

Chemical weathering promotes soil production and physical erosion, supplies nutrients to soils and streams, and modulates Earth's climate over long timescales by drawing down atmospheric CO₂. Although mineral dissolution rates show clear dependencies on temperature and moisture in laboratory experiments and in theoretical models of dissolution, the effect of climate on chemical erosion rates in natural landscapes remains uncertain, in large part because variations in factors like physical erosion rates and lithology can cloud climatic signals in measurements of chemical erosion rates. We present new estimates of long-term chemical and physical erosion rates along two altitudinal (and hence climatic) transects in the canyon of the South Fork of the Salmon River in the Idaho Batholith, inferred from measurements of soil production rates (derived from cosmogenic ¹⁰Be in soil-borne quartz), estimates of dust deposition rates, and the enrichment of chemically immobile elements in soil relative to its parent material. Our measurements suggest that mean annual soil temperature exerts a negligible influence on both chemical erosion rates and the extent to which soils are chemically weathered. These data also suggest that the annual duration of high soil moisture conditions (which at these sites depends primarily on the annual duration of snow cover) strongly influences the degree of chemical weathering, and may influence chemical erosion rates. Our measurements also show that soils at these sites tend to grow more chemically weathered with increasing soil residence time, implying that weathering at these sites is primarily limited by the kinetics

of mineral dissolution rather than by the supply rate of fresh minerals to the soil. Finally, these data suggest that influxes of mafic-rich dust are a significant source of minor and trace elements to the Idaho Batholith, and hence are an important supplier of nutrients to this terrain.

5.2 Introduction

A fisherman standing in a mountain stream and observing the terrain around him will see many features that are affected by chemical weathering. The soils on the surrounding hillslopes developed in part through chemical weathering of the parent rock, and the vegetation growing in those soils derive many of their nutrients from solutes liberated by mineral dissolution. The river running down the valley axis contains weathering-derived solutes that feed tiny aquatic biota which themselves feed the fish he is trying to catch. Above him, the shapes of the ridges and valleys have been influenced by chemical weathering through its weakening of bedrock and its acceleration of physical erosion. The temperature of the air around him has also been affected by chemical weathering. Over long timescales ($> 10^5$ years), chemical weathering of silicate minerals is Earth's primary sink for atmospheric CO_2 , and so modulates Earth's temperature via the greenhouse effect (Walker et al., 1981; Berner et al., 1983). It is the primary cause of Earth's long-term climatic stability (Kump et al., 2000). Because of this, it has even affected the fisherman's attire. By maintaining a habitable climate over millions of years, silicate weathering has indirectly influenced how many layers of clothing he chose to put on under his hip waders this morning.

Chemical weathering is clearly central to many important components of the Earth system – soil development, landscape evolution, nutrient supply, and long-term climate – and so quantifying the controls on rates of chemical weathering is of wide interest. There has recently been particular interest in measuring the effects of climate on chemical weathering rates because of the expected negative feedback between silicate chemical weathering rates and temperature. If the coupling between climate and silicate weathering rates is strong, then silicate weathering rates should increase quickly in response to increases in temperature and so quickly draw down atmospheric CO_2 , stabilizing Earth's temperature. If on the other hand silicate chemical weathering rates are only weakly dependent on temperature, then increases in temperature should produce minor increases in silicate chemical weathering rates and CO_2 consumption rates, and so only slowly stabilize Earth's climate.

Although there has been considerable progress in understanding how climatic variables affect mineral dissolution rates in theory and in the laboratory (e.g., Brady and Carroll, 1994; Blum and Stillings, 1995; Chen and Brantley, 1997; White et al., 1999a), conclusions differ about how climate should affect chemical weathering rates in nature. Many studies quantify the effects of temperature on chemical erosion rates by fitting

measured rates to an Arrhenius function,

$$W \propto \exp\left(\frac{-E_a}{RT}\right), \quad (5.1)$$

where W is the chemical erosion rate, E_a is the activation energy for the weathering reaction, R is the universal gas constant, and T is the temperature in Kelvin. With measurements of W and T , it is possible to estimate a best-fit value for E_a , which is a reflection of how strongly mineral dissolution rates depend on temperature. Values for E_a vary with the type of mineral being weathered (Kump et al., 2000), but there is considerable disagreement in field-derived estimates of E_a even for single mineral phases. For plagioclase alone, field-derived estimates of E_a vary by over a factor of five from 14 to 77 kJ mol⁻¹ (Velbel, 1993; White and Blum, 1995; Riebe et al., 2004a), making it difficult to assess how strongly W should depend on temperature.

Climate also influences chemical erosion rates through precipitation, which supplies moisture to mineral surfaces in the soil and thereby allows mineral dissolution to occur. Precipitation also promotes fluxes of water through the soil, which reduce the concentrations of mineral dissolution products in soil porewater and thereby drive net dissolution reactions forward. All else being equal, chemical erosion rates should increase with increasing moisture. This is broadly supported by compilations of measured chemical erosion rates that generally increase with mean annual precipitation or runoff, albeit with considerable scatter (e.g., Bluth and Kump, 1994; Millot et al., 2002; Dupre et al., 2003; Riebe et al., 2004a; West et al., 2005). These compilations have been made over a series of climatically diverse sites around the globe, an approach that has the advantage of being able to exploit the widest possible range of climates. However, this approach is vulnerable to site-to-site variations in other factors that may also affect chemical erosion rates, such as lithology, physical erosion rates, vegetation, and human activity, which can confound interpretation of climate's effects on chemical erosion rates and which may be responsible for much of the scatter in these compilations. An alternative approach is to measure chemical erosion rates at a series of sites along an altitudinal transect. Because climate changes continuously with altitude, and because altitudinal transects can lie along a single mountainside and thus within a small area, this approach is able to minimize variations in confounding variables like lithology and rock uplift rates while maximizing climatic variations. That is the approach taken in this study.

Previous studies along altitudinal transects have found that chemical erosion rates decrease with altitude (and hence with mean annual temperature), although the rate at which chemical erosion rates decline with altitude differs considerably between studies. Drever and Zobrist (1992) measured net alkalinity and silica concentrations in stream water along an altitudinal gradient spanning 220-2400 m in the Swiss Alps, and found that both of these proxies for chemical weathering fluxes decreased approximately exponentially with altitude. They suggested that some of this decrease could be a consequence of the decrease in temperature with altitude, but that most of it is related to the corresponding decrease in soil thickness with altitude at these field sites. Thus they did not attribute differences in chemical weathering fluxes along this transect strictly to differences in climate, but rather

to a combination of climatic factors and mineral supply factors. In the Appalachian Blue Ridge province, Velbel (1993) inferred plagioclase weathering rates from Na stream solute fluxes in two neighboring catchments with mean elevations of 849 m and 1019 m, respectively, and found that plagioclase weathering rates were 13% faster in the lower (and hence warmer) catchment. Velbel suggested that this field setting was ideally suited for isolating the effect of temperature on chemical weathering rates, because the relatively small difference in altitude between these two catchments produced few differences in factors besides temperature. In an altitudinal transect spanning 2090-2750 m in the Santa Rosa Mountains of Nevada, Riebe et al. (2004b) found that the enrichment of chemically immobile Zr in soil relative to its parent rock decreased sharply with elevation, such that the intensity of chemical weathering decreased to zero at the summit. They combined these Zr-based chemical weathering intensities with denudation rates inferred from cosmogenic ^{10}Be in soil-borne quartz to show that chemical erosion rates decreased rapidly with elevation, suggesting that changes in climate (and associated changes in vegetation) can greatly affect chemical erosion rates. In contrast to these continuous declines in chemical erosion rates with elevation, a recent study along an elevation transect spanning nearly 3 km in altitude in the Sierra Nevada concluded that total chemical erosion rates – calculated as the sum of chemical erosion rates in the saprolite and the soil – were fastest at intermediate elevations (Dixon et al., 2009). Because mean annual temperature drops with elevation and mean annual precipitation increases with elevation along this transect, Dixon et al. interpreted this pattern as a reflection of temperature-limited weathering at high altitudes and moisture-limited weathering at low altitudes.

These chemical erosion rate studies are complemented by studies that have measured the extent, rather than the rate, of chemical weathering in soils along altitudinal transects. Grieve et al. (1990) measured soil properties along a transect spanning 100-2600 m in altitude in Costa Rica, and found that the intensity of chemical weathering, as inferred from soil clay content and the ratio of free to total iron, decreased systematically with elevation. Dahlgren et al. (1997), in a thorough study of soil development along an elevation transect spanning 198-2865 m in the Sierra Nevada of California, found that two proxies for the degree of chemical weathering (total Fe oxide and clay contents in the soil column), were both greatest at intermediate altitudes and dropped off at higher and lower altitudes. Bockheim et al. (2000) examined a number of stable pedons along an altitudinal transect spanning 2700-3850 m in the Uinta Mountains of Utah, and found that a number of proxies for chemical weathering intensity (clay content, exchangeable cations, extractable Al, and solum thickness) were highest at the highest elevation sites. Rather than ascribing this pattern to differences in climate, they suggest that this may merely reflect the older age of the high-elevation soils. Egli et al. (2003, 2004, 2006) conducted detailed investigations of soils along two altitudinal gradients spanning 950-2440 m in the Italian Alps. Using the enrichment of chemically immobile Ti in upper soil horizons relative to a parent C horizon, they found that chemical losses of base cations were highest at intermediate elevations, although they found no altitudinal trends in total chemical losses. They also found that smectite concentrations were highest at intermediate elevations, and concluded that the degree of chemical weathering was highest at intermediate elevations. Thus some of these

studies have found that the highest altitude soils are the least weathered, while others have found that the highest altitude soils are the most weathered, and yet others have concluded that the most intensely weathered soils are at intermediate altitudes.

In summary, altitudinal patterns in both chemical erosion rates and the degree of chemical weathering differ markedly between studies, and this clouds interpretations about how climate should affect chemical erosion rates and soil development elsewhere.

In this contribution, we document chemical and physical erosion rates along two altitudinal (and hence climatic) transects in the canyon of the South Fork of the Salmon River in central Idaho (Figure 5.1). We measured these rates using a solid-phase mass balance technique that yields co-located estimates of long-term chemical and physical erosion rates (Stallard, 1985; Riebe et al., 2001b), which permits us to directly account for the potentially confounding effects of physical erosion rates on chemical erosion rates. Before discussing the particulars of our field sites in detail, we first present the conceptual framework we use to estimate long-term chemical and physical erosion rates.

5.3 Measuring chemical and physical erosion rates with cosmogenic nuclides and elemental abundances in soil, rock, and dust

An increasingly popular method for estimating chemical erosion rates in eroding terrain is the solid-phase mass balance method, which combines soil production rates with rock-to-soil enrichments of chemically immobile elements within a mass balance framework. This method, as conventionally applied, assumes that soil thickness and composition are steady in time and that soils are strictly a weathering product of the local bedrock (i.e., that contributions to the soil from atmospheric deposition are negligible) (Riebe et al., 2001b, 2003, 2004b,a; Green et al., 2006; Yoo et al., 2007; Burke et al., 2007, 2009; Dixon et al., 2009). Here we use the same method but add atmospheric dust deposition to the soil mass balance, following the approach applied by Owen et al. (2008) to soils in Chile's slowly-eroding, hyperarid Atacama Desert.

At its core, this is a steady-state mass balance method. That is, its central assumption is that the soil is in steady state over the soil residence time, both in terms of its mass per unit area of hillslope and in terms of its composition. This assumption demands that the total rate of mass addition to the soil, P , must be balanced by the soil denudation rate D . Similarly, it demands that the influx of each element X to the soil must be balanced by denudation of X from the soil. This can be made more concrete by considering a hillslope soil such as the one pictured in Figure 5.2. Here mass is incorporated into the soil through two pathways: first, by soil production from below at a rate P_r , and second, by dust deposition from above at a rate P_d . The soil denudation rate D is the sum of the mass loss rates by physical processes (e.g., biotic and abiotic creep) at a physical erosion rate E , and by chemical processes (e.g., mineral dissolution and

downslope solute transport) at a chemical erosion rate W . Assuming that downslope gradients in soil chemistry are negligible – a good approximation at hilltops and ridgelines (Mudd and Furbish, 2006; Yoo et al., 2007) – the steady-state mass balance equations for the bulk soil and for an element X may be written as follows.

$$P = P_r + P_d = D = E + W \quad (5.2)$$

$$P_X = P_r X_r + P_d X_d = D_X = E X_s + W_X \quad (5.3)$$

Here P_r is the soil production rate from bedrock ($\text{M L}^{-2} \text{T}^{-1}$), P_d is the dust deposition rate ($\text{M L}^{-2} \text{T}^{-1}$), P is the total mass flux into the soil from bedrock and dust ($\text{M L}^{-2} \text{T}^{-1}$), P_X is the total supply rate of element X to the soil ($\text{M L}^{-2} \text{T}^{-1}$), E is the physical erosion rate ($\text{M L}^{-2} \text{T}^{-1}$), W_X is the chemical erosion rate of X ($\text{M L}^{-2} \text{T}^{-1}$), and X_r , X_s , and X_d are the concentrations (M/M) of X in the granite, soil, and dust, respectively.

In the case of a chemically immobile element (e.g., Zr), $W_{Zr} = 0$ and Equation 5.3 may be solved for the physical erosion rate E (Equation 5.4). This expression for E may be substituted into Equations 5.2 and 5.3 to yield expressions for the bulk chemical erosion rate W and the elemental chemical erosion rate W_X .

$$E = P_r \frac{Zr_r}{Zr_s} + P_d \frac{Zr_d}{Zr_s} \quad (5.4)$$

$$W = P_r \left(1 - \frac{Zr_r}{Zr_s}\right) + P_d \left(1 - \frac{Zr_d}{Zr_s}\right) \quad (5.5)$$

$$W_X = P_r \left(X_r - X_s \frac{Zr_r}{Zr_s}\right) + P_d \left(X_d - X_s \frac{Zr_d}{Zr_s}\right) \quad (5.6)$$

This framework for estimating long-term chemical and physical erosion rates has become more accessible over the past decade thanks to advances in cosmogenic nuclide geochemistry, which now permit soil production rates to be inferred from concentrations of cosmogenic nuclides within minerals in the soil or its parent rock. Soil production rates inferred from cosmogenic ^{10}Be in quartz, for example, have now been used in several studies to estimate long-term chemical and physical erosion rates under the assumption that dust deposition is an insignificant component of the mass balance (i.e., that $P_d \rightarrow 0$) (Riebe et al., 2001b, 2003, 2004b,a; Green et al., 2006; Yoo et al., 2007; Burke et al., 2007, 2009; Dixon et al., 2009). In places where dust fluxes are significant, Equations 5.4-5.6 explicitly show that estimating chemical and physical erosion rates requires measurements of both the magnitude and the composition of the dust flux as well as the compositions of the soil and its parent rock. From a practical standpoint, at some field sites measurements of P_d may not be available, and it may be difficult to estimate P_d over the long soil residence times relevant to these mass balance equations. Even if no measurements of dust flux exist at a given field site, however, it may be possible to use geologic considerations to pinpoint the dust source and constrain the probable dust composition. In Chapter 4, I show that if one can constrain the dust composition, this mass balance framework may be

used to estimate the magnitude of the long-term dust flux, provided that there are multiple immobile elements (e.g., Zr and Ti) in the rock, soil, and dust.

Equations 5.5 and 5.6 suggest that chemical erosion rates may be closely coupled to denudation rates, a suggestion supported by many co-located measurements of physical and chemical erosion rates in the field (e.g., Stallard and Edmond, 1983; Gaillardet et al., 1999; Anderson et al., 2002; Millot et al., 2002; Riebe et al., 2004a; West et al., 2005). Because this coupling between chemical erosion rates and denudation rates can make it difficult to discern the effects of other factors like climate on chemical erosion rates, it can be useful to normalize W and W_X by the rates at which fresh material is supplied to the soil, to more sharply illustrate the susceptibility of the bulk soil and individual elements to chemical losses. The fraction of the soil denudation rate that is accounted for by chemical losses may be expressed in steady-state as the ratio of W to P , and is commonly termed the chemical depletion fraction, or CDF for short (Riebe et al., 2001b).

$$CDF = \frac{P_r}{P_r + P_d} \left(1 - \frac{Zr_r}{Zr_s}\right) + \frac{P_d}{P_r + P_d} \left(1 - \frac{Zr_d}{Zr_s}\right) \quad (5.7)$$

The fraction of the elemental denudation rate that occurs by chemical processes may similarly be expressed as the ratio of the elemental chemical erosion rate W_X to the elemental supply rate P_X , and is commonly termed CDF_X (Riebe et al., 2001b).

$$CDF_X = \frac{P_r(X_r - X_s Zr_r / Zr_s) + P_d(X_d - X_s Zr_d / Zr_s)}{P_r X_r + P_d X_d} \quad (5.8)$$

In cases where dust fluxes are negligible (i.e., where $P_d \rightarrow 0$), these expressions for CDF and CDF_X converge to the expressions for CDF and CDF_X as defined in Riebe et al. (2001b), as they should. For readers more familiar with the τ notation for describing elemental depletion relative to an immobile element (Brimhall and Dietrich, 1987; Chadwick et al., 1990), we note that in cases where dust deposition is negligible, CDF_X and τ_X are simply related by a negative sign: $CDF_X = -\tau_X$.

There are two timescales inherent in this solid-phase mass balance method. The first is the timescale associated with the accumulation of cosmogenic ^{10}Be from which soil production rates are inferred. Because the intensity of cosmogenic radiation (and therefore the rate of ^{10}Be production) drops off rapidly and approximately exponentially below the Earth's surface, this timescale is the time the sampled quartz spent in the short zone below the Earth's surface where it acquired the bulk of its ^{10}Be . In practice, this timescale is typically calculated as the so-called cosmogenic attenuation length (Λ) divided by the soil production rate, where Λ is an exponential scaling constant ($\Lambda = 160 \text{ g cm}^{-2}$; Gosse and Phillips, 2001) that describes how quickly the intensity of cosmogenic radiation decreases as it passes through matter. For example, on a typical hillslope with a soil production rate of $0.027 \text{ g cm}^{-2} \text{ yr}^{-1}$ (i.e., with a lowering rate of 0.1 mm yr^{-1} in rock with a density of 2.7 g cm^{-3}), the ^{10}Be accumulation timescale is $160 \text{ g cm}^{-2} / 0.027 \text{ g cm}^{-2} \text{ yr}^{-1} = 5900$ years.

The second timescale inherent in this solid-phase mass balance method is the time it takes soils to weather to their sampled composition, which in a steady-state system is the

soil residence time. This may be estimated as the soil thickness times the soil density divided by the physical erosion rate. For example, in a typical hillslope soil one meter thick, of density 1.5 g cm^{-3} , and eroding at $150 \text{ t km}^{-2} \text{ yr}^{-1}$, the soil residence time is 10,000 years. Thus the two timescales inherent in this solid-phase mass balance approach are often comparable but not identical, and in calculating E , W , and W_X it is implicitly assumed that the estimated value of the soil production rate (which is an estimate over the timescale of cosmogenic nuclide accumulation) is also the value of the soil production rate over the soil residence time. Because E , W and W_X are estimated using the chemical differences between the soil and its parent rock – a property that evolved over the soil residence time rather than over the cosmogenic nuclide accumulation time – the appropriate timescale to apply to estimates of E , W , and W_X is the soil residence time.

5.4 Study area: Pilot Peak and Tailholt Mountain in the Idaho Batholith

Pilot Peak and Tailholt Mountain, two mountains flanking the canyon of the South Fork of the Salmon River in the granitic Idaho Batholith (Figure 5.1), are the natural laboratory in which we have chosen to study the effects of climate on chemical erosion rates. We selected Pilot Peak and Tailholt Mountain because they span a wide range of altitudes over short horizontal distances – 1500 m and 1300 m over 5.1 and 5.7 horizontal km, respectively – and thus span a wide range in climates while maintaining minimal variation in other factors like rock uplift rates, lithology, and land use that could confound interpretations of measured chemical erosion rates. These sites lie within 87-78 Ma plutons of biotite-muscovite granite and granite-granodiorite in the Idaho Batholith (Lund, 2004). Neither mountain has mapped faults passing through it (Lund, 2004) or obvious field evidence of faulting, suggesting that neither should be subject to sharp discontinuities in rock uplift rates that could influence physical erosion rates and thereby influence chemical erosion rates. Vegetation is dominated by ponderosa pine and Idaho bluebunch grass at most elevations on both transects. Anthropogenic disturbance on these mountains has been minimal, with no roads or trails along the ridgelines where we set our field sites. Both mountains are covered with thin layers of soil (10-90 cm) and have large ($> 1 \text{ m}$) granitic boulders outcropping frequently. An expected moist atmospheric lapse rate of $5\text{-}6 \text{ }^\circ\text{C/km}$ implies that mean annual air temperature at the summits should be $8\text{-}9 \text{ }^\circ\text{C}$ cooler than at the base of the canyon – a difference in temperature nearly as large as the glacial-interglacial temperature shift inferred from Antarctic ice cores (Petit et al., 1999). These are sizable climatic gradients.

The present-day topography of central Idaho is dominated by the drainage network of the Salmon River and its tributaries, which have incised deep canyons into the Idaho Batholith. The canyon of the South Fork of the Salmon River where our field sites are located, for example, is as deep and as steep as the Grand Canyon in Arizona. In contrast to the steep topography and high relief, however, the present pace of erosion in the Idaho

Batholith is moderate, and has been for the past 50 Myr. As shown in the studies reviewed below, erosion rates in central Idaho have not been fast since the Cretaceous.

The measurements stretching farthest back in time are those by Lund et al. (1986), who used $^{40}\text{Ar}/^{39}\text{Ar}$ dating to measure mineral cooling ages approximately 50 km north of Tailholt Mountain. These cooling rates may be combined with an assumed geothermal gradient of 25 °C/km (Sweetkind and Blackwell, 1989) to estimate rock exhumation rates (Table 5.1). These data imply that exhumation rates were very fast (2.4-5.6 mm/yr) shortly after emplacement of the batholith 81 – 78 Ma, and dropped to an average of 0.14 mm/yr by 54 Ma. Complementing these $^{40}\text{Ar}/^{39}\text{Ar}$ measurements, Sweetkind and Blackwell (1989) estimated long-term exhumation rates in the Idaho Batholith by measuring fission track ages in apatites. They noted that the youngest fission-track ages are from the bottoms of canyons, and they suggest that these data imply a canyon incision rate of 0.32 ± 0.10 mm/yr since 11.4 ± 1.4 Ma, a factor of 3-10 faster than the exhumation rates their fission-track ages from 11.4 Ma to 63 Ma imply. We note that 11.4 Myr is more than adequate time to carve the currently existing canyons in the Idaho Batholith; if the canyons were incised at 0.32 mm/yr while the surrounding uplands continued to erode at 0.03-0.1 mm/yr, the 1500 m of relief in the South Fork of the Salmon River canyon could be generated in 5-7 Myr.

More recently, denudation rates averaged over the past thousands to tens of thousands of years have been inferred from ^{10}Be concentrations in stream sediment elsewhere in the Idaho Batholith (Kirchner et al., 2001). These rates range from 55 ± 8 to 327 ± 42 t km⁻² yr⁻¹ (which, when divided by the parent rock density, yield lowering rates of 0.02 ± 0.003 mm/yr to 0.12 ± 0.02 mm/yr), and are, on average, 17 times faster than short-term sediment fluxes measured in the same rivers over the previous 10-84 years. Kirchner et al. interpreted the very low 20th-century sediment fluxes as an indication that long-term average sediment fluxes in the Idaho Batholith are dominated by large, infrequent events that deliver massive amounts of sediment to streams, and that the modern-day sediment gauging records simply have not captured any of these rare events during their short monitoring periods.

The studies mentioned above document estimates of exhumation rates and denudation rates – i.e., mass effluxes at and near the Earth’s surface – in central Idaho. Surface uplift rates, which reflect the difference between rock uplift rates and denudation rates, have also been estimated near the South Fork of the Salmon River. Axelrod (1998), in a study of fossil flora in Eocene volcanic strata on Thunder Mountain (44° 57’ N, 115° 08’ W, approximately 40 km southeast of Pilot Peak) estimated that the elevation of the caldera floor of Thunder Mountain was 1730 m at the time of volcanic deposition 46-54 Ma. This paleoelevation is 580 m lower than the present elevation of the caldera floor, and implies an average surface uplift rate of 0.011-0.013 mm/yr over the past 46-54 Ma.

As a group, these studies indicate that central Idaho has been home to relatively slow erosion and only slightly faster rock uplift since the early Eocene. On short timescales, erosion appears to be highly episodic, characterized by centuries to millennia of very slow erosion punctuated by large, infrequent erosional events. When averaged over millennial or

longer timescales, the Idaho Batholith has been eroding at 0.02-0.32 mm/yr – comparable to the modern-day globally averaged denudation rate of approximately 0.05 mm/yr (Wilkinson and McElroy, 2007) – for the past 50 Myr (Table 5.1). The long-term rates reported in these studies provide a context for our new measurements of soil production rates (section 5.6.1), which are averaged over the past thousands to tens of thousands of years.

5.5 Methods

5.5.1 Field sampling of rocks and soils

In September 2005 we established a series of field sites on Pilot Peak and Tailholt Mountain (Figure 5.1; Table 5.2) to measure chemical erosion rates along two altitudinal (and hence climatic) ridgeline transects. At each field site we collected two sets of soil samples and one set of rock samples. The first set of soil samples consisted of 16 horizontally distributed soil samples collected from a small rectangular plot (typically ~10 m x 10 m; see Appendix E for site photographs). This small spread in soil sampling locations at each site was intended to quantify horizontal variability in soil composition. For consistency's sake, each of these 16 soil samples was collected 10-15 cm below the surface, which roughly corresponded to the base of the roots of the bunch grasses. Soil sampling plots at different field sites were located at different distances from the ridgeline; all were 0-45 m from the ridgeline in the direction of steepest descent. Within the soil sampling plot at each field site, one soil excavation was dug down to or close to the parent material to install soil temperature and soil moisture probes. In each soil excavation, we collected a second set of soil samples from a range of depths to quantify vertical variability in composition. Where possible, these samples included samples of the parent material below the soil. At most field sites, the parent material was a continuous layer of weathered rock, although at a few sites the parent material was not continuous but rather consisted of large (>30 cm) angular rocks packed closely together. In addition to the soil samples, 40 rock outcrop samples were collected at each site to characterize the parent material of the soil. Most rock samples were collected within 10 m up-ridge and up-slope of the soil plots. At some sites, there were few outcrops immediately next to the soil plots, and at these sites outcrops were sampled as far away as ~50 m up-ridge. At four elevations on Pilot Peak, we collected soil samples from both sides of the ridge to examine the effects of slope aspect on soil climate and chemical erosion rates. These paired sites are sites P2283S and P2281N, P1471S and P1485N, P1277S and P1264N, and P1062S and P1062N (Table 5.2). We consider the rock samples collected from the ridgeline between these paired sites to be representative of the parent rock underlying the soils on both sides of the ridge. In this site-naming convention, the site ID indicates the mountain (P for Pilot Peak, T for Tailholt Mountain), the altitude in meters, and, where soils were sampled on both sides of the ridgeline, the slope aspect. Thus site P1062S, for example, is a south-facing site on Pilot Peak at 1062 m.

In subsequent field trips, numerous soil pits were dug down to parent material within the original soil plot to estimate average soil depths. These soil depth measurements, summarized in Table 5.2, are vertical distances between the surface and the parent material, and so must be multiplied by the cosine of the hillslope gradient (also listed in Table 5.2) to yield soil thicknesses normal to the hillslope surface.

5.5.2 Installation of soil moisture and temperature probes

In September 2005 we installed soil moisture probes and temperature probes in the uphill face of a soil pit at each field site. Each site was instrumented with three Decagon ECHO-10 soil moisture probes and two Decagon temperature probes, which were connected to a single Decagon Em-5 datalogger housed in an airtight metal canister. At sites where the soil pits were deep enough to reach parent material (all sites except P1062S, T1084, and T1508), one temperature probe and one soil moisture probe were placed at the boundary between soil and its parent material. A second soil moisture probe was inserted into the soil at a depth of 5 cm, and the third soil moisture probe was placed at an intermediate depth between the upper and lower probes. The second temperature probe was originally placed such that its tip emerged just above the soil surface, and was covered with an opaque perforated plastic box 6 cm x 10 cm x 7 cm in size to shield it from direct sunlight. This was done with the intention of measuring air temperature. These upper temperature probes did not produce good data during the first year of monitoring – some probes failed during hot temperature excursions, and some were bitten off by wildlife – so during our return to these sites in 2006, these upper temperature probes were buried at a depth of 5 cm. All instruments recorded one reading every four hours, providing a coarse picture of diurnal variations in soil climates and a detailed picture of longer-period variations in soil climates.

5.5.3 Sample preparation for chemical analysis of rock and soil samples

All rock and soil samples were prepared for chemical analysis by X-ray fluorescence by standard procedures (Riebe, 2000). All samples were split, and about 30 g of one of the splits was powdered in a tungsten carbide Spex shatterbox. Powdered samples were then baked at 500 °C for 12 hours to eliminate organic material. At this point, two sets of samples were prepared, one for major element chemistry and one for trace element chemistry. Major element samples were prepared by mixing 3.5000 ± 0.0001 g of lithium tetraborate with 0.5000 ± 0.0001 g of powdered sample, homogenizing this powder in a shaker for 15 minutes, melting the mixed powders in a platinum crucible above a bunsen burner flame for 10 minutes, and pouring the melted mixture into a platinum tray. This yielded glass disks roughly 33 mm in diameter and 2 mm thick. Trace element samples were prepared by mixing 3.3 ± 0.1 g of powdered sample with five drops of polyvinyl alcohol and pressing the mixed powder into a pellet with a boric acid backing. Both trace

element pellets and major element disks were then analyzed for elemental abundances on a Phillips 2400R X-ray fluorescence spectrometer.

5.5.4 Sample preparation for cosmogenic ^{10}Be

Soil production rates were inferred from concentrations of ^{10}Be in quartz extracted from amalgamated soil samples at each site. From each of the sixteen near-surface soil samples (i.e., those collected at a depth of 10-15 cm) at each site, we split approximately 150 g of soil, and mixed these splits together. These amalgamated soil samples were themselves split, and from one of these splits 39-55 g of quartz was isolated from the > 250 micron size fraction by standard magnetic and chemical separations (Kohl and Nishiizumi, 1992; Riebe, 2000). These quartz samples were spiked with known amounts of ^9Be in solution, after which they were dissolved in a mixture of hydrofluoric and nitric acids, dried down in platinum crucibles, redissolved in sulfuric acid, dried down a second time, and redissolved in hydrochloric acid. Beryllium was then isolated from other elements in cation exchange columns and precipitated as beryllium hydroxide by raising the pH of the solution to 8 with ammonium hydroxide. Beryllium hydroxide was isolated from solution by centrifugation, placed in quartz crucibles, and baked at $750\text{ }^\circ\text{C}$ to oxidize the material to BeO . Each BeO sample was then mixed with niobium powder and packed into stainless steel sample holders for measurement at the Center for Accelerator Mass Spectrometry at Lawrence Livermore National Laboratory.

5.6 Data

5.6.1 Soil production rates inferred from cosmogenic ^{10}Be

Concentrations of ^{10}Be in our samples were measured at the Center for Accelerator Mass Spectrometry at Lawrence Livermore National Laboratory on July 15, 2007 and referenced to isotopic standard 07KNSTD3110. We used these ^{10}Be concentrations to calculate a steady-state soil production rate at each field site using the CRONUS calculator (Balco et al., 2008), a tool designed to standardize calculation of cosmogenically-inferred denudation rates. The CRONUS calculator requires as inputs the sample latitude, longitude, elevation, an atmospheric scaling convention, sample thickness, parent rock density, a shielding factor between 0 and 1, and the measured ^{10}Be concentrations. The inputs we used for sample latitude, longitude, and elevation are listed in Table 5.2, and all other inputs are listed in Table 5.3. The CRONUS calculator is also able to calculate topographic shielding factors if provided with the angular elevation of the horizon at multiple azimuths, and we used it to calculate the shielding factors listed in Table 5.3. These shielding factors were calculated from eight horizon angles that were measured with a Brunton compass at azimuths of 0, 45, 90, 135, 180, 225, 270, and 315 degrees at each site.

CRONUS-calculated soil production rates at our field sites range from 55 to 320 t

$\text{km}^{-2} \text{yr}^{-1}$, which can be divided by the parent rock density (assumed 2.7 g cm^{-3}) to yield lowering rates of 0.02 to 0.12 mm yr^{-1} (Table 5.3). Soil production rates on Tailholt Mountain tend to be faster than those on Pilot Peak (Figure 5.6). On Pilot Peak soil production rates range from 55 to $194 \text{ t km}^{-2} \text{yr}^{-1}$, while on Tailholt Mountain soil production rates range from 217 to $320 \text{ t km}^{-2} \text{yr}^{-1}$ except at the summit (site T2364), where the soil production rate is $145 \text{ t km}^{-2} \text{yr}^{-1}$ (Table 5.3). These soil production rates are comparable to other soil production rates inferred from cosmogenic ^{10}Be in the Idaho Batholith (Kirchner et al., 2001), approximately an order of magnitude faster than physical erosion rates inferred from short-term sediment yields over the past 10-84 years (Kirchner et al., 2001), and over an order of magnitude slower than exhumation rates in the period following emplacement of the batholith approximately 80 Ma (Lund et al., 1986).

In addition to the ridgeline soil production rates, we also measured ^{10}Be concentrations in quartz in a stream sediment sample from Elk Creek (site EC in Figure 5.1), a major tributary of the South Fork of the Salmon River which borders Pilot Peak directly to the south. We collected stream sediment near the outlet of Elk Creek with the intention of measuring a basin-averaged soil production rate for the 113 km^2 Elk Creek basin (as in, e.g., Brown et al., 1995). This stream sediment sample yielded a soil production rate of $448 \pm 36 \text{ t km}^{-2} \text{yr}^{-1}$, faster than the rates at any of our ridgeline sites on either mountain. As can be seen in Figure 5.1, some of the Elk Creek catchment is composed of hillslopes on Pilot Peak. If the Elk Creek sediment sample is truly representative of the basin-averaged lowering rate, and if the hillslopes on the southern side of Pilot Peak are eroding at the basin-averaged rate, then it implies that the hillslopes are eroding 2-7 times faster than the sampled ridgeline. If so, this implies that the ridgeline must be growing narrower over time, which suggests that this portion of the South Fork of the Salmon River canyon is not in topographic steady state. It must be noted, however, that the ^{10}Be concentrations measured in this stream sediment sample may not be perfectly representative of a steady-state lowering rate averaged over the entire basin. As can be seen in the topography in Figure 5.1, the upper basins of the Elk Creek catchment are scalloped in a manner consistent with the imprint left by mountain glaciers. If the upper portions of Elk Creek were glaciated during the Last Glacial Maximum and these glaciers eroded enough soil and rock to reset the concentration of cosmogenic ^{10}Be at the surface to zero, it is possible that the glaciated terrain has not yet reached the isotopic steady state assumed by the soil production rate calculation. If so, the sediment derived from the glaciated portions of the Elk Creek basin may have lower concentrations of ^{10}Be than sediment derived from the unglaciated portions of the basin. If true, a sample of mixed stream sediment in Elk Creek would produce an inferred soil production rate that is faster than the true basin-averaged soil production rate. This could account for the difference between the calculated Elk Creek soil production rate and the ridgeline soil production rates. Testing this hypothesis in future work will require comparing cosmogenic ^{10}Be concentrations in stream sediment from glaciated and unglaciated subcatchments of the Elk Creek basin. We note that glaciation should be a concern only for the Elk Creek sediment sample: none of our ridgeline field sites on either transect have a morphology

indicative of glaciation, so we do not expect glaciation to have influenced the measured ^{10}Be concentrations and hence the inferred soil production rates at these locations.

5.6.2 Chemical composition of rocks and soils

Tables 5.4-5.7 list the average chemical compositions of rock and soil samples, derived from the complete list of 916 sample compositions in Tables F.1-F.4. Average soil compositions were calculated from the sixteen horizontally distributed soil samples collected a short distance (10-15 cm) below the surface. These average soil compositions do not include the soil samples collected from the vertical soil profile at each site, because soil samples at depth may be below the zone of soil mixing and thus may not have a composition that is representative of the soil that is actively eroding, which is what the mass balance framework (Equations 5.2-5.8) requires.

At most of our field sites, the sets of rock and soil samples are well approximated by multivariate normal compositional distributions, and we assume that the mean compositions of these sample sets are accurate representations of the soil and the soil's parent granite. One of these typical distributions is shown in Figure 5.3. However, at sites T2364 and T1755, rock samples are much more variable in composition than rocks collected at other field sites, and fall into two compositional groups. One of these groups has a composition similar to rocks at the other sites on Tailholt Mountain (black crosses in Figure 5.4), while the second group has a strikingly different composition with much lower concentrations of certain elements, especially Ca, Sr and Na (red X's in Figure 5.4). In contrast to the bimodal rock samples at T2364 and T1755, the soil samples at these sites (blue dots in Figure 5.4) fall into single unimodal distributions and have compositions similar to those in soils at the other Tailholt Mountain sites, suggesting they are derived from parent rocks similar to the parent rocks elsewhere on Tailholt Mountain. If we were to consider the average composition of all sampled rocks at sites T2364 and T1755 to be representative of the parent material of the sampled soils, we would be forced into the geochemically unreasonable conclusion that highly soluble Ca and Na are much less chemically mobile than immobile Zr. Instead, we assume that the sampled soils at T2364 and T1755 are a product only of the first set of "typical" rock samples, and do not reflect contributions from the second group of "atypical" rock samples. We therefore exclude the second group of rock samples from all calculations of average rock composition at T2364 and T1755 and thus of chemical and physical erosion rates at these sites. The subsets of the sampled rocks at T2364 and T1755 that we consider representative of the parent rock are, at site T2364: X1-X5, X7, X8, X10, X19, X25, X26, X35, X37, X38; and at site T1755: X3-X8, X36, and X39. The mean rock compositions for T2364 and T1755 listed in Table 5.6 are the mean compositions of these sample subsets.

5.6.3 Chemical composition in depth profiles

In addition to the sixteen horizontally distributed soil samples from 10-15 cm depths, we also measured the composition of soil and saprolite samples in a vertical soil profile at each site to assess vertical variability in composition. Most elemental concentrations show no obvious trends as a function of depth within the soil (Figures C.1-C.15). This is especially true of the most abundant elements, Si and Al, which in their oxide forms together comprise 85-91% of each soil sample on Pilot Peak and 88-94% of each soil sample on Tailholt Mountain.

Of the seventeen elements measured in each sample, we pay particular attention to a few. Zirconium and titanium, in particular, are the elements most frequently considered to be chemically immobile, and hence most likely to be reliable indicators of chemical weathering. If the soil were not vertically mixed, vertical trends in concentrations of either of these elements would indicate progressive chemical weathering toward the surface. The absence of such gradients in Zr or Ti concentrations within our sampled soil profiles suggests either that negligible chemical weathering occurs within the soil, or that the soil is vertically mixed over the soil residence time (Figures C.1-C.15). The clear compositional difference between the soil and the parent granite suggests that some chemical weathering indeed occurs in the soil, and the presence of abundant rodent burrows in the soil suggests that the soil is indeed being mixed. Thus we suggest that the sampled soils are generally well mixed.

5.6.4 Soil climate records

Instruments installed in the soil at each site recorded temperature and a proxy for soil moisture once every four hours from September 2005 to August 2008. These time series measurements show that at any given site, soil temperature and moisture tend to be closely and inversely related to one another: soils are warm and dry during summers and cold and wet during winters (e.g., at site P2090 in Figure 5.7). These measurements also show that soils at high altitudes are colder and have longer wet seasons than soils at low altitudes. Here we discuss the details of these measurements.

Soil temperature

Figure 5.8 shows that mean annual soil temperature (MAST) broadly decreases with elevation on both Pilot Peak and Tailholt Mountain, as expected. At several sites, calculating MAST required filling data gaps in the temperature records where the instruments succumbed to electrical failure, heat, or rodents. We filled these data gaps with temperature estimates based on correlations with soil temperatures at the nearest sites, as described in Appendix D.

The annual temperature cycles at any given site reveal an interesting pattern that ends up affecting MAST and the altitudinal gradient in MAST: soil temperatures tend to

be buffered near freezing during the winter months (e.g., Figure 5.7). This is presumably a consequence of the winter snow cover that insulates the soil against cold excursions in air temperature. This effect is especially noticeable at the higher elevation sites (e.g., sites P2283S, P2281N, and T2364), where the temperature drops to 2-3 °C in November and steadily decreases to 0 ± 1 °C over the course of the winter. At a few sites (P1485N, T1755, T1294), this winter-long temperature buffering occurs at somewhat lower temperatures (-3 to -7 °C). During this time period, diurnal variations in soil temperature are very small (< 0.1 °C). The net result of this winter temperature buffering is to make the annual soil temperature cycle look (to first order) like a sinusoid with the wintertime troughs truncated at a warmer temperature than they would otherwise descend to. Because this winter temperature buffering prevents soils from getting as cold as the air during the winter, every soil that experiences this temperature buffering has a MAST that is warmer than the mean annual air temperature (MAAT) directly above it. And, because this winter temperature buffering lasts longest at the highest altitudes – as long as seven months at the highest Tailholt Mountain site (T2364, 2364 m), and as short as two months at the lowest Pilot Peak site (P1062S, 1062 m) – the difference between MAST and MAAT is bigger at higher altitudes than at lower altitudes. This results in altitudinal gradients in MAST of 2.2 °C/km on Tailholt Mountain and 3.1 °C/km on Pilot Peak, shallower than the altitudinal gradient in MAAT of 5-6 °C/km that would be expected from a standard moist atmospheric lapse rate. These data demonstrate the importance of measuring soil temperature rather than air temperature along altitudinal transects, because site-to-site differences in soil temperature – which should be the proximal thermal influence on mineral weathering – may differ greatly from differences in air temperature.

As well as being a function of altitude, soil temperature also depends on slope aspect and vegetation. South-facing slopes are systematically hotter by 1-3 °C MAST than north-facing slopes at the same altitude (compare sites P1471S and P1485N, P1277S and P1264N, and P1062S and P1062N in Table 5.2). The exception to this pattern is at the highest elevation sites on Pilot Peak, where the south facing site P2283S has soils that are slightly cooler than those at site P2281N on the north side of the ridgeline. This is likely a consequence of differences in vegetation between P2283S and P2281N. Uniquely among all of our field sites on both mountains, site P2283S lies under a thick grove of evergreen trees and is well shaded from the sun. By contrast, site P2281N is vegetated only with bunch grasses and thus is exposed directly to the sun.

Soil moisture

We found it impossible to accurately calibrate the raw measurements from the soil moisture probes. These probes do not measure soil moisture directly; instead, they determine the capacitance of their surroundings by transmitting an electromagnetic pulse into their surroundings and measuring the return voltage, which is proportional to the dielectric constant of the probe's surroundings. Because water has a much higher dielectric constant than soil, the voltage measured by the probe is strongly dependent upon the volumetric water content of the soil. The voltage, however, is also dependent on the

fraction of the blade that is in contact with the soil, because air has a much lower dielectric constant than soil. Thus, a meaningful comparison of ECHO-10 measurements between instruments, even within the same soil pit, requires that each be installed in soil with an identical porosity. It is unlikely we achieved this. The soils at our field sites are coarse-grained, and during instrument installations, the soils were hard, dry, and friable, with a texture much like the interior of a dried pretzel. This precluded the insertion of these probes into the soil without destruction of the soil structure. Instead, the instruments were installed by carving a small space into the uphill wall of the soil pit with a knife, sliding the ECHO-10 probe into this space, and filling the space around the probe with loose soil. This unquestionably led to differences between probes in the bulk density and porosity of the material surrounding the probes.

Thus we suggest that differences in instrument installation are the simplest explanation for the observed differences in the raw voltages measured by different ECHO-10 probes within the same soil pit. Consider, for example, the raw soil moisture data at site P2090 in Figure D.3. Here the raw measurements from the three ECHO-10 probes in the same soil pit show similar temporal patterns – that is, they show spikes and troughs in raw voltage at similar times – but one of the three records is offset from the others, and the sizes of contemporaneous voltage spikes from different probes are considerably different. Although it is theoretically possible that one region of a soil column experienced a far different soil moisture regime than other regions of the same soil column just a few tens of cm away, it is more likely that the differences in soil moisture records are a result of differences in the way these probes were emplaced in the soil. Thus we do not attempt to infer the absolute magnitude of volumetric soil moisture from these raw ECHO-10 measurements.

This does not mean, however, that the voltages measured by these ECHO-10 probes are completely lacking in information. The raw voltage measured by a single ECHO-10 probe should still reflect the resistivity of the material surrounding it, and the relative changes in resistivity within a single time series should still record the relative changes in soil moisture around that probe over time. For example, the minimum voltage in a single ECHO-10 time series should still represent the driest moment the soil experienced over that time series, and the maximum voltage in the time series should still represent the wettest moment during the time series. Thus, to make more direct (albeit more qualitative) comparisons between different ECHO-10 records, we have rescaled each time series individually on a 0-100 scale, such that the minimum raw value recorded by each instrument over its entire time series is rescaled to 0, and the maximum raw value over its time series is rescaled to 100. Consider again the ECHO-10 records at site P2090 (Figure D.3). In the central panel are the raw ECHO-10 measurements, which reveal the offset in one of the ECHO-10 records from the others. In the lower panel are the same ECHO-10 records, each rescaled to a 0-100 scale based on the minimum and maximum raw measurements in each time series. Note that rescaling each record in this manner resolves much of the offset between records. Thus, although it may not be possible to use these raw soil moisture probe records to calculate the absolute magnitude of soil moisture, it should nonetheless be possible to use these data to estimate the duration of high and low soil

moisture conditions. We suggest these rescaled soil moisture records (Figures D.1-D.17) thus provide self-consistent qualitative observations about annual patterns in soil moisture conditions.

These rescaled soil moisture records reveal that the wet season tends to last longer at higher elevations than at low elevations (Figure 5.8). This can be crudely quantified as follows. Consider a soil moisture time series that has been rescaled to a 0-100 scale (e.g., Figure 5.7). The transitions between the wet and dry seasons are short relative to the duration of the wet and dry seasons themselves, and thus to first order soil moisture is either high or low at any given moment during this time series. In each of the rescaled soil moisture records we defined any measurement above an arbitrary threshold of 30 as "wet", and any measurement below this threshold as "dry". We then characterized each site in terms of the annual duration of wet conditions (expressed as a fraction of the year), and called this fraction the Moisture Index. The soil in Figure 5.7, for example, spent on average 64% of the year in the "wet" state, and thus has a Moisture Index of 0.64. When the same analysis is repeated on all soil moisture records, it shows that the lowest elevation sites spend about half the year in the "wet" state and the highest elevation sites spend about three-quarters of the year in the "wet" state. Although this is a unsophisticated analysis of uncalibrated data, it nonetheless illustrates a fundamental aspect of this mountain system: high altitude soils tend to spend more time "wet" than low altitude sites do. This is likely a direct consequence of the snow cover, which lasts longer at higher altitudes and which keeps soil moisture levels high while it lasts.

5.7 Chemical evidence for atmospheric deposition at Pilot Peak and Tailholt Mountain

The widespread use of elemental rock-to-soil enrichments to infer the extent of chemical weathering is based on a simple principle: If the soil is derived only from the underlying rock (i.e., if mass fluxes into the soil by atmospheric deposition are negligible), then the rock-to-soil enrichments of various elements should reflect the relative mobilities of these elements. An important consequence of this principle is that an immobile element – i.e., one that is highly resistant to chemical dissolution and thus remains in the soil as mobile elements are preferentially leached away – should have a rock-to-soil enrichment that is higher than those for mobile elements. If there are multiple immobile elements in the parent rock, then they should be enriched in the soil to the same degree.

This is not the case at our field sites. Two characteristics of the suite of rock-to-soil enrichments across our field sites appear to violate this principle. First, the rock-to-soil enrichments of the elements most commonly assumed to be immobile – Zr and Ti – are quite different from one another. At all of our sites save one (P1277S), rock-to-soil enrichments of Ti are considerably higher than Zr enrichments (Figure 5.5), which would lead to estimates of W and CDF that are, on average, over twice as high when estimated with Ti than with Zr if dust fluxes were assumed to be negligible in Equations 5.5 and 5.7

(as has been commonly assumed in other studies). Second, rock-to-soil enrichments of other elements that are usually considered to be mobile – especially Mn and Fe, and to a lesser extent Mg – are often higher than those for presumably immobile Zr (Figure 5.5).

As discussed in Chapter 4, these observations suggest that material rich in these elements has been added to the sampled soils, most likely by deposition of mafic-rich dust. This is a common occurrence in many soils: Dust’s influence on soil composition has been documented at many sites around the globe (e.g., Marchand, 1970; Jackson et al., 1971; Litaor, 1987; Brimhall et al., 1988; Muhs et al., 1990; Reheis, 1990; Dahms, 1993; Stiles et al., 2003). We are unaware of direct measurements of dust composition or deposition rate near our field sites. In the absence of such measurements, in Chapter 4 we devised a strategy for estimating long-term average dust deposition rates using the local soil production rates and concentrations of multiple immobile elements in soil, rock, and dust, and used the composition of a probable dust source (the glacial megaflood sediments that produced the nearby Palouse loess; Sweeney et al., 2007) to estimate dust deposition rates at each field site. Here we use those estimates of dust deposition rates and dust composition to help estimate chemical and physical erosion rates.

Before discussing the calculated chemical and physical erosion rates, however, we first discuss the anomalously high Mn concentrations in our sampled soils, because they are not explained by the addition of dust from the proposed dust source and suggest addition of Mn from a second, more recent atmospheric source.

5.7.1 What accounts for the unusually high rock-to-soil enrichments of Mn?

When averaged over all field sites on Pilot Peak and Tailholt Mountain, the rock-to-soil enrichment of Mn is higher than that of any other element (Figure 5.5). This is unexpected. Mn is not typically considered an immobile element, and the fact that its enrichment is higher than the enrichments of Zr and Ti suggests that additional Mn may have been added to the soil from an outside source. A further idiosyncrasy is the rapid increase of Mn concentrations toward the soil surface in the upper 20 cm of the soil profile at several field sites, most notably at sites P1850, T1755, and T1508 (Figures C.4, C.14, and C.15). In this regard Mn differs from all other elements at our field sites except P, which tends to mimic the upward-rising concentrations that Mn exhibits in several soil profiles, although less dramatically. These vertical patterns are consistent with recent deposition of Mn at the soil surface and gradual incorporation of that Mn into the soil. The absence of strong vertical trends in other elements suggests that the other elements have been vertically well mixed, unlike Mn. We therefore propose that a considerable quantity of Mn was deposited from the atmosphere to the sampled soils relatively recently, and we suggest that this may be derived in part from 20th-century anthropogenic activity.

We suggest an anthropogenic source for Mn because high Mn concentrations in soils have been linked to anthropogenic emissions elsewhere. At the Shale Hills Observatory in

Pennsylvania, for example, concentrations of Mn in soils are as much as 13 times higher than those in the parent material (Herndon et al., 2009). These high Mn concentrations in soils have been linked to industrial and population centers at a wide range of field sites (Herndon et al., 2009). In central Idaho, one possible atmospheric source of Mn in the recent past is Stibnite Mine, which is 30-35 km southeast of Pilot Peak and Tailholt Mountain and which was for a brief time a major ore producer: during World War II it was the largest supplier of antimony and tungsten in the United States (Mitchell, 2000). In 1943 the mine was converted to an open pit mine, and in 1948 a smelter was added to the site. It is possible that high concentrations of Mn may have been added to the atmosphere as dust during rock crushing, or as finer particles in smelter stack emissions. We have not found measurements of atmospheric emissions from Stibnite Mine during this period, and thus cannot model the influence it may have had on the sampled soils at Pilot Peak and Tailholt Mountain. However, measurements of soil chemistry on hillslopes next to the mine show concentrations as high as 1580 ppm (Jin and Scheff, 2003), higher than any in the soil profile samples on Pilot Peak or Tailholt Mountain, consistent with aeolian deposition of Mn from mining activity.

Thus, rather than proposing Mn as a new immobile element, we suggest that 20th-century aeolian deposition of Mn, possibly sourced in the nearby Stibnite Mine, is the probable cause of the high Mn enrichments in our sampled soils. More work will be necessary to test this hypothesis. Because atmospheric deposition of anthropogenically-derived Mn is a possible explanation for the high Mn enrichments in the sampled soils, and because concentrations of Mn in our soil samples are low enough to have a negligible effect on estimates of chemical and physical erosion rates, we do not consider Mn further in the calculations that follow.

5.8 Chemical erosion rates and CDFs

Using our measurements of soil production rates (Table 5.3), the compositions of soil, rock, and dust (Tables 5.4-5.7), and the estimates of dust deposition rates in Chapter 4 (Table 5.8), we calculate the bulk chemical erosion rate and CDF at each site with Equations 5.5 and 5.7. These calculations show that physical erosion is responsible for 84-100% of the mass flux out of the sampled soils, and chemical erosion accounts for the remaining 0-16%.

These calculations reveal that chemical erosion rates on Pilot Peak are fastest at the highest altitudes, where soils are coldest and where soil moisture levels remain high for the longest portion of the year. Chemical erosion rates on Tailholt Mountain, by contrast, reach a minimum at an intermediate altitude and are of comparable magnitude at the top and bottom of the altitudinal transect. Plotting these rates against climatic variables permits us to make several observations about the influence of climate on chemical erosion rates and the extent of chemical weathering in these soils.

First, chemical erosion rates show no dependence on mean annual soil temperature

(MAST; Figure 5.9). Because chemical erosion rates are expected to increase with temperature, all else being equal, this suggests that whatever effect temperature has on chemical erosion rates along these transects is overwhelmed by the influences of other factors.

Second, chemical erosion rates on Pilot Peak tend to be fastest at the sites with the highest moisture indices (Figure 5.9). On Tailholt Mountain, however, chemical erosion rates show no trend with moisture index. Thus our measurements are equivocal about the notion that the length of the wet season should influence chemical erosion rates: the data from Pilot Peak support it, and the data from Tailholt Mountain do not.

The third and fourth observations can be made by normalizing the chemical erosion rates by the rate of material supply to the soil. This reveals that the degree of chemical weathering (i.e., the CDF) is insensitive to MAST, just as chemical erosion rates are insensitive to MAST (Figure 5.9). By contrast, the CDF shows a positive correlation with the moisture index: the most weathered soils at our field sites tend to be at the sites with the longest wet seasons (Figure 5.9). This is the clearest climatic signal in our measurements.

The same estimates of soil production rates, dust deposition rates, and rock, soil, and dust composition (Tables 5.3-5.8) permit calculation of elemental chemical erosion rates W_X with Equation 5.6. As expected, chemical erosion rates for SiO_2 are by far the largest among any oxide, reflecting the dominance of Si in the parent material contributing to the soils. Chemical erosion rates for Al_2O_3 are the next largest elemental chemical weathering flux, followed in size by the chemical erosion rates of the major cations K, Na, and Ca.

Patterns in Si and Al chemical erosion rates with MAST and moisture index tend to mimic the patterns in bulk chemical erosion rates on both mountains (Figures 5.11-5.12). This is expected; at most field sites W_{SiO_2} and $W_{\text{Al}_2\text{O}_3}$ sum to nearly 90% of the bulk chemical erosion rate W , so to first order W should be roughly the sum of W_{SiO_2} and $W_{\text{Al}_2\text{O}_3}$. As is the case with bulk chemical erosion rates, elemental chemical erosion rates show no trends with MAST for any major element (Figure 5.11). Similarly, on Pilot Peak $W_{\text{Na}_2\text{O}}$, W_{CaO} , W_{SiO_2} , and $W_{\text{Al}_2\text{O}_3}$ broadly mimic the bulk chemical erosion rate in that they are generally fastest at the highest moisture indices (Figure 5.12). Because Na and Ca are likely derived primarily from the plagioclase feldspar that dominates the parent granite, these patterns in $W_{\text{Na}_2\text{O}}$ and W_{CaO} likely reflect plagioclase weathering. And, because the patterns in W_{SiO_2} and $W_{\text{Al}_2\text{O}_3}$ on Pilot Peak are similar to those in $W_{\text{Na}_2\text{O}}$ and W_{CaO} , it is reasonable to conclude that chemical erosion of Si and Al is likely dominated by plagioclase weathering as well.

Elemental depletion factors (i.e., CDF_X) have patterns that are broadly similar to those in the bulk CDF. That is, estimates of CDF_X show no trends with MAST for any major element, but tend to be higher at higher moisture indices for Ca, Na, and Si (Figures 5.14-5.15). This is consistent with weathering of plagioclase feldspar that has progressed farthest in soils with the longest wet seasons.

In summary, mean annual soil temperature appears to play an insignificant role in

setting long-term chemical erosion rates and the degree of chemical weathering at these field sites, both for the bulk soil and for individual elements. By contrast, the length of the wet season appears to play an important role in setting the degree to which soils are chemically depleted at these sites, particularly for Ca and Na, and to a lesser extent for Si.

5.8.1 Limitations to this approach for estimating chemical erosion rates

Two field sites on Pilot Peak do not fit the assumptions underlying this solid-phase mass balance method for estimating chemical erosion rates, as Table 5.8 shows. The first is site P1277S. As noted in Chapter 4, this is the only site on either Pilot Peak or Tailholt Mountain where the rock-to-soil enrichment of Ti is smaller than that of Zr (Figure 5.5). As a result, the addition of dust with a higher Ti/Zr ratio than the parent granite cannot resolve the differences between rock-to-soil enrichments of Zr and Ti. Thus, applying the dust model with the proposed dust source to site P1277S yields the impossible result that $-3 \pm 1\%$ of the soil's parent material is dust, which itself produces a negative calculated dust flux of $-4.5 \pm 1.5 \text{ t km}^{-2} \text{ yr}^{-1}$, another impossibility. Thus site P1277S, alone among our seventeen field sites, does not fit the proposed dust model with the proposed dust source. It is not immediately clear why P1277S differs from all the other sites in this respect. However, it is notable that although the rock sample composition at this site is not unusual for rocks from Pilot Peak, the P1277S soil samples are on one end of the compositional spectrum for Pilot Peak soils, with more Si and less Al, Fe, Ti, Mg, Nb, and Rb than all other Pilot Peak soils. This suggests that the rock samples collected from the ridgeline between sites P1277S and P1264N are likely a poor reflection of the parent granite underlying site P1277S.

Site P1850 is the other site that yields a spurious result, although for a different reason. At P1850 the rock and soil compositions are consistent with the addition of mafic-rich dust, but the estimated bulk CDF is below zero, which in turn results in a negative chemical erosion rate, which is an impossibility. This odd result occurs at P1850 because some of the P1850 soil samples have a much different composition than the others. The rectangular plot from which soils were sampled at P1850 lies just a few meters off the north-facing side of the ridgeline, and ten of the sixteen soil samples – all in the western half of the soil plot – are much rockier than the other soil samples, and have lower Zr concentrations than the other P1850 soils and the bulk of the P1850 rock samples. Meanwhile, in the eastern half of the soil plot just a few meters away, the other P1850 soil samples have a composition much closer to that of the sampled P1850 rocks. To show how much excluding the soil samples in the western half of the sampling plot affects the calculated soil composition at P1850, in Table 5.5 we report the average composition of all soil samples (labeled P1850) and the average composition of the subset of soil samples from the eastern half of the soil plot (labeled P1850sub, based on samples P1850-B5, B6, B9, B10, B13, B14). In Figures 5.9-5.16, values for W , W_X , CDF, and CDF_X calculated from P1850 and P1850sub are designated with a white square and a white diamond, respectively.

These demonstrate that excluding the anomalously rocky soil samples in the western half of the sampling plot yields values for chemical erosion rates that are no longer negative.

We also note that although using the proposed dust source within the dust-granite mixing model helps resolve most of the unexpected granite-to-soil elemental enrichments, it does not resolve all of them. In particular, after including dust influxes from the proposed dust source, several CDF_{Fe} on Tailholt Mountain are still negative (although they are much less negative than they would be if dust had been neglected) (Table 5.9). This may indicate that the dust falling on these sites had a higher Fe concentration than the proposed dust source. This can result from compositional sorting during transport, as Fe may be preferentially sited in small secondary Fe-oxide minerals that are more likely to be transported long distances (e.g., Jickells et al., 2005). Future measurements of dust composition in the South Fork of the Salmon River canyon will be able to test this hypothesis. At present, we suggest this highlights the importance of knowing the composition of the incoming dust.

5.9 Supply-limited vs. kinetically-limited weathering

Chemical weathering of soil and of elements within the soil is often described as occurring in one of two end-member regimes: supply-limited or kinetically-limited (e.g., Stallard and Edmond, 1983; West et al., 2005). In supply-limited weathering, chemical erosion rates are limited by the rate at which fresh material is supplied to the soil. For the bulk soil, this supply rate is the total mass flux into the soil P , and in the case of an element X , this supply rate is P_X (Equations 5.2-5.3). In the supply-limited weathering regime, chemical erosion rates are linearly proportional to supply rates, and the degree of chemical depletion in the soil – i.e., the CDF – is constant across a range of soil production rates and is independent of the soil residence time. In its simplest and most extreme form, supply-limited weathering of a given element occurs where 100% of that element is lost by chemical processes because it is present only in highly soluble minerals which themselves undergo complete weathering. This has been observed, for example, in tropical weathering profiles where 100% of the Na in the parent rock is lost by complete weathering of plagioclase feldspar, which is the sole host of Na in the parent rock (e.g., White et al., 1998). In such a situation $W_{Na} = P_{Na}$ because the proportionality constant between W_{Na} and P_{Na} – i.e., CDF_{Na} – is 1. However, the CDF does not need to be 1 for a direct proportionality to arise between chemical erosion rates and supply rates. Consider, for example, a rock in which element X is hosted by several different mineral phases, some of which are highly soluble and some of which are insoluble. If, during weathering of this rock, element X were completely lost from the soluble minerals and completely retained by the insoluble minerals, regardless of supply rate, this would yield a CDF_X with a value less than 1 that is constant across all supply rates. Close correlations between chemical erosion rates and supply rates have been observed over a wide range of field sites where measured CDFs are much lower than 1 (Riebe et al., 2004a; Dixon et al., 2009). These studies suggest that supply-limited weathering appears to be a useful descriptor of chemical

erosion at a wide range of sites, in that it can account for a great deal of the measured differences in chemical erosion rates between sites. In contrast to supply-limited weathering, kinetically-limited weathering is characterized by chemical erosion rates that are limited not by the rate of fresh mineral supply but by how slowly the minerals themselves weather. In this regime, chemical erosion rates are less than linearly proportional to soil production rates, and soils grow more chemically depleted (i.e., the CDF increases) with soil residence time.

In short, previous studies have shown that the concepts of supply-limited and kinetically-limited weathering can be useful in determining what controls chemical weathering in natural systems, and that the two regimes can be distinguished from one another by their distinct CDF signatures. Are the CDFs at Pilot Peak and Tailholt Mountain consistent with supply-limited or kinetically-limited weathering?

It appears that the bulk soil and most of the elements are experiencing kinetically-limited weathering at our field sites. Bulk CDFs do not systematically increase or decrease with soil production rates, which on its own is broadly consistent with supply-limited weathering, but there is considerable scatter in measured CDFs that imply chemical erosion rates are affected by something besides the rate of mineral supply (Figure 5.10). Plotting bulk CDFs against soil residence time yields a clearer picture. The smallest bulk CDFs on both Pilot Peak and Tailholt Mountain tend to be clustered at the shortest soil residence times (Figure 5.10). (Here soil residence time is calculated as the soil thickness times soil density divided by the physical erosion rate. Soil density was not measured in the field, and is assumed to be 1640 kg m^{-3} at each site based on the dry density of soil collected on Pilot Peak and measured in the lab.) This pattern in the data – lower CDFs at shorter soil residence times and higher CDFs at longer soil residence times – is broadly consistent with kinetically-limited weathering of the bulk soil. This pattern is especially clear on Tailholt Mountain, which has one cluster of CDFs near zero at short soil residence times and a second cluster of CDFs at 0.11-0.15 at longer soil residence times. On Pilot Peak, by contrast, many but not all of the data are consistent with a rising trend in CDF with soil residence time. The Pilot Peak sites with the smallest CDFs tend to cluster at the shortest soil residence times, but CDFs do not increase continuously with soil residence time over all Pilot Peak sites. The sites with the two longest soil residence times (P1062S and P1062N) have CDFs of 0.15 ± 0.02 and 0.16 ± 0.01 , respectively, identical within uncertainty to CDFs at other sites on Pilot Peak with considerably shorter residence times. This pattern suggests that these soils may grow more chemically depleted over time, but only up to a certain point at which the bulk CDF plateaus at around 0.16. If that is the case, soils may transition from a kinetically-limited weathering regime to a supply-limited weathering regime after roughly one-sixth of the parent material has weathered away, which at our field sites appears after approximately 8-10 kyr.

Although most of the elemental CDF_X measurements are broadly similar to the bulk CDF measurements – i.e., the smallest CDF_X values for each element tend to cluster at the shortest soil residence times – there is one notable exception to this general pattern, and that is K at Pilot Peak. Aside from the unusual site P1850 (see section 5.8.1), all CDF_K on

Pilot Peak are the same within uncertainty, and imply that roughly 20% of the K supplied to the soil leaves in solution across a wide range of soil residence times (Figure 5.16). As a result, W_K is linearly proportional to the rate at which K is supplied to the soil, consistent with supply-limited chemical weathering of K on Pilot Peak (Figure 5.13). It may be that 20% of the K in the parent material is in easily weatherable minerals and the other 80% is in less soluble minerals, and that to first order all of the K in easily weatherable minerals and none of the K in other minerals is lost during a single soil residence time. Future work on the quantitative mineralogy of the parent material and the elemental distributions within the parent minerals will be able to shed light on the pathways of elemental weathering in this system, and will be able to test hypotheses for the cause of supply-limited weathering behavior displayed by K on Pilot Peak and the cause of kinetically-limited weathering behavior displayed by the bulk soil.

In summary, our data broadly support the notion that chemical weathering of the bulk soil, and of most elements in the soil, is proceeding at rates that are limited by the kinetics of mineral dissolution, rather than the supply rates of minerals to the soil.

5.10 Conclusions

In this paper we have presented new measurements of soil production rate and bulk soil and rock chemistry along two altitudinal transects in the Idaho Batholith. Several first-order observations about the dependence of chemical erosion rates on climate and supply rates can be gleaned from this new dataset. First, chemical erosion rates at Pilot Peak and Tailholt Mountain do not increase with mean annual soil temperature, contrary to the relationship predicted by theory and laboratory experiments. Second, chemical erosion rates on Pilot Peak tend to be fastest in soils with the highest moisture indices (i.e., in soils with the longest wet seasons), although this pattern is not repeated on Tailholt Mountain. Third, chemical erosion rates do not increase linearly with the rate of fresh mineral supply. Fourth, the degree of chemical weathering (i.e., the CDF) is positively correlated with the moisture index: soils that spend more time each year under high soil moisture conditions are more weathered. Fifth, estimates of CDF are also positively correlated with the soil residence time: soils that spend more time on the hillslope are more weathered.

We draw two primary conclusions from these observations. First, we conclude that chemical erosion rates at these field sites are largely insensitive to mean annual temperature. In this respect these data are consistent with a number of studies that have shown weak climatic controls on chemical erosion rates over both decadal and millennial timescales (Dupre et al., 2003; Riebe et al., 2004a; West et al., 2005), and they differ from studies that have inferred strong climatic signals in chemical erosion rates along altitudinal transects in Nevada (Riebe et al., 2004b) and the Sierra Nevada (Dixon et al., 2009). Second, we conclude that chemical weathering at these field sites is proceeding in a kinetically-limited regime – i.e., a regime in which the rate of chemical erosion is limited by

how slowly mineral dissolution reactions can proceed – rather than in a supply-limited regime. In this regard Pilot Peak and Tailholt Mountain differ from the measurements of Riebe et al. (2004a), which found that chemical erosion rates were proportional to mineral supply rates over a wide range of rates.

We close by noting that dust plays an important role in nutrient supply in the Idaho Batholith, much as it does elsewhere (e.g., in Hawaii (Jackson et al., 1971; Chadwick et al., 1999), Australia (Brimhall et al., 1988), and the Caribbean (Muhs et al., 1990)). Our data strongly suggest that mafic-rich dust has contributed to the otherwise granitic soils in the South Fork of the Salmon River canyon, and our calculations confirm that dust can strongly influence soil composition even in places where the bulk dust flux is a small fraction of the soil production rate from bedrock. The proposed source of mafic dust has a much different composition than the granitic Idaho Batholith, and thus dust influxes have major consequences for nutrient supply in the soils and streams of the Idaho Batholith. At our field sites this is especially important for Mg and Fe. The proposed dust source has concentrations of Mg and Fe that are, respectively, 6 and 4 times higher than those in the average Pilot Peak granite and 12 and 7 times higher than those in the average Tailholt Mountain granite. Thus, even though our estimated dust fluxes are on average only 5% of the total mass flux into the soil at Pilot Peak and 3% at Tailholt Mountain, our calculations predict that dust is nonetheless responsible for, on average, 21% and 26% of the Mg fluxes into the soil at Pilot Peak and Tailholt Mountain, respectively, and 18% and 17% of the Fe fluxes into the soil at Pilot Peak and Tailholt Mountain, respectively. If the proposed dust source is, as we suggest, responsible for the observed elemental enrichments, this mafic-rich dust is a significant contributor of nutrients to the granitic soils of the Idaho Batholith, and it underscores the importance of accounting for dust fluxes in solid-phase mass balance studies of chemical and physical erosion rates.

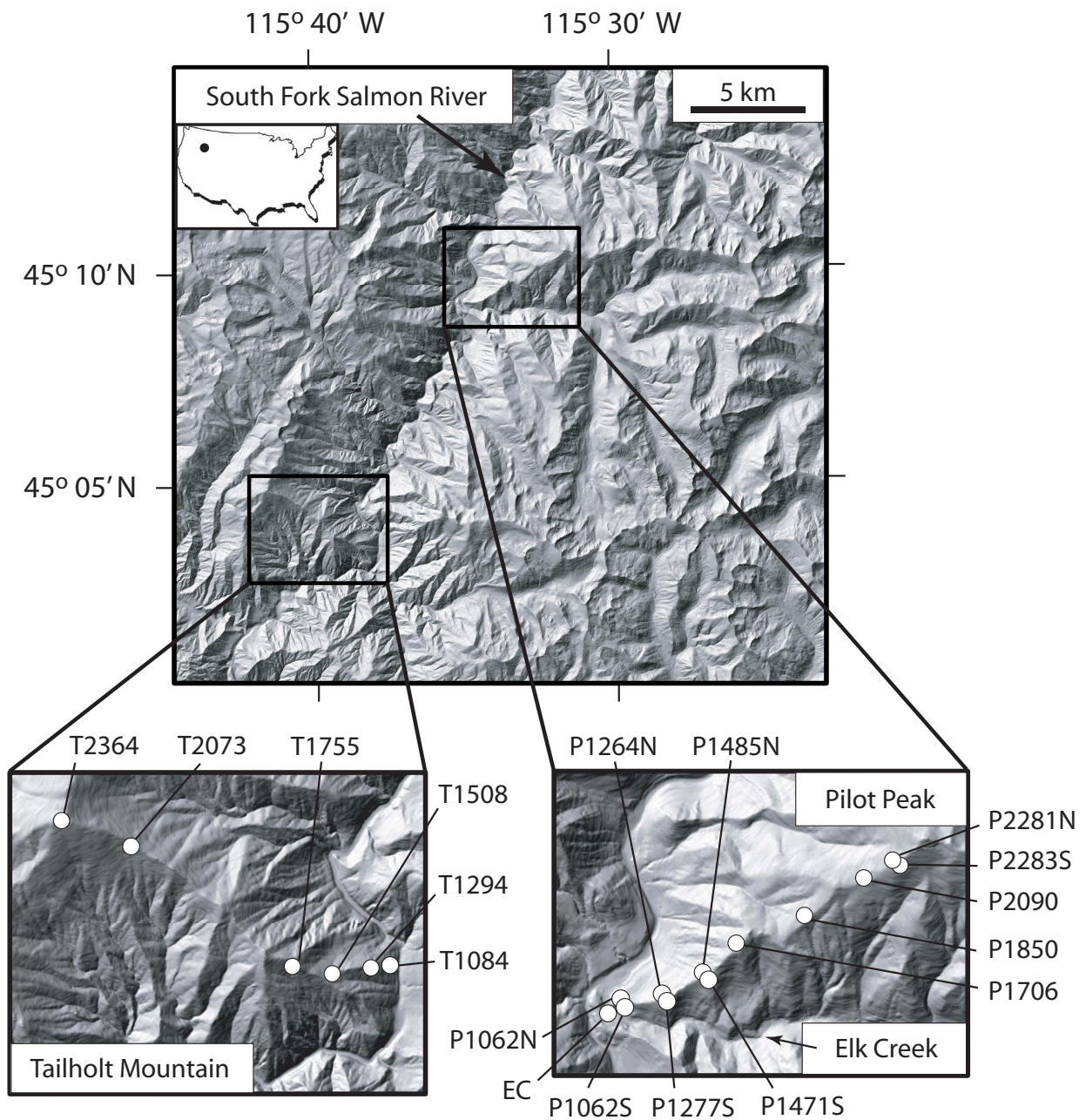


Figure 5.1. Field sites at Pilot Peak and Tailholt Mountain. Shaded relief map generated from 10-meter USGS DEM.

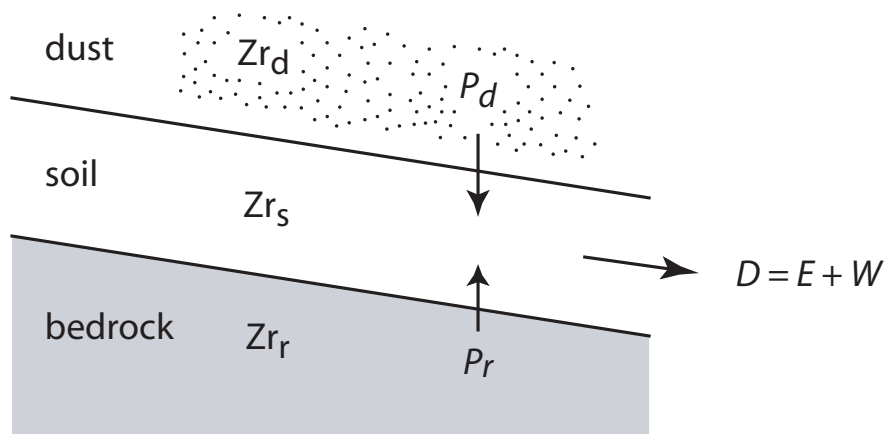


Figure 5.2. Conceptual mass balance model for estimating physical and chemical erosion rates on a soil-mantled hillslope. In steady state, mass fluxes into the soil (i.e., the sum of the soil production rate P_r and the dust deposition rate P_d) are balanced by the denudation flux out of the soil, D . If the magnitudes of P_r and P_d are known, concentrations of an immobile element (e.g., Zr) in the bedrock, soil, and dust can reveal the magnitudes of the physical erosion rate E and chemical erosion rate W .

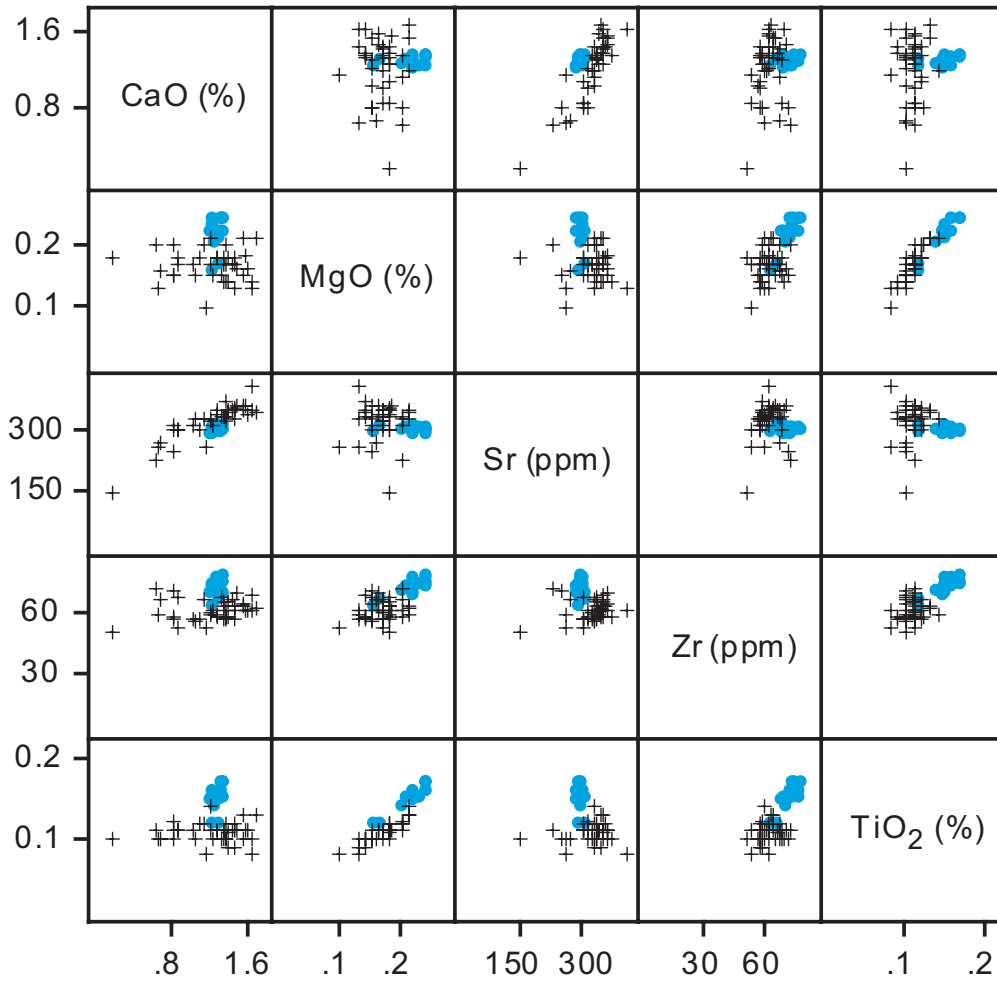


Figure 5.3. At site T1084, as at most of our field sites, soil and rock compositions are well approximated by multivariate normal distributions. Here blue dots are soil samples, and black crosses (+) are rock outcrop samples.

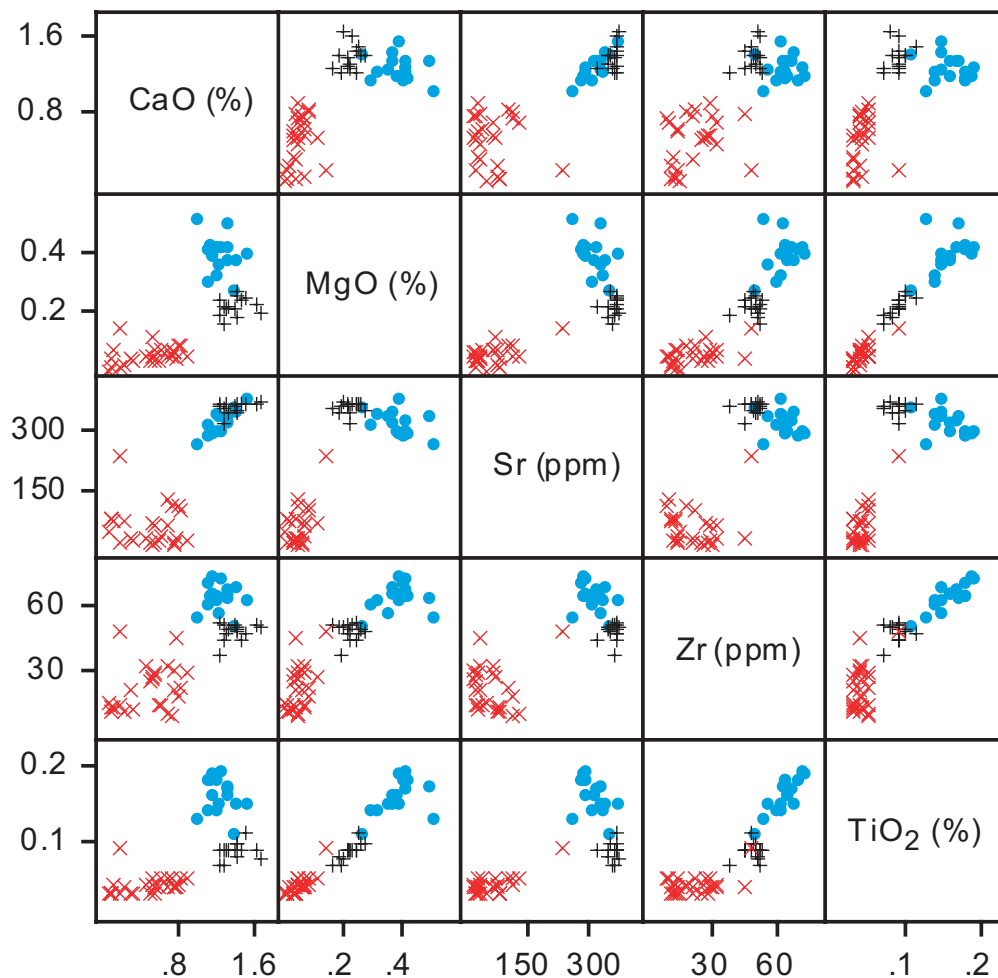


Figure 5.4. Justification for excluding some rock samples as outliers at site T2364. Here the rock samples fall into a bimodal distribution, in which one group of rock samples has a composition similar to that of other rocks on Tailholt Mountain (black + symbols), and the second group has a much different composition, with far less Ca, Mg, and Sr, among other elements (red × symbols). Blue circles are soil samples. If the second group of atypical rock samples were included in an estimate of the mean granite composition at T2364, Equation 5.7 would predict that mobile elements Ca and Sr are less mobile than immobile elements Zr and Ti, which is geochemically unreasonable. We therefore consider this second group of rock samples unlikely to have contributed to the sampled soil, and exclude them as outliers from the estimated mean rock composition. Site T1755 has a similarly bimodal set of rock samples, and we excluded a subset of its rock samples in the same manner (see text).

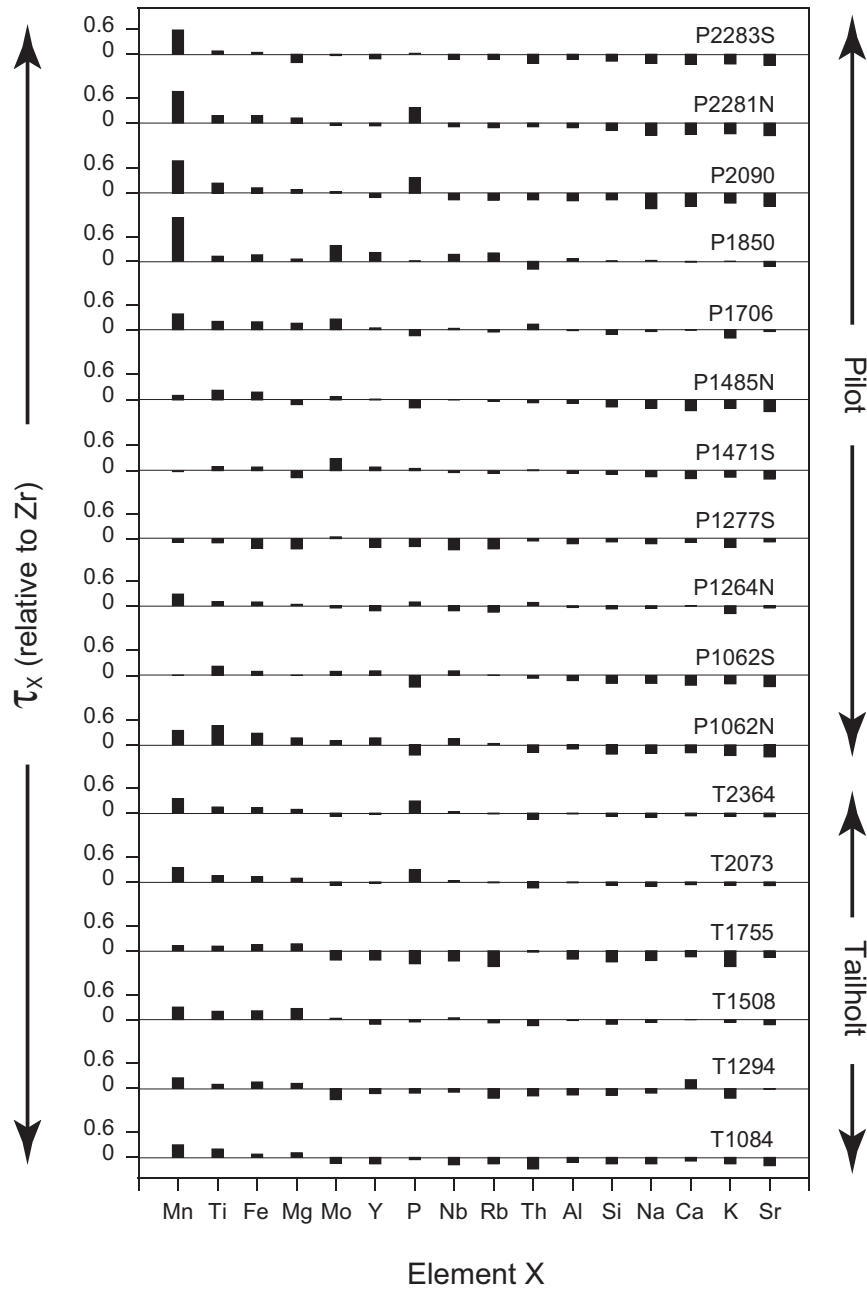


Figure 5.5. For an element X, the mass transfer coefficient ($\tau_X = X_s Zr_r / X_r Zr_s - 1$) expresses the gain or loss of X relative to an immobile element (here Zr) in the soil compared to its parent rock (Brimhall and Dietrich, 1987; Chadwick et al., 1990). At many of the field sites on Pilot Peak and Tailholt Mountain, τ_{Ti} , τ_{Mn} , τ_{Fe} , and τ_{Mg} are > 0 , implying that the soils have been enriched in these elements relative to Zr. Because Zr should be chemically immobile in this environment, this suggests that these elements have been added to the soil by a second source rich in these elements. We suggest the most likely source is dust deposition.

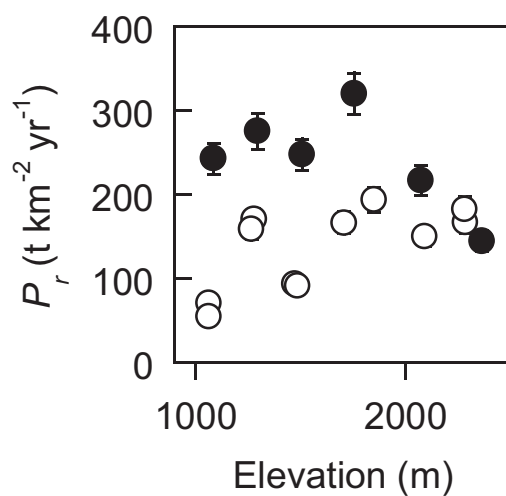


Figure 5.6. Soil production rates P_r inferred from cosmogenic ^{10}Be in soil-borne quartz. Aside from site T2364, soil production rates are faster on Tailholt Mountain (black circles) than on Pilot Peak (white circles). On Pilot Peak, soil production rates on opposite sides of the ridgeline at the same elevation are identical within uncertainty, implying that climatic factors related to slope aspect are not affecting bedrock lowering rates at these sites.

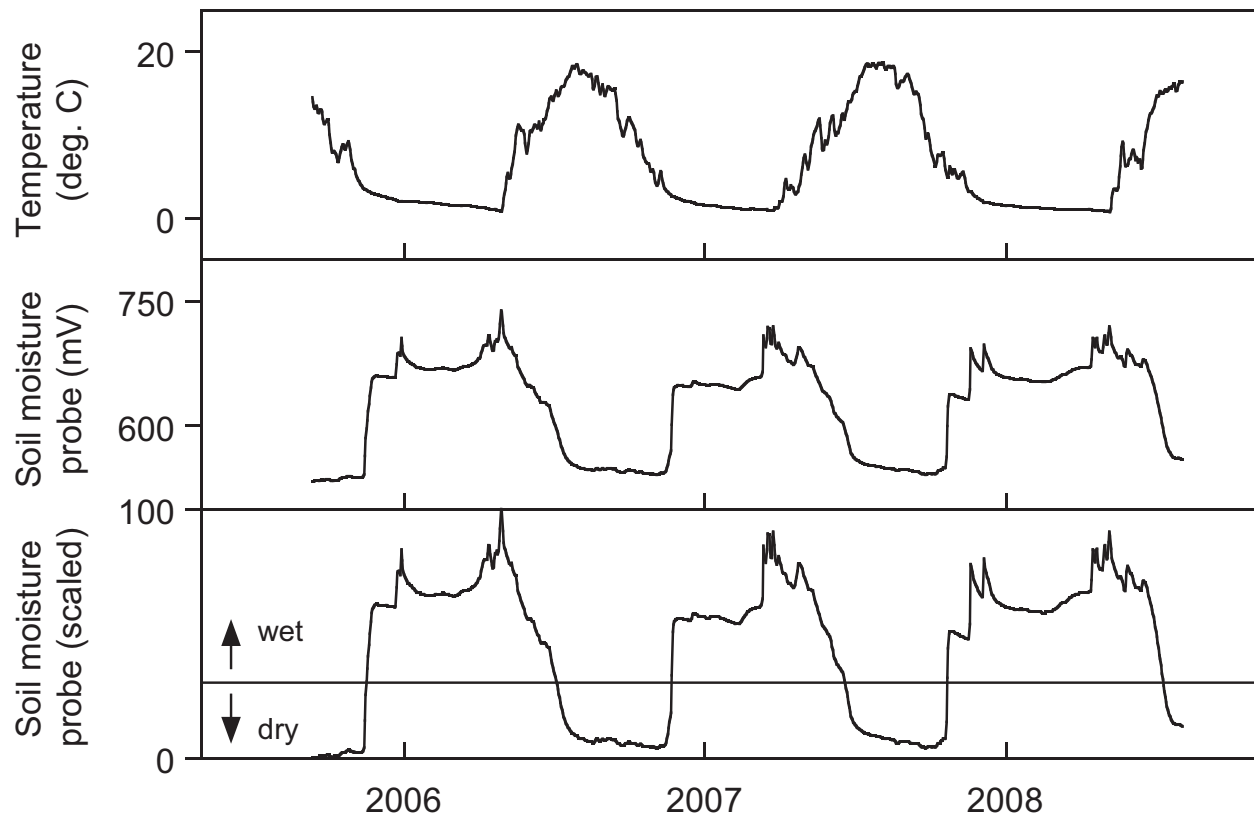


Figure 5.7. Daily average soil moisture and temperature records from site P2090 at the base of the soil column (70 cm depth). In the middle panel are the raw measurements from the soil moisture probe in mV. In the lower panel are the same soil moisture measurements normalized to a 0-100 scale, where 0 corresponds to the minimum (driest) reading and 100 to the maximum (wettest) reading over the time series. This scaling, although qualitative, eliminates offsets between soil moisture records from different instruments in the same soil profile, and permits simpler comparisons between soil moisture records. Under this rescaling, the soil in this figure spent on average 64% of each year in "wet" conditions, which we define as anything higher than a threshold value of 30 in the rescaled soil moisture data.

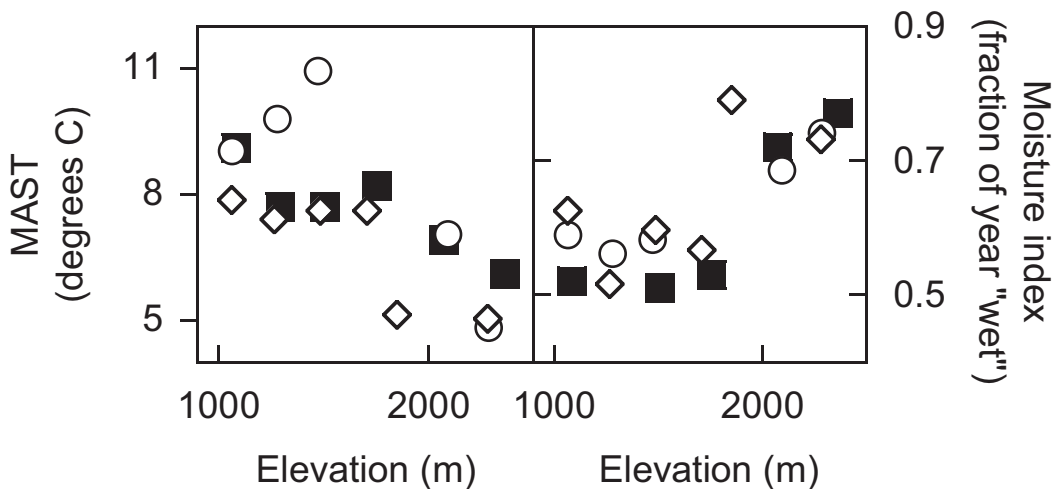


Figure 5.8. Left panel: mean annual soil temperatures (MAST) on Pilot Peak (8/1/2006-7/31/2008; white markers) and Tailholt Mountain (10/1/2005-9/30/2006; black markers). For the purposes of calculating annual means, some records include interpolations to fill gaps in temperature time series; see Appendix D for details. Right panel: soil moisture indices represent the fraction of the year the soil spends in the "wet" condition (defined in Figure 5.7). Soils at higher elevations tend to spend a greater proportion of each year under high soil moisture conditions because snow cover keeps soils wet and snow cover lasts longest at the highest altitudes. On Pilot Peak, where we sampled soils from both sides of the ridgeline, white diamonds refer to sites on the north side of the ridgeline, and white circles refer to sites on the south side.

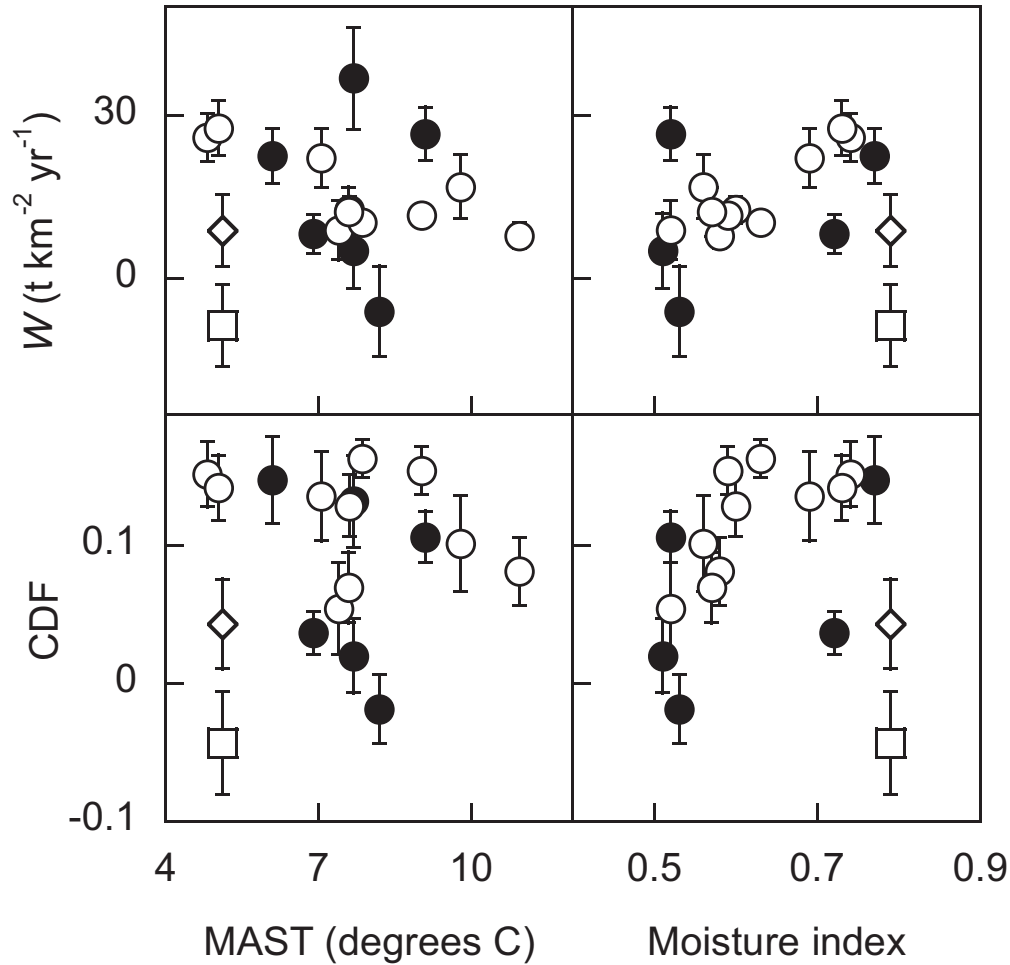


Figure 5.9. Contrary to expectations, estimates of chemical erosion rate W do not increase with mean annual soil temperature (MAST) on either Pilot Peak (white markers) or Tailholt Mountain (black markers). This suggests that mean annual soil temperature exerts little influence on W at these field sites. On Pilot Peak, estimates of W generally increase with higher moisture indices – i.e., longer wet seasons, as defined in Figure 5.7 – but this pattern is not repeated on Tailholt Mountain. Chemical depletion fractions (CDF) – i.e., the degree of chemical weathering in the soil – show no trend with MAST, and broadly increase with the moisture index. The white square (P1850) and white diamond (P1850sub) represent site P1850 including and excluding anomalous soil samples, respectively (see section 5.8.1).

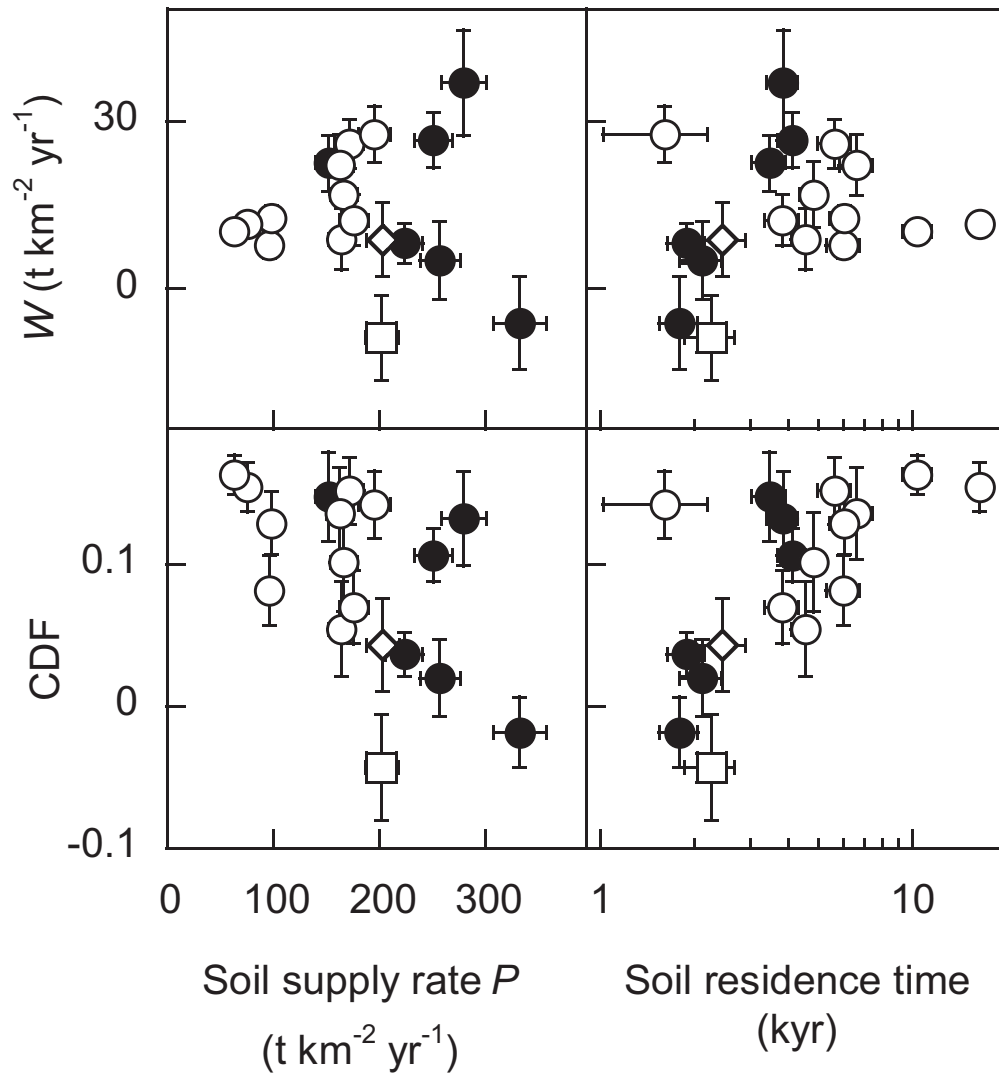


Figure 5.10. Chemical erosion rates W do not increase linearly with the rate of mineral supply to the soil, $P = P_r + P_d$, implying that chemical erosion rates at these sites are not supply-limited. The degree of chemical weathering in the bulk soil (i.e., the CDF) shows no trend with supply rate P but broadly increases with the soil residence time on both Pilot Peak (white markers) and Tailholt Mountain (black markers), consistent with weathering that is limited by the kinetics of mineral dissolution rather than the rate of fresh mineral supply to the soils. The white square (P1850) and white diamond (P1850sub) represent site P1850 including and excluding anomalous soil samples, respectively (see section 5.8.1).

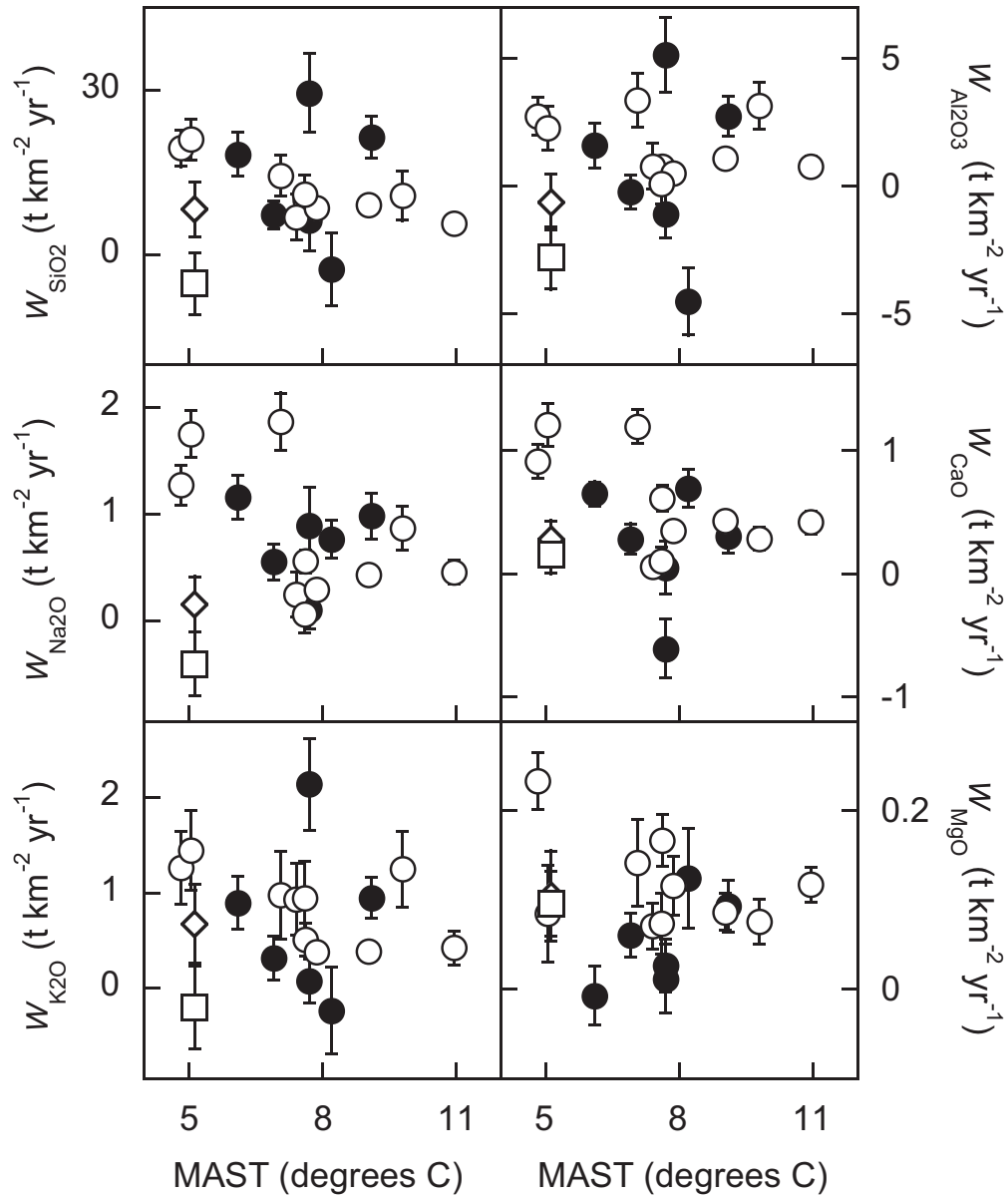


Figure 5.11. As is the case with bulk chemical erosion rates, elemental chemical erosion rates W_X do not increase with mean annual soil temperature (MAST), suggesting that the influence of temperature on chemical erosion rates is overwhelmed by other factors that control chemical erosion rates. White markers = Pilot Peak, black markers = Tailholt Mountain. The white square (P1850) and white diamond (P1850sub) represent site P1850 including and excluding anomalous soil samples, respectively (see section 5.8.1).

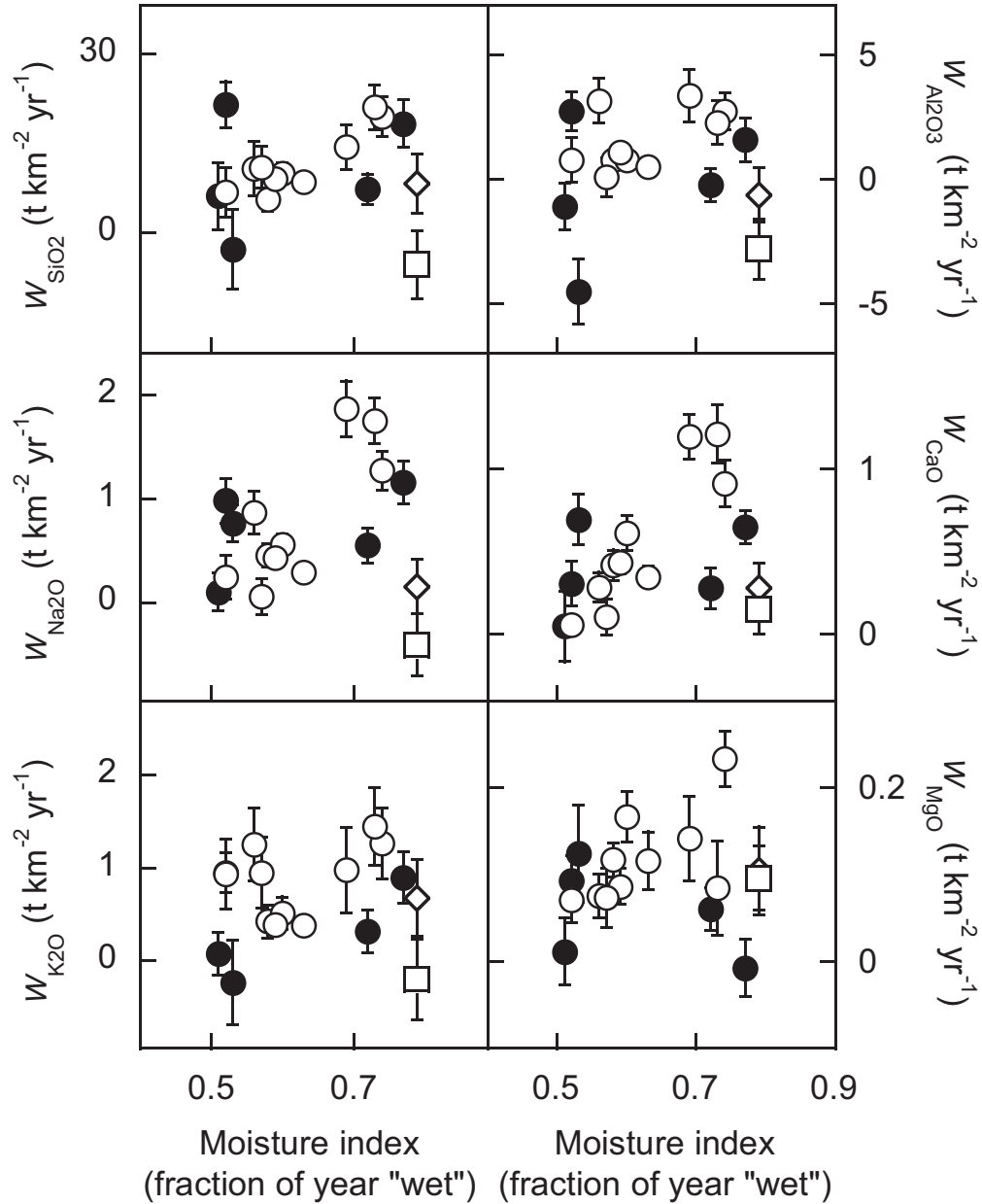


Figure 5.12. As is the case with the bulk chemical erosion rates, on Pilot Peak (white markers), the fastest elemental chemical erosion rates for Si, Na, and Ca tend to be at the highest altitudes, where the soils spend the longest portion of the year under high soil moisture conditions. On Tailholt Mountain (black markers), elemental chemical erosion rates display no trend with moisture index. See Figure 5.7 for definition of moisture index. The white square (P1850) and white diamond (P1850sub) represent site P1850 including and excluding anomalous soil samples, respectively (see section 5.8.1).

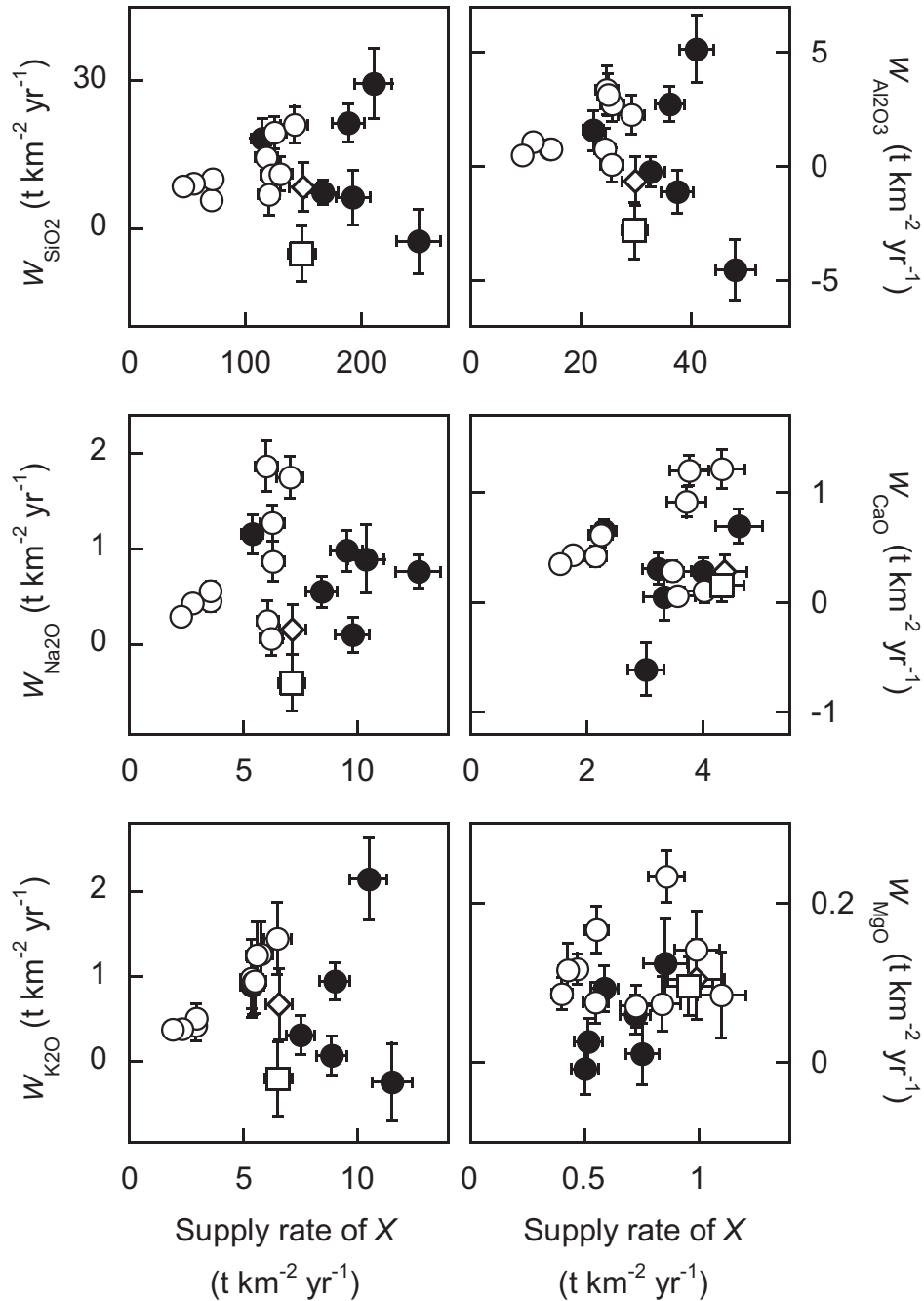


Figure 5.13. Elemental chemical erosion rates on Pilot Peak (white markers) and Tailholt Mountain (black markers) tend to show no systematic dependence on elemental supply rates. The exception to this tendency is K, which on Pilot Peak displays a linear increase in chemical erosion rates with its supply rate, consistent with supply-limited weathering of K. This pattern in W_{K_2O} is not repeated on Tailholt Mountain. The white square (P1850) and white diamond (P1850sub) represent site P1850 including and excluding anomalous soil samples, respectively (see section 5.8.1).

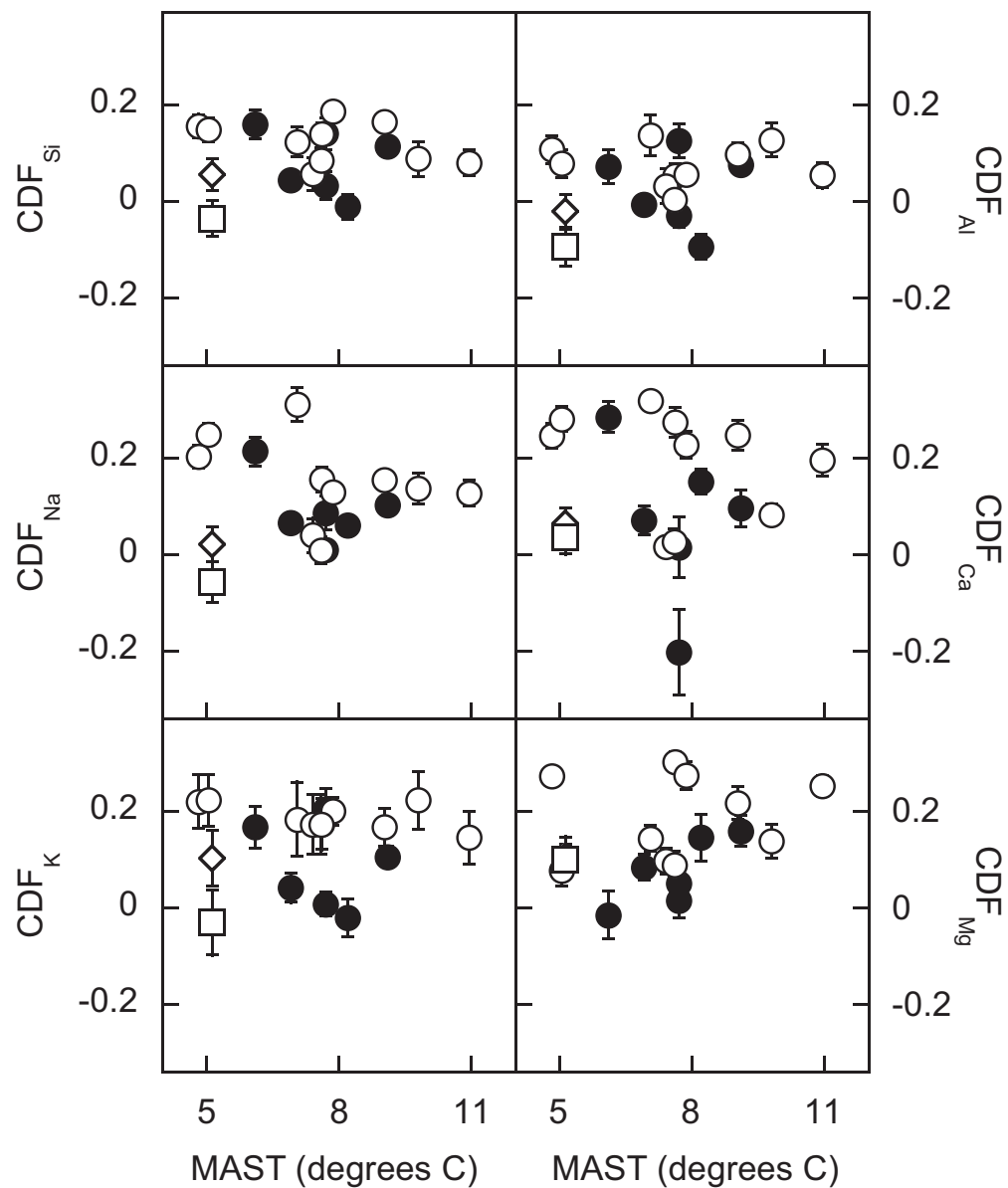


Figure 5.14. The degree of elemental depletion (i.e., CDF_X) does not vary systematically with mean annual soil temperature (MAST) for any major element. White markers = Pilot Peak, black markers = Tailholt Mountain. The white square (P1850) and white diamond (P1850sub) represent site P1850 including and excluding anomalous soil samples, respectively (see section 5.8.1).

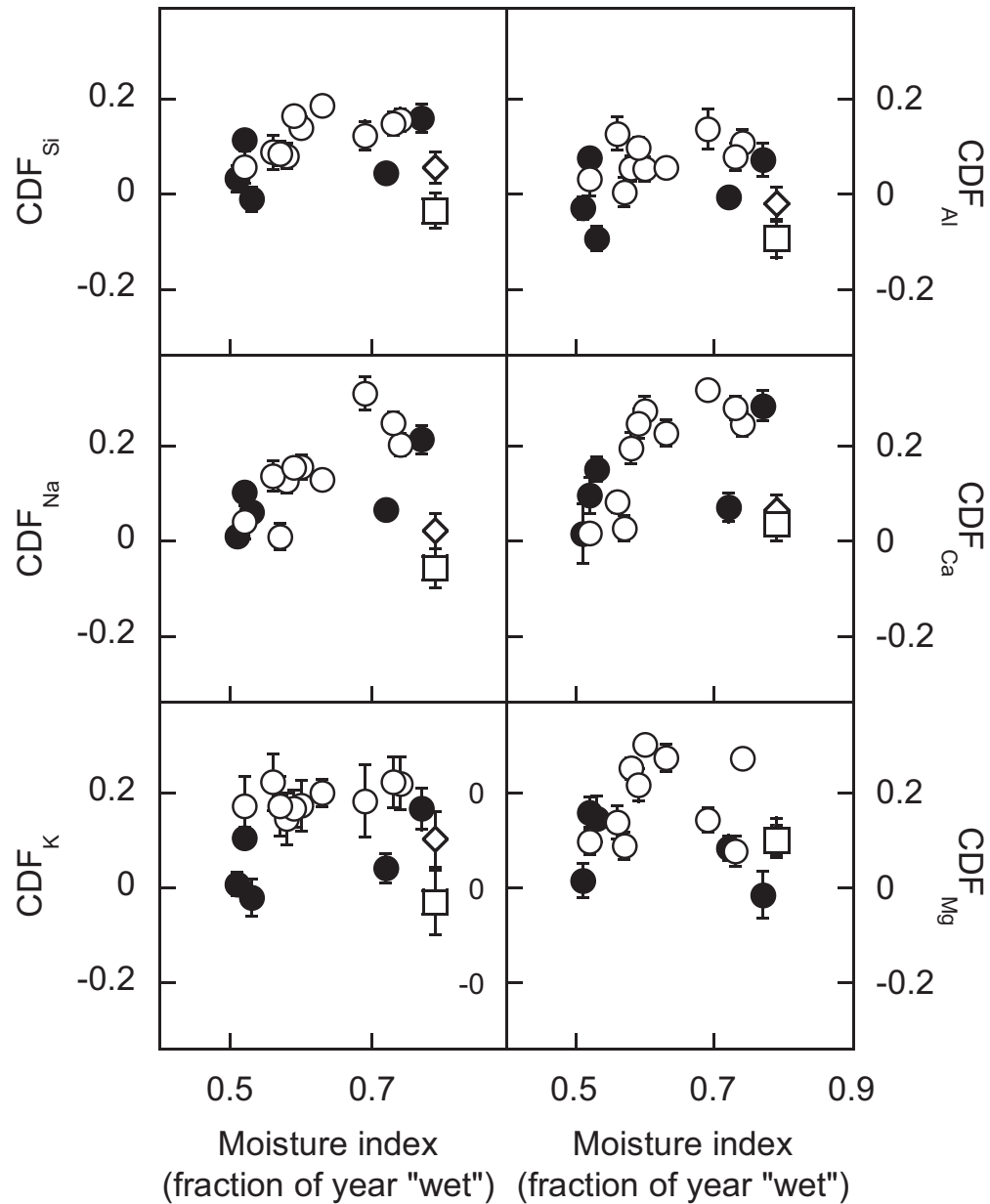


Figure 5.15. The degree of elemental depletion (i.e., CDF_X) broadly increases with the moisture index (defined in Figure 5.8) for Ca, Na, and Si, but not for K, Al, or Mg. This is consistent with more extensive weathering of plagioclase feldspar at the sites with longer wet seasons. White markers = Pilot Peak, black markers = Tailholt Mountain. The white square (P1850) and white diamond (P1850sub) represent site P1850 including and excluding anomalous soil samples, respectively (see section 5.8.1).

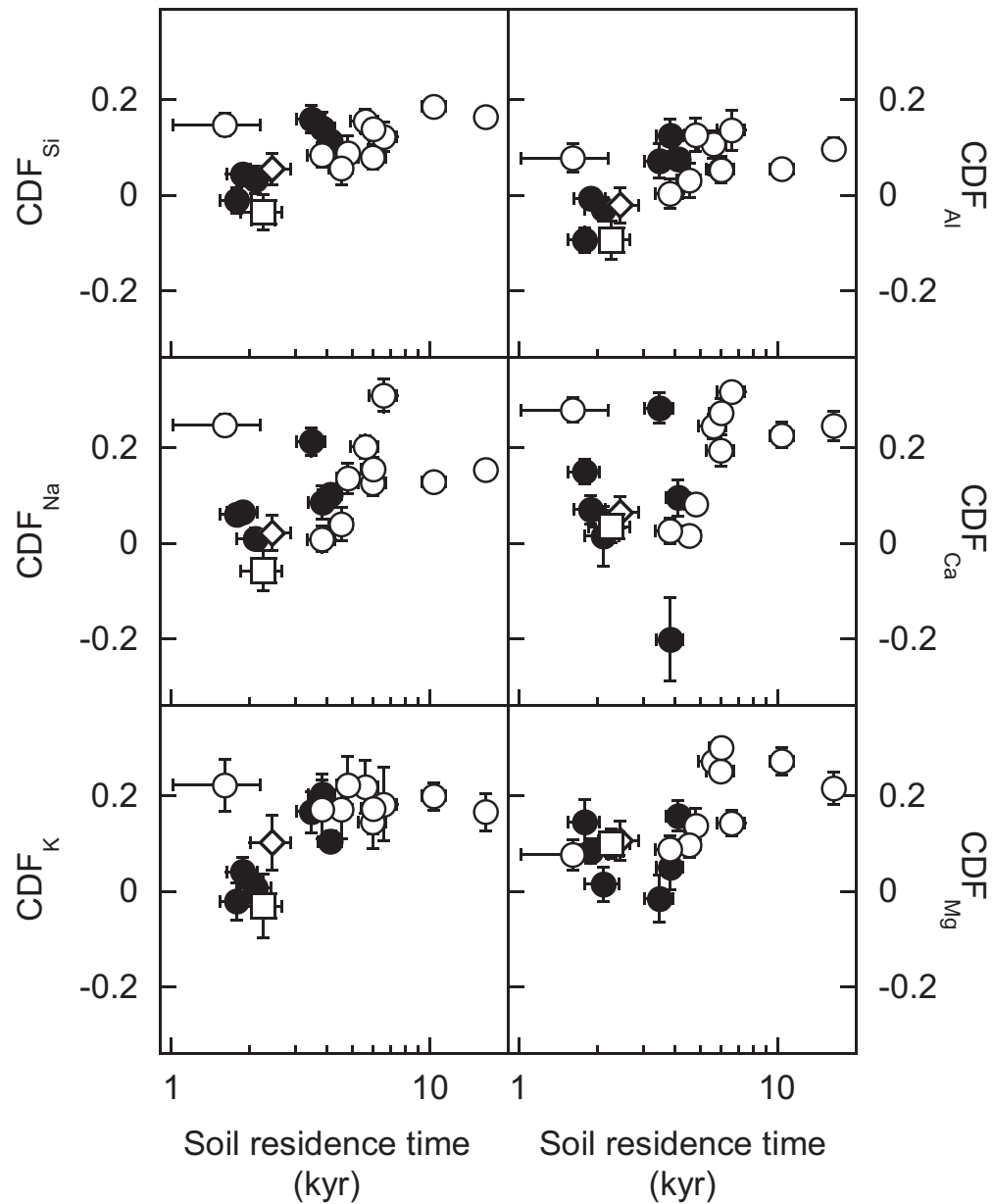


Figure 5.16. The degree of elemental depletion (i.e., CDF_X) is generally higher at longer soil residence times for several elements, most notably Si, consistent with kinetically-limited weathering. White markers = Pilot Peak, black markers = Tailholt Mountain. The white square (P1850) and white diamond (P1850sub) represent site P1850 including and excluding anomalous soil samples, respectively (see section 5.8.1).

Table 5.1. Exhumation rates and denudation rates in the Idaho Batholith

Time period	Rate (mm/yr)	Measurement type	Source
81 – 78 Ma	3.8 (+1.8/-1.4)	$^{40}\text{Ar}/^{39}\text{Ar}$	Lund et al. (1986)
74 – 67 Ma	1.0 (+0.4/-0.3)	$^{40}\text{Ar}/^{39}\text{Ar}$	Lund et al. (1986)
67 – 54 Ma	0.14 (+0.4/-0.05)	$^{40}\text{Ar}/^{39}\text{Ar}$	Lund et al. (1986)
54 Ma-present	0.07	$^{40}\text{Ar}/^{39}\text{Ar}$	Lund et al. (1986)
50 – 10 Ma	0.03 – 0.1	fission-track	Sweetkind and Blackwell (1989)
10 Ma-present	0.32 ± 0.10	fission-track	Sweetkind and Blackwell (1989)
4 – 26 ka-present	0.02 – 0.15	cosmogenic ^{10}Be	this study
5 – 26 ka-present	0.02 – 0.12	cosmogenic ^{10}Be	Kirchner et al. (2001)
10 – 84 ya-present	0.001 – 0.011	sediment yield	Kirchner et al. (2001)

Table 5.2. Field site characteristics

Site	Latitude (°N)	Longitude (°W)	Altitude (m)	Soil depth (cm) (n) ^a	Slope (°)	MAST (°C) ^b	Moisture index ^c	Aspect
<i>Pilot Peak</i>								
P2283S	45° 10.263'	115° 31.869'	2283	50 ± 4 (11)	20-25	4.8	0.74	S
P2281N	45° 10.270'	115° 31.895'	2281	16 ± 6 (7)	20-30	5.0	0.73	W
P2090	45° 10.156'	115° 32.234'	2090	57 ± 5 (7)	15-20	7.1	0.69	SW
P1850	45° 09.867'	115° 32.882'	1850	29 ± 5 (13)	25	5.1	0.79	W
P1706	45° 09.675'	115° 33.620'	1706	38 ± 3 (14)	20-26	7.6	0.57	W
P1485N	45° 09.438'	115° 33.960'	1485	31 ± 2 (16)	23-26	7.6	0.60	W
P1471S	45° 09.419'	115° 33.960'	1471	32 ± 3 (15)	26	10.9	0.58	SW
P1277S	45° 09.259'	115° 34.403'	1277	44 ± 2 (21)	25-35	9.8	0.56	SW
P1264N	45° 09.276'	115° 34.406'	1264	43 ± 3 (20)	33	7.4	0.52	NW
P1062S	45° 09.228'	115° 34.924'	1062	> 75 (1)	10-20	9.0	0.59	SW
P1062N	45° 09.238'	115° 34.949'	1062	33 ± 2 (19)	23-30	7.9	0.63	N
<i>Tailholt Mt.</i>								
T2364	45° 04.867'	115° 41.654'	2364	28 ± 2 (10)	11-16	6.1	0.77	SE
T2073	45° 04.657'	115° 40.896'	2073	25 ± 3 (7)	9	6.9	0.72	E
T1755	45° 03.688'	115° 39.095'	1755	37 ± 4 (13)	22-27	8.2	0.53	NE
T1508	45° 03.632'	115° 38.651'	1508	32 ± 4 (16)	30	7.7	0.51	N
T1294	45° 03.674'	115° 38.226'	1294	57 ± 4 (15)	24-39	7.7 ^d	no data	E
T1084	45° 03.682'	115° 38.016'	1084	56 ± 4 (12)	35-40	9.1	0.52	E

^a Soil depths (mean±s.e., from n measurements) are vertical distances between the parent material and the hillslope surface.

^b Mean annual soil temperatures (MAST) are averages over 8/1/2006-7/31/2008 on Pilot Peak and over 10/1/2005-9/30/2006 on Tailholt Mountain. These ranges were chosen to include as many complete climate records as possible. Some MAST values were calculated with the help of interpolations to fill gaps in time series; see Appendix D.

^c We define the moisture index as the fraction of the year the soil is "wet", a state we define as wetter than an arbitrary moisture threshold (Figure 5.7).

^d Because the instruments at site T1294 did not record good data during the first year of monitoring, T1294's MAST is reported here as 1.45 °C cooler than the nearest site, T1084, as was the case from 11/1/2006-10/31/2007 when instruments at both T1294 and T1084 recorded good data.

Table 5.3: ^{10}Be concentrations and CRONUS-inferred soil production rates^a

Site Name	Topographic shielding ^b	[^{10}Be] (10^4 atoms/g)	Soil production rate ($\text{t km}^{-2} \text{ yr}^{-1}$)
<i>Pilot Peak</i>			
P2283S	0.989	28.7 ± 0.7	167 ± 14
P2281N	0.996	26.3 ± 0.7	183 ± 15
P2090	0.996	28.3 ± 0.6	150 ± 12
P1850	0.988	18.8 ± 0.4	194 ± 15
P1706	0.991	20.0 ± 0.5	166 ± 13
P1485N	0.989	31.0 ± 0.6	91 ± 7
P1471S	0.987	29.8 ± 0.7	94 ± 7
P1277S	0.967	14.4 ± 0.3	171 ± 13
P1264N	0.977	15.5 ± 0.4	159 ± 12
P1062S	0.992	29.8 ± 0.7	71 ± 5
P1062N	0.975	37.6 ± 1.0	55 ± 4
<i>Tailholt Mt.</i>			
T2364	0.999	34.9 ± 1.2	145 ± 12
T2073	0.998	19.6 ± 0.5	217 ± 17
T1755	0.985	10.8 ± 0.2	320 ± 24
T1508	0.978	11.8 ± 0.2	248 ± 19
T1294	0.952	9.1 ± 0.2	275 ± 21
T1084	0.935	8.8 ± 0.2	243 ± 18
<i>Elk Creek</i>			
EC ^c	0.946	9.5 ± 0.3	448 ± 36

^a All soil production rates were calculated with the CRONUS-Earth online calculator (Balco et al., 2008). Inputs to the CRONUS calculator for latitude, longitude, and altitude were taken from Table 5.2, and other inputs were assumed to be: Sample thickness 0 cm, parent material density 2.7 g cm^{-3} , and the standard atmospheric scaling.

^b All topographic shielding factors were calculated with the CRONUS calculator using eight horizon shielding angles at azimuths of 0, 45, 90, 135, 180, 225, 270, and 315 degrees.

^c Inputs to the CRONUS calculator for Elk Creek are latitude 45.12°N , longitude 115.50°W , mean altitude 2142 m, and a topographic shielding factor calculated using a basin-average hillslope gradient of 24.3° . All ^{10}Be samples were run at LLNL-CAMS on 15 July 2007, and referenced to isotopic standard 07KNSTD3110.

Table 5.4. Pilot Peak elemental concentrations in granite outcrops (mean \pm s.e.)

Site	Al ₂ O ₃ (%)	CaO (%)	Fe ₂ O ₃ (%)	K ₂ O (%)	MgO (%)	MnO (%)	Mo (ppm)	Na ₂ O (%)	Nb (ppm)
P2283S	15.1 \pm 0.1	2.1 \pm 0.08	1.6 \pm 0.05	3.4 \pm 0.16	0.45 \pm 0.02	0.033 \pm 0.001	1.4 \pm 0.08	3.7 \pm 0.07	15 \pm 0.4
P2281N	15.1 \pm 0.1	2.1 \pm 0.08	1.6 \pm 0.05	3.4 \pm 0.16	0.45 \pm 0.02	0.033 \pm 0.001	1.4 \pm 0.08	3.7 \pm 0.07	15 \pm 0.4
P2090	15.3 \pm 0.2	2.2 \pm 0.07	1.6 \pm 0.06	3.4 \pm 0.20	0.46 \pm 0.02	0.031 \pm 0.002	1.0 \pm 0.06	3.8 \pm 0.08	14 \pm 0.5
P1850	14.8 \pm 0.2	2.1 \pm 0.06	1.6 \pm 0.04	3.3 \pm 0.14	0.40 \pm 0.01	0.029 \pm 0.001	1.0 \pm 0.05	3.6 \pm 0.07	13 \pm 0.6
P1706	14.6 \pm 0.2	2.2 \pm 0.07	1.5 \pm 0.06	3.2 \pm 0.16	0.37 \pm 0.02	0.026 \pm 0.001	1.1 \pm 0.06	3.6 \pm 0.07	13 \pm 0.5
P1485N	15.0 \pm 0.1	2.2 \pm 0.10	1.6 \pm 0.04	3.0 \pm 0.13	0.43 \pm 0.02	0.031 \pm 0.001	0.9 \pm 0.04	3.7 \pm 0.08	14 \pm 0.3
P1471S	15.0 \pm 0.1	2.2 \pm 0.10	1.6 \pm 0.04	3.0 \pm 0.13	0.43 \pm 0.02	0.031 \pm 0.001	0.9 \pm 0.04	3.7 \pm 0.08	14 \pm 0.3
P1277S	15.0 \pm 0.1	2.1 \pm 0.08	1.5 \pm 0.06	3.3 \pm 0.14	0.38 \pm 0.02	0.030 \pm 0.002	1.2 \pm 0.03	3.7 \pm 0.04	16 \pm 0.3
P1264N	15.0 \pm 0.1	2.1 \pm 0.08	1.5 \pm 0.06	3.3 \pm 0.14	0.38 \pm 0.02	0.030 \pm 0.002	1.2 \pm 0.03	3.7 \pm 0.04	16 \pm 0.3
P1062S	15.0 \pm 0.1	2.2 \pm 0.04	1.6 \pm 0.03	3.1 \pm 0.07	0.40 \pm 0.01	0.029 \pm 0.001	0.9 \pm 0.05	3.8 \pm 0.03	14 \pm 0.2
P1062N	15.0 \pm 0.1	2.2 \pm 0.04	1.6 \pm 0.03	3.1 \pm 0.07	0.40 \pm 0.01	0.029 \pm 0.001	0.9 \pm 0.05	3.8 \pm 0.03	14 \pm 0.2

Site	P ₂ O ₅ (%)	Rb (ppm)	SiO ₂ (%)	Sr (ppm)	Th (ppm)	TiO ₂ (%)	Y (ppm)	Zr (ppm)
P2283S	0.083 \pm 0.003	81 \pm 4	73.3 \pm 0.3	643 \pm 17	6.8 \pm 0.3	0.23 \pm 0.006	8.8 \pm 0.2	117 \pm 3
P2281N	0.083 \pm 0.003	81 \pm 4	73.3 \pm 0.3	643 \pm 17	6.8 \pm 0.3	0.23 \pm 0.006	8.8 \pm 0.2	117 \pm 3
P2090	0.082 \pm 0.002	77 \pm 3	72.9 \pm 0.2	642 \pm 21	5.6 \pm 0.4	0.22 \pm 0.008	9.0 \pm 0.3	115 \pm 4
P1850	0.075 \pm 0.003	78 \pm 3	73.9 \pm 0.3	627 \pm 13	8.5 \pm 0.7	0.22 \pm 0.006	9.4 \pm 0.3	123 \pm 3
P1706	0.079 \pm 0.003	74 \pm 2	74.3 \pm 0.3	635 \pm 16	7.5 \pm 0.5	0.20 \pm 0.008	9.0 \pm 0.4	123 \pm 3
P1485N	0.073 \pm 0.002	77 \pm 4	73.6 \pm 0.3	655 \pm 21	7.2 \pm 0.2	0.22 \pm 0.006	9.3 \pm 0.5	127 \pm 3
P1471S	0.073 \pm 0.002	77 \pm 4	73.6 \pm 0.3	655 \pm 21	7.2 \pm 0.2	0.22 \pm 0.006	9.3 \pm 0.5	127 \pm 3
P1277S	0.069 \pm 0.002	84 \pm 5	73.7 \pm 0.2	593 \pm 27	7.1 \pm 0.4	0.20 \pm 0.009	10.6 \pm 0.8	119 \pm 4
P1264N	0.069 \pm 0.002	84 \pm 5	73.7 \pm 0.2	593 \pm 27	7.1 \pm 0.4	0.20 \pm 0.009	10.6 \pm 0.8	119 \pm 4
P1062S	0.070 \pm 0.001	71 \pm 1	73.6 \pm 0.2	660 \pm 7	7.8 \pm 0.3	0.22 \pm 0.003	8.8 \pm 0.1	130 \pm 2
P1062N	0.070 \pm 0.001	71 \pm 1	73.6 \pm 0.2	660 \pm 7	7.8 \pm 0.3	0.22 \pm 0.003	8.8 \pm 0.1	130 \pm 2

These are mean concentrations of the 39 or 40 rock samples collected at each site, and include all samples except the outlier P1850-X13.

Table 5.5. Pilot Peak elemental concentrations in soils (mean \pm s.e.)

Site	Al ₂ O ₃ (%)	CaO (%)	Fe ₂ O ₃ (%)	K ₂ O (%)	MgO (%)	MnO (%)	Mo (ppm)	Na ₂ O (%)	Nb (ppm)
P2283S	15.8 \pm 0.1	1.9 \pm 0.03	2.1 \pm 0.03	3.1 \pm 0.07	0.43 \pm 0.01	0.063 \pm 0.002	1.6 \pm 0.04	3.4 \pm 0.03	16 \pm 0.2
P2281N	16.1 \pm 0.2	1.9 \pm 0.03	2.3 \pm 0.05	3.0 \pm 0.05	0.61 \pm 0.02	0.070 \pm 0.002	1.5 \pm 0.05	3.2 \pm 0.05	16 \pm 0.3
P2090	15.2 \pm 0.2	1.8 \pm 0.03	2.2 \pm 0.04	3.1 \pm 0.05	0.60 \pm 0.01	0.066 \pm 0.001	1.3 \pm 0.06	2.9 \pm 0.03	14 \pm 0.2
P1850	15.5 \pm 0.1	2.0 \pm 0.03	1.8 \pm 0.04	3.2 \pm 0.06	0.41 \pm 0.01	0.059 \pm 0.003	1.4 \pm 0.06	3.6 \pm 0.02	15 \pm 0.3
P1850sub	15.7 \pm 0.2	2.1 \pm 0.02	2.0 \pm 0.06	3.0 \pm 0.08	0.45 \pm 0.01	0.061 \pm 0.006	1.4 \pm 0.12	3.6 \pm 0.03	15 \pm 0.6
P1706	15.6 \pm 0.1	2.4 \pm 0.03	1.9 \pm 0.03	2.8 \pm 0.08	0.47 \pm 0.01	0.040 \pm 0.001	1.5 \pm 0.04	3.8 \pm 0.05	15 \pm 0.2
P1485N	16.2 \pm 0.1	1.9 \pm 0.02	2.2 \pm 0.04	2.9 \pm 0.04	0.45 \pm 0.01	0.040 \pm 0.001	1.1 \pm 0.06	3.5 \pm 0.03	16 \pm 0.3
P1471S	15.4 \pm 0.1	2.0 \pm 0.03	1.9 \pm 0.03	2.8 \pm 0.04	0.39 \pm 0.01	0.033 \pm 0.001	1.3 \pm 0.06	3.5 \pm 0.02	14 \pm 0.2
P1277S	14.6 \pm 0.1	2.1 \pm 0.02	1.2 \pm 0.03	2.9 \pm 0.04	0.32 \pm 0.01	0.030 \pm 0.001	1.4 \pm 0.06	3.6 \pm 0.03	13 \pm 0.4
P1264N	15.3 \pm 0.1	2.3 \pm 0.03	1.7 \pm 0.05	2.9 \pm 0.06	0.42 \pm 0.01	0.042 \pm 0.001	1.2 \pm 0.03	3.8 \pm 0.03	15 \pm 0.3
P1062S	15.9 \pm 0.1	2.1 \pm 0.07	2.1 \pm 0.07	3.0 \pm 0.06	0.49 \pm 0.02	0.035 \pm 0.002	1.1 \pm 0.05	3.7 \pm 0.04	19 \pm 0.6
P1062N	16.7 \pm 0.1	2.2 \pm 0.04	2.5 \pm 0.05	2.9 \pm 0.03	0.58 \pm 0.01	0.048 \pm 0.002	1.2 \pm 0.05	3.7 \pm 0.02	21 \pm 0.3

Site	P ₂ O ₅ (%)	Rb (ppm)	SiO ₂ (%)	Sr (ppm)	Th (ppm)	TiO ₂ (%)	Y (ppm)	Zr (ppm)
P2283S	0.101 \pm 0.003	85 \pm 1	72.8 \pm 0.2	563 \pm 5	6.4 \pm 0.2	0.30 \pm 0.005	9.4 \pm 0.1	139 \pm 1
P2281N	0.136 \pm 0.004	85 \pm 1	72.4 \pm 0.3	541 \pm 5	7.4 \pm 0.4	0.33 \pm 0.006	9.9 \pm 0.1	140 \pm 1
P2090	0.134 \pm 0.002	77 \pm 1	73.7 \pm 0.3	532 \pm 6	5.7 \pm 0.2	0.33 \pm 0.005	9.8 \pm 0.1	137 \pm 1
P1850	0.074 \pm 0.002	92 \pm 2	73.2 \pm 0.2	537 \pm 15	6.8 \pm 0.2	0.24 \pm 0.008	11.2 \pm 0.4	120 \pm 3
P1850sub	0.068 \pm 0.002	87 \pm 2	72.7 \pm 0.3	596 \pm 13	7.2 \pm 0.3	0.27 \pm 0.012	10.1 \pm 0.3	131 \pm 3
P1706	0.075 \pm 0.001	77 \pm 1	72.7 \pm 0.2	662 \pm 4	9.3 \pm 0.3	0.26 \pm 0.005	10.3 \pm 0.1	134 \pm 1
P1485N	0.070 \pm 0.001	87 \pm 1	72.4 \pm 0.2	561 \pm 6	7.9 \pm 0.2	0.32 \pm 0.005	11.1 \pm 0.1	149 \pm 1
P1471S	0.084 \pm 0.002	79 \pm 1	73.6 \pm 0.1	578 \pm 6	8.1 \pm 0.3	0.27 \pm 0.004	11.0 \pm 0.1	139 \pm 1
P1277S	0.061 \pm 0.001	70 \pm 1	74.9 \pm 0.1	601 \pm 4	7.4 \pm 0.3	0.20 \pm 0.005	9.2 \pm 0.1	131 \pm 2
P1264N	0.080 \pm 0.002	76 \pm 1	73.3 \pm 0.2	601 \pm 4	8.2 \pm 0.4	0.24 \pm 0.006	10.0 \pm 0.1	127 \pm 1
P1062S	0.061 \pm 0.001	86 \pm 2	72.4 \pm 0.2	587 \pm 12	8.9 \pm 0.4	0.32 \pm 0.013	11.8 \pm 0.3	156 \pm 3
P1062N	0.065 \pm 0.003	91 \pm 1	70.9 \pm 0.2	588 \pm 5	8.0 \pm 0.3	0.40 \pm 0.007	12.8 \pm 0.2	161 \pm 1

These are mean concentrations of the 16 soil samples collected at 10-15 cm depths at each site, and do not include samples from the soil profile at each site. P1850sub refers to the subset of soil samples in the eastern half of the soil plot (P1850-B5, B6, B9, B10, B13, B14), which excludes the anomalously rocky soil samples in the western half of the soil sampling plot (see section 5.8.1).

Table 5.6. Tailholt Mountain elemental concentrations in granite outcrops (mean \pm s.e.)

Site	Al ₂ O ₃ (%)	CaO (%)	Fe ₂ O ₃ (%)	K ₂ O (%)	MgO (%)	MnO (%)	Mo (ppm)	Na ₂ O (%)	Nb (ppm)
T2364	14.6 \pm 0.2	1.4 \pm 0.04	0.9 \pm 0.04	3.6 \pm 0.11	0.22 \pm 0.008	0.042 \pm 0.003	0.22 \pm 0.008	3.6 \pm 0.06	11 \pm 0.3
T2073	14.6 \pm 0.1	1.7 \pm 0.03	1.2 \pm 0.02	3.4 \pm 0.06	0.26 \pm 0.005	0.033 \pm 0.001	0.26 \pm 0.005	3.8 \pm 0.02	14 \pm 0.2
T1755	14.5 \pm 0.1	1.3 \pm 0.06	1.1 \pm 0.05	3.5 \pm 0.05	0.18 \pm 0.013	0.033 \pm 0.002	0.18 \pm 0.013	3.9 \pm 0.04	16 \pm 0.5
T1508	14.7 \pm 0.1	1.2 \pm 0.09	1.0 \pm 0.03	3.5 \pm 0.06	0.22 \pm 0.006	0.038 \pm 0.003	0.22 \pm 0.006	3.9 \pm 0.05	15 \pm 0.3
T1294	14.7 \pm 0.1	1.0 \pm 0.07	0.9 \pm 0.04	3.8 \pm 0.07	0.15 \pm 0.006	0.033 \pm 0.002	0.15 \pm 0.006	3.7 \pm 0.05	15 \pm 0.5
T1084	14.5 \pm 0.1	1.2 \pm 0.05	1.0 \pm 0.03	3.6 \pm 0.05	0.17 \pm 0.004	0.036 \pm 0.002	0.17 \pm 0.004	3.8 \pm 0.03	17 \pm 0.4

Site	P ₂ O ₅ (%)	Rb (ppm)	SiO ₂ (%)	Sr (ppm)	Th (ppm)	TiO ₂ (%)	Y (ppm)	Zr (ppm)
T2364	0.064 \pm 0.003	107 \pm 2	75.5 \pm 0.3	356 \pm 4	2.8 \pm 0.3	0.09 \pm 0.003	9.5 \pm 0.3	48 \pm 1
T2073	0.054 \pm 0.002	96 \pm 1	74.7 \pm 0.1	412 \pm 4	7.4 \pm 0.2	0.14 \pm 0.002	11.0 \pm 0.4	83 \pm 1
T1755	0.056 \pm 0.002	116 \pm 1	75.3 \pm 0.2	336 \pm 10	5.2 \pm 0.2	0.12 \pm 0.004	13.3 \pm 0.7	75 \pm 2
T1508	0.058 \pm 0.002	125 \pm 2	75.3 \pm 0.2	328 \pm 15	5.2 \pm 0.2	0.12 \pm 0.003	15.0 \pm 0.9	70 \pm 2
T1294	0.061 \pm 0.004	129 \pm 3	75.5 \pm 0.1	303 \pm 10	4.0 \pm 0.2	0.11 \pm 0.003	13.9 \pm 0.7	58 \pm 2
T1084	0.062 \pm 0.002	124 \pm 4	75.5 \pm 0.1	324 \pm 7	4.7 \pm 0.3	0.11 \pm 0.002	15.9 \pm 0.6	61 \pm 1

At sites T2073, T1084, T1294, and T1508, these are mean concentrations of the 40 rock samples collected at each site, and include all samples except the outlier T1508-X25. At sites T2364 and T1755, these are mean concentrations of subsets of the rock samples, as described in the text.

Table 5.7. Elemental concentrations in Tailholt Mountain soils and Eureka Flat sediments (mean \pm s.e.)

Site	Al ₂ O ₃ (%)	CaO (%)	Fe ₂ O ₃ (%)	K ₂ O (%)	MgO (%)	MnO (%)	Mo (ppm)	Na ₂ O (%)	Nb (ppm)
T2364	15.9 \pm 0.1	1.3 \pm 0.03	1.4 \pm 0.04	3.4 \pm 0.07	0.39 \pm 0.02	0.067 \pm 0.003	1.8 \pm 0.07	3.3 \pm 0.07	13 \pm 0.2
T2073	15.3 \pm 0.1	1.7 \pm 0.03	1.5 \pm 0.03	3.3 \pm 0.05	0.31 \pm 0.01	0.047 \pm 0.001	1.3 \pm 0.09	3.7 \pm 0.04	15 \pm 0.2
T1755	15.6 \pm 0.2	1.2 \pm 0.03	1.3 \pm 0.04	3.5 \pm 0.02	0.22 \pm 0.01	0.063 \pm 0.004	1.3 \pm 0.09	3.5 \pm 0.05	18 \pm 0.4
T1508	15.3 \pm 0.1	1.3 \pm 0.03	1.4 \pm 0.03	3.5 \pm 0.03	0.29 \pm 0.01	0.053 \pm 0.003	1.4 \pm 0.10	3.9 \pm 0.03	18 \pm 0.4
T1294	14.8 \pm 0.1	1.5 \pm 0.02	1.3 \pm 0.04	3.4 \pm 0.02	0.20 \pm 0.01	0.048 \pm 0.002	1.2 \pm 0.06	3.9 \pm 0.02	17 \pm 0.5
T1084	14.9 \pm 0.1	1.3 \pm 0.01	1.3 \pm 0.03	3.6 \pm 0.03	0.22 \pm 0.01	0.055 \pm 0.003	1.3 \pm 0.05	3.8 \pm 0.02	16 \pm 0.3
EF ^b	13.5 \pm 0.4	3.6 \pm 0.4	6.8 \pm 0.8	2.5 \pm 0.2	2.3 \pm 0.3	0.12 \pm 0.02	no data	2.4 \pm 0.1	13.9 \pm 0.5

Site	P ₂ O ₅ (%)	Rb (ppm)	SiO ₂ (%)	Sr (ppm)	Th (ppm)	TiO ₂ (%)	Y (ppm)	Zr (ppm)
T2364	0.080 \pm 0.003	108 \pm 1	74.0 \pm 0.2	316 \pm 7	3.0 \pm 0.2	0.16 \pm 0.006	9.5 \pm 0.3	64 \pm 2
T2073	0.074 \pm 0.002	98 \pm 1	73.9 \pm 0.2	391 \pm 4	6.5 \pm 0.3	0.18 \pm 0.003	11.6 \pm 0.3	88 \pm 1
T1755	0.052 \pm 0.001	126 \pm 1	74.5 \pm 0.3	296 \pm 3	4.7 \pm 0.2	0.15 \pm 0.004	13.6 \pm 0.3	77 \pm 1
T1508	0.061 \pm 0.001	124 \pm 1	74.1 \pm 0.2	308 \pm 5	4.8 \pm 0.2	0.16 \pm 0.004	14.4 \pm 0.5	75 \pm 1
T1294	0.064 \pm 0.001	117 \pm 1	74.6 \pm 0.1	353 \pm 2	3.9 \pm 0.2	0.14 \pm 0.004	14.5 \pm 0.6	69 \pm 1
T1084	0.069 \pm 0.002	123 \pm 1	74.6 \pm 0.1	304 \pm 2	4.0 \pm 0.2	0.15 \pm 0.004	15.9 \pm 0.6	72 \pm 1
EF ^b	0.19 \pm 0.03	87 \pm 10	68.2 \pm 1.7	328 \pm 12	6.2 \pm 1.4	1.04 \pm 0.14	24.4 \pm 2.7	166 \pm 14

^a Tailholt Mountain elemental concentrations are means of the 16 soil samples collected at 10–15 cm depths at each site, and do not include samples from the soil profile at each site.

^b Eureka Flat (EF) sediment concentrations from Sweeney et al. (2007).

Table 5.8: Results of the dust-granite mixing model mass balance

Site Name	f_d	CDF	P_d t km ⁻² yr ⁻¹	E t km ⁻² yr ⁻¹	W t km ⁻² yr ⁻¹
<i>Pilot Peak</i>					
P2283S	0.03±0.01	0.15±0.02	5±2	145±13	26±4
P2281N	0.06±0.01	0.14±0.02	12±3	167±15	28±5
P2090	0.08±0.01	0.14±0.03	13±3	141±13	22±5
P1850	0.04±0.01	-0.04±0.04	8±3	210±19	-9±8
P1850sub	0.05±0.01	0.04±0.03	9±3	194±17	9±7
P1706	0.05±0.01	0.07±0.03	10±3	163±14	12±5
P1485N	0.07±0.01	0.13±0.02	7±1	85±7	13±2
P1471S	0.03±0.01	0.08±0.02	3±1	89±7	8±2
P1277S	-0.03±0.01	0.10±0.03	-5±1	149±12	17±6
P1264N	0.03±0.01	0.05±0.03	5±2	155±13	9±6
P1062S	0.06±0.01	0.15±0.02	5±1	64±5	12±2
P1062N	0.14±0.02	0.16±0.01	9±2	53±4	10±1
<i>Tailholt Mt.</i>					
T2364	0.05±0.01	0.15±0.03	8±2	130±14	22±5
T2073	0.03±0.01	0.04±0.02	7±2	215±18	8±4
T1755	0.04±0.01	-0.02±0.02	12±3	338±27	-6±8
T1508	0.04±0.01	0.02±0.03	9±2	252±21	5±7
T1294	0.01±0.01	0.13±0.03	4±2	242±21	37±9
T1084	0.03±0.01	0.11±0.02	8±2	224±17	27±5

^a The fraction of the soil's parent material derived from dust, f_d , was estimated in Chapter 4, under the assumption that the soil composition is a mixture of the sampled granite and mafic dust from Columbia Plateau paleoflood sediments (Sweeney et al., 2007).

^b Estimates of CDF are calculated as the fraction of the total soil production rate that is lost by chemical processes (Equation 5.7).

^c Estimates of dust deposition rate P_d were calculated in Chapter 4.

^d Physical and chemical erosion rates E and W are calculated with Equations 5.4 and 5.5, respectively.

^e P1850sub results are calculated using a subset of soil samples at site P1850 (section 5.8.1).

^f All uncertainties listed in this table are standard errors.

Table 5.9. Elemental CDF_X (mean ± s.e.) estimated with Equation 5.8

Site	CDF _{Al}	CDF _{Ca}	CDF _{Fe}	CDF _K	CDF _{Mg}	CDF _{Na}	CDF _{Si}
<i>Pilot Peak</i>							
P2283S	0.11±0.03	0.25±0.03	0.02±0.01	0.22±0.06	0.27±0.02	0.20±0.02	0.16±0.02
P2281N	0.08±0.03	0.28±0.02	-0.01±0.02	0.22±0.05	0.08±0.03	0.25±0.02	0.15±0.02
P2090	0.14±0.04	0.32±0.02	0.07±0.02	0.18±0.08	0.14±0.03	0.31±0.03	0.12±0.03
P1850	-0.09±0.04	0.04±0.03	-0.05±0.02	-0.03±0.07	0.10±0.03	-0.06±0.04	-0.04±0.04
P1850sub	-0.02±0.04	0.06±0.03	-0.02±0.03	0.10±0.06	0.11±0.04	0.02±0.04	0.06±0.03
P1706	0.00±0.03	0.03±0.03	-0.01±0.02	0.17±0.06	0.09±0.03	0.01±0.03	0.09±0.03
P1485N	0.05±0.03	0.27±0.03	0.02±0.02	0.17±0.05	0.30±0.02	0.16±0.03	0.14±0.02
P1471S	0.05±0.03	0.20±0.03	0.00±0.01	0.15±0.05	0.25±0.02	0.13±0.03	0.08±0.03
P1277S	0.13±0.03	0.08±0.02	0.16±0.02	0.22±0.06	0.14±0.04	0.14±0.03	0.09±0.04
P1264N	0.03±0.04	0.02±0.01	0.00±0.02	0.17±0.06	0.10±0.03	0.04±0.03	0.06±0.03
P1062S	0.10±0.02	0.25±0.03	0.08±0.03	0.17±0.04	0.22±0.03	0.15±0.02	0.16±0.02
P1062N	0.06±0.02	0.23±0.03	0.09±0.02	0.20±0.03	0.27±0.03	0.13±0.01	0.19±0.01
<i>Tailholt Mt.</i>							
T2364	0.07±0.04	0.28±0.03	-0.03±0.03	0.17±0.04	-0.01±0.05	0.21±0.03	0.16±0.03
T2073	-0.01±0.02	0.07±0.03	-0.02±0.02	0.04±0.03	0.08±0.03	0.07±0.02	0.04±0.01
T1755	-0.09±0.03	0.15±0.03	-0.03±0.03	-0.02±0.04	0.15±0.05	0.06±0.01	-0.01±0.03
T1508	-0.03±0.02	0.02±0.06	-0.06±0.02	0.01±0.02	0.02±0.04	0.01±0.02	0.03±0.03
T1294	0.13±0.03	-0.20±0.09	-0.08±0.03	0.20±0.04	0.05±0.05	0.09±0.03	0.14±0.03
T1084	0.08±0.02	0.10±0.04	0.03±0.02	0.10±0.02	0.16±0.03	0.10±0.02	0.11±0.02

P1850sub results are calculated using a subset of soil samples at site P1850 (section 5.8.1).

Table 5.10. Elemental chemical erosion rates (mean \pm s.e. in $t\ km^{-2}\ yr^{-1}$) estimated with Equation 5.6

Site	$W_{Al_2O_3}$	W_{CaO}	$W_{Fe_2O_3}$	W_{K_2O}	W_{MgO}	W_{Na_2O}	W_{SiO_2}
<i>Pilot Peak</i>							
P2283S	2.8 \pm 0.8	0.9 \pm 0.1	0.08 \pm 0.06	1.3 \pm 0.4	0.23 \pm 0.03	1.3 \pm 0.2	19 \pm 3
P2281N	2.3 \pm 0.9	1.2 \pm 0.2	-0.05 \pm 0.11	1.4 \pm 0.4	0.08 \pm 0.05	1.7 \pm 0.2	21 \pm 4
P2090	3.4 \pm 1.1	1.2 \pm 0.1	0.22 \pm 0.11	1.0 \pm 0.5	0.14 \pm 0.05	1.9 \pm 0.3	14 \pm 4
P1850	-2.8 \pm 1.2	0.2 \pm 0.2	-0.19 \pm 0.10	-0.2 \pm 0.4	0.10 \pm 0.04	-0.4 \pm 0.3	-5 \pm 6
P1850sub	-0.6 \pm 0.3	0.3 \pm 0.2	-0.07 \pm 0.12	0.7 \pm 0.4	0.10 \pm 0.05	0.15 \pm 0.3	8 \pm 5
P1706	0.1 \pm 0.8	0.1 \pm 0.1	-0.04 \pm 0.08	0.9 \pm 0.4	0.07 \pm 0.03	0.1 \pm 0.2	11 \pm 3
P1485N	0.8 \pm 0.4	0.6 \pm 0.1	0.03 \pm 0.05	0.5 \pm 0.2	0.17 \pm 0.03	0.6 \pm 0.1	10 \pm 2
P1471S	0.8 \pm 0.4	0.4 \pm 0.1	0.00 \pm 0.03	0.4 \pm 0.2	0.12 \pm 0.02	0.5 \pm 0.1	6 \pm 2
P1277S	3.2 \pm 0.9	0.3 \pm 0.1	0.36 \pm 0.06	1.2 \pm 0.4	0.08 \pm 0.03	0.9 \pm 0.2	11 \pm 5
P1264N	0.8 \pm 0.9	0.1 \pm 0.1	-0.01 \pm 0.06	0.9 \pm 0.4	0.07 \pm 0.03	0.2 \pm 0.2	7 \pm 4
P1062S	1.1 \pm 0.3	0.4 \pm 0.1	0.12 \pm 0.05	0.4 \pm 0.1	0.09 \pm 0.02	0.4 \pm 0.1	9 \pm 1
P1062N	0.5 \pm 0.2	0.3 \pm 0.1	0.13 \pm 0.07	0.4 \pm 0.1	0.12 \pm 0.03	0.3 \pm 0.0	9 \pm 1
<i>Tailholt Mt.</i>							
T2364	1.6 \pm 0.9	0.7 \pm 0.1	-0.06 \pm 0.07	0.9 \pm 0.3	-0.01 \pm 0.03	1.2 \pm 0.2	18 \pm 4
T2073	-0.2 \pm 0.7	0.3 \pm 0.1	-0.06 \pm 0.06	0.3 \pm 0.2	0.06 \pm 0.02	0.5 \pm 0.2	7 \pm 3
T1755	-4.5 \pm 1.3	0.7 \pm 0.2	-0.12 \pm 0.13	-0.2 \pm 0.5	0.12 \pm 0.06	0.8 \pm 0.2	-3 \pm 7
T1508	-1.1 \pm 0.9	0.1 \pm 0.2	-0.20 \pm 0.09	0.1 \pm 0.2	0.01 \pm 0.04	0.1 \pm 0.2	6 \pm 6
T1294	5.2 \pm 1.5	-0.6 \pm 0.2	-0.23 \pm 0.08	2.1 \pm 0.5	0.03 \pm 0.03	0.9 \pm 0.4	29 \pm 7
T1084	2.8 \pm 0.8	0.3 \pm 0.1	0.10 \pm 0.07	0.9 \pm 0.2	0.09 \pm 0.03	1.0 \pm 0.2	21 \pm 4

P1850sub results are calculated using a subset of soil samples at site P1850 (section 5.8.1).

Bibliography

- Alexander, L. E., Klug, H. P., Kummer, E., 1948. Statistical factors affecting the intensity of X-rays diffracted by crystalline powders. *Journal of Applied Physics* 19 (8), 742–753.
- Anbeek, C., van Breemen, N., Meijer, E. L., van der Plas, L., 1994. The dissolution of naturally weathered feldspar and quartz. *Geochimica et Cosmochimica Acta* 58 (21), 4601–4613.
- Anderson, S. P., Dietrich, W. E., Jr., G. H. B., 2002. Weathering profiles, mass-balance analysis, and rates of solute loss: Linkages between weathering and erosion in a small, steep catchment. *Geological Society of America Bulletin* 114 (9), 1143–1158.
- Andrews, J. T., Eberl, D. D., 2007. Quantitative mineralogy of surface sediments on the Iceland shelf, and application to down-core studies of Holocene ice-rafted sediments. *Journal of Sedimentary Research* 77, 469–479.
- Axelrod, D. I., 1998. The Eocene Thunder Mountain flora of Central Idaho. *University of California Publications in Geological Sciences* 142, 1–61.
- Bacon, C. R., Druitt, T. H., 1988. Compositional evolution of the zoned calcalkaline magma chamber of Mount Mazama, Crater Lake, Oregon. *Contributions to Mineralogy and Petrology* 98, 224–256.
- Bacon, C. R., Lanphere, M. A., 2006. Eruptive history and geochronology of Mount Mazama and the Crater Lake region, Oregon. *GSA Bulletin* 118 (11/12), 1331–1359.
- Balco, G., Stone, J. O., Lifton, N. A., Dunai, T. J., 2008. A complete and easily accessible means of calculating surface exposure ages or erosion rates from ^{10}Be and ^{26}Al measurements. *Quaternary Geochronology* 3, 174–195.
- Barshad, I., 1957. Factors affecting clay formation. In: *Proceedings of the 6th National Conference on Clays and Clay Minerals*. National Academy of Sciences – National Research Council, Washington, D.C., pp. 110–132.
- Berner, R. A., Lasaga, A. C., Garrels, R. M., 1983. The carbonate-silicate geochemical cycle and its effect on atmospheric carbon dioxide over the past 100 million years. *American Journal of Science* 283 (7), 641–683.

- Blum, A. E., Stillings, L. L., 1995. Feldspar dissolution kinetics. In: *Reviews in Mineralogy*. Vol. 31 of *Developments in Quaternary Science*. Elsevier, pp. 291–351.
- Bluth, G. S., Kump, L. R., 1994. Lithologic and climatic controls of river chemistry. *Geochimica et Cosmochimica Acta* 58, 2341–2359.
- Bockheim, J. G., Munroe, J. S., Douglass, D., Koerner, D., 2000. Soil development along an elevational gradient in the southeastern Uinta Mountains, Utah, USA. *Catena* 39, 169–185.
- Brady, P. V., Carroll, S. A., 1994. Direct effects of CO₂ and temperature on silicate weathering: Possible implications for climate control. *Geochimica et Cosmochimica Acta* 58 (8), 1853–1856.
- Brantley, S. L., 2008. Kinetics of water-rock interaction. Springer, Ch. 5: Kinetics of mineral dissolution, pp. 151–210.
- Brimhall, G. H., Chadwick, O. A., Lewis, C. J., Compston, W., Williams, I. S., Danti, K. J., Dietrich, W. E., Power, M. E., Hendricks, D., Bratt, J., 1991. Deformational mass transport and invasive processes in soil evolution. *Science* 255, 695–702.
- Brimhall, G. H., Dietrich, W. E., MAR 1987. Constitutive mass balance relations between chemical composition, volume, density, porosity, and strain in metasomatic hydrochemical systems: Results on weathering and pedogenesis. *Geochimica et Cosmochimica Acta* 51 (3), 567–587.
- Brimhall, G. H., Lewis, C. J., Ague, J. J., Dietrich, W. E., Hampel, J., Teague, T., Rix, P., 1988. Metal enrichment in bauxites by deposition of chemically mature aeolian dust. *Nature* 333, 819–824.
- Brown, E. T., Stallard, R. F., Larsen, M. C., Raisbeck, G. M., Yiou, F., 1995. Denudation rates determined from the accumulation of in situ-produced ¹⁰Be in the Luquillo Experimental Forest, Puerto Rico. *Earth and Planetary Science Letters* 129, 193–202.
- Bryan, K., 1927. The "Palouse soil" problem. *USGS Bulletin* 790, 21–45.
- Burke, B. C., Heimsath, A. M., Dixon, J. L., Chappell, J., Yoo, K., 2009. Weathering the escarpment: chemical and physical rates and processes, south-eastern Australia. *Earth Surface Processes and Landforms*.
- Burke, B. C., Heimsath, A. M., White, A. F., 2007. Coupling chemical weathering with soil production across soil-mantled landscapes. *Earth Surface Processes and Landforms* 32 (6), 853–873.
- Busacca, A. J., Beget, J. E., Markewich, H. W., Muhs, D. R., Lancaster, N., Sweeney, M. R., 2004. Eolian sediments. In: Gillespie, A. R., Porter, S. C., Atwater, B. F. (Eds.), *The Quaternary Period in the United States*. Vol. 1 of *Developments in Quaternary Science*. Elsevier, pp. 275–309.

- Busacca, A. J., Nelstead, K. T., McDonald, E. V., Purser, M. D., 1992. Correlation of distal tephra layers in loess in the Channeled Scablands and Palouse of Washington State. *Quaternary Research* 37, 281–303.
- Busenberg, E., Clemency, C. V., 1976. Dissolution kinetics of feldspars at 25 degrees C and 1 atm CO₂ partial pressure. *Geochimica et Cosmochimica Acta* 40 (1), 41–49.
- Buss, H. L., Bruns, M. A., Schultz, M. J., Moore, J., Mathur, C. F., Brantley, S. L., 2005. The coupling of biological iron cycling and mineral weathering during saprolite formation, Luquillo Mountains, Puerto Rico. *Geobiology* 3, 247–260.
- Buss, H. L., Sak, P. B., Webb, S. M., Brantley, S. L., 2008. Weathering of the Rio Blanco quartz diorite, Luquillo Mountains, Puerto Rico: Coupling oxidation, dissolution, and fracturing. *Geochimica et Cosmochimica Acta* 72, 4488–4507.
- Cama, J., Metz, V., Ganor, J., NOV 2002. The effect of pH and temperature on kaolinite dissolution rate under acidic conditions. *Geochimica et Cosmochimica Acta* 66 (22), 3913–3926.
- Chadwick, O. A., Brimhall, G. H., Hendricks, D. M., 1990. From a black to a gray box – a mass balance interpretation of pedogenesis. *Geomorphology* 3, 369–390.
- Chadwick, O. A., Davis, J. O., 1990. Soil-forming intervals caused by eolian sediment pulses in the Lahontan basin, northwestern Nevada. *Geology* 18, 243–246.
- Chadwick, O. A., Derry, L. A., Vitousek, P. M., Huebert, B. J., Hedin, L. O., 1999. Changing sources of nutrients during four millions years of ecosystem development. *Nature* 397, 491–497.
- Chamberlain, C. P., Waldbauer, J. R., Jacobson, A. D., 2005. Strontium, hydrothermal systems and steady-state chemical weathering in active mountain belts. *Earth and Planetary Science Letters* 238 (3-4), 351–366.
- Chartres, C. J., Chivas, A. R., Walker, P. H., 1988. The effect of aeolian accessions on soil development on granitic rocks in south-eastern Australia. II. Oxygen-isotope, mineralogical and geochemical evidence for aeolian deposition. *Australian Journal of Soil Research* 26, 17–31.
- Chen, Y., Brantley, S. L., 1997. Temperature- and pH-dependence of albite dissolution rate at acid pH. *Chemical Geology* 135, 275–290.
- Chipera, S. J., Bish, D. L., 2002. FULLPAT: a full-pattern quantitative analysis program for X-ray powder diffraction using measured and calculated patterns. *Journal of Applied Crystallography* 35, 744–749.
- Chou, L., Wollast, R., 1984. Study of the weathering of albite at room temperature and pressure with a fluidized bed reactor. *Geochimica et Cosmochimica Acta* 48 (11), 2205–2217.

- Chung, F. H., 1974. Quantitative interpretation of X-ray diffraction patterns of mixtures. 1. Matrix-flushing method for quantitative multicomponent analysis. *Journal of Applied Crystallography* 7, 519–525.
- Clayton, J. L., 1986. An estimate of plagioclase weathering rate in the Idaho Batholith based upon geochemical transport rates. In: Colman, S. M., Dethier, D. P. (Eds.), *Rates of Chemical Weathering of Rocks and Minerals*. Academic Press, Ch. 19, pp. 453–466.
- Cleaves, E. T., Godfrey, A. E., Bricker, O. P., 1970. Geochemical balance of a small watershed and its geomorphic implications. *Geological Society of America Bulletin* 81 (10), 3015–3032.
- Clow, D. W., Drever, J. I., 1996. Weathering rates as a function of flow through an alpine soil. *Chemical Geology* 132 (1-4), 131–141.
- Colin, F., Alarcon, C., Viellard, P., 1993. Zircon: an immobile index in soils? *Chemical Geology* 107, 273–276.
- Dahlgren, R. A., Boettinger, J. L., Huntington, G. L., Amundson, R. G., 1997. Soil development along an elevational transect in the western Sierra Nevada, California. *Geoderma*, 207–236.
- Dahms, D. E., 1993. Mineralogical evidence for eolian contribution to soils of late Quaternary moraines, Wind River Mountains, Wyoming, USA. *Geoderma* 59, 175–196.
- Dixon, J. L., Heimsath, A. M., Amundson, R., 2009. The critical role of climate and saprolite weathering in landscape evolution. *Earth Surface Processes and Landforms*, 1507–1521.
- Dong, H., Peacor, D. R., Murphy, S. F., 1998. TEM study of progressive alteration of igneous biotite to kaolinite throughout a weathered soil profile. *Geochimica et Cosmochimica Acta* 62 (11), 1881–1887.
- Drever, J. I., Zobrist, J., 1992. Chemical weathering of silicate rocks as a function of elevation in the southern Swiss Alps. *Geochimica et Cosmochimica Acta* 56, 3209–3216.
- Dupre, B., Dessert, C., Oliva, P., Godderis, Y., Viers, J., Francois, L., Millot, R., Gaillardet, J., 2003. Rivers, chemical weathering and Earth's climate. *Comptes Rendus Geoscience* 335, 1141–1160.
- Eberl, D. D., Smith, D. B., 2009. Mineralogy of soils from two continental-scale transects across the United States and Canada and its relation to soil geochemistry and climate. *Applied Geochemistry* 24, 1394–1404.
- Egli, M., Mirabella, A., Mancabelli, A., Sartori, G., 2004. Weathering of soils in alpine areas as influenced by climate and parent material. *Clays and Clay Minerals* 52 (3), 287–303.

- Egli, M., Mirabella, A., Sartori, G., Fitze, P., 2003. Weathering rates as a function of climate: results from a climosequence of the Val Genova (Trentino, Italian Alps). *Geoderma* 111, 99–121.
- Egli, M., Mirabella, A., Sartori, G., Zanelli, R., Bischof, S., 2006. Effect of north and south exposure on weathering rates and clay mineral formation in Alpine soils. *Catena* 67, 155–174.
- Ferrier, K. L., Kirchner, J. W., 2008. Effects of physical erosion on chemical denudation rates: A numerical modeling study of soil-mantled hillslopes. *Earth and Planetary Science Letter* 272, 591–599.
- Ferrier, K. L., Kirchner, J. W., Finkel, R. C., 2005. Erosion rates over millennial and decadal timescales at Caspar Creek and Redwood Creek, Northern California Coast Ranges. *Earth Surface Processes and Landforms* 30, 1025–1038.
- Fletcher, R. C., Buss, H. L., Brantley, S. L., 2006. A spheroidal weathering model coupling porewater chemistry to soil thicknesses during steady-state denudation. *Earth and Planetary Science Letters* 244, 444–457.
- Fung, I., Meyn, S. K., Tegen, I., Doney, S., John, J., Bishop, J., 2000. Iron supply and demand in the upper ocean. *Global Biogeochemical Cycles* 14, 281–295.
- Gabet, E. J., 2007. A theoretical model coupling chemical weathering and physical erosion in landslide-dominated landscapes. *Earth and Planetary Science Letters* 264, 259–265.
- Gaillardet, J., Dupre, B., Louvat, P., Allegre, C. J., 1999. Global silicate weathering and CO₂ consumption rates from the chemistry of large rivers. *Chemical Geology* 159, 3–30.
- Garrels, R. M., Mackenzie, F., 1967. Origin of the chemical compositions of some springs and lakes. In: Colman, S. M., Dethier, D. P. (Eds.), *Advances in Chemistry Series*. Vol. 67. American Chemical Society, pp. 222–242.
- Glaccum, R. A., Prospero, J. M., 1980. Saharan aerosols over the tropical North Atlantic – Mineralogy. *Marine Geology* 37, 295–321.
- Goldstein, H. L., Reynolds, R. L., Reheis, M. C., Yount, J. C., Neff, J. C., 2008. Compositional trends in aeolian dust along a transect across the southwestern United States. *Journal of Geophysical Research* 113, F02S02.
- Gosse, J. C., Phillips, F. M., 2001. Terrestrial in situ cosmogenic nuclides: theory and application. *Quaternary Science Reviews* 20 (14), 1475–1560.
- Granger, D. E., Kirchner, J. W., Finkel, R., 1996. Spatially averaged long-term erosion rates measured from in situ-produced cosmogenic nuclides in alluvial sediment. *Journal of Geology* 104 (3), 249–257.

- Green, E. G., Dietrich, W. E., Banfield, J. F., 2006. Quantification of chemical weathering rates across an actively eroding hillslope. *Earth and Planetary Science Letters* 242, 155–169.
- Grieve, I. C., Proctor, J., Cousins, S. A., 1990. Soil variations with altitude on Volcan Barva, Costa Rica. *Catena* 17, 525–534.
- Harden, J. W., 1988. Genetic interpretations of elemental and chemical differences in a soil chronosequence, California. *Geoderma* 43, 179–193.
- Harrison, S. P., Kohfeld, K. E., Roelandt, C., Claquin, T., 2001. The role of dust in climate changes today, at the Last Glacial Maximum and in the future. *Earth Science Reviews* 54, 43–80.
- Heimsath, A. M., Chappell, J., Dietrich, W. E., Nishiizumi, K., Finkel, R. C., 2000. Soil production on a retreating escarpment in southeastern Australia. *Geology* 28 (9), 787–790.
- Heimsath, A. M., Dietrich, W. E., Nishiizumi, K., Finkel, R. C., 1997. The soil production function and landscape equilibrium. *Nature* 388 (6640), 358–361.
- Heimsath, A. M., Dietrich, W. E., Nishiizumi, K., Finkel, R. C., 1999. Cosmogenic nuclides, topography, and the spatial variation of soil depth. *Geomorphology* 27 (1-2), 151–172.
- Heimsath, A. M., Dietrich, W. E., Nishiizumi, K., Finkel, R. C., 2001. Stochastic processes of soil production and transport: Erosion rates, topographic variation and cosmogenic nuclides in the Oregon Coast Range. *Earth Surface Processes and Landforms* 26 (5), 531–552.
- Heimsath, A. M., Furbish, D. J., Dietrich, W. E., 2005. The illusion of diffusion: Field evidence for depth-dependent sediment transport. *Geology* 33 (12), 949–952.
- Herndon, E. M., Jin, L. X., Brantley, S. L., 2009. Impact of aeolian deposition on Mn cycling in soils. *Geochimica et Cosmochimica Acta* 73 (13), A525.
- Herwitz, S. R., Muhs, D. R., Prospero, J. M., Mahan, S., Vaughn, B., 1996. Origin of Bermuda's clay-rich Quaternary paleosols and their paleoclimatic significance. *Journal of Geophysical Research* 101 (D18), 23389–23400.
- Hill, I. G., Worden, R. H., Meighan, I. G., 2000. Yttrium: The immobility-mobility transition during basalt weathering. *Geology* 28 (10), 923–926.
- Hillier, S., 2000. Accurate quantitative analysis of clay and other minerals in sandstones by XRD: comparison of a Rietveld and a reference intensity ratio (RIR) method and the importance of sample preparation. *Clay Minerals* 35, 291–302.
- Hodson, M. E., 2002. Experimental evidence for mobility of Zr and other trace elements in soils. *Geochimica et Cosmochimica Acta* 66, 819–828.

- Huertas, F. J., Chou, L., Wollast, R., 1999. Mechanism of kaolinite dissolution at room temperature and pressure Part II: Kinetic study. *Geochimica et Cosmochimica Acta* 63 (19-20), 3261–3275.
- ICDD, 2003. Powder Diffraction File 2, Release 2003. International Center for Diffraction Data, 12 Campus Boulevard, Newton Square, Pennsylvania, USA, 19073.
- Jackson, M. L., Levelt, T. W. M., Syers, J. K., Rex, R. W., Clayton, R. N., Sherman, G. D., Uehara, G., 1971. Geomorphological relationships of tropospherically derived quartz in the soils of the Hawaiian Island. *Soil Science Society of America Proceedings* 35, 515–525.
- Jenkins, R., Snyder, R. L., 1996. *Introduction to X-ray Powder Diffractometry*. John Wiley and Sons.
- Jeong, G. I., Hillier, S., Kemp, R. A., 2008. Quantitative bulk and single-particle mineralogy of a thick Chinese loess-paleosol section: implications for loess provenance and weathering. *Quaternary Science Reviews* 27, 1271–1287.
- Jickells, T. D., An, Z. S., Andersen, K. K., Baker, A. R., Bergametti, G., Brooks, N., Cao, J. J., Boyd, P. W., Duce, R. A., Hunter, K. A., Kawahata, H., Kubilay, N., laRoche, J., Liss, P. S., Mahowald, N., Prospero, J. M., Ridgwell, A. J., Tegen, I., Torres, R., 2005. Global iron connections between desert dust, ocean biogeochemistry, and climate. *Science* 308, 67–71.
- Jin, L., Scheff, A., 2003. Public health assessment: Stibnite/Yellow Pine Mining Area, Stibnite, Valley County, Idaho. Tech. rep., Agency for Toxic Substances and Disease Registry (ATSDR).
- Kirchner, J. W., Finkel, R. C., Riebe, C. S., Granger, D. E., Clayton, J. L., King, J. G., Megahan, W. F., 2001. Mountain erosion over 10 yr, 10 k.y., and 10 m.y. time scales. *Geology* 29 (7), 591–594.
- Kirchner, J. W., Granger, D. E., Riebe, C. S., 1997. Cosmogenic isotope methods for measuring catchment erosion and weathering rates. In: *Journal of Conference Abstracts*. Vol. 2. p. 217.
- Kleeberg, R., Monecke, T., Hillier, S., 2008. Preferred orientation of mineral grains in sample mounts for quantitative XRD measurements: How random are powder samples? *Clays and Clay Minerals* 56 (4), 404–415.
- Kohl, C. P., Nishiizumi, K., 1992. Chemical isolation of quartz for measurement of in situ-produced cosmogenic nuclides. *Geochimica et Cosmochimica Acta* 56 (9), 3583–3587.
- Kump, L. R., Brantley, S. L., Arthur, M. A., 2000. Chemical weathering, atmospheric CO₂, and climate. *Annual Review of Earth and Planetary Science* 28, 611–667.

- Kurtz, A. C., Derry, L. A., Chadwick, O. A., 2001. Accretion of Asian dust to Hawaiian soils: Isotopic, elemental, and mineral mass balances. *Geochimica et Cosmochimica Acta* 65, 1971–1983.
- Kurtz, A. C., Derry, L. A., Chadwick, O. A., Alfano, M. J., 2000. Refractory element mobility in volcanic soils. *Geology* 28 (8), 683–686.
- Lal, D., 1991. Cosmic ray labeling of erosion surfaces: in situ nuclide production rates and erosion models. *Earth and Planetary Science Letters* 104 (2-4), 424–439.
- Litaor, M. I., 1987. The influence of eolian dust on the genesis of alpine soils in the Front Range, Colorado. *Soil Science Society of America Journal* 51, 142–147.
- Lund, K., 2004. Geology of the Payette National Forest and vicinity, west-central Idaho. USGS Professional Paper 1666.
- Lund, K., Snee, L. W., Evans, K. V., 1986. Age and genesis of precious-metals deposits, Buffalo Hump district, central Idaho – Implications for depth of emplacement of quartz veins. *Economic Geology* 81, 990–996.
- Mahowald, N. M., Muhs, D. R., Levis, S., Rasch, P. J., Yoshioka, M., Zender, C. S., Luo, C., 2006. Change in atmospheric mineral aerosols in response to climate: Last glacial period, preindustrial, modern, and doubled carbon dioxide climates. *Journal of Geophysical Research* 111, D10202.
- Marchand, D. E., 1970. Soil contamination in the White Mountains, eastern California. *Geological Society of America Bulletin* 81, 2497–2506.
- McDowell, W. H., Asbury, C. E., 1994. Export of carbon, nitrogen, and major ions from three tropical montane watersheds. *Limnology and Oceanography* 39 (1), 111–125.
- Merritts, D. J., Chadwick, O. A., Hendricks, D. M., 1991. Rates and processes of soil evolution on upland marine terraces, northern California. *Geoderma* 51, 241–275.
- Millot, R., Gaillardet, J., Dupre, B., Allegre, C. J., 2002. The global control of silicate weathering rates and the coupling with physical erosion: new insights from rivers of the Canadian Shield. *Earth and Planetary Science Letters* 196 (1-2), 83–98.
- Mitchell, V. E., 2000. History of the Stibnite Mining Area, Valley County, Idaho. Tech. rep., Idaho Geological Survey.
- Mudd, S. M., Furbish, D. J., 2004. Influence of chemical denudation on hillslope morphology. *Journal of Geophysical Research* 109, F02001.
- Mudd, S. M., Furbish, D. J., 2006. Using chemical tracers in hillslope soils to estimate the importance of chemical denudation under conditions of downslope sediment transport. *Journal of Geophysical Research-Earth Surface* 111 (F2), F02021.

- Muhs, D. R., Budahn, J. R., Prospero, J. M., Carey, S. N., 2007. Geochemical evidence for African dust inputs to soils of western Atlantic islands: Barbados, the Bahamas, and Florida. *Journal of Geophysical Research* 112, F02009.
- Muhs, D. R., Bush, C. A., Stewart, K. D., Rowland, T. R., Crittenden, R. C., 1990. Geochemical evidence of Saharan dust parent material for soils developed on Quaternary limestones of Caribbean and western Atlantic islands. *Quaternary Research* 33, 157–177.
- Murphy, S. F., 1995. The weathering of biotite in a tropical forest soil, Luquillo Mountains, Puerto Rico. Master's thesis, Penn State University.
- Murphy, S. F., Brantley, S. L., Blum, A. E., White, A. F., Dong, H., 1998. Chemical weathering in a tropical watershed, Luquillo Mountains, Puerto Rico: II. Rate and mechanism of biotite weathering. *Geochimica et Cosmochimica Acta* 62 (2), 227–243.
- Omotoso, O., McCarty, D. K., Hillier, S., Kleeberg, R., 2006. Some successful approaches to quantitative mineral analysis as revealed by the 3rd Reynolds Cup contest. *Clays and Clay Minerals* 54 (6), 748–760.
- Owen, J. J., Dietrich, W. E., Nishiizumi, K., Bellugi, D., Amundson, R., 2008. Boundary condition effects on hillslope form and soil development along a climatic gradient from semiarid to hyperarid in northern Chile. In: AGU Fall Meeting Supplement. pp. H53G–04.
- Paces, T., 1983. Rate constants of dissolution derived from the measurements of mass balance in hydrological catchments. *Geochimica et Cosmochimica Acta* 47 (11), 1855–1863.
- Petit, J. R., Jouzel, J., Barkov, N. I., Barnola, J. M., Basile, I., Bender, M., Chappellaz, J., Davis, M., Delaygue, G., Delmotte, M., Kotlyakov, V. M., Legrand, M., Lipenkov, V. Y., Lorius, C., Pepin, L., Ritz, C., Saltzman, E., Stievenard, M., 1999. Climate and atmospheric history of the past 420,000 years from the Vostok ice core, Antarctica. *Nature* 399, 429–436.
- Pett-Ridge, J. C., Derry, L. A., Kurtz, A. C., 2009. Sr isotopes as a tracer of weathering processes and dust inputs in a tropical granitoid watershed, Luquillo Mountains, Puerto Rico. *Geochimica et Cosmochimica Acta* 73, 25–43.
- Porder, S., Vitousek, P. M., Chadwick, O. A., Chamberlain, C. P., Hilley, G. E., 2007. Uplift, erosion, and phosphorus limitation in terrestrial ecosystems. *Ecosystems* 10, 158–170.
- Press, W. H., Teukolsky, S. A., Vetterling, W. T., Flannery, B. P., 1992. *Numerical Recipes in C: The Art of Scientific Computing*. Cambridge University Press, New York.
- Price, J. R., Velbel, M. A., Patino, L. C., 2005. Rates and time scales of clay-mineral formation by weathering in saprolitic regoliths of the southern Appalachians from geochemical mass balance. *Geological Society of America Bulletin* 117 (5-6), 783–794.

- Prospero, J. M., Bonatti, E., Schubert, C., Carlson, T. N., 1970. Dust in the Caribbean atmosphere traced to an African dust storm. *Earth and Planetary Science Letters* 9, 287–293.
- Prospero, J. M., Glaccum, R. A., Nees, R. T., 1981. Atmospheric transport of soil dust from Africa to South America. *Nature* 289, 570–572.
- Prospero, J. M., Lamb, P. J., 2003. African droughts and dust transport to the Caribbean: Climate change implications. *Science* 302, 1024–1027.
- Raymo, M. E., Ruddiman, W. F., Froelich, P. N., 1988. Influence of late Cenozoic mountain building on ocean geochemical cycles. *Geology* 16 (7), 649–653.
- Reheis, M., 1990. Influence of climate and eolian dust on the major-element chemistry and clay mineralogy of soils in the northern Bighorn basin, USA. *Catena* 17, 219–248.
- Reheis, M., Goodmacher, J. C., Harden, J. W., McFadden, L. D., Rockwell, T. K., Shroba, R. R., Sowers, J. M., Taylor, E. M., 1995. Quaternary soils and dust deposition in southern Nevada and California. *GSA Bulletin* 107, 1003–1022.
- Reheis, M., Kihl, R., 1995. Dust deposition in southern Nevada and California, 1984–1989: Relations to climate, source area, and source lithology. *Journal of Geophysical Research-Atmospheres* 100, 8893–8918.
- Reheis, M. C., Budahn, J. R., Lamothe, P. J., Reynolds, R. L., 2009. Compositions of modern dust and surface sediments in the Desert Southwest, United States. *Journal of Geophysical Research* 114, F01028.
- Reid, E. A., Reid, J. S., Meier, M. M., Dunlap, M. R., Cliff, S. S., Broumas, A., Perry, K., Maring, H., 2003. Characterization of African dust transported to Puerto Rico by individual particle and size segregated bulk analysis. *Journal of Geophysical Research* 108 (D19).
- Rex, R. W., Syers, J. K., Jackson, M. L., Clayton, R. N., 1969. Eolian origin of quartz in soils of the Hawaiian islands and in Pacific pelagic sediments. *Science* 163, 277–279.
- Reynolds, R. L., Reheis, M., Yount, J., Lamothe, P., 2006. Composition of aeolian dust in natural traps on isolated surface of the central Mojave Desert – Insights to mixing, sources, and nutrient inputs. *Journal of Arid Environments* 66, 42–61.
- Riebe, C. S., 2000. Tectonic and climatic control of physical erosion rates and chemical weathering rates in the Sierra Nevada, California, inferred from cosmogenic nuclides and geochemical mass balance. Ph.D. thesis, University of California, Berkeley.
- Riebe, C. S., Ferrier, K. L., Kirchner, J. W., in review. Solid-phase mass balance approaches for determining long-term chemical weathering rates.

- Riebe, C. S., Kirchner, J. W., Finkel, R. C., 2003. Long-term rates of chemical weathering and physical erosion from cosmogenic nuclides and geochemical mass balance. *Geochimica et Cosmochimica Acta* 67 (22), 4411–4427.
- Riebe, C. S., Kirchner, J. W., Finkel, R. C., 2004a. Erosional and climatic effects on long-term chemical weathering rates in granitic landscapes spanning diverse climate regimes. *Earth and Planetary Science Letters* 224 (3-4), 547–562.
- Riebe, C. S., Kirchner, J. W., Finkel, R. C., 2004b. Sharp decrease in long-term chemical weathering rates along an altitudinal transect. *Earth and Planetary Science Letters* 218 (3-4), 421–434.
- Riebe, C. S., Kirchner, J. W., Granger, D. E., 2001a. Quantifying quartz enrichment and its consequences for cosmogenic measurements of erosion rates from alluvial sediment and regolith. *Geomorphology* 40 (1-2), 15–19.
- Riebe, C. S., Kirchner, J. W., Granger, D. E., Finkel, R. C., 2001b. Strong tectonic and weak climatic control of long-term chemical weathering rates. *Geology* 29 (6), 511–514.
- Schildgen, T. F., Phillips, W. M., Purves, R. S., 2005. Simulation of snow shielding corrections for cosmogenic nuclide surface exposure studies. *Geomorphology* 64, 67–85.
- Schulz, M. S., White, A. F., 1999. Chemical weathering in a tropical watershed, Luquillo Mountains, Puerto Rico III: Quartz dissolution rates. *Geochimica et Cosmochimica Acta* 63 (3-4), 337–350.
- Seiders, V. M., 1971. Geologic map of the El Yunque quadrangle, Puerto Rico, Map I-658. U.S. Geological Survey.
- Small, E. E., Anderson, R. S., Hancock, G. S., 1999. Estimates of the rate of regolith production using ^{10}Be and ^{26}Al from an alpine hillslope. *Geomorphology* 27 (1-2), 131–150.
- Stallard, R. F., 1985. River chemistry, geology, geomorphology, and soils in the Amazon and Orinoco basins. In: Drever, J. I. (Ed.), *The Chemistry of Weathering*. Springer, pp. 293–316.
- Stallard, R. F., Edmond, J. M., 1983. Geochemistry of the Amazon 2. The influence of geology and weathering environment on the dissolved load. *Journal of Geophysical Research* 88 (C14), 9671–9688.
- Stiles, C. A., Mora, C. I., Driese, S. G., 2003. Pedogenic processes and domain boundaries in a Vertisol climosequence: evidence from titanium and zirconium distribution and morphology. *Geoderma* 116, 279–299.
- Stone, J. O., 2000. Air pressure and cosmogenic isotope production. *Journal of Geophysical Research* 105 (B10), 23753–23759.

- Stone, J. O. H., Evans, J. M., Fifield, L. K., Allan, G. L., Cresswell, R. G., 1998. Cosmogenic chlorine-36 production in calcite by muons. *Geochimica et Cosmochimica Acta* 62 (3), 433–454.
- Stonestrom, D. A., White, A. F., Akstin, K. C., 1998. Determining rates of chemical weathering in soils – solute transport versus profile evolution. *Journal of Hydrology* 209, 331–345.
- Sweeney, M. R., Gaylord, D. R., Busacca, A. J., 2007. Evolution of Eureka Flat: A dust-producing engine of the Palouse loess, USA. *Quaternary International* 162-163, 76–96.
- Sweetkind, D. S., Blackwell, D. D., 1989. Fission-track evidence of the Cenozoic thermal history of the Idaho batholith. *Tectonophysics* 157, 241–250.
- Swoboda-Colberg, N. G., Drever, J. I., 1993. Mineral dissolution rates in plot-scale field and laboratory experiments. *Chemical Geology* 105 (1-3), 51–69.
- Taylor, A. B., Velbel, M. A., 1991. Geochemical mass balances and weathering rates in forested watersheds of the southern Blue Ridge II. Effects of botanical uptake terms. *Geoderma* 51 (1-4), 29–50.
- Turner, B. F., Stallard, R. F., Brantley, S. L., 2003. Investigation of in situ weathering of quartz diorite bedrock in the Rio Icacos basin, Luquillo Experimental Forest, Puerto Rico. *Chemical Geology* 202, 313–341.
- Velbel, M. A., 1985. Geochemical mass balances and weathering rates in forested watersheds of the southern Blue Ridge. *American Journal of Science* 285 (10), 904–930.
- Velbel, M. A., 1993. Temperature dependence of silicate weathering in nature: How strong a negative feedback on long-term accumulation of atmospheric CO₂ and global greenhouse warming? *Geology* 21, 1059–1062.
- von Blanckenburg, F., 2009. A geochemist learns that mountain building does not accelerate rock weathering. *Nature* 460, 309.
- von Blanckenburg, F., Hewawasam, T., Kubik, P. W., 2004. Cosmogenic nuclide evidence for low weathering and denudation in the wet, tropical highlands of Sri Lanka. *Journal of Geophysical Research* 109 (F3), F03008.
- Walker, J. C. G., Hays, P. B., Kasting, J. F., 1981. A negative feedback mechanism for the long-term stabilization of Earth's surface temperature. *Journal of Geophysical Research - Oceans and Atmospheres* 86 (NC10), 9776–9782.
- West, A. J., Galy, A., Bickle, M., 2005. Tectonic and climatic controls on silicate weathering. *Earth and Planetary Science Letters* 235, 211–228.

- White, A. F., 1995. Chemical weathering rates of silicate minerals in soils. *Chemical Weathering Rates of Silicate Minerals* 31, 407–461.
- White, A. F., 2002. Determining mineral weathering rates based on solid and solute weathering gradients and velocities: application to biotite weathering in saprolites. *Chemical Geology* 190, 69–89.
- White, A. F., 2003. Natural weathering rates of silicate minerals. In: Drever, J. I. (Ed.), *Treatise in Geochemistry* 5. Elsevier, pp. 133–169.
- White, A. F., Blum, A. E., 1995. Effects of climate on chemical weathering in watersheds. *Geochimica et Cosmochimica Acta* 59 (9), 1729–1747.
- White, A. F., Blum, A. E., Bullen, T. D., Vivit, D. V., Schulz, M., Fitzpatrick, J., 1999a. The effect of temperature on experimental and natural chemical weathering rates of granitoid rocks. *Geochimica et Cosmochimica Acta* 63 (19-20), 3277–3291.
- White, A. F., Blum, A. E., Schulz, M. S., Bullen, T. D., Harden, J. W., Peterson, M. L., 1996. Chemical weathering rates of a soil chronosequence on granitic alluvium: I. Quantification of mineralogical and surface area changes and calculation of primary silicate reaction rates. *Geochimica et Cosmochimica Acta* 60 (14), 2533–2550.
- White, A. F., Blum, A. E., Schulz, M. S., Vivit, D. V., Stonestrom, D. A., Larsen, M., Murphy, S. F., Eberl, D., 1998. Chemical weathering in a tropical watershed, Luquillo Mountains, Puerto Rico: I. Long-term versus short-term weathering fluxes. *Geochimica et Cosmochimica Acta* 62 (2), 209–226.
- White, A. F., Brantley, S. L., 2003. The effect of time on the weathering of silicate minerals: why do weathering rates differ in the laboratory and field? *Chemical Geology* 202 (3-4), 479–506.
- White, A. F., Bullen, T. D., Vivit, D. V., Schulz, M. S., Clow, D. W., 1999b. The role of disseminated calcite in the chemical weathering of granitoid rocks. *Geochimica et Cosmochimica Acta* 63 (13-14), 1939–1953.
- White, A. F., Schulz, M. S., Stonestrom, D. A., Vivit, D. V., Fitzpatrick, J., Bullen, T., 2008. Solute profiles in soils, weathering gradients and exchange equilibrium/disequilibrium. *Mineralogical Magazine* 72 (1), 149–153.
- White, A. F., Schulz, M. S., Vivit, D. V., Blum, A. E., Stonestrom, D. A., Harden, J. W., 2005. Chemical weathering of a soil chronosequence on granitic alluvium: III. Hydrochemical evolution and contemporary solute fluxes and rates. *Geochimica et Cosmochimica Acta* 69 (8), 1975–1996.
- Wilkinson, B. H., McElroy, B. J., 2007. The impact of humans on continental erosion and sedimentation. *GSA Bulletin* 119 (1/2), 140–156.

Yoo, K., Amundson, R., Heimsath, A. M., Dietrich, W. E., Brimhall, G. H., 2007.
Integration of geochemical mass balance with sediment transport to calculate rates of
soil chemical weathering and transport on hillslopes. *Journal of Geophysical Research*
112, F02013.

Appendix A

Supplementary information for the numerical model in Chapter 2

A.1 Derivation of model equations

We begin creating the model by deriving an equation for the rate of change in soil thickness H . We assume that mass is added to the soil only by conversion of bedrock to soil from below. Because we are applying mass conservation to a unit column of soil, the dimensions of soil mass are $[\text{M L}^{-2}]$.

$$\frac{d(\text{soil mass per unit area})}{dt} = \text{mass input rate} - \text{mass loss rate} \quad (\text{A.1})$$

$$\frac{d(\rho_s H)}{dt} = \epsilon_b - D_{inst} \quad (\text{A.2})$$

Here H is the soil thickness $[\text{L}]$, ϵ_b is the rate of bedrock lowering due to conversion of bedrock to soil (also termed the soil production rate) $[\text{M L}^{-2} \text{T}^{-1}]$, ρ_s is the density of soil $[\text{M L}^{-3}]$, and D_{inst} is the denudation rate $[\text{M L}^{-2} \text{T}^{-1}]$, defined as the rate of soil mass loss per unit area. We assume that the soil production rate ϵ_b depends exponentially on soil thickness as in the formulation of Heimsath et al. (1997, 1999, 2000, 2001, 2005).

$$\epsilon_b = \epsilon_0 e^{-\alpha H} \quad (\text{A.3})$$

Here ϵ_0 represents the soil production rate in the absence of soil, and α $[\text{L}^{-1}]$ is a constant that describes the exponential dependence of soil production rate on soil thickness. If we assume ρ_s is constant in time and that D_{inst} is the sum of instantaneous physical erosion rates E_{inst} and instantaneous chemical denudation rates W_{inst} , then the rate of change in soil thickness H is:

$$\frac{dH}{dt} = \frac{1}{\rho_s} (\epsilon_0 e^{-\alpha H} - E_{inst} - W_{inst}). \quad (\text{A.4})$$

Noting that in a well-mixed soil the CRN concentration N_s [atoms M^{-1}] is the total number of CRN atoms in the soil column, n_s [atoms L^{-2}], divided by the mass of the soil column, $\rho_s H$ [$M L^{-2}$], and assuming that ρ_s is constant in time,

$$\frac{dN_s}{dt} = N_s \left(\frac{1}{n_s} \frac{dn_s}{dt} - \frac{1}{H} \frac{dH}{dt} \right). \quad (\text{A.5})$$

We then assume that the soil gains CRN only through in-situ production of CRN and through incorporation of CRN from bedrock during soil production at the soil-bedrock boundary, and loses CRN only through soil denudation.

$$\begin{aligned} \frac{dn_s}{dt} = & \frac{dn_s}{dt}(\text{in-situ CRN production}) + \frac{dn_s}{dt}(\text{soil production}) \\ & - \frac{dn_s}{dt}(\text{loss to denudation}) \end{aligned} \quad (\text{A.6})$$

Because Equation A.6 neglects radioactive decay, it is suitable for stable CRN (^3He , ^{21}Ne) and CRN with half-lives that are much longer than the residence time of minerals within the penetration depth of cosmogenic radiation (^{10}Be , ^{26}Al), and unsuitable for CRN with much shorter half-lives (e.g., ^{14}C). The production rate of CRN in the soil decreases exponentially with depth, and thus the in-situ production rate of CRN in the soil column is, expressed in [$\text{atoms } L^{-2} T^{-1}$],

$$\begin{aligned} \frac{dn_s}{dt}(\text{in-situ CRN production}) &= \rho_s \int_0^H P_0 e^{-\rho_s z / \Lambda} dz \\ &= \Lambda P_0 (1 - e^{-\rho_s H / \Lambda}). \end{aligned} \quad (\text{A.7})$$

Defining N_{z_b} as the concentration of CRN in bedrock at the soil-bedrock boundary at depth z_b , the rate of CRN supply to the soil by soil production is N_{z_b} times the soil production rate:

$$\frac{dn_s}{dt}(\text{soil production}) = N_{z_b} \epsilon_0 e^{-\alpha H}. \quad (\text{A.8})$$

N_{z_b} varies in time as the cosmic ray flux produces new CRN at the soil-bedrock boundary (the first term in Equation A.9) and as soil production pushes the soil-bedrock boundary deeper below the surface where CRN concentrations are smaller (the second term).

$$\frac{dN_{z_b}}{dt} = P(z_b) + \frac{\epsilon_0 e^{-\alpha H}}{\rho_r} \left(\frac{\partial N(z \geq z_b)}{\partial z} \right) \quad (\text{A.9})$$

Because the CRN production rate drops off exponentially as it passes through matter, and because CRN concentrations below the soil-bedrock boundary drop off exponentially according to Equation A.10,

$$N(z \geq z_b) = N_{z_b} e^{-\rho_r(z-z_b)/\Lambda}, \quad (\text{A.10})$$

the rate of change of N_{z_b} over time is given by:

$$\frac{dN_{z_b}}{dt} = P_0 e^{-\rho_s H / \Lambda} - \epsilon_0 e^{-\alpha H} \frac{N_{z_b}}{\Lambda}. \quad (\text{A.11})$$

The loss of CRN through soil denudation is the soil CRN concentration N_s times the denudation rate.

$$\begin{aligned}\frac{dn_s}{dt}(\text{loss to denudation}) &= N_s D_{inst} \\ &= N_s(\epsilon_0 e^{-\alpha H} - \rho_s \frac{dH}{dt})\end{aligned}\quad (\text{A.12})$$

The rate of change of n_s is thus

$$\frac{dn_s}{dt} = \Lambda P_0(1 - e^{-\rho_s H/\Lambda}) + N_{z_b} \epsilon_0 e^{-\alpha H} - N_s(\epsilon_0 e^{-\alpha H} - \rho_s \frac{dH}{dt}), \quad (\text{A.13})$$

which can be substituted into Equation A.5 to yield an expression for CRN concentrations in a well-mixed soil.

$$\frac{dN_s}{dt} = \frac{1}{\rho_s H} \left(\epsilon_0 e^{-\alpha H} (N_{z_b} - N_s) + \Lambda P_0 (1 - e^{-\rho_s H/\Lambda}) \right) \quad (\text{A.14})$$

Lastly, we derive an expression for the rate of change of mineral concentrations in the soil column. We define the average concentration of mineral X in soil, $[X]_s$ [mol M⁻¹], as the number of moles of mineral X in the soil column, Q_X [mol L⁻²], divided by the mass of the soil column, $\rho_s H$ [M L⁻²]. Thus the rate of change of $[X]_s$ is, assuming a constant soil density,

$$\frac{d[X]_s}{dt} = \frac{1}{\rho_s H} \left(\frac{dQ_X}{dt} - [X]_s \rho_s \frac{dH}{dt} \right). \quad (\text{A.15})$$

We now derive an expression for dQ_X/dt to substitute into Equation A.15 by applying conservation of mass to mineral X in the soil column:

$$\begin{aligned}\frac{dQ_X}{dt} &= \frac{dQ_X}{dt}(\text{soil production}) + \frac{dQ_X}{dt}(\text{mineral generation}) \\ &\quad - \frac{dQ_X}{dt}(\text{mineral dissolution}) - \frac{dQ_X}{dt}(\text{physical erosion}).\end{aligned}\quad (\text{A.16})$$

In this expression the first two terms represent inputs of mineral X to the soil, and the last two terms represent losses of mineral X from the soil. The first term is the rate at which mineral X is supplied to the soil by conversion of bedrock to soil, and is given by Equation A.17, in which $[X]_r$ is the concentration of X in bedrock.

$$\frac{dQ_X}{dt}(\text{soil production}) = \epsilon_0 e^{-\alpha H} [X]_r \quad (\text{A.17})$$

This second term is the rate of mineral production within the soil, and we assume it to be nonzero only for secondary minerals. We follow Chamberlain et al. (2005) in defining s_X to be the rate of secondary mineral production per unit volume [mol L⁻³ T⁻¹], such that the total rate of secondary mineral production in the soil column is

$$\frac{dQ_X}{dt}(\text{mineral generation}) = s_X H. \quad (\text{A.18})$$

The third term is the rate of mineral dissolution, and we follow the approach of Chamberlain et al. (2005) in modeling the dissolution rate of mineral phase X as a linear function of its specific surface area A_X [$\text{L}^2 \text{mol}^{-1}$] and its concentration in the soil $[X]_s$ [mol M^{-1}].

$$\frac{d[X]_s}{dt}(\text{mineral dissolution}) = -k_X A_X [X]_s \quad (\text{A.19})$$

Here k_X is the dissolution rate constant [$\text{mol L}^{-2} \text{T}^{-1}$]. Over the entire soil column, the total number of moles of mineral X lost to dissolution is then

$$\frac{dQ_X}{dt}(\text{mineral dissolution}) = -k_X A_X [X]_s \rho_s H. \quad (\text{A.20})$$

For all primary minerals we calculate specific surface area A_X as

$$A_X = \frac{6R_X w_X}{\rho_X d_X} \quad (\text{A.21})$$

following White (1995), where ρ_X is the density of mineral X [M L^{-3}], w_X is the molar mass of mineral X [M mol^{-1}], d_X is the grain diameter of mineral X [L], and R_X is the surface roughness of mineral X [unitless], which we calculate following Anbeek et al. (1994). For secondary minerals, which tend to be much smaller and hence have much larger specific surface areas, we use empirically-determined specific surface areas. Table A.1 provides a list of published values for each of these parameters.

Lastly, the fourth term of the mass balance in Equation A.16 is the number of moles of mineral X lost by physical erosion of soil, and is given by the physical erosion rate times the concentration of mineral X in the soil.

$$\frac{dQ_X}{dt}(\text{physical erosion}) = -E_{inst}[X]_s \quad (\text{A.22})$$

Substitution of Equations A.17, A.18, A.20, and A.22 into Equation A.16 yields the following expression for dQ_X/dt .

$$\frac{dQ_X}{dt} = \epsilon_0 e^{-\alpha H} [X]_r + s_X H - k_X A_X [X]_s \rho_s H - E_{inst}[X]_s \quad (\text{A.23})$$

Finally, substitution of Equations A.23, A.4, and 15 into Equation A.15 yields the rate of change in the concentration of mineral X (Equation A.24). We use Equation A.24 to calculate the evolution of all soil mineral concentrations over time, including the concentration of an insoluble mineral, a quantity that is needed to infer chemical denudation rates via Equation 6.

$$\begin{aligned} \frac{d[X]_s}{dt} = & \frac{\epsilon_0 e^{-\alpha H}}{\rho_s H} ([X]_r - [X]_s) + \frac{s_X}{\rho_s} - k_X A_X [X]_s \\ & + [X]_s \sum_{j=1}^n (k_j A_j [X_j]_s w_j - \frac{s_j w_j}{\rho_s}) \end{aligned} \quad (\text{A.24})$$

Here n is the number of mineral phases in the soil, $[X_j]_s$ is the concentration of the j^{th} soil mineral phase in the summation [mol M^{-1}], and k_j , A_j , s_j , and w_j are the dissolution rate constant, specific surface area, secondary mineral production rate, and molar mass, respectively, of the j^{th} mineral phase in the summation.

A.2 Derivation of nondimensional model equations

The dimensional differential equations for H , N_s , N_{z_b} , and $[X]_s$ depend on a number of independent parameters. Here we nondimensionalize these equations to remove the model's dependence on soil production parameters ϵ_0 and α and on CRN production parameters P_0 and Λ in order to clarify the dominant controls on soil thickness, CRN concentrations, and soil mineral concentrations. We do not ascribe particular meaning or importance to the nondimensionalizations presented here; we applied these nondimensionalizations merely to eliminate particular dimensional parameters. We note that other nondimensionalization schemes are possible, and that in all schemes nondimensional parameters are easily scaled back to their dimensional counterparts.

We begin nondimensionalizing the model by noting that time can be scaled by a soil production timescale $T_P = \Lambda\epsilon_0^{-1}$, such that nondimensional time \hat{t} is given by

$$\hat{t} = \frac{t}{T_P} = \frac{t\epsilon_0}{\Lambda}. \quad (\text{A.25})$$

Here and below we denote nondimensional quantities with a carat. We nondimensionalize soil density by dividing by $\alpha\Lambda$,

$$\hat{\rho}_s = \frac{\rho_s}{\alpha\Lambda}, \quad (\text{A.26})$$

and scale soil depth with the soil production parameter α .

$$\hat{H} = H\alpha \quad (\text{A.27})$$

We nondimensionalize CRN concentrations N_{z_b} and N_s by scaling them to the hypothetical soil CRN concentration that would occur at a steady-state denudation rate of the maximum soil production rate ϵ_0 .

$$\hat{N}_{z_b} = \frac{N_{z_b}\epsilon_0}{P_0\Lambda}, \hat{N}_s = \frac{N_s\epsilon_0}{P_0\Lambda} \quad (\text{A.28})$$

Molar mineral concentrations are scaled by their molar masses to yield nondimensional concentrations

$$[\hat{X}]_r = [X]_r w_X, [\hat{X}]_s = [X]_s w_X, \quad (\text{A.29})$$

and mineral dissolution and production parameters are scaled as follows.

$$\hat{k}_X = \frac{k_X w_X}{\epsilon_0}, \hat{A}_X = \frac{A_X \Lambda}{w_X}, \hat{s}_X = \frac{s_X w_X \Lambda}{\rho_s \epsilon_0} \quad (\text{A.30})$$

Here \hat{k}_X is the ratio of the dissolution rate of mineral phase X to the maximum soil production rate ϵ_0 , \hat{A}_X is the specific surface area of X relative to the inverse of the gamma-ray neutron penetration depth, and \hat{s}_X relates the clay production rate of X to the

maximum soil production rate ϵ_0 . We lastly scale all inferred and instantaneous denudation and erosion rates by the maximum soil production rate ϵ_0 .

$$\begin{aligned}
\hat{E}_{inst} &= \frac{E_{inst}}{\epsilon_0} \\
\hat{D}_{inf} &= \frac{D_{inf}}{\epsilon_0} = \frac{1}{\hat{N}_s} \\
\hat{W}_{inf} &= \frac{W_{inf}}{\epsilon_0} = \frac{1}{\hat{N}_s} \left(1 - \frac{[\hat{Z}r]_r}{[\hat{Z}r]_s} \right) \\
\hat{W}_{inst} &= \frac{W_{inst}}{\epsilon_0} = \hat{\rho}_s \hat{H} \sum_{j=1}^n (\hat{k}_j \hat{A}_j [\hat{X}_j]_s - \hat{s}_j)
\end{aligned} \tag{A.31}$$

Under the transformations in Equations A.25-A.31, the governing equations assume the following nondimensional forms.

$$\frac{d\hat{H}}{d\hat{t}} = \frac{1}{\hat{\rho}_s} \left(e^{-\hat{H}} - \hat{E}_{inst} - \hat{\rho}_s \hat{H} \sum_{j=1}^n (\hat{k}_j \hat{A}_j [\hat{X}_j]_s - \hat{s}_j) \right) \tag{A.32}$$

$$\frac{d\hat{N}_{z_b}}{d\hat{t}} = e^{-\hat{\rho}_s \hat{H}} - \hat{N}_{z_b} e^{-\hat{H}} \tag{A.33}$$

$$\frac{d\hat{N}_s}{d\hat{t}} = \frac{1}{\hat{\rho}_s \hat{H}} \left(e^{-\hat{H}} (\hat{N}_{z_b} - \hat{N}_s) + 1 - e^{-\hat{\rho}_s \hat{H}} \right) \tag{A.34}$$

$$\begin{aligned}
\frac{d[\hat{X}]_s}{d\hat{t}} &= \frac{e^{-\hat{H}}}{\hat{\rho}_s \hat{H}} ([\hat{X}]_r - [\hat{X}]_s) + \hat{s}_X - \hat{k}_X \hat{A}_X [\hat{X}]_s + \\
&\quad [\hat{X}]_s \sum_{j=1}^n (\hat{k}_j \hat{A}_j [\hat{X}_j]_s - \hat{s}_j)
\end{aligned} \tag{A.35}$$

A.3 Tables of parameter values used in model runs

Table A.1. Mineral parameter values used in Figure 2.2

Mineral ^a	Molar mass w ($\frac{\text{g}}{\text{mol}}$)	Density ρ ($\frac{\text{kg}}{\text{m}^3}$)	Dissolution rate ^b k ($\frac{\text{mol}}{\text{m}^2 \text{ yr}}$)	Production rate ^c s ($\frac{\text{mol}}{\text{m}^3 \text{ yr}}$)	Surface roughness ^d R	Surface area ^e A ($\frac{\text{m}^2}{\text{mol}}$)	Relative Solubility ^f $kA/(kA)_{qz}$
Quartz	60.09	2650	5.0×10^{-8}	0	3	2	1
Plagioclase	265.44	2650	5.0×10^{-6}	0	39	117	5465
K-feldspar	278.35	2560	5.0×10^{-7}	0	8	26	122
Biotite	464.60	3090	2.0×10^{-6}	0	237	1069	19690
Zircon	183.31	4600	0	0	3	4	0
Kaolinite	258.18	2600	5.0×10^{-8}	0.51	n/a	4776	2234

^a We model plagioclase as a standard oligoclase (20% Ca, 80%Na), and assume biotite has the stoichiometric formula $\text{KMg}_{1.5}\text{Fe}_{1.5}\text{Si}_3\text{AlO}_{10}(\text{OH})_2$.

^b We use field-based dissolution rate constants for plagioclase, K-feldspar and biotite from Clow and Drever (1996), the mean field-based dissolution rate constant from Schulz and White (1999) for quartz, and assume zircon is insoluble. In the absence of field-based dissolution rate constants for kaolinite, we assume that the ratio of $k_{kaolinite}$ to $k_{oligoclase}$ in the field is the same as the ratio measured in lab experiments (Cama et al., 2002; Huertas et al., 1999; White, 2003); that is, we assume that $k_{kaolinite}$ is two orders of magnitude lower than the field-based $k_{oligoclase}$.

^c We assume that the mineral production rate in the soil is zero for each primary mineral, and we use a kaolinite production rate of $0.1 \text{ g kg}^{-1} \text{ yr}^{-1}$, a value that falls within the range of $0.001\text{-}0.2 \text{ g kg}^{-1} \text{ yr}^{-1}$ given in Barshad (1957), as cited by Price et al. (2005).

^d We calculate surface roughness for each primary mineral following Anbeek et al. (1994).

^e For each primary mineral we calculate surface area as $A = 6Ru\rho^{-1}d^{-1}$ following White (1995), where d is the mineral grain diameter, which we assume to be 200 microns. Because secondary kaolinite crystals are generally much smaller than 200 microns, we use an experimentally-determined surface area for kaolinite (Cama et al., 2002).

^f The relative solubility here is the product of the dissolution rate constant k and the specific surface area A , scaled by the product of k and A for quartz.

Table A.2. Nondimensional parameter values used in Figures 3-7

	$[\hat{X}]_r$	\hat{k}	\hat{A}	\hat{s}
quartz	0.2499	8.0×10^{-9}	3.1×10^4	0
plagioclase	0.4000	3.6×10^{-6}	3.9×10^5	0
K-feldspar	0.2000	3.7×10^{-7}	8.3×10^4	0
biotite	0.1500	2.5×10^{-6}	2.0×10^6	0
zircon	0.0001	0	1.8×10^4	0
kaolinite	0	3.5×10^{-8}	1.6×10^7	0.43
$\hat{\rho}_s = 0.276$				

Appendix B

Mineral abundances in rock, soil, and saprolite samples at Rio Icacos, Puerto Rico

As described in the main text, we determined mineral abundances in rock, saprolite and soil samples by processing each samples XRD pattern in FULLPAT (Chipera and Bish, 2002), a full-pattern inversion method. The average mineral abundances in the bulk rock, saprolite, and soil at sites RI-1 and RI-4 are recorded in Tables 3.3 and 3.4, and we present in Table B.2 all of the sample mineral abundances from which the average abundances were derived. These abundances were converted to units of mol/kg with the molar masses in Table B.1.

Table B.1. Mineral molar masses (after White et al., 1998)

Mineral	Formula	Molar mass (g/mol)
Quartz	SiO_2	60.08
Plagioclase	$\text{Na}_{0.60}\text{Ca}_{0.40}\text{Al}_{1.36}\text{Si}_{2.63}\text{O}_8$	268.38
Hornblende	$(\text{Na}_{0.34}\text{K}_{0.05})(\text{Ca}_{1.71}\text{Mg}_{2.84}\text{Fe}_{2.06}\text{Al}_{0.89})(\text{Al}_{1.00}\text{Si}_{6.68})\text{O}_{22}(\text{OH})_2$	886.98
Biotite	$\text{K}_{0.85}(\text{Al}_{0.10}\text{Ti}_{0.20}\text{Fe}_{1.35}\text{Mg}_{1.25})(\text{Si}_{2.8}\text{Al}_{1.2})\text{O}_{10}(\text{OH})_2$	456.30
Kaolinite	$\text{Al}_2\text{Si}_2\text{O}_5(\text{OH})_4$	258.16

Table B.2: FULLPAT-determined mineral abundances
(weight %) at RI-1 and RI-4, Rio Icacos, Puerto Rico

Sample	Quartz (%)	Plagioclase (%)	Hornblende (%)	Biotite (%)
RI-4 soils				
RI-4P1A	48.0	0.0	0.9	0.0
RI-4P1B	48.6	0.0	0.0	0.0
RI-4P2A	59.6	5.7	4.1	0.0
RI-4P2B1	56.3	4.1	5.4	0.0
RI-4P2B2	56.2	5.1	4.1	0.0
RI-4P3W1	41.5	9.8	11.1	0.0
RI-4P3W2	43.7	8.6	7.5	0.0
RI-4P4A	66.3	6.3	6.3	0.0
RI-4P4B1	63.6	7.0	5.3	0.0
RI-4P4B2	62.6	6.1	5.8	0.0
RI-4P5W1	82.7	0.0	1.7	0.0
RI-4P5W2	76.7	0.0	0.0	0.0
RI-4P6W1	45.1	0.0	0.0	0.0
RI-4P6W2	47.2	0.0	0.0	0.0
RI-4P7B	33.3	4.3	10.6	0.0
RI-4P8A	58.8	0.0	2.3	0.0
RI-4P8B1	63.7	0.0	1.8	0.0
RI-4P8B2	61.5	0.0	2.5	0.0
RI-4P8W1	70.4	0.0	3.1	0.0
RI-4P8W2	58.5	0.0	2.9	0.0
RI-4P9AB1	52.9	0.0	0.0	0.0
RI-4P9B2	62.4	0.0	0.0	0.0
RI-4P9B3	64.0	0.0	0.0	0.0
RI-4P9B4(26)	51.7	0.0	0.0	0.0
RI-4P9B4(27)	31.7	0.0	0.0	0.0
RI-4P10A	71.1	0.0	0.0	0.0
RI-4P10B1	67.4	0.0	0.0	0.0
RI-4P10B2(38)	70.0	0.0	0.0	0.0
RI-4P10B2(40)	56.7	0.0	0.0	0.0
RI-4P10B3	34.9	0.0	0.0	0.0
mean±s.e.	56.9±2.3	1.9±0.6	2.5±0.6	0.0±0.0
RI-4 rocks				
RI-4X1	22.4	51.9	12.7	0.3
RI-4X2	24.1	57.7	13.8	0.5
RI-4X3	19.3	58.4	22.4	0.8
RI-4X4	23.8	n/d	23.8	1.1
RI-4X5	19.3	n/d	24.5	1.5
mean±s.e.	21.8±1.1	56.0±2.1	19.4±2.6	0.8±0.2

Sample	Quartz (%)	Plagioclase (%)	Hornblende (%)	Biotite (%)
RI-4 saprolite				
RI-4P9S(28)	27.8	0.0	0.0	0.0
RI-4P9S(29)	24.3	0.0	0.0	0.0
RI-4P9S(30)	24.9	0.0	0.0	0.0
RI-4P9S(31)	24.1	0.0	0.0	0.0
RI-4P9S(32)	24.1	0.0	0.0	0.0
RI-4P9S(33)	26.6	0.0	0.0	0.0
RI-4P9S(34)	27.6	0.0	0.0	0.0
RI-4S1	28.1	0.0	0.0	0.0
RI-4S2	21.4	15.5	20.4	0.0
RI-4P10S(45)	24.8	0.0	0.0	0.0
RI-4P10S(46)	26.2	0.0	0.0	0.0
RI-4P10S(47)	24.9	0.0	0.0	0.0
RI-4P10S(48)	27.5	0.0	0.0	0.0
mean±s.e.	25.6±0.5	1.2±1.2	1.6±1.6	0.0±0.0
RI-1 soils				
RI-1P1B	57.1	0.0	0.9	0.0
RI-1P2B	60.7	0.0	2.0	0.0
RI-1P3B	34.7	0.0	0.0	0.0
RI-1P3BC	25.6	0.0	1.6	0.0
RI-1P4B1	62.3	4.1	3.3	0.0
RI-1P4B2	43.0	0.0	2.2	0.0
RI-1P5A	50.8	0.0	0.0	0.0
RI-1P5B	47.9	0.0	0.0	0.0
RI-1P6B	50.8	3.2	11.2	0.0
RI-1P7A	45.1	4.9	4.7	0.0
RI-1P7B	52.6	3.4	5.0	0.0
RI-1P8A	48.1	0.0	0.0	0.0
RI-1P8B	51.6	0.0	0.0	0.0
mean±s.e.	48.5±2.8	1.2±0.5	2.4±0.9	0.0±0.0
RI-1 rocks				
RI-1X1	24.5	56.7	13.6	0.6
RI-1X2	28.2	61.6	12.4	0.6
RI-1X3	26.2	57.4	10.5	0.2
RI-1X4	23.9	51.8	12.8	0.4
RI-1X5	25.2	53.4	10.1	0.6
RI-1P4X	7.7	n/d	n/d	0.1
mean±s.e.	22.6±3.0	56.2±1.7	11.9±0.7	0.4±0.1

Appendix C

Chemical composition of soil profile samples at Pilot Peak and Tailholt Mountain, Idaho

At each field site on Pilot Peak and Tailholt Mountain, we dug one soil excavation down to or close to the parent material, and collected soil samples at various depths within the soil profile. Where possible, we also collected saprolite samples within the profile.

In this appendix we present the chemical compositions of the samples in these profiles. Soil samples in these figures are marked as solid circles and saprolite samples as open squares. For reference, we also plot the average rock outcrop composition as a gray box centered on the mean rock composition, with a width of one standard error on either side of the mean.

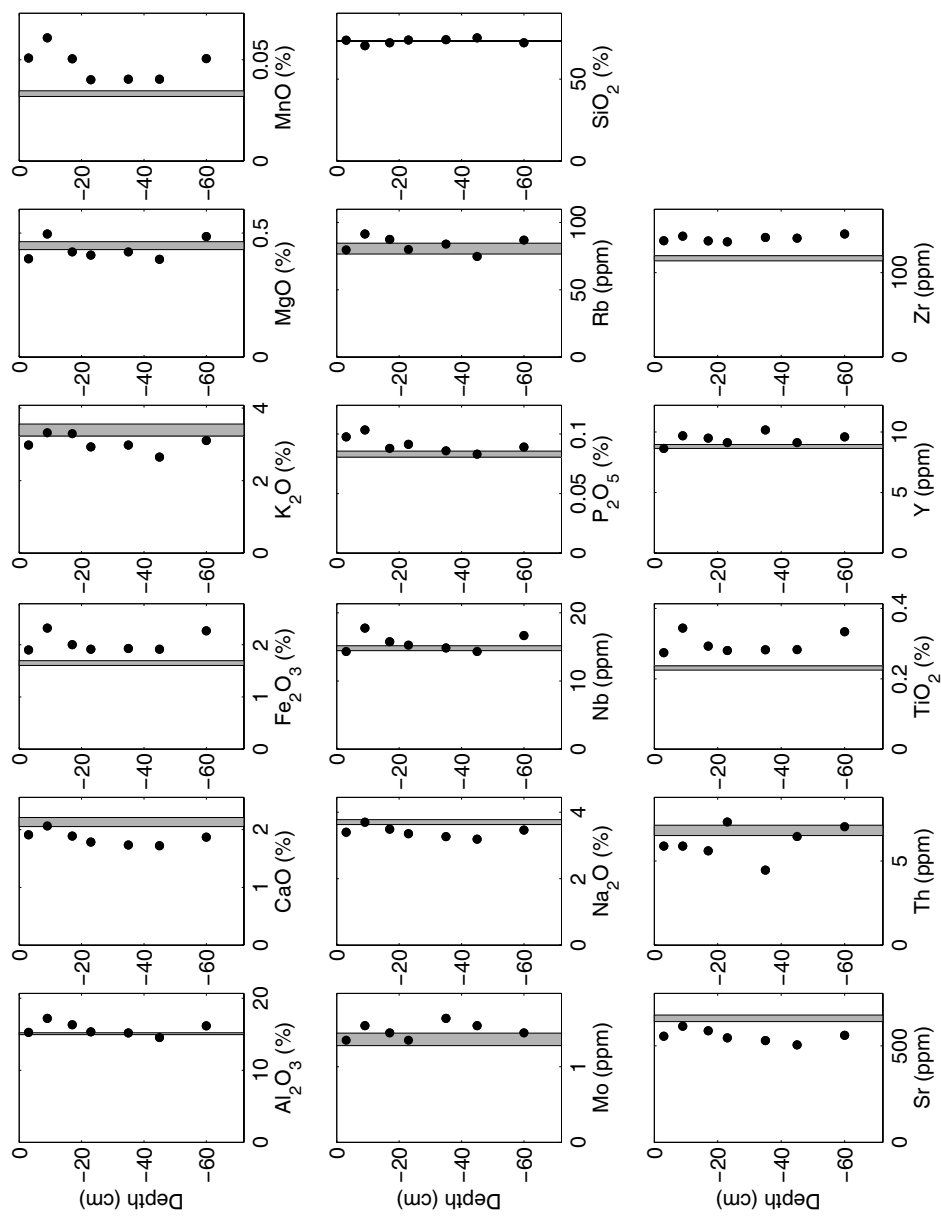


Figure C.1. Elemental concentrations in the soil profile at site P2283S. Solid circles represent soil samples and the gray box represents the average rock outcrop composition (mean and s.e.).

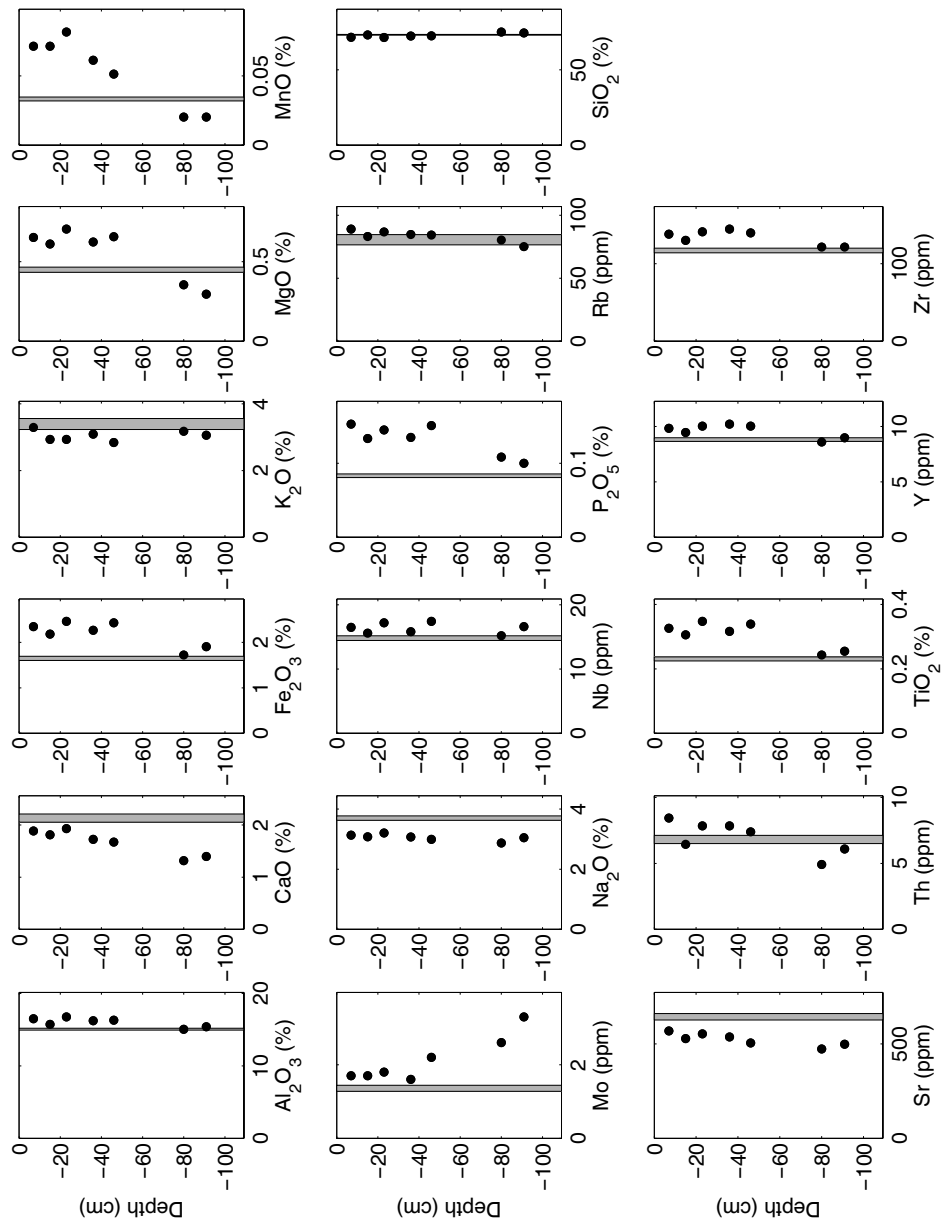


Figure C.2. Elemental concentrations in the soil profile at site P2281N. Solid circles represent soil samples and the gray box represents the average rock outcrop composition (mean and s.e.).

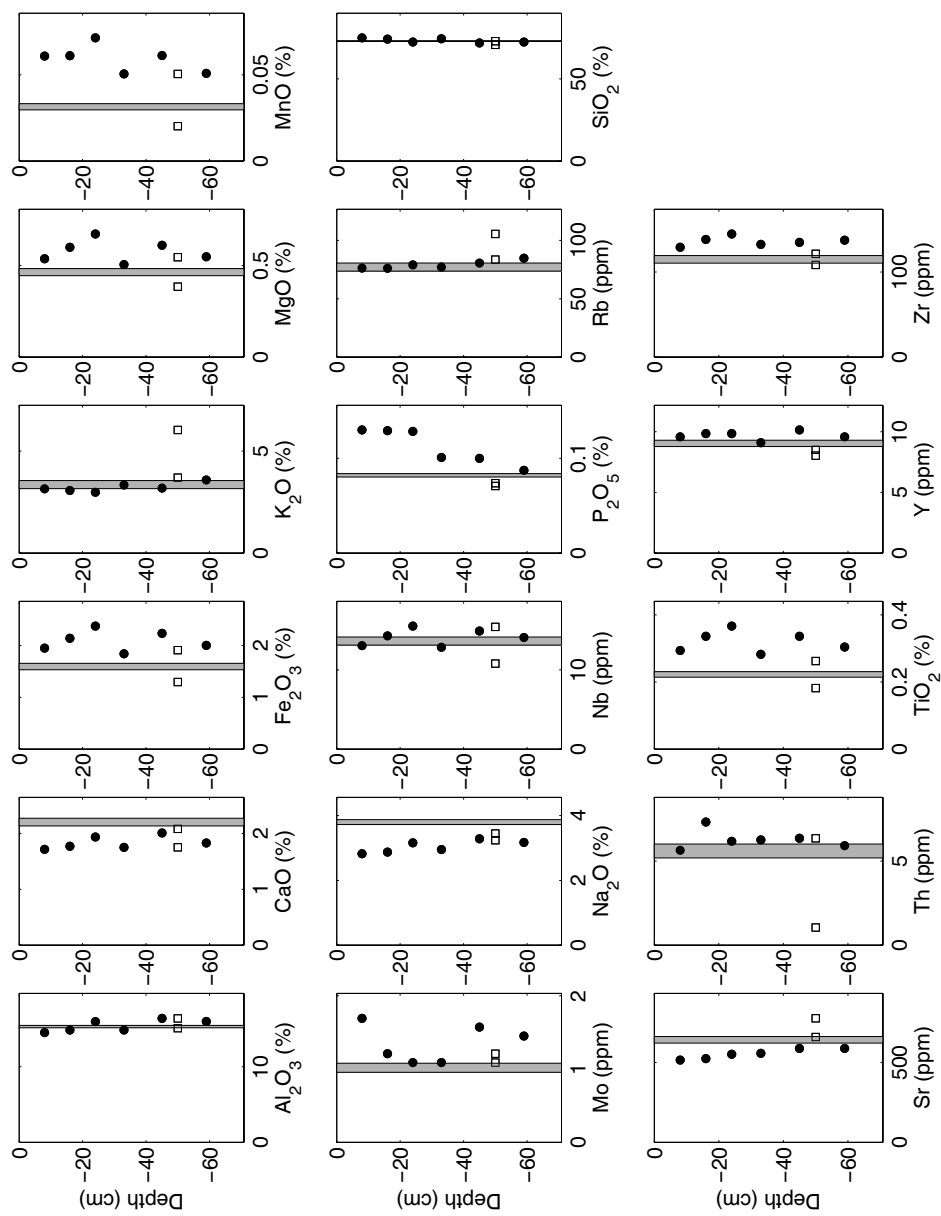


Figure C.3. Elemental concentrations in the soil profile at site P2090. Solid circles represent soil samples, open squares represent saprolite samples, and the gray box represents the average rock outcrop composition (mean and s.e.).

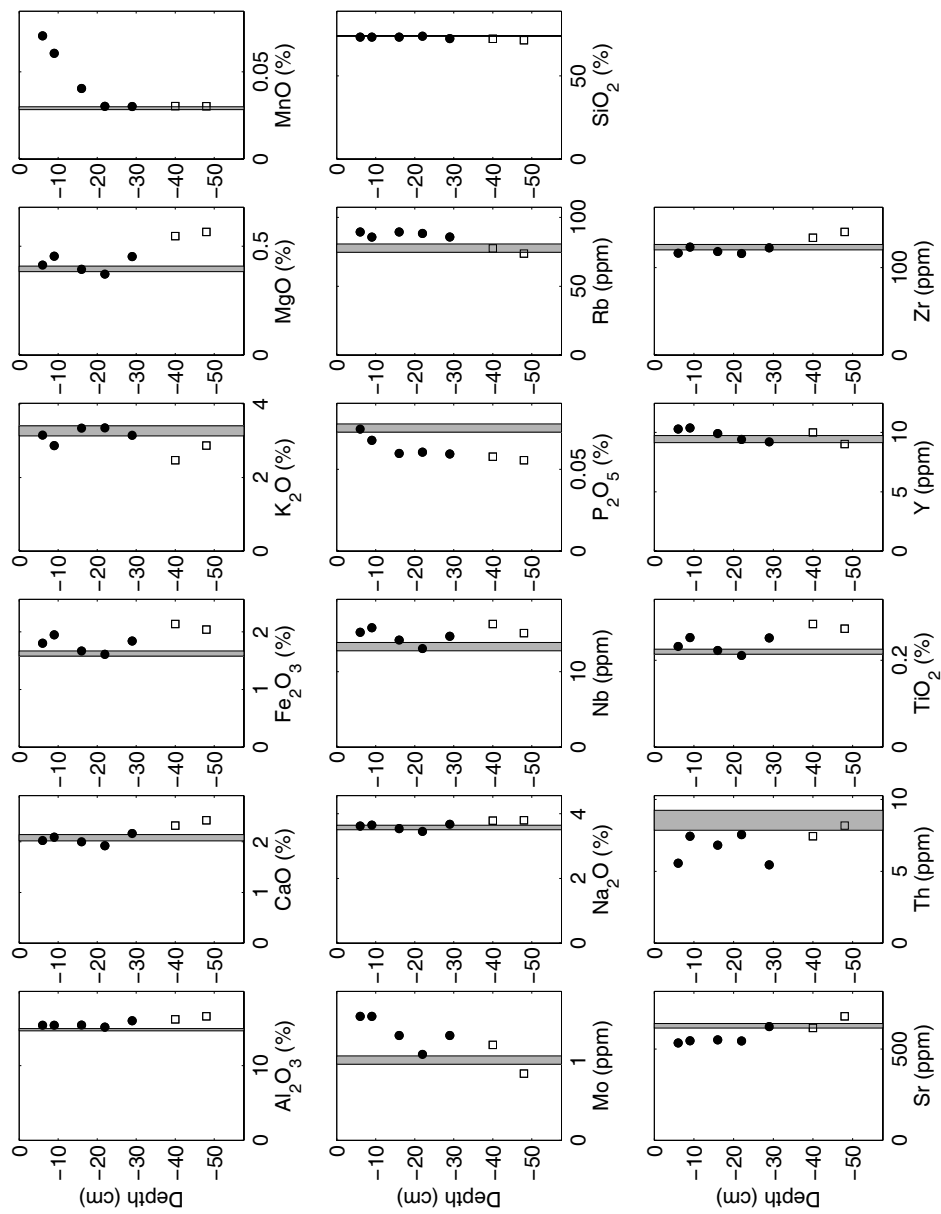


Figure C.4. Elemental concentrations in the soil profile at site P1850. Solid circles represent soil samples, open squares represent saprolite samples, and the gray box represents the average rock outcrop composition (mean and s.e.).

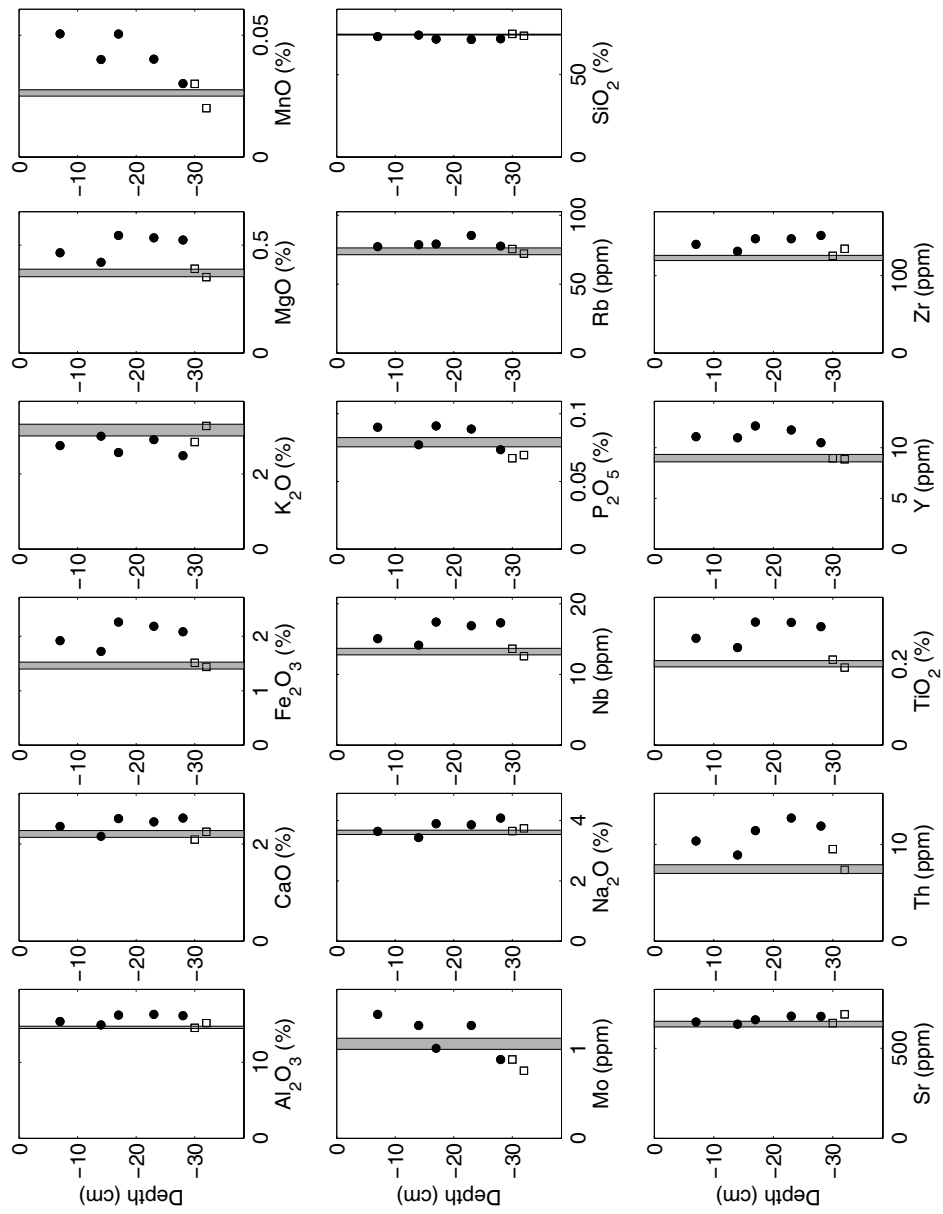


Figure C.5. Elemental concentrations in the soil profile at site P1706. Solid circles represent soil samples, open squares represent saprolite samples, and the gray box represents the average rock outcrop composition (mean and s.e.).

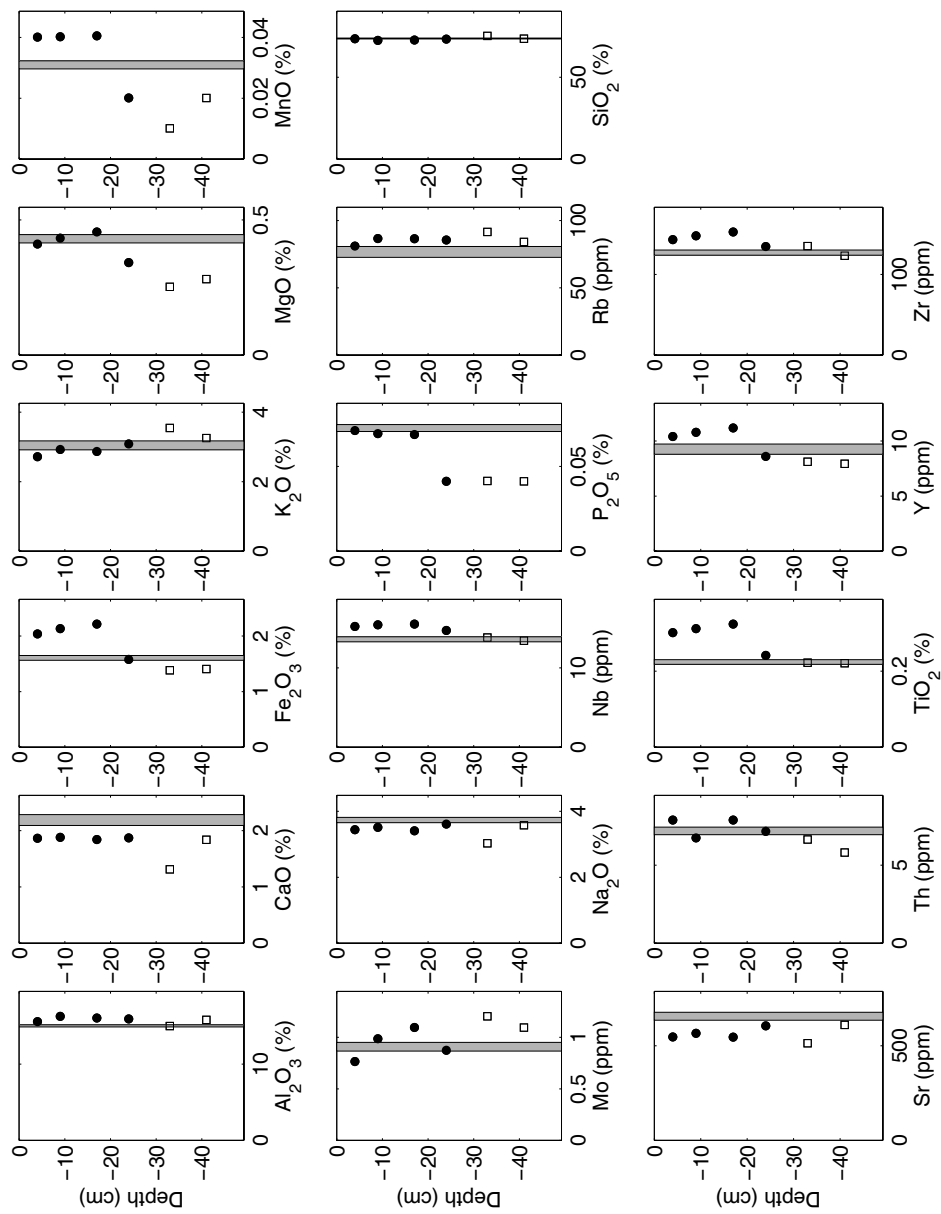


Figure C.6. Elemental concentrations in the soil profile at site P1485N. Solid circles represent soil samples, open squares represent saprolite samples, and the gray box represents the average rock outcrop composition (mean and s.e.).

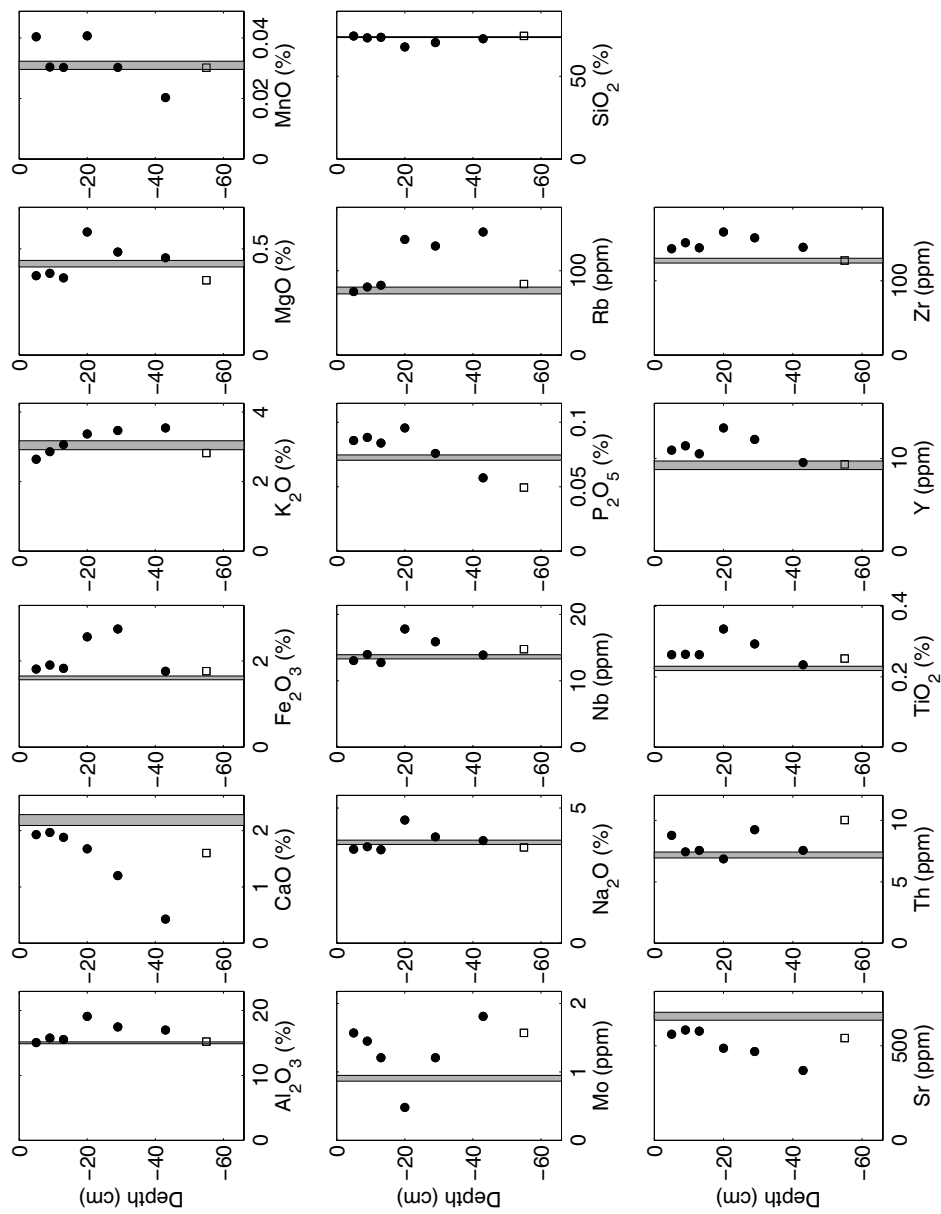


Figure C.7. Elemental concentrations in the soil profile at site P1471S. Solid circles represent soil samples, open squares represent saprolite samples, and the gray box represents the average rock outcrop composition (mean and s.e.).

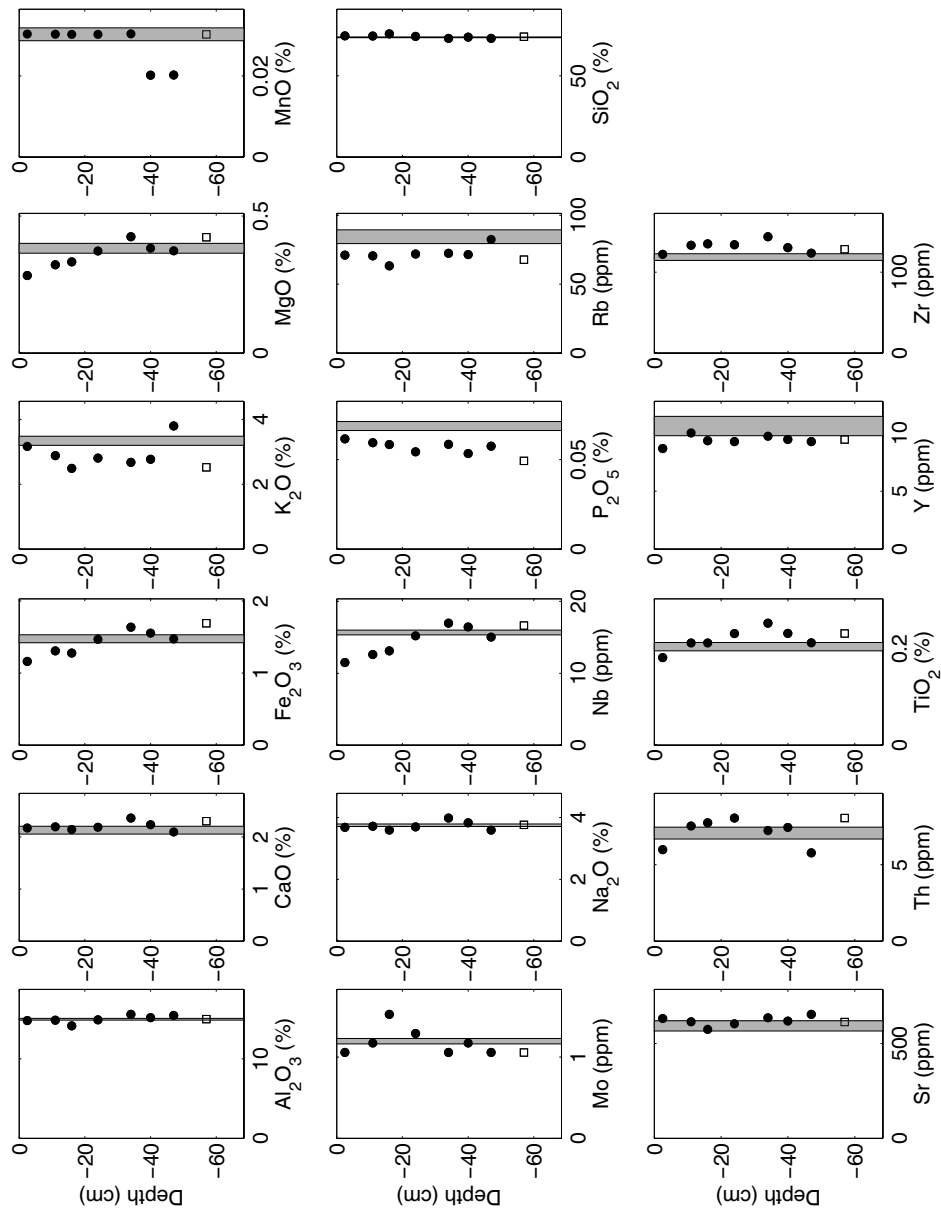


Figure C.8. Elemental concentrations in the soil profile at site P1277S. Solid circles represent soil samples, open squares represent saprolite samples, and the gray box represents the average rock outcrop composition (mean and s.e.).

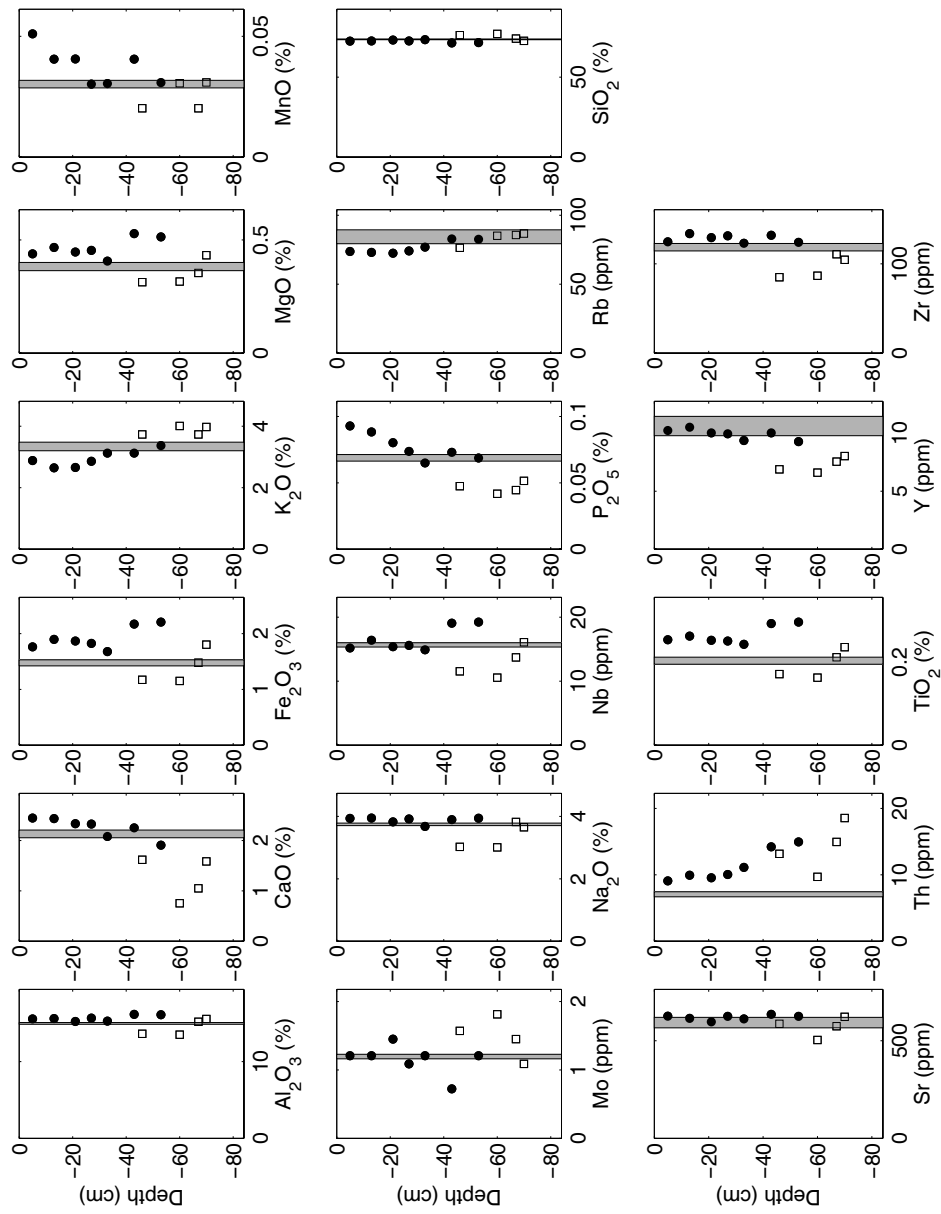


Figure C.9. Elemental concentrations in the soil profile at site P1264N. Solid circles represent soil samples, open squares represent saprolite samples, and the gray box represents the average rock outcrop composition (mean and s.e.).

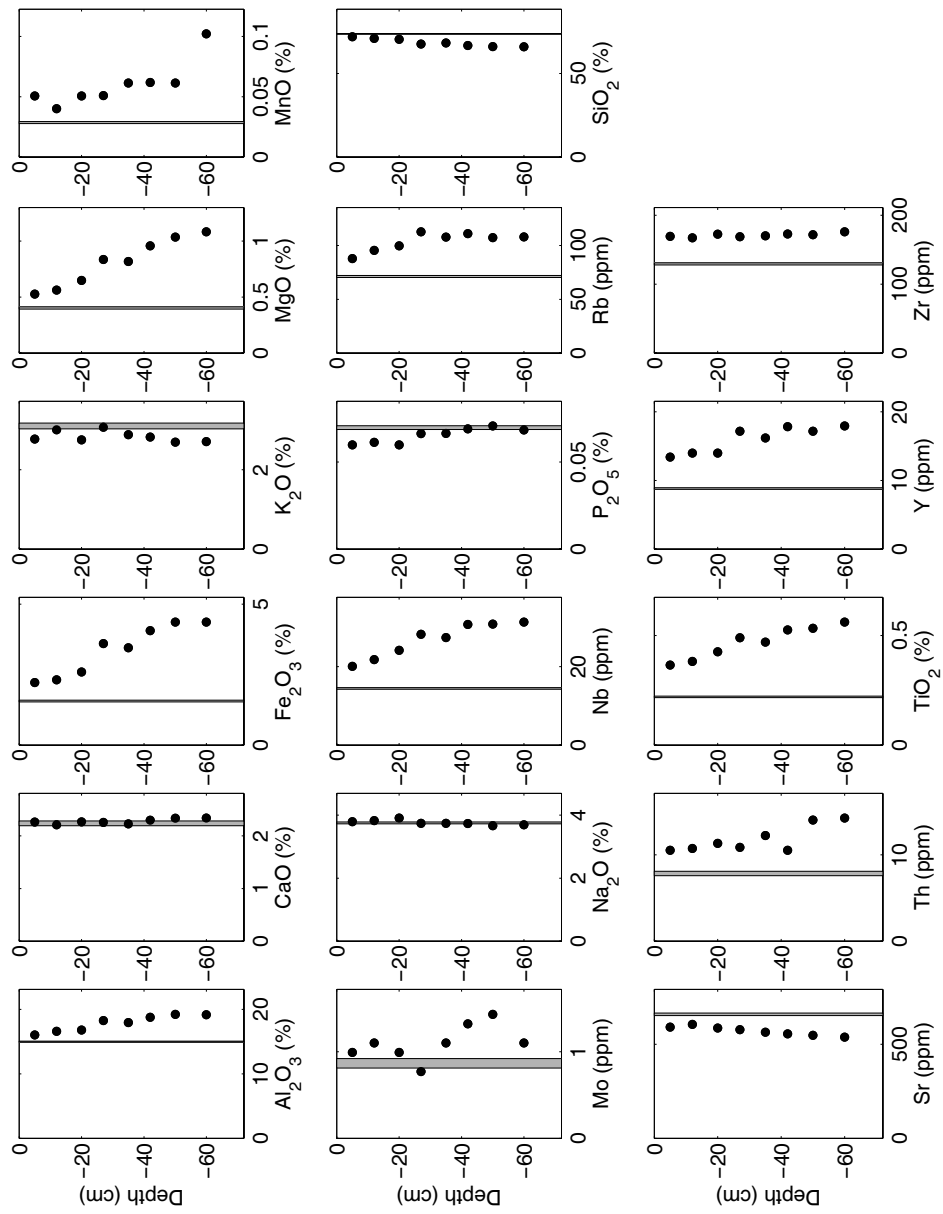


Figure C.10. Elemental concentrations in the soil profile at site P1062S. Solid circles represent soil samples and the gray box represents the average rock outcrop composition (mean and s.e.).

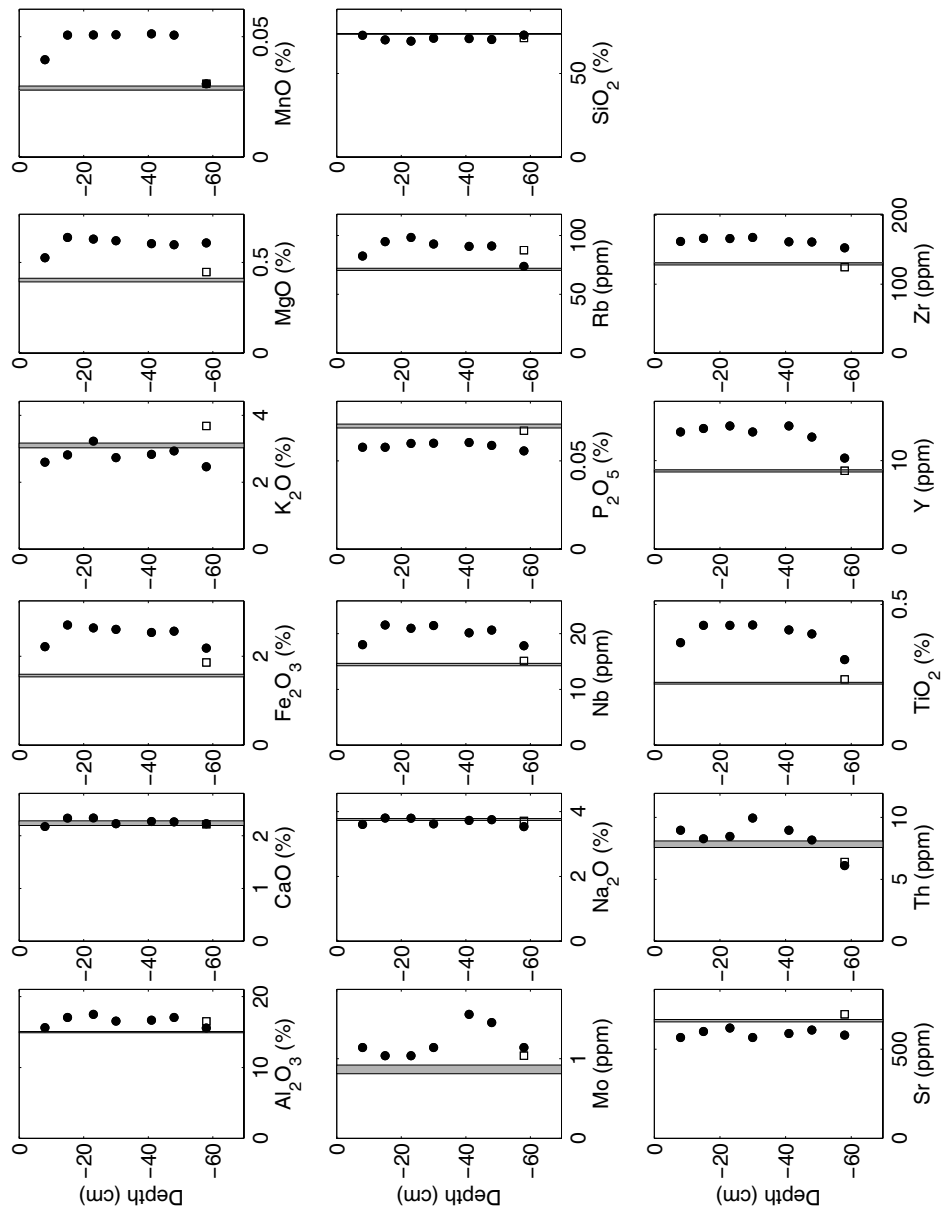


Figure C.11. Elemental concentrations in the soil profile at site P1062N. Solid circles represent soil samples, open squares represent saprolite samples, and the gray box represents the average rock outcrop composition (mean and s.e.).

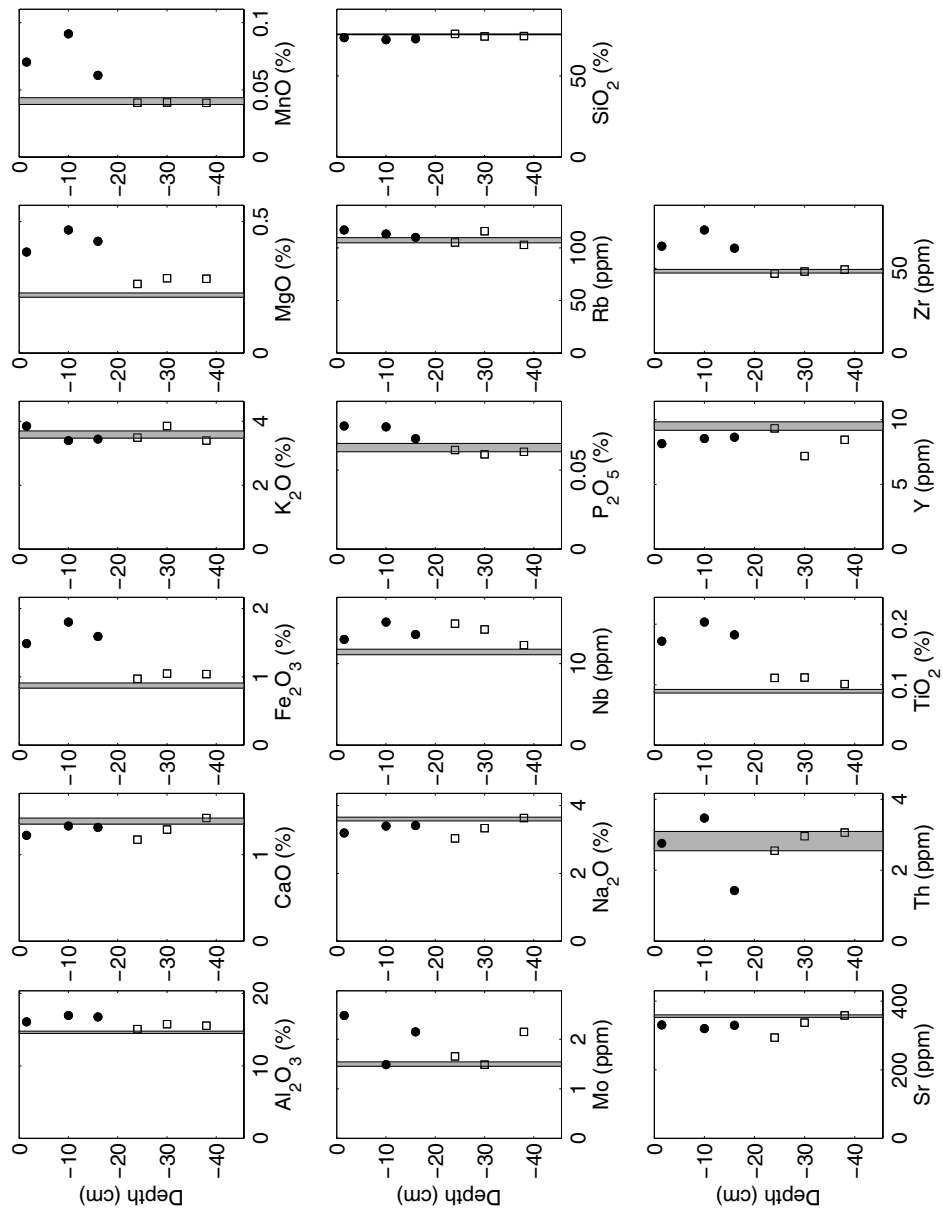


Figure C.12. Elemental concentrations in the soil profile at site T2364. Solid circles represent soil samples, open squares represent saprolite samples, and the gray box represents the average rock outcrop composition (mean and s.e.).

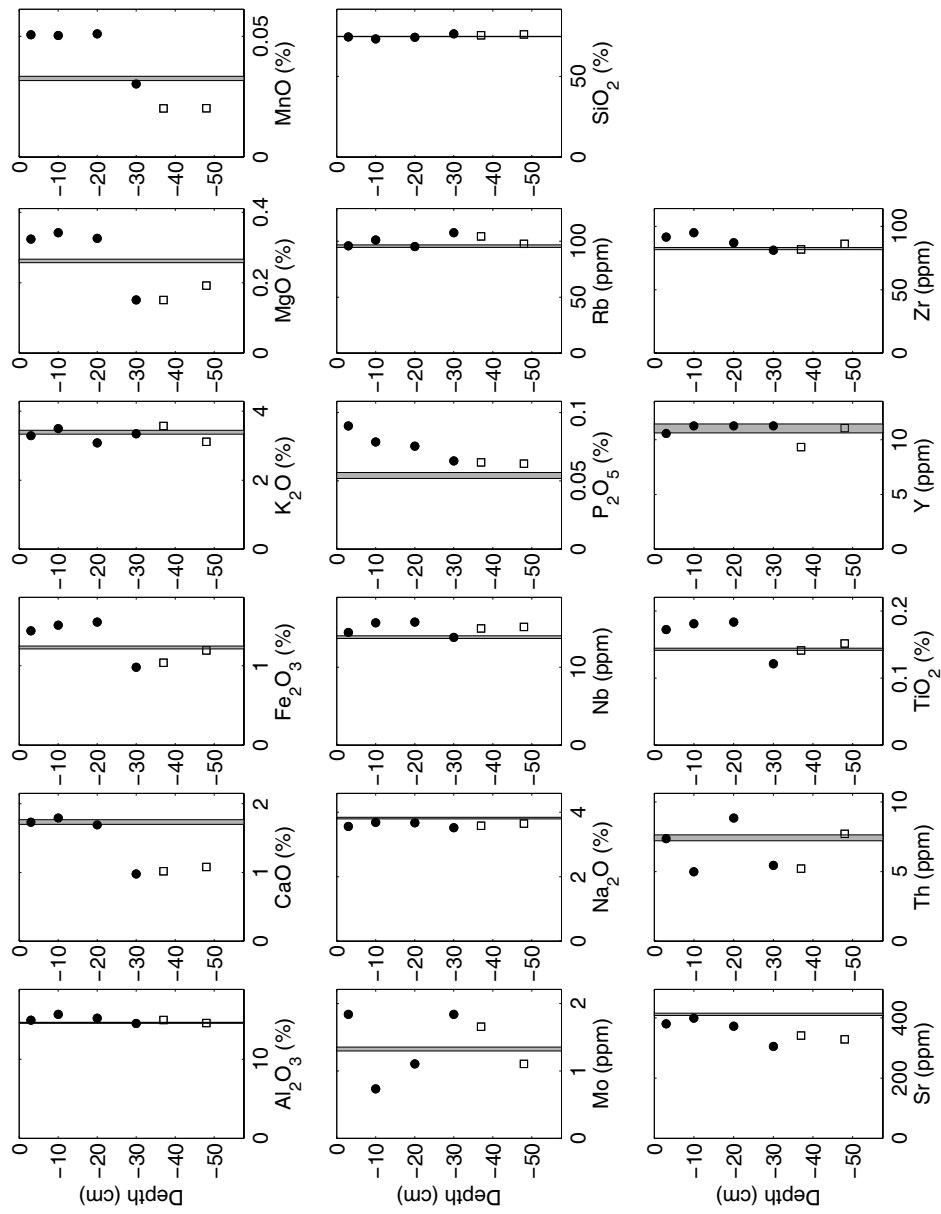


Figure C.13. Elemental concentrations in the soil profile at site T2073. Solid circles represent soil samples, open squares represent saprolite samples, and the gray box represents the average rock outcrop composition (mean and s.e.).

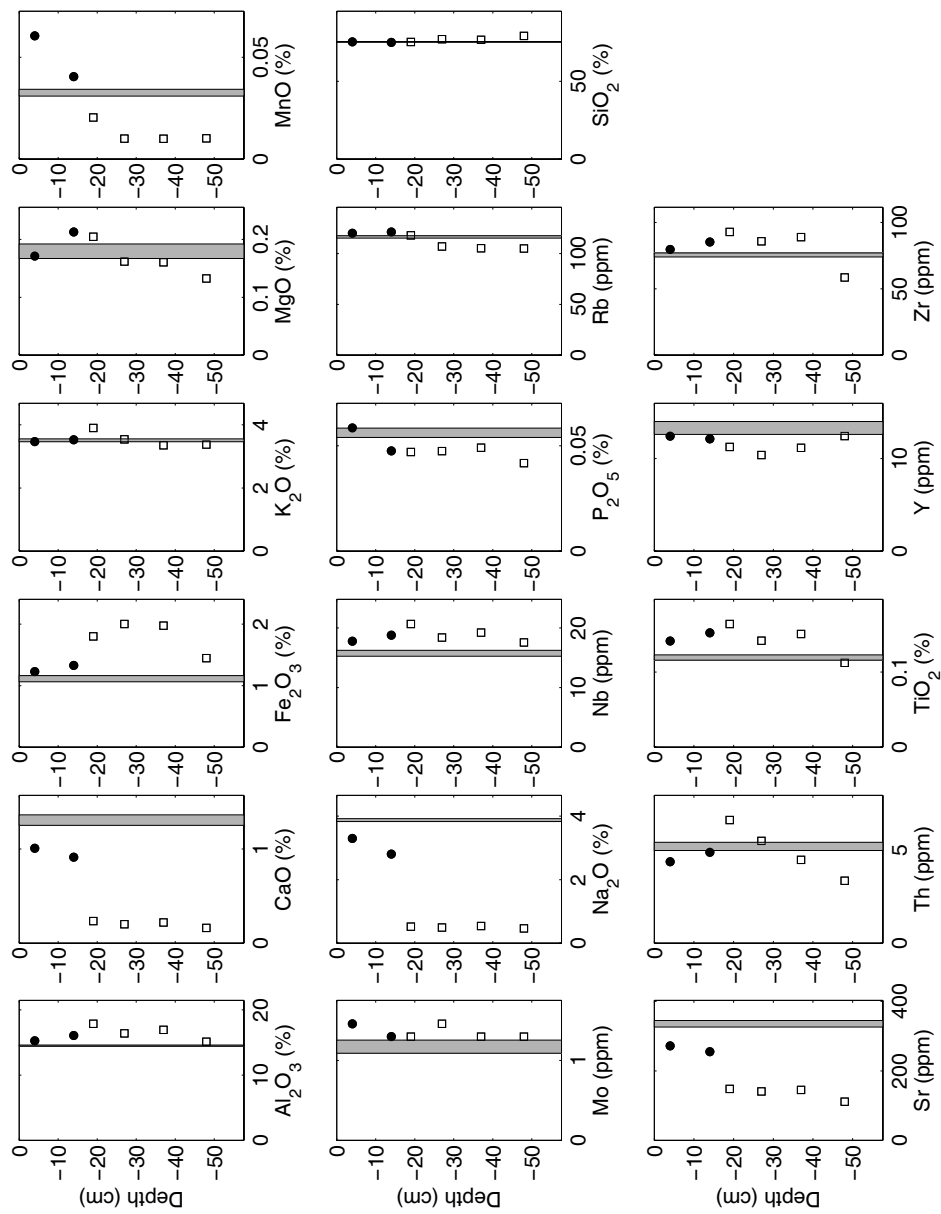


Figure C.14. Elemental concentrations in the soil profile at site T1755. Solid circles represent soil samples, open squares represent saprolite samples, and the gray box represents the average rock outcrop composition (mean and s.e.).

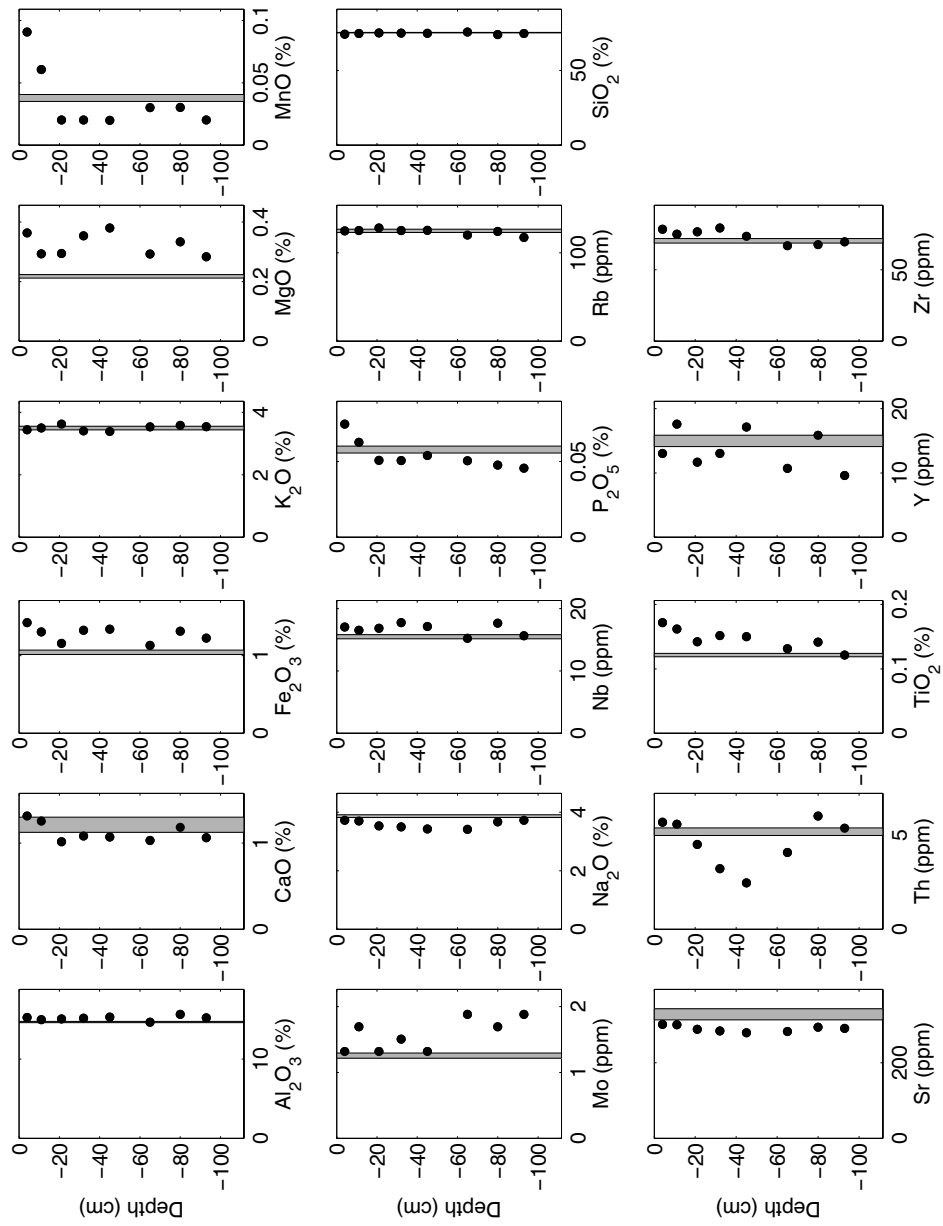


Figure C.15. Elemental concentrations in the soil profile at site T1508. Solid circles represent soil samples and the gray box represents the average rock outcrop composition (mean and s.e.).

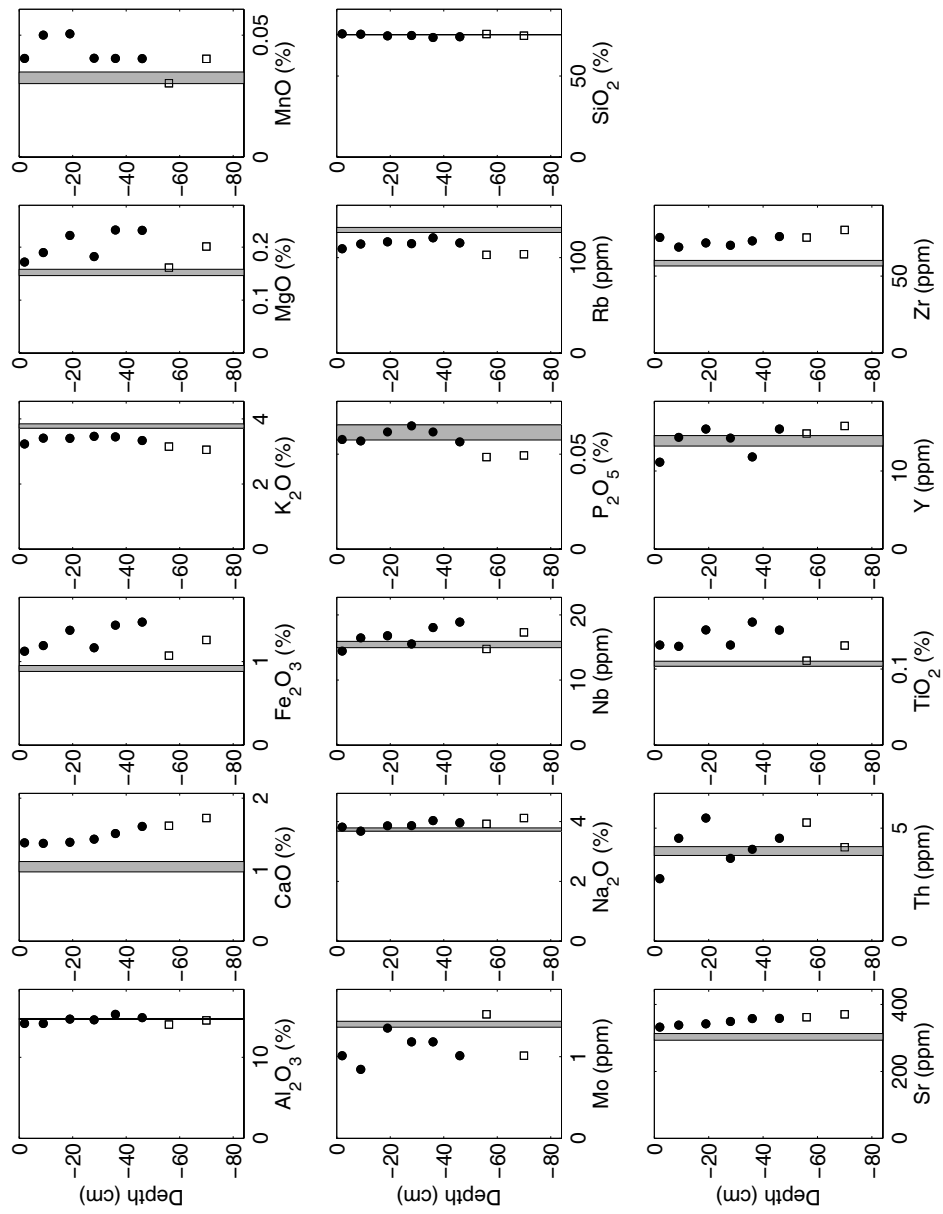


Figure C.16. Elemental concentrations in the soil profile at site T1294. Solid circles represent soil samples, open squares represent saprolite samples, and the gray box represents the average rock composition (mean and s.e.).

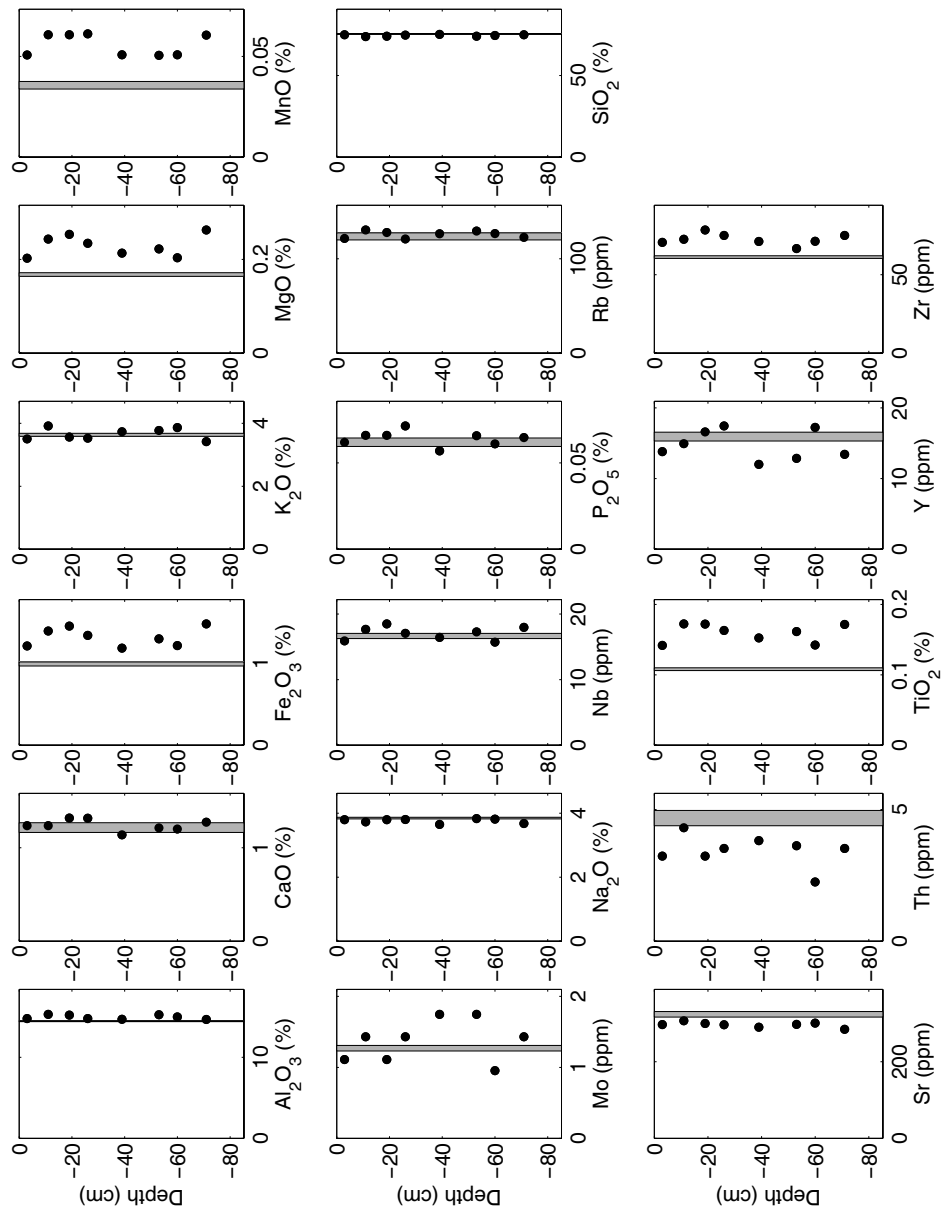


Figure C.17. Elemental concentrations in the soil profile at site T1084. Solid circles represent soil samples and the gray box represents the average rock outcrop composition (mean and s.e.).

Appendix D

Soil climate records at Pilot Peak and Tailholt Mountain, Idaho

In this appendix we present the soil climate time series measurements from which mean annual soil temperatures (MAST) and moisture indices were calculated. Calculating MAST at several of the sites required filling data gaps in the temperature records where the instruments succumbed to electrical failure, heat, or rodents. We filled these data gaps with temperature estimates based on correlations with soil temperatures at the nearest sites, as described below.

At Pilot Peak there are two sets of temperature data gaps over the two-year time interval for which we calculated MAST (8/1/2006-7/31/2008). The first set of gaps are in the first twelve or thirteen days of August 2006 at sites P2283S, P1471S, and P1062S. To fill these gaps, we used linear correlations between temperatures at these sites and their nearest neighbors (P2281N, P1485N, and P1062N, respectively) based on temperature measurements at these six sites during the remainder of August 2006. These gaps are short (<2 weeks) relative to the two-year time interval over which we calculated MAST for Pilot Peak, and thus the manner in which we filled these data gaps had a negligible effect on calculated MAST values.

The second set of data gaps at sites P1471S and P1485N is in July-October 2006, during which soil temperatures declined at a near-linear rate at the sites nearest P1471S and P1485N. To fill these gaps, we calculated soil temperatures at P1471S and P1485N as a multivariate linear function of the soil temperatures at their nearest neighbors (P1706, P1277S, and P1264N). These functions are based on the July-October soil temperatures at P1471S, P1485N, P1706, P1277S, and P1264N in 2005, 2006, and 2008.

At Tailholt Mountain, more than half of the sensors had major data gaps during the second year of monitoring. Rather than attempt to fill each of these long gaps with temperature estimates, we instead report MAST at Tailholt only for the first year of monitoring (10/1/2005-9/30/2006). Because site T1294 did not record any good data during the first year of monitoring, we assume its MAST during this year is 1.45 °C lower

than the MAST of the nearest site (T1084), as was the case during the second year of monitoring when both T1294 and T1084 recorded good temperature data.

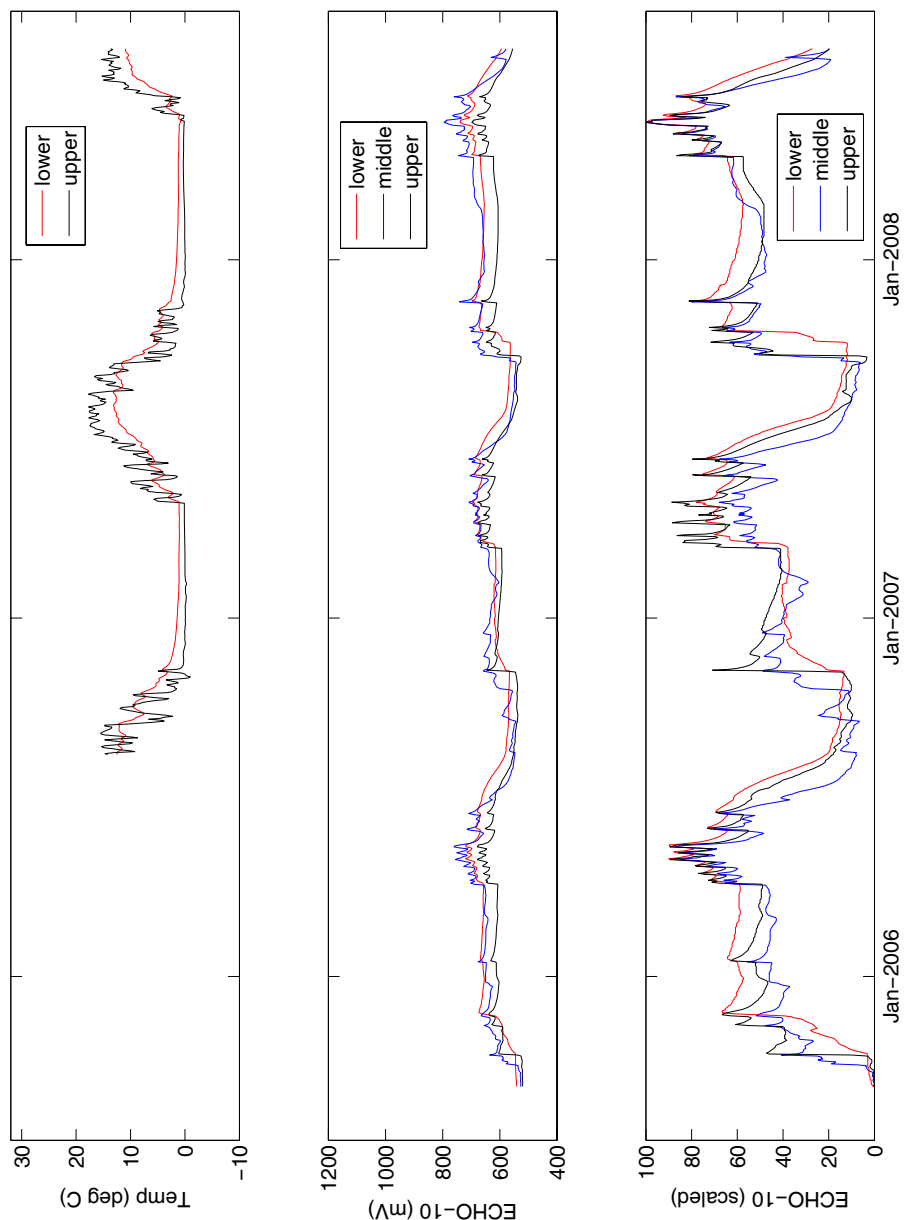


Figure D.1. P2283S soil climates. The middle graph shows the ECHO-10 measurements in mV, a proxy for soil moisture, and the lower graph shows the same ECHO-10 readings rescaled such that the minimum value of each is 0 and maximum value 100. All values are daily averages.

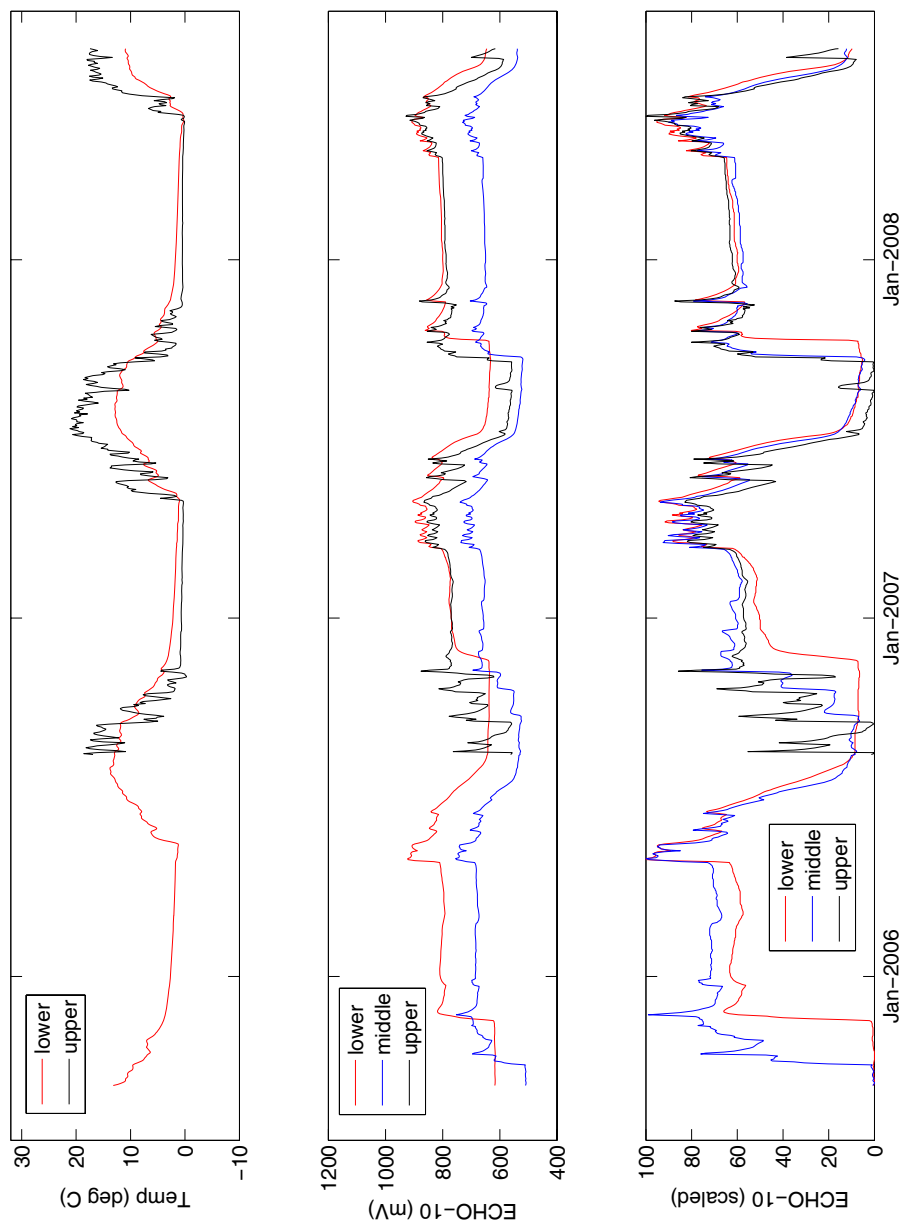


Figure D.2. P2281N soil climates. The middle graph shows the ECHO-10 measurements in mV, a proxy for soil moisture, and the lower graph shows the same ECHO-10 readings rescaled such that the minimum value of each is 0 and maximum value 100. All values are daily averages.

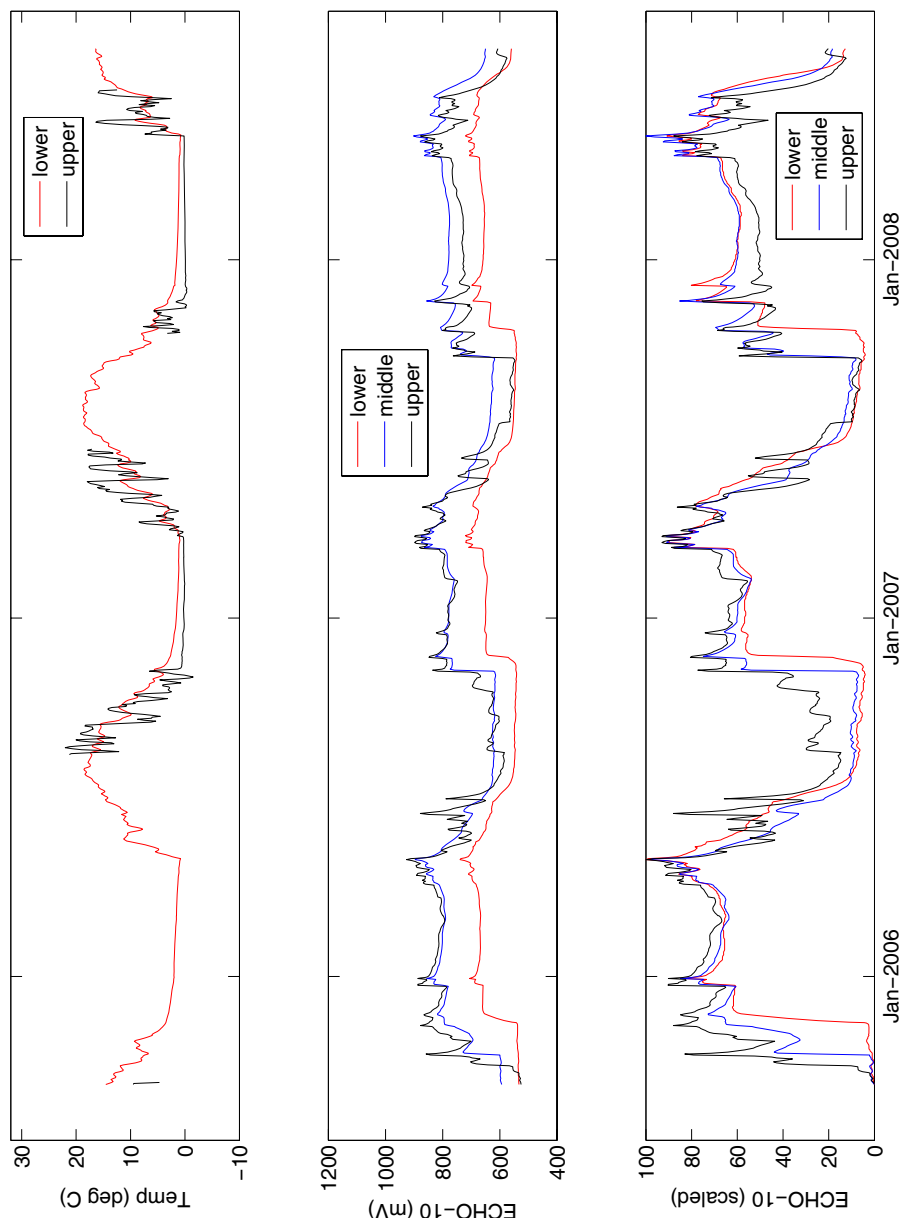


Figure D.3. P2090 soil climates. The middle graph shows the ECHO-10 measurements in mV, a proxy for soil moisture, and the lower graph shows the same ECHO-10 readings rescaled such that the minimum value of each is 0 and maximum value 100. All values are daily averages.

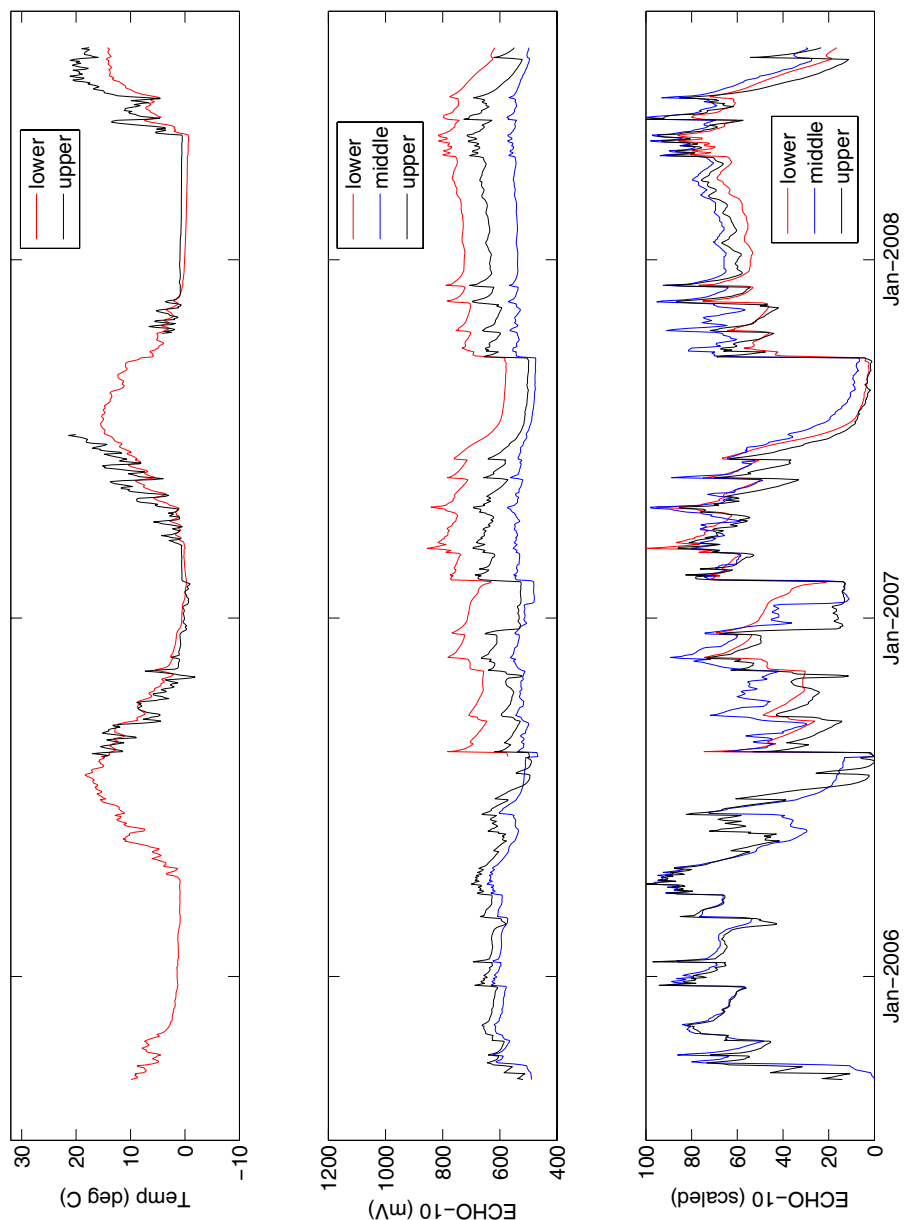


Figure D.4. P1850 soil climates. The middle graph shows the ECHO-10 measurements in mV, a proxy for soil moisture, and the lower graph shows the same ECHO-10 readings rescaled such that the minimum value of each is 0 and maximum value 100. All values are daily averages.

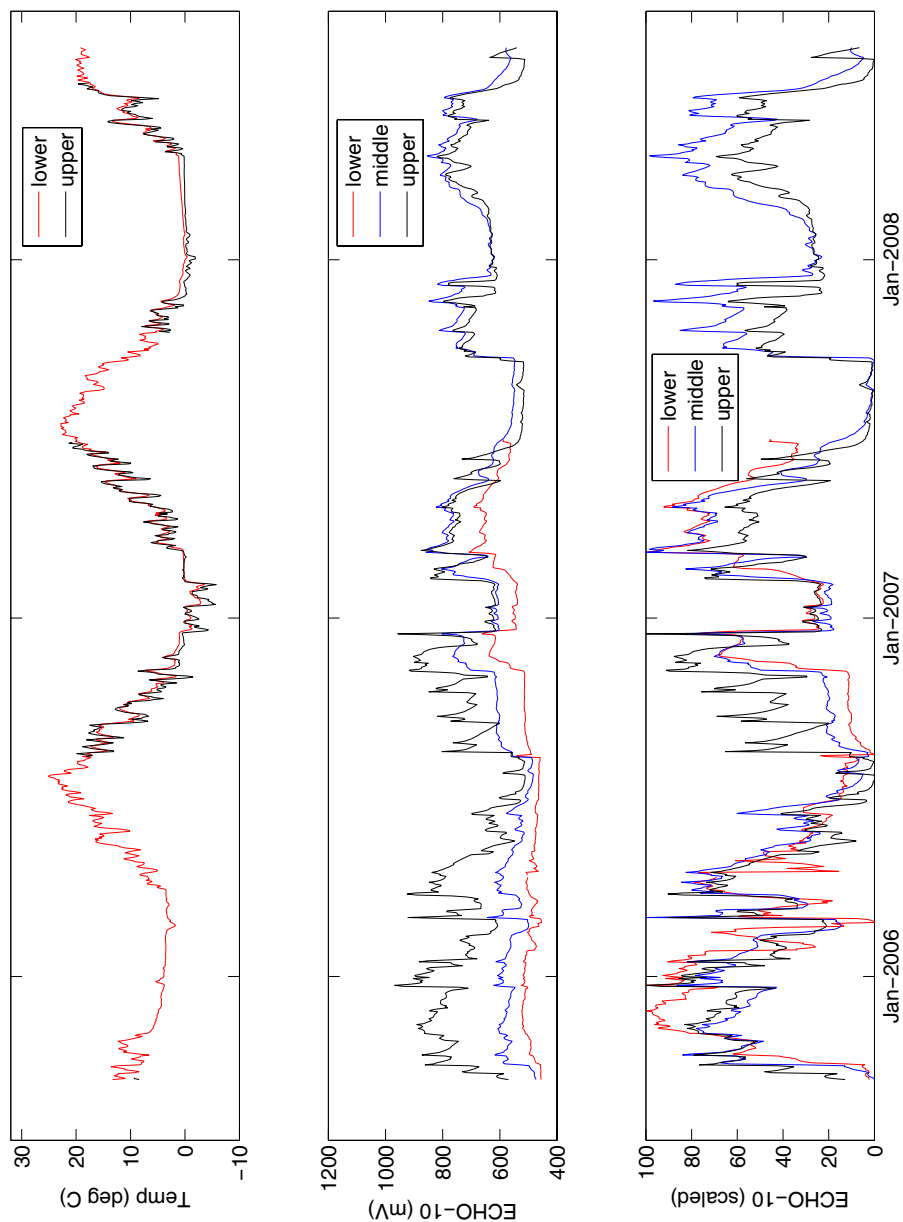


Figure D.5. P1706 soil climates. The middle graph shows the ECHO-10 measurements in mV, a proxy for soil moisture, and the lower graph shows the same ECHO-10 readings rescaled such that the minimum value of each is 0 and maximum value 100. All values are daily averages.

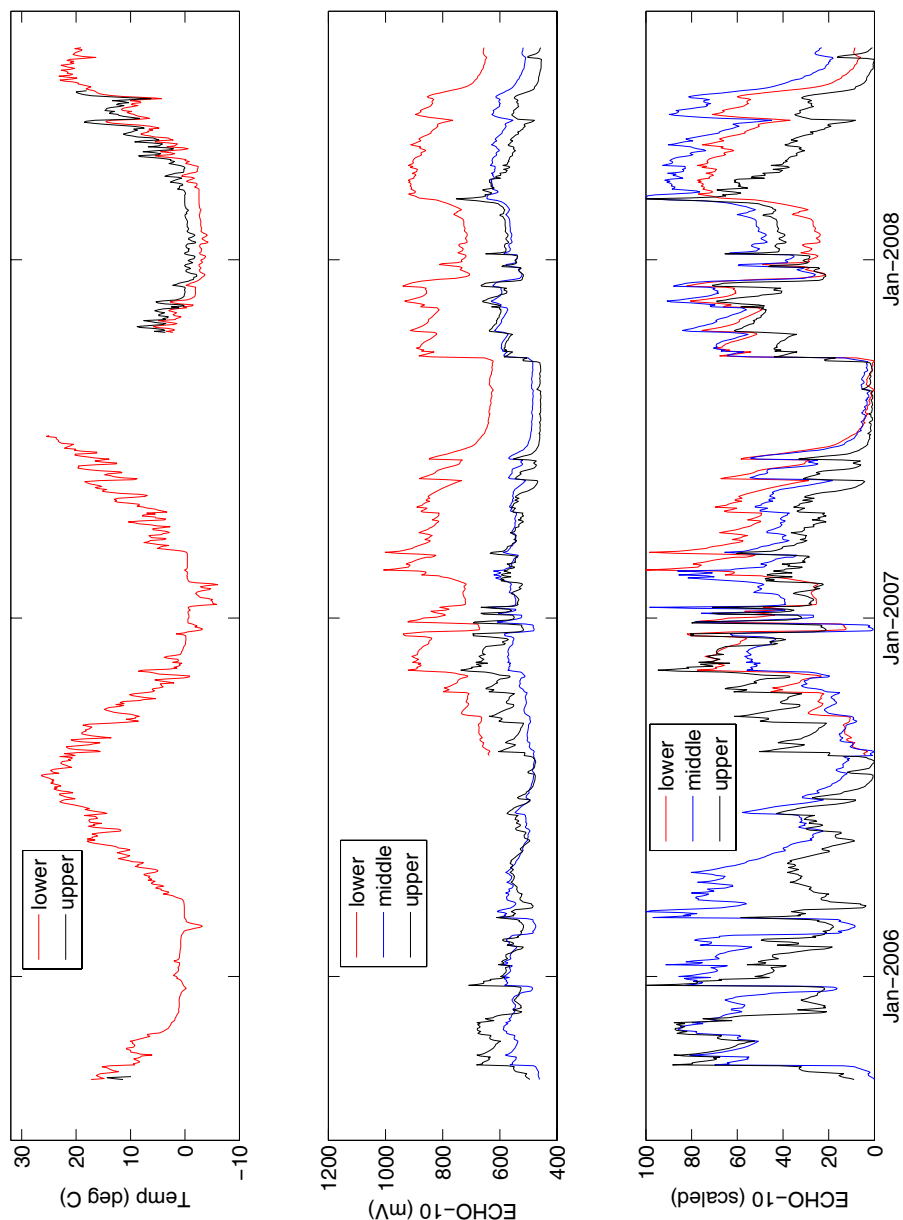


Figure D.6. P1485N soil climates. The middle graph shows the ECHO-10 measurements in mV, a proxy for soil moisture, and the lower graph shows the same ECHO-10 readings rescaled such that the minimum value of each is 0 and maximum value 100. All values are daily averages.

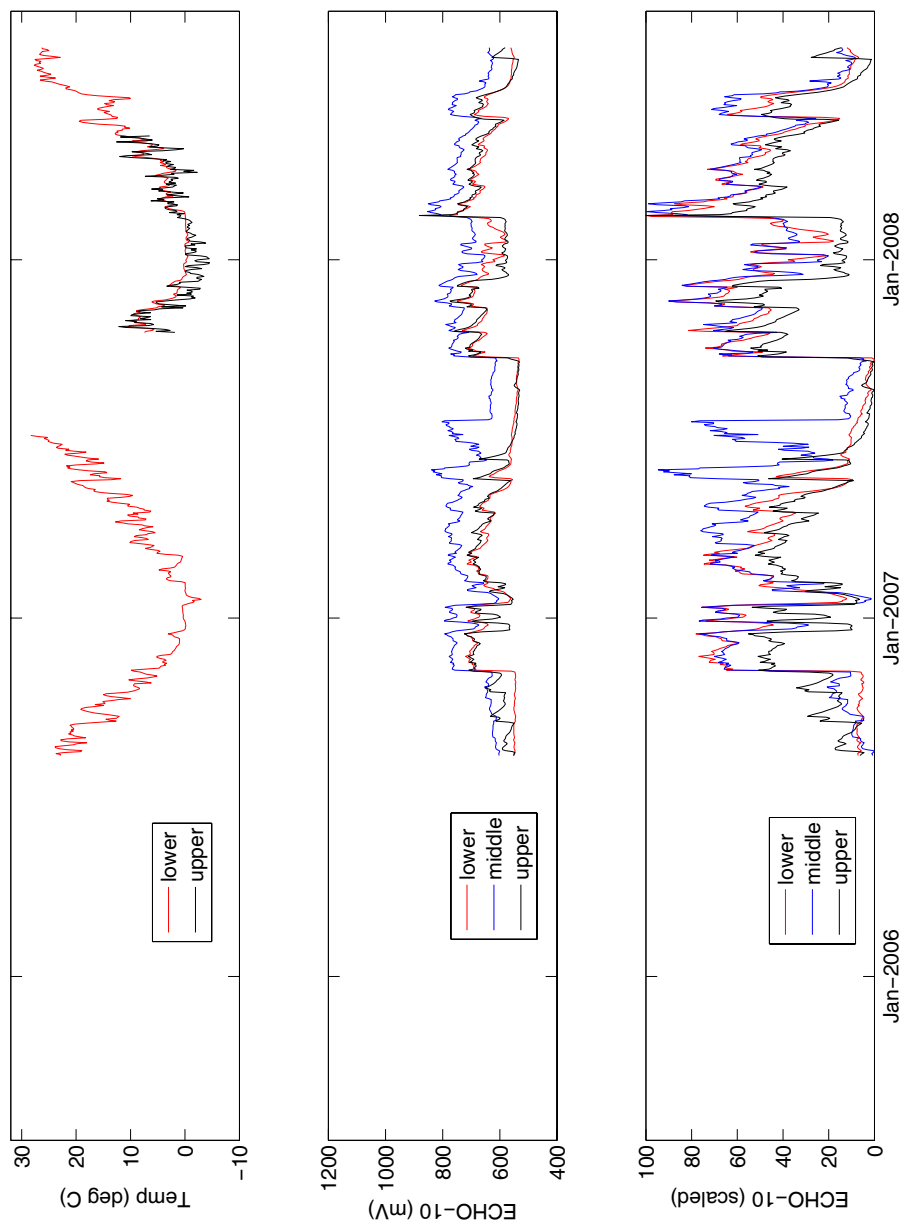


Figure D.7. P1471S soil climates. The middle graph shows the ECHO-10 measurements in mV, a proxy for soil moisture, and the lower graph shows the same ECHO-10 readings rescaled such that the minimum value of each is 0 and maximum value 100. All values are daily averages.

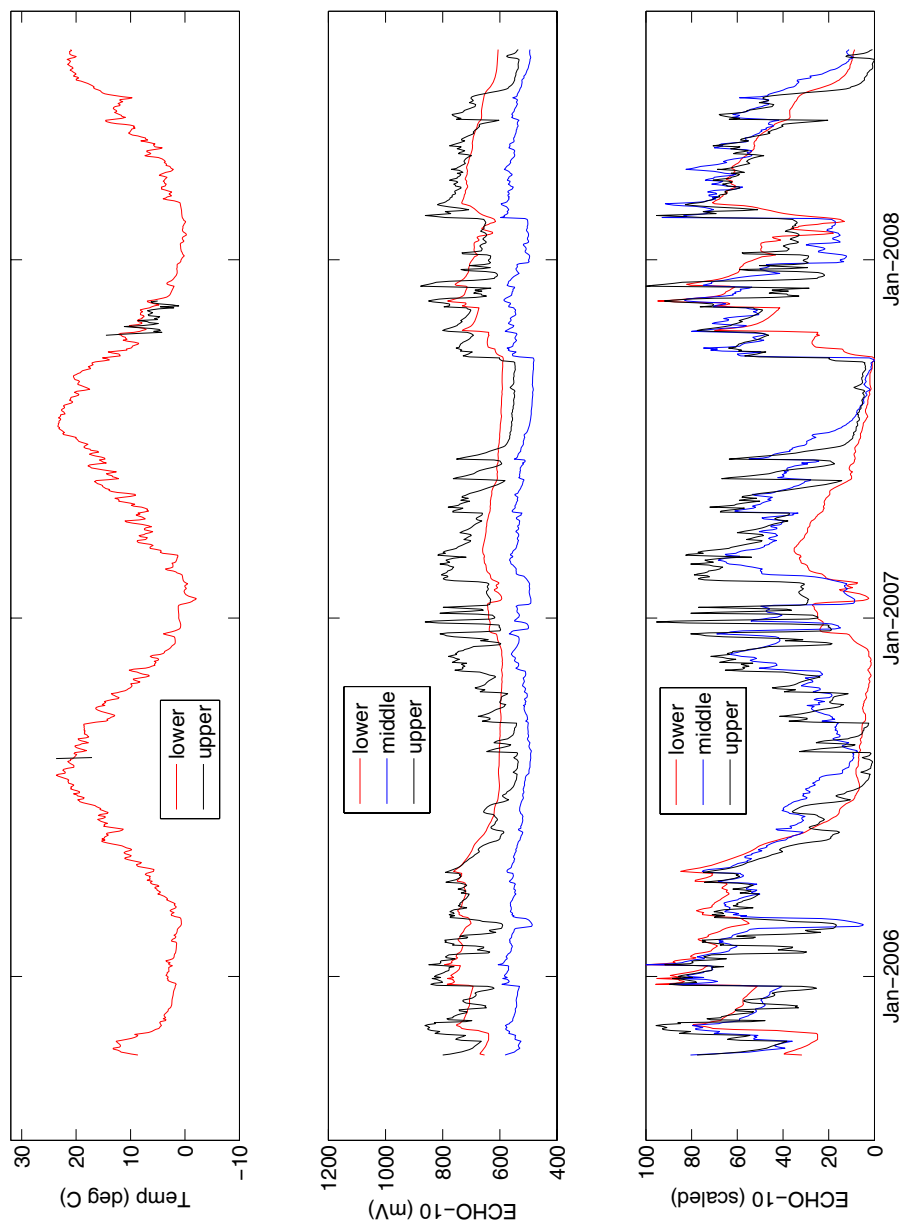


Figure D.8. P1277S soil climates. The middle graph shows the ECHO-10 measurements in mV, a proxy for soil moisture, and the lower graph shows the same ECHO-10 readings rescaled such that the minimum value of each is 0 and maximum value 100. All values are daily averages.

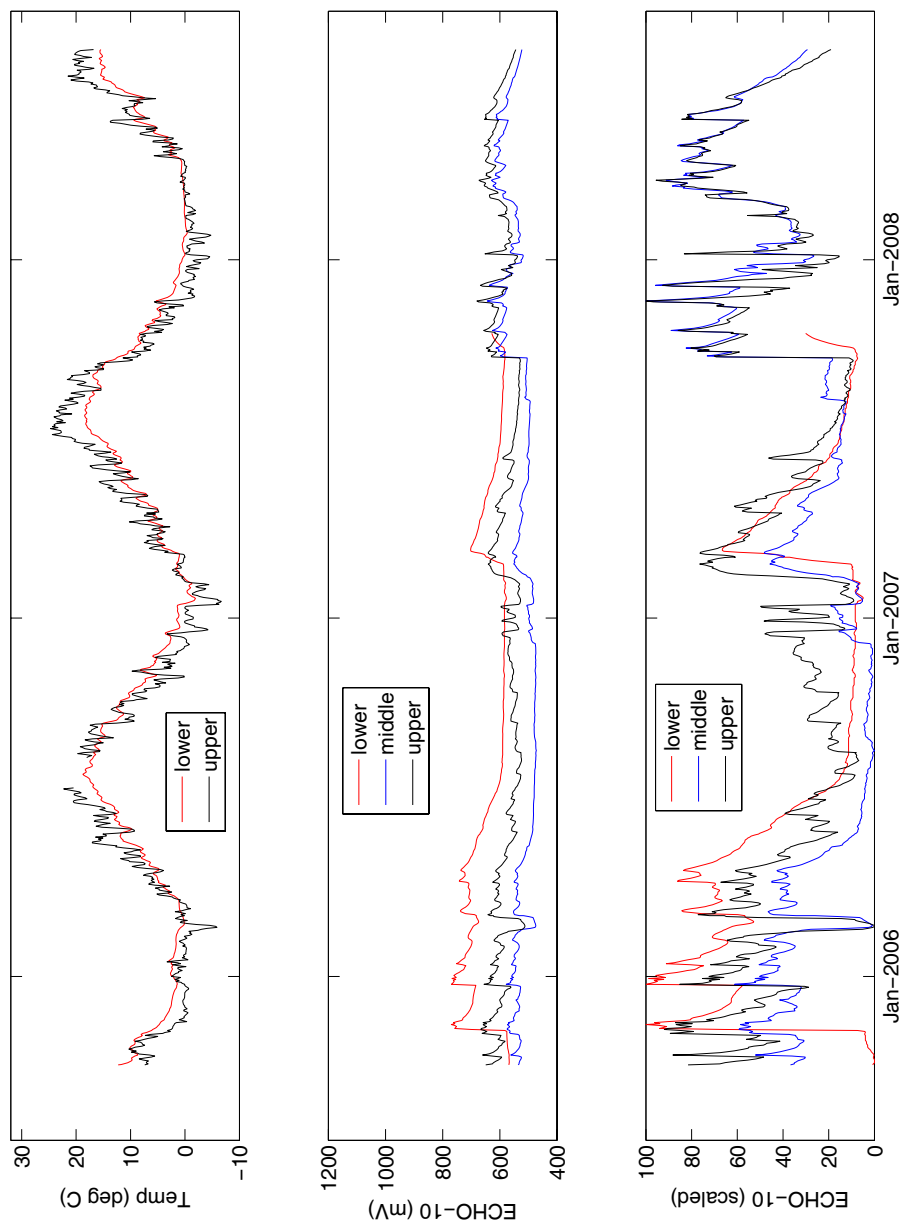


Figure D.9. P1264N soil climates. The middle graph shows the ECHO-10 measurements in mV, a proxy for soil moisture, and the lower graph shows the same ECHO-10 readings rescaled such that the minimum value of each is 0 and maximum value 100. All values are daily averages.

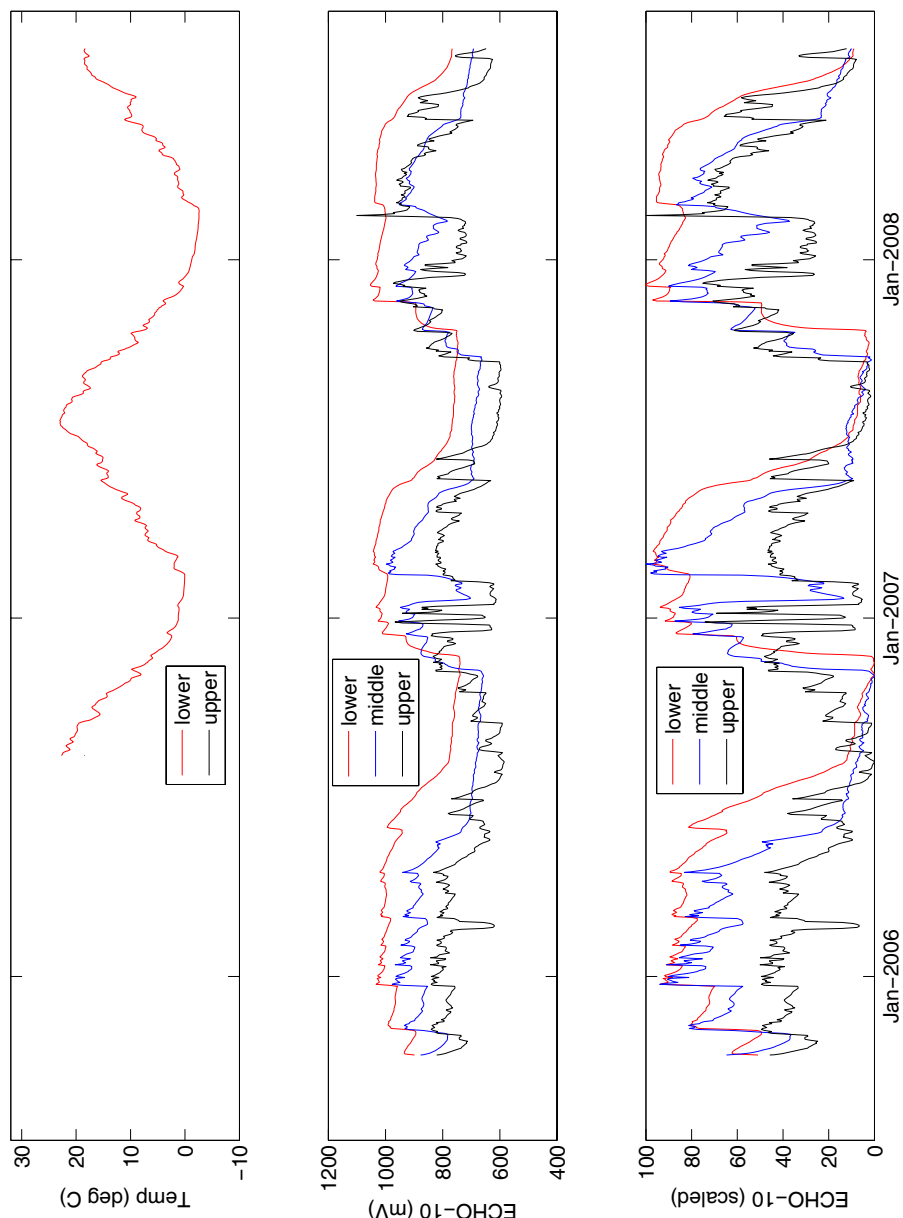


Figure D.10. P1062S soil climates. The middle graph shows the ECHO-10 measurements in mV, a proxy for soil moisture, and the lower graph shows the same ECHO-10 readings rescaled such that the minimum value of each is 0 and maximum value 100. All values are daily averages.

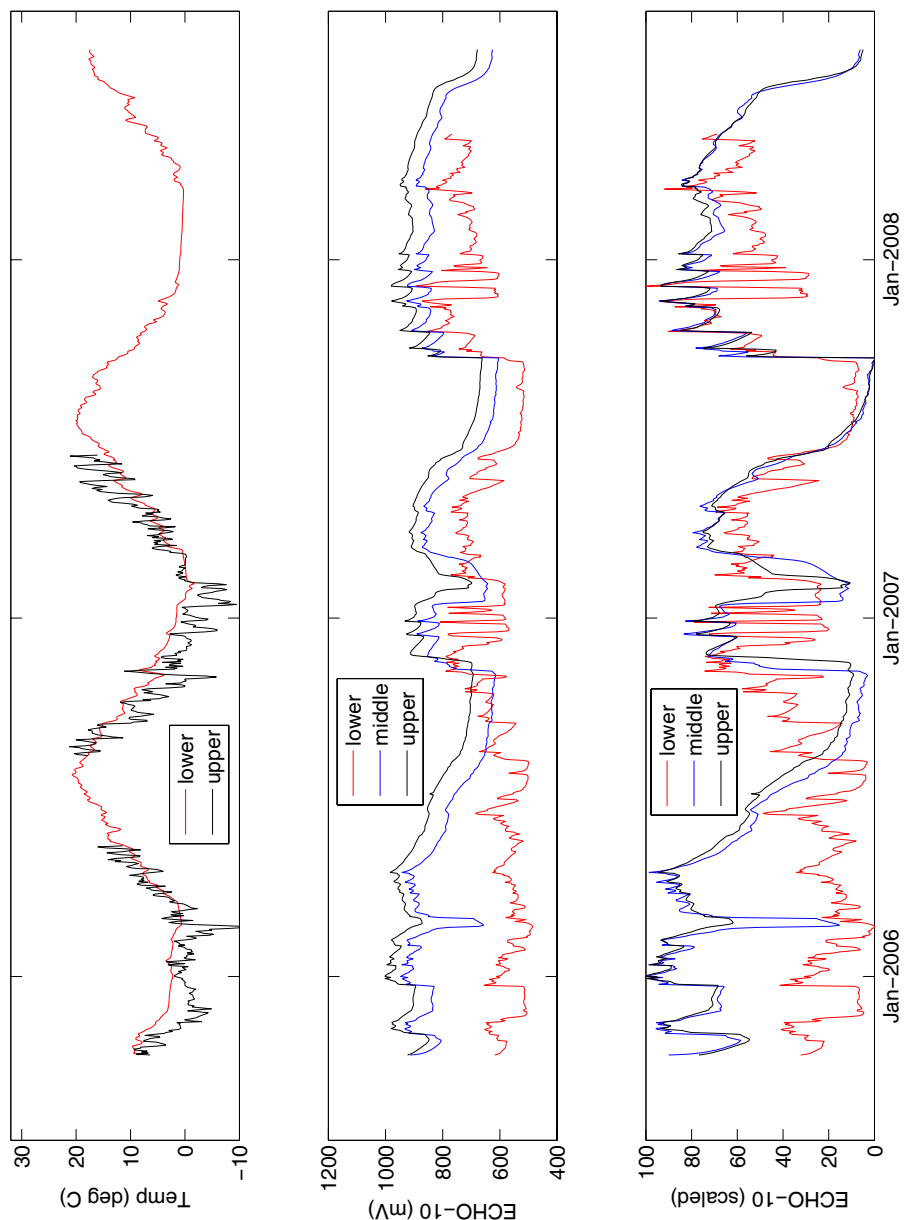


Figure D.11. P1062N soil climates. The middle graph shows the ECHO-10 measurements in mV, a proxy for soil moisture, and the lower graph shows the same ECHO-10 readings rescaled such that the minimum value of each is 0 and maximum value 100. All values are daily averages.

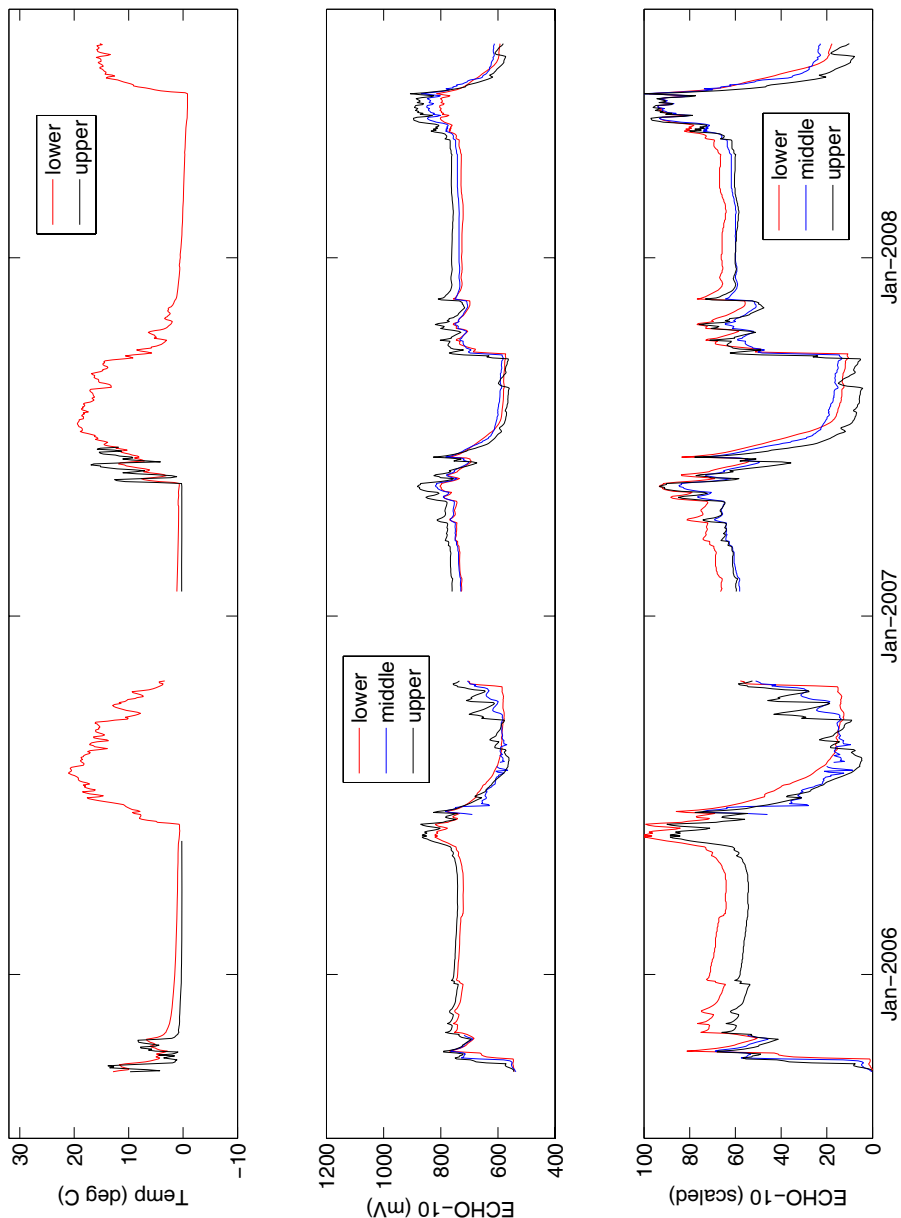


Figure D.12. T2364 soil climates. The middle graph shows the ECHO-10 measurements in mV, a proxy for soil moisture, and the lower graph shows the same ECHO-10 readings rescaled such that the minimum value of each is 0 and maximum value 100.

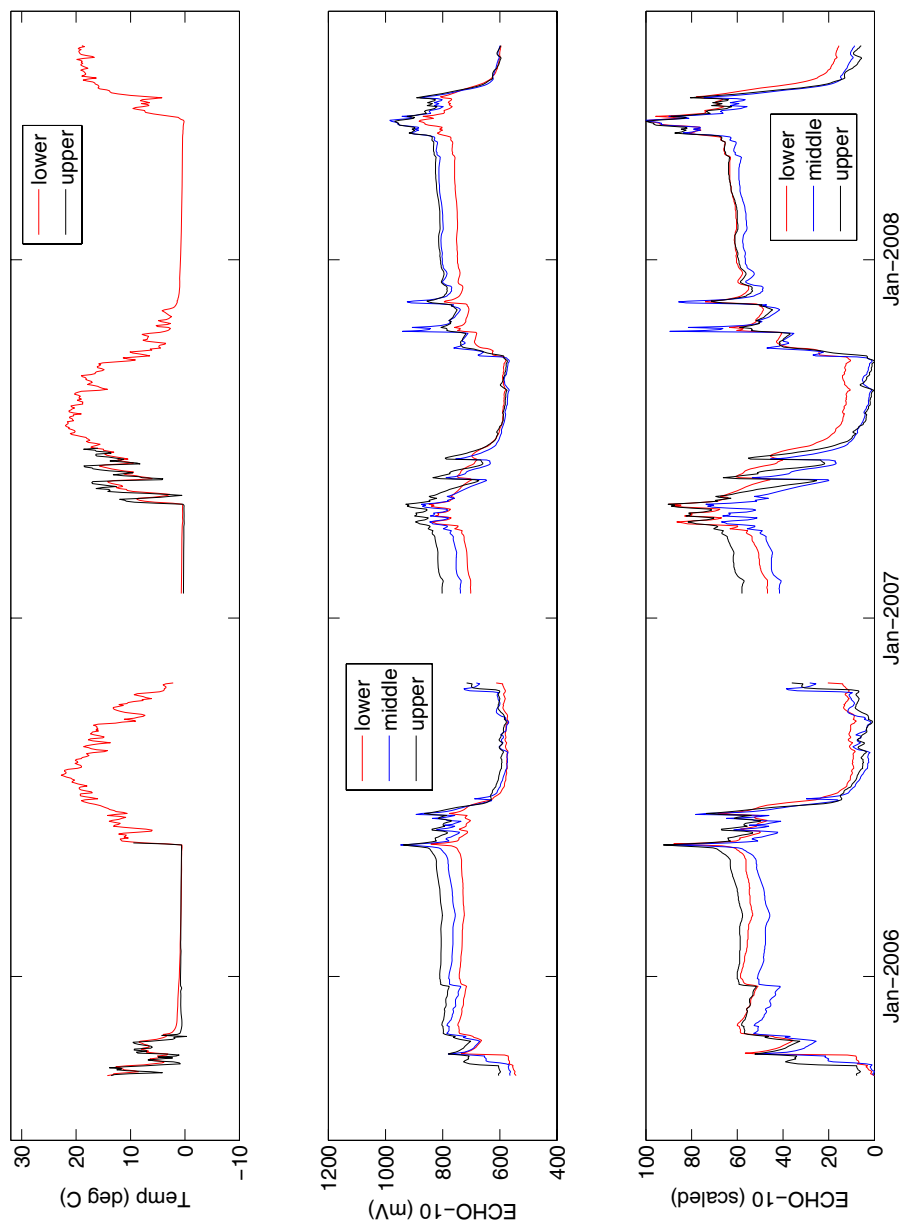


Figure D.13. T2073 soil climates. The middle graph shows the ECHO-10 measurements in mV, a proxy for soil moisture, and the lower graph shows the same ECHO-10 readings rescaled such that the minimum value of each is 0 and maximum value 100. All values are daily averages.

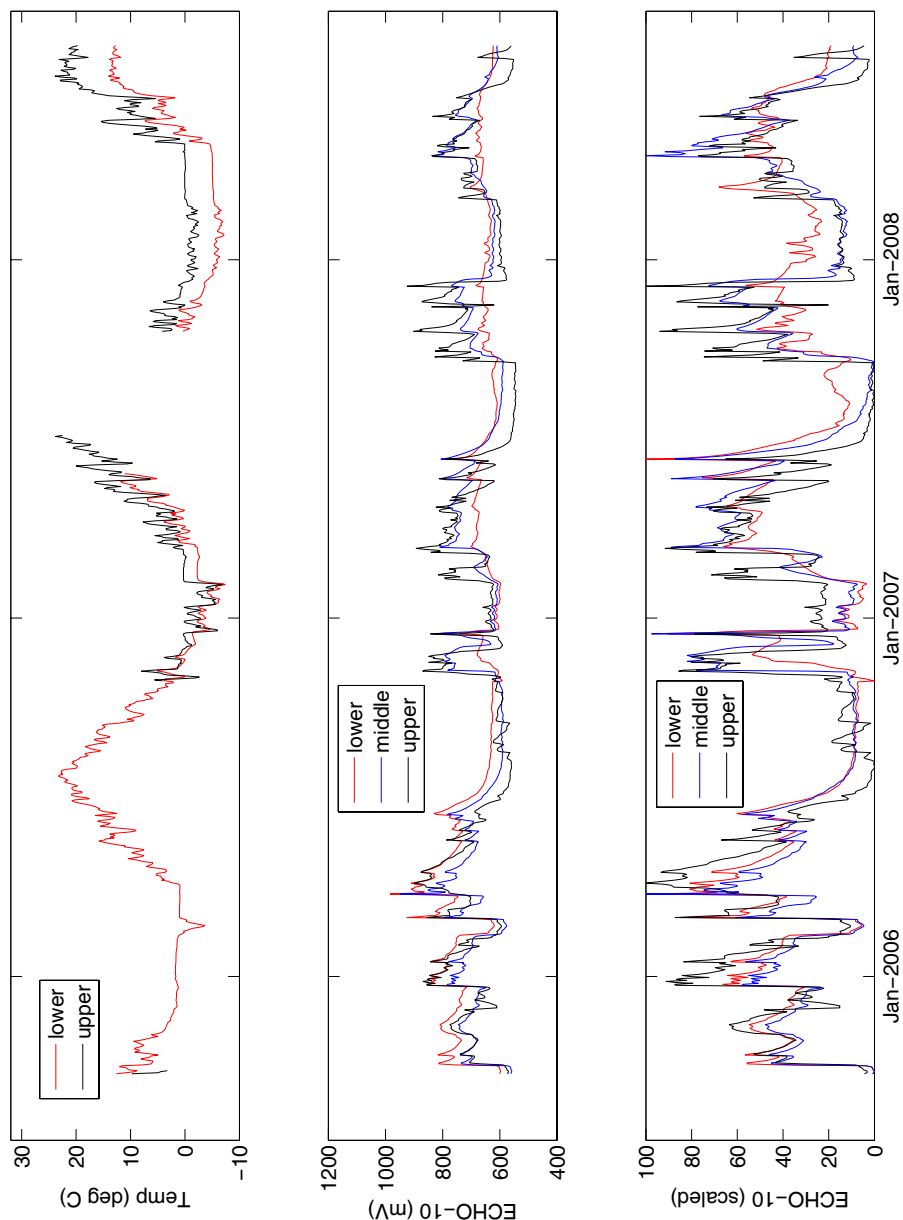


Figure D.14. T1755 soil climates. The middle graph shows the ECHO-10 measurements in mV, a proxy for soil moisture, and the lower graph shows the same ECHO-10 readings rescaled such that the minimum value of each is 0 and maximum value 100. All values are daily averages.

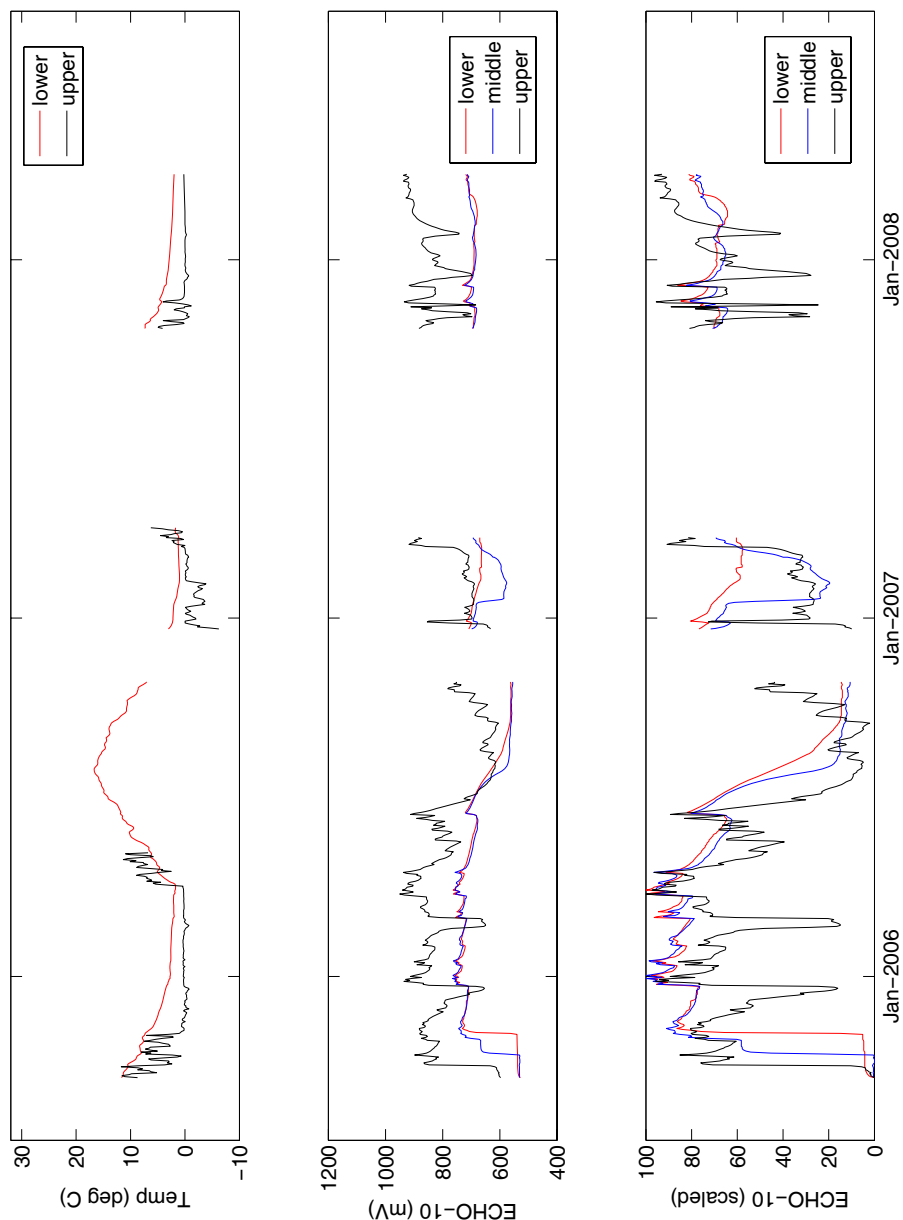


Figure D.15. T1508 soil climates. The middle graph shows the ECHO-10 measurements in mV, a proxy for soil moisture, and the lower graph shows the same ECHO-10 readings rescaled such that the minimum value of each is 0 and maximum value 100. All values are daily averages.

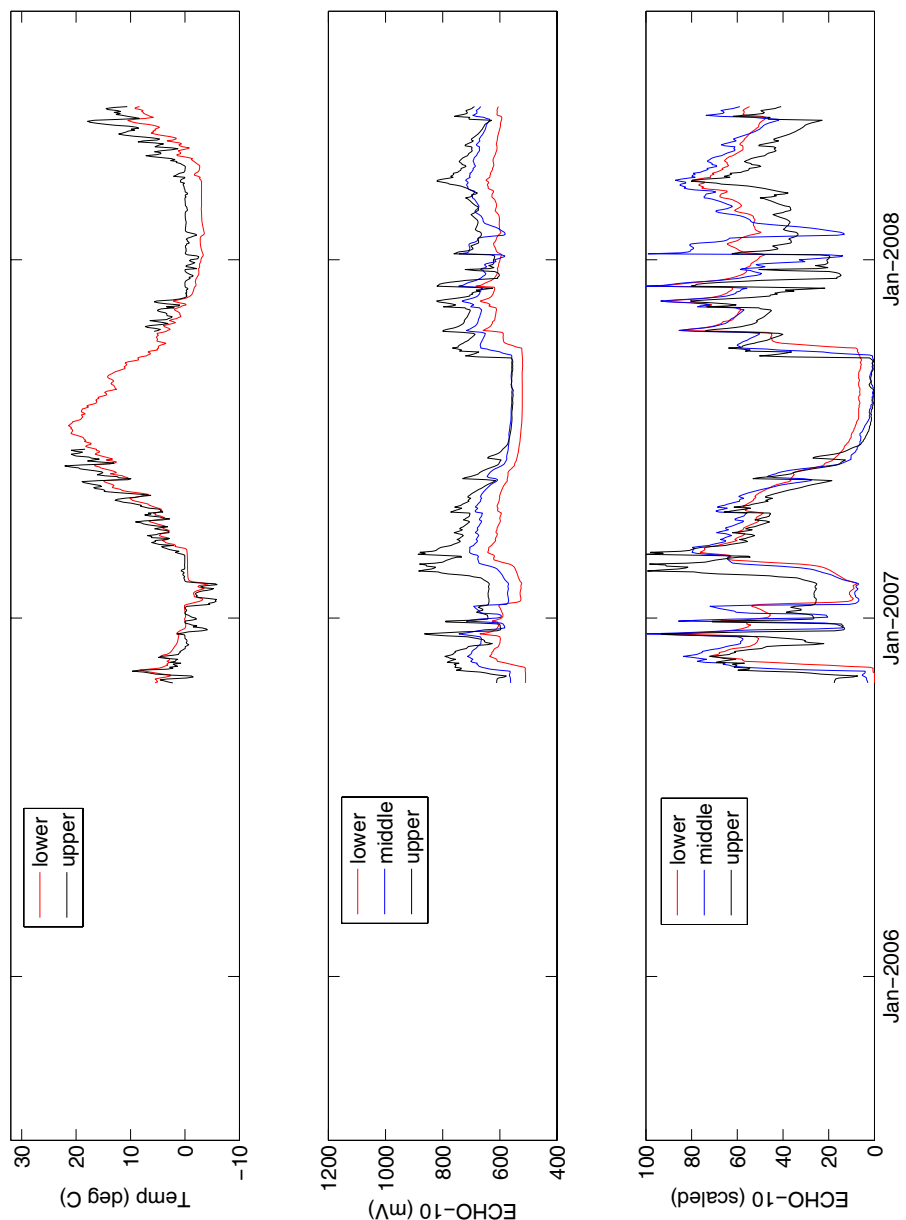


Figure D.16. T1294 soil climates. The middle graph shows the ECHO-10 measurements in mV, a proxy for soil moisture, and the lower graph shows the same ECHO-10 readings rescaled such that the minimum value of each is 0 and maximum value 100. All values are daily averages.

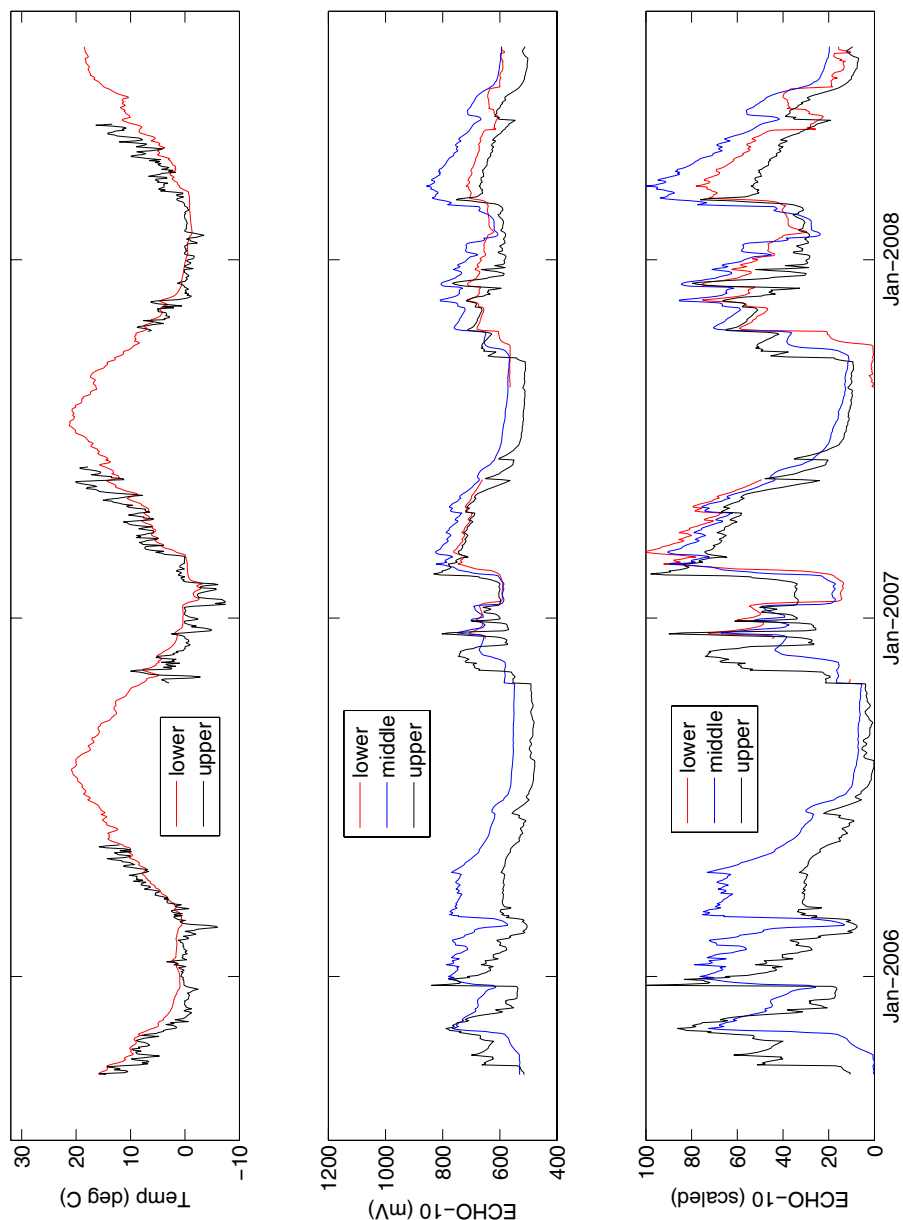


Figure D.17. T1084 soil climates. The middle graph shows the ECHO-10 measurements in mV, a proxy for soil moisture, and the lower graph shows the same ECHO-10 readings rescaled such that the minimum value of each is 0 and maximum value 100. All values are daily averages.

Appendix E

Photographs of field sites at Pilot Peak and Tailholt Mountain, Idaho

At each of our seventeen field sites on Pilot Peak and Tailholt Mountain, we collected soil samples from small soil plots (no larger than 10 meters by 10 meters in size). To give a sense for the local setting at each site, in this appendix we show photographs of each site, and in each photograph we outline the area from which soils were sampled. In almost every photo, Michael Ferrier (approximately 187 cm when erect) is present for scale.



Figure E.1. Photograph of site P2283S, at $45^{\circ}10.263'$ N, $115^{\circ}31.869'$ W, and 2283 m. Soil sampling plot is outlined in red, and is approximately 43-48 m from the ridge in the direction of steepest ascent.



Figure E.2. Photograph of site P2281N, at $45^{\circ}10.270'$ N, $115^{\circ}31.895'$ W, and 2281 m. Soil sampling plot is outlined in red, and is approximately 30-40 m from the ridge in the direction of steepest ascent.



Figure E.3. Photograph of site P2090, at $45^{\circ}10.156'$ N, $115^{\circ}32.234'$ W, and 2090 m. Soil sampling plot is outlined in red, and is approximately 40-46 m from the ridge in the direction of steepest ascent.



Figure E.4. Photograph of site P1850, at $45^{\circ}09.867'$ N, $115^{\circ}32.882'$ W, and 1850 m. Soil sampling plot is outlined in red, and is approximately 2-9 m from the ridge in the direction of steepest ascent.



Figure E.5. Photograph of site P1706, at $45^{\circ}09.675'$ N, $115^{\circ}33.620'$ W, and 1706 m. Soil sampling plot is outlined in red, and is approximately 10-16 m from the ridge in the direction of steepest ascent.



Figure E.6. Photograph of site P1485N, at $45^{\circ}09.438'$ N, $115^{\circ}33.960'$ W, and 1485 m. Soil sampling plot is outlined in red, and is approximately 21-27 m from the ridge in the direction of steepest ascent.



Figure E.7. Photograph of site P1471S, at $45^{\circ}09.419'$ N, $115^{\circ}33.960'$ W, and 1471 m. Soil sampling plot is outlined in red, and is approximately 24-30 m from the ridge in the direction of steepest ascent.



Figure E.8. Photograph of site P1277S, at $45^{\circ}09.259'$ N, $115^{\circ}34.403'$ W, and 1277 m. Soil sampling plot is outlined in red, and is approximately 17-26 m from the ridge in the direction of steepest ascent.



Figure E.9. Photograph of site P1264N at $45^{\circ}09.276'$ N, $115^{\circ}34.406'$ W, and 1264 m. Soil sampling plot is outlined in red, and is approximately 9-18 m from the ridge in the direction of steepest ascent.



Figure E.10. Photograph of site P1062S at $45^{\circ}09.228'$ N, $115^{\circ}34.924'$ W, and 1062 m. Soil sampling plot is outlined in red, and is approximately 2-7 m from the ridge in the direction of steepest ascent.



Figure E.11. Photograph of site P1062N at $45^{\circ}09.238'$ N, $115^{\circ}34.949'$ W, and 1062 m. Soil sampling plot is outlined in red, and is approximately 2-6 m from the ridge in the direction of steepest ascent.



Figure E.12. Photograph of site T2364 at $45^{\circ}04.867'$ N, $115^{\circ}41.654'$ W, and 2364 m. Soil sampling plot is outlined in red, and is approximately 27-36 m from the summit of Tailholt Mountain in the direction of steepest ascent.



Figure E.13. Photograph of site T2073 at $45^{\circ}04.657'$ N, $115^{\circ}40.896'$ W, and 2073 m. Soil sampling plot is outlined in red, and is approximately 0-5 m from the ridge in the direction of steepest ascent.



Figure E.14. Photograph of site T1755 at $45^{\circ}03.688'$ N, $115^{\circ}39.095'$ W, and 1755 m. Soil sampling plot is outlined in red, and is approximately 5-11 m from the ridge in the direction of steepest ascent.



Figure E.15. Photograph of site T1508 at $45^{\circ}03.632'$ N, $115^{\circ}38.651'$ W, and 1508 m. Soil sampling plot is outlined in red, and is approximately 1-8 m from the ridge in the direction of steepest ascent.



Figure E.16. Photograph of site T1294 at $45^{\circ}03.674'$ N, $115^{\circ}38.226'$ W, and 1294 m. Soil sampling plot is outlined in red, and is located within a long, roughly planar hillslope.



Figure E.17. Photograph of site T1084 at $45^{\circ}03.682'$ N, $115^{\circ}38.016'$ W, and 1084 m. Soil sampling plot is 6-12 m upslope of the person in this photograph, and is near the base of a long, roughly planar hillslope.

Appendix F

Chemical composition of rock and soil samples at Pilot Peak and Tailholt Mountain, Idaho

Rock and soil samples from Pilot Peak and Tailholt Mountain, Idaho, were prepared for chemical analysis by X-ray fluorescence by standard procedures (Riebe, 2000). All samples were split, and about 30 g of one of the splits was powdered in a tungsten carbide Spex shatterbox. Powdered samples were then baked at 500 °C for 12 hours to eliminate organic material. At this point, two sets of samples were prepared, one for major element chemistry and one for trace element chemistry. Major element samples were prepared by mixing 3.5000 ± 0.0001 g of lithium tetraborate with 0.5000 ± 0.0001 g of powdered sample, homogenizing this powder in a shaker for 15 minutes, melting the mixed powders in a platinum crucible above a bunsen burner flame for 10 minutes, and pouring the melted mixture into a platinum tray. This yielded glass disks roughly 33 mm in diameter and 2 mm thick. Trace element samples were prepared by mixing 3.3 ± 0.1 g of powdered sample with five drops of polyvinyl alcohol and pressing the mixed powder into a pellet with a boric acid backing. Both trace element pellets and major element disks were then analyzed for elemental abundances on a Phillips 2400R X-ray fluorescence spectrometer at the University of California, Berkeley.

In this sample-naming convention, the sample ID indicates the site and the sample type. The site name indicates the mountain (P for Pilot Peak, T for Tailholt Mountain), the altitude in meters, and, where soils were sampled on both sides of the ridgeline, the slope aspect. Thus site P1062S, for example, is a south-facing site on Pilot Peak at 1062 m. Rock samples are denoted with the suffix X (e.g., P1062S-X1), soil samples with the suffix B (e.g., P1062S-B2), and samples from the soil excavation with the suffix PF (e.g., P1062S-B1-PF1).

Table F.1: Pilot Peak sample compositions (Al to Na)
 Type X=rock, B=soil, S=saprolite

Sample Name	Type	Al ₂ O ₃ %	CaO %	Fe ₂ O ₃ %	K ₂ O %	MgO %	MnO %	Mo ppm	Na ₂ O %
P2280-X1	X	15.4	2.5	1.8	2.9	0.52	0.030	1.0	4.0
P2280-X2	X	15.0	2.2	1.5	3.6	0.42	0.030	1.1	3.7
P2280-X3	X	14.8	2.0	2.0	3.7	0.57	0.041	1.0	3.5
P2280-X4	X	14.8	2.4	1.8	2.8	0.51	0.030	1.0	3.8
P2280-X5	X	12.3	1.5	1.1	3.5	0.28	0.020	1.3	2.8
P2280-X6	X	17.1	3.0	1.6	2.7	0.44	0.030	1.6	4.5
P2280-X7	X	16.3	2.5	1.8	3.6	0.47	0.030	1.3	4.1
P2280-X8	X	15.1	2.4	1.8	2.5	0.47	0.030	1.1	4.0
P2280-X9	X	17.0	3.1	1.7	2.6	0.46	0.030	1.3	4.5
P2280-X10	X	15.0	2.2	1.7	3.3	0.45	0.020	1.2	3.7
P2280-X11	X	14.9	2.3	1.8	2.7	0.53	0.030	1.1	3.9
P2280-X12	X	14.8	2.2	1.7	3.1	0.49	0.040	1.2	3.7
P2280-X13	X	15.8	2.1	1.8	3.8	0.55	0.060	1.2	3.6
P2280-X14	X	14.8	2.0	1.2	3.1	0.23	0.020	1.2	3.7
P2280-X15	X	15.6	2.4	1.7	2.9	0.46	0.030	1.3	4.1
P2280-X16	X	14.5	2.3	1.6	2.8	0.46	0.030	0.9	3.8
P2280-X17	X	13.7	2.0	1.4	3.0	0.38	0.020	1.3	3.5
P2280-X18	X	14.4	2.4	1.6	2.5	0.48	0.030	0.9	3.8
P2280-X19	X	15.9	2.2	1.7	4.5	0.50	0.030	1.2	3.7
P2280-X20	X	14.9	2.3	1.8	2.9	0.48	0.040	1.4	3.8
P2280-X21	X	14.8	2.1	1.4	3.2	0.31	0.040	1.8	3.5
P2280-X22	X	15.0	2.4	1.8	2.8	0.54	0.030	1.2	3.9
P2280-X23	X	14.5	1.2	1.5	3.3	0.36	0.041	4.0	3.0
P2280-X24	X	15.2	2.5	1.8	3.0	0.52	0.030	1.1	4.0
P2280-X25	X	14.8	2.3	1.7	2.6	0.47	0.030	1.2	3.8
P2280-X26	X	14.5	0.6	0.4	5.4	0.08	0.030	1.3	2.8
P2280-X27	X	15.8	2.3	1.7	3.6	0.50	0.030	1.1	3.9
P2280-X28	X	15.5	2.4	1.7	3.3	0.52	0.041	1.2	3.9
P2280-X29	X	15.5	0.8	2.1	8.4	0.64	0.031	1.4	2.0
P2280-X30	X	13.5	1.0	2.0	3.3	0.34	0.050	2.7	2.8
P2280-X31	X	15.0	2.3	1.3	3.3	0.38	0.020	1.5	3.9
P2280-X32	X	16.2	2.0	1.6	4.8	0.45	0.030	1.0	3.6
P2280-X33	X	14.4	2.0	1.5	3.0	0.39	0.040	1.4	3.7
P2280-X34	X	14.5	2.3	1.9	2.4	0.51	0.041	1.4	3.9
P2280-X35	X	15.5	2.4	1.8	3.3	0.50	0.030	1.2	4.0
P2280-X36	X	14.9	2.1	1.5	3.2	0.37	0.051	1.4	3.8
P2280-X37	X	14.6	2.3	1.9	2.9	0.52	0.031	1.1	3.7
P2280-X38	X	15.4	1.9	1.5	4.4	0.43	0.031	1.5	3.6
P2280-X39	X	15.5	2.4	1.8	3.0	0.53	0.051	1.5	4.0
P2280-X40	X	16.0	2.1	1.6	4.3	0.45	0.030	1.5	3.8
P2090-X1	X	14.3	2.5	1.8	2.2	0.53	0.030	0.7	3.7
P2090-X2	X	14.3	2.5	1.7	2.3	0.55	0.030	1.0	3.7
P2090-X3	X	16.8	1.6	1.0	7.0	0.34	0.020	1.3	3.0
P2090-X4	X	15.4	2.3	1.6	3.3	0.46	0.030	0.8	3.9
P2090-X5	X	14.8	2.5	1.7	2.2	0.55	0.030	0.7	3.8
P2090-X6	X	15.1	2.3	1.6	2.8	0.43	0.040	1.3	3.9
P2090-X7	X	14.4	2.3	1.7	2.7	0.50	0.030	0.7	3.6

Sample Name	Type	Al ₂ O ₃ %	CaO %	Fe ₂ O ₃ %	K ₂ O %	MgO %	MnO %	Mo ppm	Na ₂ O %
P2090-X8	X	14.7	2.4	1.8	2.7	0.56	0.081	0.8	3.7
P2090-X9	X	15.0	2.3	1.8	3.5	0.53	0.030	0.2	3.6
P2090-X10	X	14.1	1.9	1.5	3.7	0.40	0.030	1.0	3.2
P2090-X11	X	16.3	2.8	1.9	2.9	0.50	0.030	0.6	4.1
P2090-X12	X	15.9	2.3	1.7	3.6	0.48	0.040	0.6	3.8
P2090-X13	X	13.5	2.3	1.5	2.1	0.48	0.030	1.1	3.5
P2090-X14	X	15.7	2.0	1.5	4.3	0.42	0.020	1.1	3.6
P2090-X15	X	15.1	2.2	1.6	3.8	0.47	0.030	0.3	3.6
P2090-X16	X	16.1	2.0	1.6	3.6	0.38	0.031	0.6	4.0
P2090-X17	X	15.7	2.5	1.9	2.9	0.54	0.031	0.9	4.1
P2090-X18	X	14.9	2.5	1.8	2.5	0.56	0.030	0.9	3.8
P2090-X19	X	14.9	2.4	1.6	2.9	0.50	0.020	0.9	3.7
P2090-X20	X	15.2	2.3	1.7	3.2	0.53	0.030	1.2	3.7
P2090-X21	X	15.4	2.3	1.9	2.9	0.50	0.031	1.2	4.0
P2090-X22	X	15.6	2.4	1.7	2.6	0.48	0.030	0.6	4.1
P2090-X23	X	19.9	1.3	0.3	5.4	0.06	0.010	1.7	6.1
P2090-X24	X	14.8	1.6	2.2	4.5	0.63	0.040	0.9	3.2
P2090-X25	X	15.8	2.6	1.9	2.3	0.54	0.040	1.1	4.3
P2090-X26	X	14.7	1.2	1.0	4.9	0.21	0.020	1.9	3.4
P2090-X27	X	15.7	2.3	1.7	3.3	0.49	0.030	1.4	3.9
P2090-X28	X	15.3	2.3	1.9	2.6	0.49	0.040	1.5	4.0
P2090-X29	X	14.8	2.0	2.1	2.8	0.48	0.040	0.6	3.8
P2090-X30	X	15.7	2.3	1.7	3.1	0.47	0.030	0.8	4.0
P2090-X31	X	15.3	2.2	1.2	2.6	0.36	0.030	1.2	3.9
P2090-X32	X	14.9	2.4	1.8	2.7	0.53	0.040	1.4	3.8
P2090-X33	X	16.2	0.5	0.2	8.5	0.04	0.000	1.7	2.9
P2090-X34	X	15.5	2.4	1.6	3.4	0.50	0.030	1.5	3.7
P2090-X35	X	15.0	2.3	1.6	3.1	0.48	0.040	1.2	3.7
P2090-X36	X	15.1	2.4	1.6	3.2	0.51	0.030	0.5	3.8
P2090-X37	X	15.8	2.7	1.8	2.9	0.57	0.030	0.9	4.0
P2090-X38	X	14.8	2.5	1.3	2.8	0.42	0.030	1.4	3.7
P2090-X39	X	14.6	2.5	1.8	2.3	0.60	0.040	1.4	3.8
P2090-X40	X	15.4	2.2	1.4	4.2	0.42	0.030	1.1	3.6
P1850-X1	X	15.0	1.8	1.3	3.9	0.30	0.030	1.1	3.4
P1850-X2	X	14.7	2.3	1.7	2.8	0.46	0.030	0.8	3.7
P1850-X3	X	15.5	2.4	1.5	2.8	0.36	0.030	1.1	3.9
P1850-X4	X	14.8	2.2	1.3	3.4	0.35	0.030	1.1	3.6
P1850-X5	X	15.8	2.5	1.5	3.3	0.42	0.030	0.7	3.9
P1850-X6	X	15.3	2.5	1.7	2.5	0.42	0.030	1.1	4.0
P1850-X7	X	14.6	2.3	1.7	2.8	0.46	0.040	1.2	3.6
P1850-X8	X	15.2	2.4	1.6	2.9	0.43	0.030	1.0	3.8
P1850-X9	X	15.5	1.7	2.1	3.3	0.39	0.040	0.9	3.8
P1850-X10	X	15.2	2.6	1.5	2.2	0.39	0.020	0.9	4.1
P1850-X11	X	16.8	1.9	2.5	4.9	0.61	0.040	0.9	3.6
P1850-X12	X	13.6	2.2	1.6	2.1	0.39	0.030	1.1	3.6
P1850-X13	X	13.8	2.1	2.0	2.3	0.44	0.050	-1.5	3.2
P1850-X14	X	13.1	2.0	1.2	2.4	0.25	0.020	1.5	3.3
P1850-X15	X	14.1	2.1	1.5	2.8	0.37	0.030	0.8	3.6
P1850-X16	X	13.6	1.3	1.4	4.6	0.32	0.030	1.3	2.7
P1850-X17	X	14.9	1.5	1.8	4.6	0.38	0.030	1.7	3.2

Sample Name	Type	Al ₂ O ₃ %	CaO %	Fe ₂ O ₃ %	K ₂ O %	MgO %	MnO %	Mo ppm	Na ₂ O %
P1850-X18	X	14.3	2.3	1.6	2.6	0.43	0.030	0.9	3.7
P1850-X19	X	13.6	1.1	1.0	4.9	0.18	0.020	1.7	2.8
P1850-X20	X	15.1	2.5	1.7	2.7	0.45	0.030	1.3	3.9
P1850-X21	X	13.9	2.0	1.5	3.2	0.38	0.020	1.1	3.2
P1850-X22	X	14.0	2.1	1.9	2.9	0.45	0.030	1.7	3.4
P1850-X23	X	14.3	1.9	1.5	3.5	0.39	0.030	0.8	3.3
P1850-X24	X	15.9	2.5	1.8	2.9	0.46	0.030	1.5	4.1
P1850-X25	X	12.9	2.0	1.4	2.4	0.36	0.030	0.6	3.3
P1850-X26	X	14.9	2.2	1.7	2.6	0.44	0.030	0.8	3.7
P1850-X27	X	15.7	2.1	1.7	3.7	0.44	0.030	0.8	3.6
P1850-X28	X	13.4	1.5	1.0	3.8	0.19	0.020	1.3	2.9
P1850-X29	X	14.0	0.9	2.1	6.2	0.49	0.030	1.1	2.0
P1850-X30	X	14.1	2.2	1.6	2.8	0.38	0.030	0.9	3.6
P1850-X31	X	14.9	1.9	1.3	3.7	0.27	0.020	0.7	3.8
P1850-X32	X	13.5	2.0	1.7	2.9	0.42	0.030	0.5	3.2
P1850-X33	X	16.0	2.5	1.9	2.9	0.49	0.030	0.7	4.0
P1850-X34	X	14.6	2.2	1.7	2.8	0.43	0.030	1.2	3.7
P1850-X35	X	15.9	2.2	1.6	3.7	0.42	0.030	0.7	3.7
P1850-X36	X	15.6	2.3	1.6	3.0	0.37	0.030	0.7	3.9
P1850-X37	X	15.2	2.1	1.6	3.7	0.40	0.030	1.0	3.5
P1850-X38	X	14.6	2.4	1.8	2.2	0.47	0.030	1.2	3.8
P1850-X39	X	16.6	2.5	1.6	3.0	0.40	0.020	0.7	4.2
P1850-X40	X	16.2	2.0	1.9	3.6	0.39	0.030	0.5	4.0
P1706-X1	X	13.8	1.7	0.6	4.5	0.15	0.010	1.3	3.0
P1706-X2	X	15.1	2.5	1.8	2.8	0.49	0.030	1.2	3.8
P1706-X3	X	13.5	2.4	1.6	1.9	0.39	0.030	1.2	3.6
P1706-X4	X	14.5	2.3	1.6	2.3	0.42	0.030	1.2	3.8
P1706-X5	X	14.7	2.5	1.7	2.5	0.42	0.030	1.2	3.8
P1706-X6	X	14.1	2.5	1.5	2.2	0.39	0.020	1.6	3.8
P1706-X7	X	16.0	2.6	1.6	3.3	0.42	0.030	1.3	4.0
P1706-X8	X	15.0	2.5	1.8	2.4	0.44	0.030	1.2	4.0
P1706-X9	X	11.1	1.3	1.3	3.2	0.31	0.020	2.0	2.4
P1706-X11	X	13.1	2.3	1.6	1.8	0.38	0.030	1.7	3.5
P1706-X12	X	13.5	2.3	1.8	2.4	0.47	0.040	0.7	3.4
P1706-X13	X	14.7	1.4	0.6	6.3	0.13	0.010	1.1	2.6
P1706-X14	X	15.0	2.2	1.3	3.7	0.32	0.020	0.6	3.6
P1706-X15	X	15.8	2.4	1.6	3.6	0.44	0.030	1.3	3.8
P1706-X16	X	14.3	2.3	1.7	2.6	0.41	0.030	1.3	3.6
P1706-X17	X	14.7	1.2	0.5	4.8	0.12	0.010	1.8	3.1
P1706-X18	X	14.6	2.0	1.2	3.6	0.30	0.020	0.9	3.4
P1706-X19	X	12.4	1.6	1.3	3.6	0.32	0.020	1.7	2.6
P1706-X20	X	14.4	2.4	1.7	2.6	0.45	0.030	0.7	3.7
P1706-X21	X	14.9	2.3	1.7	3.4	0.42	0.030	0.9	3.7
P1706-X22	X	15.2	2.4	1.7	3.1	0.45	0.030	0.6	3.8
P1706-X23	X	14.2	2.5	1.6	2.3	0.40	0.030	0.7	3.8
P1706-X24	X	15.0	2.3	1.4	3.6	0.36	0.020	1.1	3.6
P1706-X25	X	14.8	2.4	1.6	2.8	0.43	0.030	0.7	3.8
P1706-X26	X	14.7	1.5	0.9	4.6	0.22	0.020	1.1	3.2
P1706-X28	X	15.1	1.4	0.9	4.2	0.19	0.010	0.7	3.3
P1706-X29	X	14.9	2.4	1.5	3.1	0.38	0.030	1.1	3.8

Sample Name	Type	Al ₂ O ₃ %	CaO %	Fe ₂ O ₃ %	K ₂ O %	MgO %	MnO %	Mo ppm	Na ₂ O %
P1706-X30	X	14.7	1.9	1.0	4.3	0.23	0.020	0.6	3.4
P1706-X31	X	15.7	2.7	1.8	2.7	0.47	0.040	1.1	4.2
P1706-X32	X	15.6	2.8	2.1	2.2	0.54	0.040	0.6	4.2
P1706-X33	X	15.0	2.4	1.6	2.9	0.39	0.030	0.9	3.8
P1706-X34	X	14.5	2.4	1.7	2.4	0.42	0.030	0.9	3.9
P1706-X27	X	15.0	2.5	1.9	2.6	0.47	0.030	1.3	3.9
P1706-X35	X	14.3	2.5	1.7	2.0	0.42	0.030	0.2	3.9
P1706-X36	X	14.8	2.4	1.5	2.8	0.39	0.030	0.5	3.8
P1706-X37	X	14.1	1.5	0.6	5.0	0.13	0.010	1.4	3.0
P1706-X38	X	15.4	2.4	1.6	3.4	0.42	0.030	1.1	3.9
P1706-X39	X	15.5	2.4	1.6	3.6	0.42	0.030	0.7	3.8
P1706-X40	X	15.7	2.8	2.0	2.4	0.49	0.030	1.3	4.3
P1480-X1	X	16.4	2.4	1.5	3.9	0.41	0.030	0.7	4.0
P1480-X2	X	16.2	2.6	1.5	3.0	0.42	0.030	0.7	4.3
P1480-X3	X	16.0	1.8	1.3	4.1	0.33	0.040	0.8	3.8
P1480-X4	X	15.5	2.2	1.6	3.5	0.45	0.030	0.8	3.8
P1480-X5	X	14.3	2.5	1.6	1.9	0.42	0.030	1.0	4.0
P1480-X6	X	15.3	1.3	1.2	4.2	0.21	0.030	1.0	3.7
P1480-X7	X	15.1	2.3	1.6	2.8	0.41	0.030	1.2	3.9
P1480-X8	X	14.7	2.5	1.6	2.2	0.43	0.030	0.8	4.0
P1480-X9	X	14.5	2.3	1.3	2.7	0.33	0.030	1.2	3.8
P1480-X10	X	14.9	2.5	1.8	2.2	0.47	0.030	0.7	4.1
P1480-X11	X	13.9	2.4	1.8	2.1	0.53	0.030	0.9	3.6
P1480-X12	X	14.7	2.4	1.6	3.0	0.46	0.030	0.6	3.7
P1480-X13	X	14.9	2.5	1.7	2.4	0.50	0.030	1.3	3.8
P1480-X14	X	16.8	2.7	1.7	3.2	0.52	0.030	0.6	4.2
P1480-X15	X	15.2	2.5	1.7	2.7	0.48	0.030	1.3	3.8
P1480-X16	X	15.6	2.6	2.2	2.7	0.63	0.050	0.6	3.9
P1480-X17	X	14.2	2.5	1.9	2.0	0.51	0.040	0.9	3.8
P1480-X18	X	14.4	2.4	1.8	2.6	0.51	0.030	0.7	3.6
P1480-X19	X	15.7	2.6	1.8	2.8	0.51	0.030	0.4	3.9
P1480-X20	X	15.5	2.7	1.8	2.5	0.51	0.030	1.1	4.1
P1480-X21	X	14.7	2.4	1.6	2.6	0.48	0.030	0.9	3.6
P1480-X22	X	12.5	1.9	1.6	2.5	0.41	0.030	1.3	3.0
P1480-X23	X	13.1	0.1	2.1	3.8	0.49	0.062	0.9	1.3
P1480-X24	X	15.2	2.5	1.8	2.6	0.48	0.030	0.7	4.1
P1480-X25	X	16.2	0.6	1.5	3.9	0.39	0.020	0.6	3.5
P1480-X26	X	15.8	2.6	1.6	3.2	0.45	0.020	1.5	4.0
P1480-X27	X	15.7	2.8	1.7	2.4	0.47	0.030	0.9	4.2
P1480-X28	X	16.0	2.4	1.8	3.5	0.49	0.030	0.9	3.9
P1480-X29	X	14.8	2.3	1.8	2.8	0.51	0.050	0.7	3.8
P1480-X30	X	14.6	2.4	1.8	2.5	0.48	0.030	0.7	3.8
P1480-X31	X	15.1	2.1	1.4	3.8	0.37	0.030	1.4	3.6
P1480-X32	X	13.8	0.4	0.5	5.5	0.09	0.010	1.1	2.5
P1480-X33	X	15.3	2.0	1.2	4.2	0.28	0.030	1.1	3.6
P1480-X34	X	14.1	2.3	1.7	2.3	0.41	0.030	0.7	3.8
P1480-X35	X	15.9	2.3	1.6	3.4	0.37	0.030	0.9	4.0
P1480-X36	X	14.3	2.1	1.7	2.8	0.40	0.030	0.7	3.7
P1480-X37	X	15.6	2.3	1.5	2.8	0.36	0.020	0.5	4.1
P1480-X38	X	15.9	1.9	1.4	5.0	0.38	0.030	1.1	3.4

Sample Name	Type	Al ₂ O ₃ %	CaO %	Fe ₂ O ₃ %	K ₂ O %	MgO %	MnO %	Mo ppm	Na ₂ O %
P1480-X39	X	14.1	1.6	1.2	3.6	0.29	0.020	1.1	3.4
P1480-X40	X	14.8	2.5	1.7	2.3	0.48	0.030	1.3	3.9
P1270-X1	X	14.6	2.3	1.6	2.6	0.42	0.030	1.4	3.9
P1270-X2	X	15.5	2.0	1.2	4.9	0.33	0.020	1.1	3.4
P1270-X3	X	14.2	2.4	1.6	2.4	0.43	0.030	1.2	3.8
P1270-X4	X	14.1	2.3	1.6	2.5	0.42	0.030	0.8	3.7
P1270-X5	X	15.2	2.3	1.4	3.4	0.40	0.030	1.7	3.8
P1270-X6	X	15.5	2.4	1.7	3.3	0.45	0.030	0.9	3.9
P1270-X7	X	15.2	2.2	1.5	3.4	0.42	0.030	1.1	3.7
P1270-X8	X	14.6	1.5	1.1	3.6	0.24	0.081	0.9	3.2
P1270-X9	X	14.3	0.7	0.5	3.8	0.04	0.030	1.1	4.2
P1270-X10	X	15.6	1.9	1.1	5.0	0.31	0.020	1.3	3.4
P1270-X11	X	15.8	2.3	1.5	3.8	0.38	0.030	1.2	3.9
P1270-X12	X	16.0	2.0	1.3	4.8	0.34	0.030	1.7	3.6
P1270-X13	X	14.8	2.4	1.7	2.5	0.44	0.030	1.4	3.9
P1270-X14	X	14.7	2.2	1.7	3.2	0.45	0.040	1.2	3.7
P1270-X15	X	14.3	2.3	1.7	2.4	0.46	0.030	1.1	3.7
P1270-X16	X	16.0	2.5	1.7	3.4	0.44	0.040	1.3	4.1
P1270-X17	X	14.5	2.3	1.5	2.8	0.41	0.030	1.3	3.8
P1270-X18	X	14.4	0.6	0.5	4.5	0.04	0.030	1.5	3.8
P1270-X19	X	15.1	2.2	1.4	3.4	0.39	0.030	1.4	3.7
P1270-X20	X	14.3	2.4	1.5	2.2	0.39	0.030	1.2	3.8
P1270-X21	X	15.7	2.4	1.6	3.2	0.45	0.030	1.3	4.0
P1270-X22	X	14.6	2.1	1.5	3.7	0.40	0.030	0.8	3.4
P1270-X23	X	14.7	2.2	1.5	2.9	0.37	0.030	1.2	3.8
P1270-X24	X	14.2	2.3	1.6	2.4	0.41	0.030	1.2	3.8
P1270-X25	X	15.3	2.3	1.6	3.4	0.43	0.030	1.1	3.8
P1270-X26	X	15.5	2.4	1.5	3.2	0.40	0.030	1.1	4.0
P1270-X27	X	15.0	2.3	1.5	3.3	0.37	0.020	1.3	3.8
P1270-X28	X	14.9	2.2	1.7	3.3	0.43	0.030	1.4	3.7
P1270-X29	X	14.7	2.4	1.7	2.4	0.44	0.030	1.2	3.9
P1270-X30	X	15.9	2.2	1.6	4.2	0.42	0.030	0.7	3.7
P1270-X31	X	16.1	2.5	1.4	3.6	0.37	0.020	1.3	4.1
P1270-X32	X	15.8	2.2	1.6	3.8	0.40	0.030	1.1	3.8
P1270-X33	X	14.5	2.5	1.8	2.1	0.45	0.030	1.1	3.9
P1270-X34	X	13.7	2.2	1.7	2.6	0.45	0.030	1.1	3.5
P1270-X35	X	14.7	0.6	0.5	6.4	0.03	0.010	1.2	2.8
P1270-X36	X	14.1	2.2	1.5	2.6	0.38	0.020	1.1	3.6
P1270-X37	X	15.9	2.2	2.3	3.8	0.62	0.040	1.2	3.7
P1270-X38	X	13.5	2.1	1.3	2.7	0.35	0.020	1.2	3.5
P1270-X39	X	15.6	2.5	1.5	3.1	0.38	0.030	1.5	4.1
P1270-X40	X	15.3	2.5	1.7	2.9	0.44	0.030	1.1	4.0
P1062-X1	X	15.4	2.2	1.4	3.9	0.39	0.030	1.4	3.7
P1062-X2	X	14.7	2.3	1.7	2.9	0.45	0.030	1.1	3.7
P1062-X3	X	14.5	2.0	1.2	4.0	0.32	0.020	0.9	3.3
P1062-X4	X	15.3	2.5	1.5	2.6	0.41	0.030	1.2	4.1
P1062-X5	X	14.6	2.3	1.7	3.1	0.43	0.030	1.2	3.6
P1062-X6	X	15.5	2.5	1.7	3.0	0.43	0.030	1.2	4.0
P1062-X7	X	14.7	2.4	1.8	2.5	0.47	0.030	1.5	3.9

Sample Name	Type	Al ₂ O ₃ %	CaO %	Fe ₂ O ₃ %	K ₂ O %	MgO %	MnO %	Mo ppm	Na ₂ O %
P1062-X8	X	14.1	2.4	1.7	2.2	0.46	0.030	1.2	3.7
P1062-X9	X	15.0	2.4	1.6	3.0	0.44	0.030	1.1	3.8
P1062-X10	X	14.8	2.2	1.6	3.1	0.41	0.030	1.4	3.7
P1062-X11	X	15.5	2.4	1.5	3.3	0.39	0.030	0.7	3.9
P1062-X12	X	13.7	2.0	1.5	3.1	0.43	0.030	1.0	3.3
P1062-X13	X	15.5	2.3	1.6	3.2	0.39	0.030	0.9	3.9
P1062-X14	X	15.8	2.3	1.5	3.6	0.38	0.030	0.3	3.7
P1062-X15	X	14.5	1.1	1.1	2.9	0.19	0.010	1.2	3.6
P1062-X16	X	15.3	2.5	1.7	2.7	0.46	0.030	0.7	3.9
P1062-X17	X	14.7	2.2	1.8	2.9	0.45	0.030	0.9	3.6
P1062-X18	X	15.2	2.1	1.5	3.7	0.35	0.030	0.2	3.7
P1062-X19	X	15.5	2.2	1.7	3.1	0.43	0.030	1.0	3.7
P1062-X20	X	15.7	2.6	1.8	2.7	0.47	0.040	0.9	4.1
P1062-X21	X	15.1	1.8	1.0	4.3	0.25	0.020	0.9	3.5
P1062-X22	X	15.2	2.4	1.6	3.2	0.45	0.030	1.0	3.8
P1062-X23	X	14.6	2.3	1.8	2.5	0.45	0.030	0.5	3.8
P1062-X24	X	14.7	2.4	1.7	2.7	0.46	0.030	1.2	3.8
P1062-X25	X	15.9	2.4	1.5	3.6	0.42	0.030	1.2	3.9
P1062-X26	X	15.0	2.1	1.4	3.5	0.35	0.020	0.7	3.6
P1062-X27	X	14.7	2.3	1.8	2.6	0.47	0.030	0.5	3.7
P1062-X28	X	15.3	2.5	1.5	3.0	0.41	0.030	0.7	4.0
P1062-X29	X	15.8	2.2	1.7	3.8	0.41	0.030	0.3	3.8
P1062-X30	X	14.8	2.3	1.9	3.1	0.48	0.030	0.5	3.7
P1062-X31	X	13.5	2.0	1.7	2.7	0.40	0.030	1.2	3.4
P1062-X32	X	16.2	1.5	1.5	3.1	0.27	0.020	0.9	4.0
P1062-X33	X	15.2	2.2	1.2	3.4	0.30	0.020	1.0	3.8
P1062-X34	X	14.7	2.3	1.4	3.0	0.37	0.030	0.2	3.7
P1062-X35	X	15.1	2.4	1.6	3.1	0.41	0.030	0.5	3.8
P1062-X36	X	14.9	2.2	1.4	3.4	0.37	0.030	0.9	3.6
P1062-X37	X	15.5	2.7	1.6	2.6	0.43	0.040	1.0	4.2
P1062-X38	X	14.6	2.4	1.6	2.6	0.43	0.030	0.3	3.9
P1062-X39	X	14.6	1.9	1.6	3.2	0.34	0.020	0.5	3.6
P1062-X40	X	14.7	2.3	1.6	3.2	0.41	0.030	0.7	3.6
P2283S-B2	B	16.2	1.9	2.1	3.1	0.46	0.071	1.4	3.6
P2283S-B3	B	15.7	1.7	1.9	3.8	0.39	0.061	1.5	3.2
P2283S-B4	B	15.4	1.9	2.2	2.9	0.45	0.061	1.9	3.4
P2283S-B5	B	15.8	2.0	2.0	2.9	0.41	0.060	1.5	3.6
P2283S-B6	B	15.6	1.9	2.0	2.9	0.42	0.061	1.5	3.5
P2283S-B7	B	16.0	2.0	2.1	3.2	0.43	0.061	1.4	3.5
P2283S-B8	B	16.5	2.1	2.1	3.3	0.45	0.071	1.6	3.6
P2283S-B9	B	16.2	2.1	2.1	3.1	0.45	0.081	1.7	3.5
P2283S-B10	B	16.3	2.0	2.3	3.0	0.50	0.061	1.6	3.5
P2283S-B11	B	15.1	1.8	2.0	3.2	0.38	0.061	1.5	3.2
P2283S-B12	B	15.9	1.9	2.0	3.2	0.40	0.061	1.3	3.5
P2283S-B13	B	15.6	1.9	1.9	3.3	0.41	0.061	1.6	3.3
P2283S-B14	B	16.5	2.0	2.2	3.1	0.48	0.071	1.6	3.6
P2283S-B15	B	15.4	1.9	1.9	2.9	0.39	0.041	1.4	3.4
P2283S-B16	B	14.8	1.9	1.9	2.6	0.39	0.050	1.4	3.3
P2283S-B17	B	16.0	2.0	2.2	3.0	0.47	0.071	1.7	3.5
P2283S-B1-PF1	B	15.2	1.9	1.9	3.0	0.40	0.051	1.4	3.4

Sample Name	Type	Al ₂ O ₃ %	CaO %	Fe ₂ O ₃ %	K ₂ O %	MgO %	MnO %	Mo ppm	Na ₂ O %
P2283S-B1-PF2	B	17.2	2.1	2.3	3.3	0.50	0.061	1.5	3.7
P2283S-B1-PF3	B	16.3	1.9	2.0	3.3	0.42	0.051	1.4	3.5
P2283S-B1-PF4	B	15.3	1.8	1.9	2.9	0.41	0.040	1.4	3.4
P2283S-B1-PF5	B	15.2	1.7	1.9	3.0	0.42	0.040	1.6	3.3
P2283S-B1-PF6	B	14.6	1.7	1.9	2.7	0.39	0.040	1.5	3.2
P2283S-B1-PF7	B	16.2	1.9	2.3	3.1	0.49	0.051	1.4	3.5
P2281N-B2	B	16.8	2.1	2.6	2.7	0.65	0.071	1.7	3.4
P2281N-B3	B	15.8	1.8	2.2	3.0	0.60	0.061	1.5	3.1
P2281N-B4	B	15.4	1.8	2.1	2.9	0.59	0.061	1.6	3.0
P2281N-B5	B	16.9	1.9	2.5	3.5	0.64	0.061	1.8	3.3
P2281N-B6	B	16.6	1.9	2.4	3.4	0.68	0.081	1.0	3.1
P2281N-B7	B	15.7	2.0	2.1	3.1	0.59	0.071	1.5	3.1
P2281N-B8	B	16.2	1.8	2.4	3.1	0.66	0.071	1.5	3.0
P2281N-B9	B	16.4	1.8	2.4	3.1	0.67	0.082	1.4	3.1
P2281N-B10	B	15.6	1.8	2.2	2.8	0.61	0.071	1.4	3.0
P2281N-B11	B	16.2	1.8	2.5	3.0	0.67	0.092	1.6	3.1
P2281N-B12	B	14.9	1.6	2.1	2.9	0.56	0.071	1.7	2.8
P2281N-B13	B	16.2	1.8	2.3	3.1	0.64	0.072	1.7	3.1
P2281N-B14	B	15.0	1.8	1.9	3.0	0.44	0.051	1.4	3.2
P2281N-B15	B	16.7	2.0	2.4	3.0	0.56	0.061	1.6	3.5
P2281N-B16	B	16.3	2.0	2.5	3.0	0.56	0.071	1.7	3.4
P2281N-B17	B	16.6	2.0	2.4	2.8	0.58	0.071	1.6	3.5
P2281N-B1-PF1	B	16.5	1.9	2.3	3.3	0.65	0.071	1.7	3.1
P2281N-B1-PF2	B	15.7	1.8	2.2	2.9	0.61	0.071	1.7	3.1
P2281N-B1-PF3	B	16.8	1.9	2.5	2.9	0.70	0.082	1.8	3.2
P2281N-B1-PF4	B	16.2	1.7	2.3	3.1	0.62	0.061	1.6	3.1
P2281N-B1-PF5	B	16.3	1.7	2.4	2.8	0.66	0.051	2.2	3.0
P2281N-B1-PF6	B	15.0	1.3	1.7	3.2	0.35	0.020	2.6	2.9
P2281N-B1-PF7	B	15.4	1.4	1.9	3.1	0.30	0.020	3.3	3.0
P2090-B2	B	16.5	2.0	2.3	3.4	0.67	0.071	1.3	3.2
P2090-B3	B	13.8	1.7	2.0	2.7	0.54	0.062	1.6	2.7
P2090-B4	B	16.0	2.1	2.3	3.1	0.66	0.072	1.1	3.2
P2090-B5	B	15.6	1.9	2.4	3.0	0.72	0.061	1.2	2.9
P2090-B6	B	14.9	1.8	2.1	3.1	0.60	0.061	1.5	2.9
P2090-B7	B	15.5	1.9	2.2	3.2	0.59	0.071	1.2	3.1
P2090-B8	B	15.0	1.7	2.2	3.1	0.59	0.071	0.8	2.9
P2090-B9	B	15.4	2.0	2.2	3.0	0.63	0.071	1.5	3.0
P2090-B10	B	15.2	1.8	2.1	3.3	0.59	0.061	1.2	2.9
P2090-B11	B	15.9	1.9	2.3	3.2	0.65	0.072	1.1	3.1
P2090-B12	B	14.6	1.8	2.1	2.8	0.58	0.061	0.8	3.0
P2090-B13	B	15.1	1.7	2.0	3.4	0.54	0.061	1.3	2.9
P2090-B14	B	14.9	1.8	2.1	3.2	0.60	0.071	1.6	2.9
P2090-B15	B	14.5	1.8	2.0	3.0	0.58	0.061	1.5	2.8
P2090-B16	B	14.9	1.8	2.2	2.9	0.62	0.071	1.6	2.9
P2090-B17	B	14.8	1.7	1.9	3.5	0.51	0.061	1.1	2.8
P2090-B1PF1	B	14.5	1.7	1.9	3.2	0.54	0.061	1.7	2.8
P2090-B1PF2	B	14.9	1.8	2.1	3.1	0.60	0.061	1.2	2.9
P2090-B1PF3	B	16.0	1.9	2.4	3.0	0.67	0.071	1.1	3.2
P2090-B1PF4	B	14.9	1.7	1.8	3.3	0.51	0.051	1.1	2.9

Sample Name	Type	Al ₂ O ₃ %	CaO %	Fe ₂ O ₃ %	K ₂ O %	MgO %	MnO %	Mo ppm	Na ₂ O %
P2090-B1PF5	B	16.4	2.0	2.2	3.2	0.61	0.061	1.6	3.3
P2090-B1PF6	B	16.0	1.8	2.0	3.6	0.55	0.051	1.5	3.2
P2090-B1PF7	S	15.1	2.1	1.9	3.7	0.55	0.051	1.1	3.4
P2090-B1PF8	S	16.4	1.8	1.3	6.0	0.38	0.020	1.2	3.2
P1850-B2	B	15.5	2.0	1.7	3.5	0.37	0.072	1.6	3.6
P1850-B3	B	15.1	1.8	1.7	3.4	0.35	0.071	1.5	3.5
P1850-B4	B	15.5	1.9	1.8	3.4	0.39	0.051	1.1	3.6
P1850-B5	B	15.4	2.0	1.8	3.0	0.42	0.061	1.1	3.5
P1850-B6	B	16.3	2.1	2.2	3.1	0.50	0.081	1.8	3.7
P1850-B7	B	15.6	1.9	1.8	3.4	0.38	0.061	1.6	3.7
P1850-B8	B	15.4	1.9	1.8	3.6	0.38	0.062	1.5	3.6
P1850-B9	B	15.6	2.1	1.9	3.3	0.42	0.040	1.2	3.6
P1850-B10	B	15.6	2.1	2.0	3.0	0.44	0.071	1.6	3.5
P1850-B11	B	15.4	1.9	1.9	3.0	0.39	0.050	1.3	3.6
P1850-B12	B	15.7	1.9	1.7	3.5	0.37	0.061	1.2	3.6
P1850-B13	B	15.4	2.1	1.9	2.7	0.45	0.051	1.6	3.7
P1850-B14	B	16.1	2.1	2.2	3.0	0.50	0.060	1.1	3.6
P1850-B15	B	15.4	2.0	1.8	3.1	0.42	0.061	1.5	3.5
P1850-B16	B	14.8	2.0	1.7	2.9	0.39	0.040	1.1	3.5
P1850-B17	B	14.8	1.9	1.6	3.2	0.35	0.050	1.5	3.4
P1850-B1PF1	B	15.4	2.0	1.8	3.2	0.41	0.071	1.6	3.6
P1850-B1PF2	B	15.4	2.1	1.9	2.9	0.45	0.061	1.6	3.6
P1850-B1PF3	B	15.4	2.0	1.7	3.3	0.39	0.040	1.3	3.5
P1850-B1PF4	B	15.1	1.9	1.6	3.3	0.37	0.030	1.1	3.5
P1850-B1PF5	S	16.0	2.2	1.8	3.1	0.45	0.030	1.3	3.7
P1850-B1PF6	S	16.2	2.3	2.1	2.5	0.55	0.030	1.2	3.8
P1850-B1PF7	S	16.6	2.4	2.0	2.9	0.57	0.030	0.8	3.8
P1706-B2	B	15.4	2.5	1.9	2.5	0.46	0.050	1.5	3.9
P1706-B3	B	15.3	2.5	1.8	2.4	0.44	0.040	1.5	4.0
P1706-B4	B	16.1	2.5	2.1	2.7	0.53	0.040	1.8	3.9
P1706-B5	B	15.3	2.4	1.9	2.7	0.45	0.030	1.4	3.7
P1706-B6	B	14.8	2.1	1.7	3.2	0.41	0.040	1.4	3.4
P1706-B7	B	16.2	2.4	2.0	3.2	0.53	0.041	1.5	3.8
P1706-B8	B	15.9	2.6	2.0	2.5	0.51	0.041	1.4	4.0
P1706-B9	B	15.6	2.4	1.9	2.7	0.47	0.041	1.8	3.8
P1706-B10	B	15.2	2.3	1.8	2.8	0.44	0.040	1.3	3.6
P1706-B11	B	15.8	2.3	1.9	3.1	0.45	0.040	1.4	3.7
P1706-B12	B	15.6	2.5	2.0	2.5	0.48	0.040	1.4	3.9
P1706-B13	B	15.6	2.4	1.8	2.6	0.43	0.030	1.4	3.9
P1706-B14	B	15.7	2.5	2.0	2.5	0.50	0.040	1.4	3.9
P1706-B15	B	15.8	2.5	2.0	2.8	0.48	0.041	1.3	3.8
P1706-B16	B	15.9	2.3	1.9	3.3	0.47	0.041	1.3	3.7
P1706-B17	B	15.0	2.1	1.8	3.1	0.42	0.040	1.8	3.4
P1706-B1PF1	B	15.4	2.4	1.9	2.8	0.47	0.051	1.4	3.6
P1706-B1PF2	B	14.9	2.2	1.7	3.0	0.42	0.040	1.3	3.4
P1706-B1PF3	B	16.2	2.5	2.3	2.6	0.55	0.051	1.0	3.9
P1706-B1PF4	B	16.3	2.5	2.2	2.9	0.53	0.040	1.3	3.9
P1706-B1PF5	B	16.1	2.5	2.1	2.5	0.52	0.030	0.9	4.1
P1706-B1PF6	S	15.1	2.3	1.4	3.3	0.35	0.020	0.8	3.7

Sample Name	Type	Al ₂ O ₃ %	CaO %	Fe ₂ O ₃ %	K ₂ O %	MgO %	MnO %	Mo ppm	Na ₂ O %
P1706-B1PF7	S	14.5	2.1	1.5	2.8	0.39	0.030	0.9	3.6
P1485N-B2	B	16.1	1.9	2.3	2.7	0.47	0.040	1.1	3.4
P1485N-B3	B	16.9	1.9	2.4	2.8	0.51	0.040	1.5	3.7
P1485N-B4	B	15.6	1.8	2.1	2.8	0.42	0.041	1.0	3.4
P1485N-B5	B	16.7	1.8	2.4	3.1	0.48	0.041	1.2	3.5
P1485N-B6	B	15.7	1.8	2.3	2.8	0.46	0.041	0.7	3.4
P1485N-B7	B	16.4	2.0	2.3	2.8	0.47	0.040	1.4	3.6
P1485N-B8	B	16.3	1.9	2.3	2.9	0.45	0.050	1.1	3.5
P1485N-B9	B	16.4	1.9	2.3	2.9	0.47	0.041	1.2	3.5
P1485N-B10	B	16.1	2.1	2.0	2.9	0.42	0.030	0.9	3.7
P1485N-B11	B	15.9	1.8	2.1	3.0	0.41	0.040	1.1	3.4
P1485N-B12	B	16.4	2.0	2.2	2.7	0.46	0.040	1.5	3.6
P1485N-B13	B	16.5	2.0	2.4	2.7	0.49	0.041	1.1	3.6
P1485N-B14	B	15.6	1.9	1.9	2.8	0.41	0.040	1.0	3.5
P1485N-B15	B	17.1	2.0	2.3	3.2	0.47	0.040	1.4	3.6
P1485N-B16	B	16.5	1.9	2.2	2.9	0.44	0.040	1.2	3.6
P1485N-B17	B	15.6	1.8	2.0	2.7	0.39	0.040	1.0	3.4
P1485N-B1PF1	B	15.6	1.9	2.0	2.7	0.41	0.040	0.8	3.4
P1485N-B1PF2	B	16.3	1.9	2.1	2.9	0.43	0.040	1.0	3.5
P1485N-B1PF3	B	16.1	1.8	2.2	2.9	0.46	0.040	1.1	3.4
P1485N-B1PF4	S	15.9	1.9	1.6	3.1	0.34	0.020	0.9	3.6
P1485N-B1PF5	S	15.0	1.3	1.4	3.5	0.25	0.010	1.2	3.0
P1485N-B1PF6	S	15.8	1.8	1.4	3.3	0.28	0.020	1.1	3.6
P1471S-B2	B	14.9	1.9	1.7	2.8	0.35	0.030	1.3	3.4
P1471S-B3	B	16.0	2.1	1.9	3.0	0.41	0.030	1.5	3.6
P1471S-B4	B	15.6	2.0	1.9	2.9	0.40	0.030	1.1	3.6
P1471S-B5	B	15.8	1.9	2.1	2.9	0.42	0.040	1.2	3.5
P1471S-B6	B	15.1	1.9	2.0	2.6	0.38	0.030	1.1	3.5
P1471S-B7	B	15.3	2.0	2.0	2.8	0.42	0.030	1.0	3.5
P1471S-B8	B	15.0	1.9	1.7	3.0	0.37	0.030	1.6	3.3
P1471S-B9	B	15.5	2.0	2.0	2.7	0.41	0.040	1.2	3.5
P1471S-B10	B	15.7	2.0	1.9	3.0	0.39	0.030	1.7	3.6
P1471S-B11	B	15.6	1.8	1.9	2.8	0.34	0.030	1.2	3.5
P1471S-B12	B	15.5	2.1	2.0	2.7	0.43	0.040	0.8	3.5
P1471S-B13	B	15.9	2.1	2.0	2.6	0.44	0.040	1.5	3.7
P1471S-B14	B	15.5	2.1	2.0	2.7	0.42	0.030	1.3	3.6
P1471S-B15	B	15.3	1.9	1.7	3.1	0.35	0.030	1.2	3.4
P1471S-B16	B	15.2	1.9	2.0	2.8	0.38	0.040	1.6	3.4
P1471S-B17	B	15.1	1.8	2.0	2.6	0.36	0.030	1.2	3.4
P1471S-B1-PF1	B	15.1	1.9	1.8	2.6	0.37	0.040	1.6	3.5
P1471S-B1-PF2	B	15.8	2.0	1.9	2.9	0.39	0.030	1.5	3.6
P1471S-B1-PF3	B	15.5	1.9	1.8	3.1	0.36	0.030	1.2	3.5
P1471S-B1-PF4	B	19.1	1.7	2.6	3.4	0.58	0.041	0.5	4.6
P1471S-B1-PF5	B	17.5	1.2	2.7	3.5	0.49	0.030	1.2	3.9
P1471S-B1-PF6	B	17.0	0.4	1.8	3.5	0.46	0.020	1.8	3.8
P1471S-B1-PF7	S	15.2	1.6	1.8	2.8	0.35	0.030	1.6	3.5
P1277S-B2	B	14.5	2.2	1.1	2.9	0.28	0.030	1.4	3.7
P1277S-B3	B	15.3	2.3	1.3	3.0	0.34	0.030	1.8	3.8

Sample Name	Type	Al ₂ O ₃ %	CaO %	Fe ₂ O ₃ %	K ₂ O %	MgO %	MnO %	Mo ppm	Na ₂ O %
P1277S-B4	B	14.6	2.1	1.4	2.9	0.34	0.030	1.9	3.6
P1277S-B5	B	15.0	2.2	1.2	3.0	0.32	0.030	1.4	3.7
P1277S-B6	B	14.1	2.1	1.1	3.0	0.28	0.030	1.5	3.6
P1277S-B7	B	14.4	2.2	1.1	2.8	0.28	0.030	1.3	3.6
P1277S-B8	B	14.5	2.1	1.3	2.7	0.33	0.030	1.3	3.6
P1277S-B9	B	14.6	2.1	1.2	3.0	0.30	0.030	1.3	3.6
P1277S-B10	B	14.7	2.2	1.2	2.9	0.31	0.040	1.4	3.7
P1277S-B11	B	14.6	2.2	1.2	2.9	0.31	0.030	1.1	3.7
P1277S-B12	B	13.9	2.0	1.2	2.9	0.29	0.030	1.1	3.4
P1277S-B13	B	15.1	2.2	1.4	2.7	0.38	0.020	1.3	3.8
P1277S-B14	B	14.2	2.0	1.2	3.2	0.30	0.030	1.3	3.4
P1277S-B15	B	14.6	2.2	1.2	2.8	0.32	0.030	1.6	3.7
P1277S-B16	B	14.6	2.1	1.2	3.2	0.30	0.030	1.4	3.5
P1277S-B17	B	14.6	2.0	1.3	2.8	0.33	0.030	1.1	3.6
P1277S-B1-PF1	B	14.8	2.2	1.2	3.2	0.28	0.030	1.1	3.7
P1277S-B1-PF2	B	14.8	2.2	1.3	2.9	0.32	0.030	1.2	3.7
P1277S-B1-PF3	B	14.1	2.1	1.3	2.5	0.33	0.030	1.5	3.6
P1277S-B1-PF4	B	14.9	2.2	1.5	2.8	0.37	0.030	1.3	3.7
P1277S-B1-PF5	B	15.6	2.4	1.6	2.7	0.42	0.030	1.1	4.0
P1277S-B1-PF6	B	15.2	2.2	1.6	2.8	0.38	0.020	1.2	3.8
P1277S-B1-PF7	B	15.5	2.1	1.5	3.8	0.37	0.020	1.1	3.6
P1277S-B1-PF8	S	15.0	2.3	1.7	2.5	0.42	0.030	1.1	3.8
P1264N-B2	B	14.9	2.3	1.7	2.6	0.43	0.041	1.1	3.7
P1264N-B3	B	15.2	2.2	1.8	2.9	0.42	0.040	1.2	3.7
P1264N-B4	B	15.3	2.2	1.6	3.1	0.38	0.040	1.6	3.7
P1264N-B5	B	15.3	2.2	1.5	3.1	0.36	0.040	1.3	3.8
P1264N-B6	B	14.2	2.1	1.4	2.9	0.33	0.040	1.2	3.5
P1264N-B7	B	15.4	2.2	1.7	3.1	0.41	0.040	1.2	3.7
P1264N-B8	B	15.0	2.3	1.8	2.5	0.44	0.040	1.3	3.8
P1264N-B9	B	15.9	2.4	1.9	2.8	0.46	0.040	1.1	4.0
P1264N-B10	B	15.1	2.2	1.7	2.9	0.43	0.041	1.2	3.7
P1264N-B11	B	16.1	2.4	2.1	2.8	0.52	0.040	1.2	4.0
P1264N-B12	B	15.3	2.2	1.6	3.3	0.39	0.041	1.2	3.7
P1264N-B13	B	14.8	2.2	1.7	2.7	0.39	0.040	1.3	3.7
P1264N-B14	B	15.5	2.2	1.7	3.4	0.42	0.040	1.1	3.7
P1264N-B15	B	15.5	2.4	2.0	2.6	0.49	0.051	1.1	3.9
P1264N-B16	B	15.4	2.3	1.7	2.8	0.41	0.041	1.2	3.8
P1264N-B17	B	15.4	2.4	1.9	2.8	0.46	0.051	1.1	3.8
P1264N-B1PF1	B	15.6	2.4	1.8	2.9	0.44	0.051	1.2	3.9
P1264N-B1PF2	B	15.6	2.4	1.9	2.6	0.47	0.041	1.2	3.9
P1264N-B1PF3	B	15.2	2.3	1.9	2.7	0.45	0.041	1.5	3.8
P1264N-B1PF4	B	15.6	2.3	1.8	2.9	0.45	0.030	1.1	3.9
P1264N-B1PF5	B	15.3	2.1	1.7	3.1	0.41	0.030	1.2	3.7
P1264N-B1PF6	B	16.2	2.3	2.2	3.1	0.53	0.041	0.7	3.9
P1264N-B1PF7	B	16.1	1.9	2.2	3.4	0.51	0.031	1.2	3.9
P1264N-B1PF8	S	13.5	0.8	1.2	4.0	0.32	0.031	1.8	3.0
P1264N-B1PF9	S	15.5	1.6	1.8	4.0	0.43	0.031	1.1	3.7
P1264N-B1PF10	S	15.2	1.1	1.5	3.7	0.35	0.020	1.5	3.8
P1264N-B1PF11	S	13.6	1.6	1.2	3.7	0.31	0.020	1.6	3.0

Sample Name	Type	Al ₂ O ₃ %	CaO %	Fe ₂ O ₃ %	K ₂ O %	MgO %	MnO %	Mo ppm	Na ₂ O %
P1062S-B2	B	16.5	2.3	2.4	2.9	0.60	0.051	0.8	3.8
P1062S-B3	B	16.4	2.1	2.3	3.0	0.54	0.041	1.3	3.8
P1062S-B4	B	15.3	2.0	1.9	3.1	0.45	0.030	1.3	3.5
P1062S-B5	B	15.9	2.3	2.1	2.8	0.51	0.041	1.3	3.8
P1062S-B6	B	15.6	1.2	2.3	3.3	0.39	0.020	1.1	3.1
P1062S-B7	B	16.3	2.0	1.8	3.7	0.43	0.031	1.2	3.7
P1062S-B8	B	16.1	2.1	2.2	3.1	0.55	0.041	1.0	3.7
P1062S-B9	B	15.6	2.2	1.8	2.8	0.43	0.040	1.3	3.7
P1062S-B10	B	16.4	2.2	2.3	2.8	0.57	0.041	1.0	3.8
P1062S-B11	B	16.5	2.2	2.5	2.8	0.62	0.040	0.8	3.8
P1062S-B12	B	15.5	1.8	1.8	3.1	0.41	0.020	1.2	3.5
P1062S-B13	B	16.5	2.2	2.3	2.9	0.56	0.040	1.1	3.8
P1062S-B14	B	15.6	2.2	2.0	2.9	0.46	0.030	1.1	3.7
P1062S-B15	B	15.2	2.1	1.8	2.8	0.42	0.030	1.3	3.6
P1062S-B16	B	15.8	2.1	2.0	3.0	0.47	0.031	1.3	3.7
P1062S-B17	B	15.3	2.2	1.7	3.3	0.42	0.030	1.1	3.6
P1062S-B1-PF1	B	16.0	2.3	2.2	2.8	0.53	0.051	1.0	3.8
P1062S-B1-PF2	B	16.6	2.2	2.3	3.0	0.56	0.040	1.1	3.8
P1062S-B1-PF3	B	16.8	2.3	2.6	2.8	0.65	0.051	1.0	3.9
P1062S-B1-PF4	B	18.3	2.3	3.6	3.1	0.84	0.051	0.8	3.7
P1062S-B1-PF5	B	18.0	2.2	3.5	2.9	0.82	0.061	1.1	3.7
P1062S-B1-PF6	B	18.8	2.3	4.1	2.8	0.96	0.062	1.3	3.7
P1062S-B1-PF7	B	19.2	2.3	4.4	2.7	1.03	0.061	1.4	3.7
P1062S-B1-PF8	B	19.2	2.3	4.4	2.7	1.08	0.102	1.1	3.7
P1062N-B2	B	16.9	2.3	2.5	2.9	0.60	0.040	1.2	3.7
P1062N-B3	B	17.1	2.4	2.7	2.8	0.64	0.051	1.2	3.8
P1062N-B4	B	17.2	2.4	2.7	2.9	0.65	0.041	1.1	3.8
P1062N-B5	B	16.1	2.0	2.1	3.2	0.46	0.040	1.0	3.6
P1062N-B6	B	16.4	2.1	2.4	2.8	0.55	0.041	0.9	3.7
P1062N-B7	B	16.9	2.4	2.5	2.9	0.61	0.051	1.6	3.8
P1062N-B8	B	17.0	2.4	2.6	2.8	0.62	0.051	1.2	3.8
P1062N-B9	B	16.4	1.9	2.3	3.0	0.50	0.040	1.4	3.6
P1062N-B10	B	17.0	2.5	2.7	3.0	0.64	0.061	0.9	3.7
P1062N-B11	B	16.5	2.2	2.3	2.9	0.52	0.040	1.4	3.7
P1062N-B12	B	16.5	2.2	2.6	2.7	0.60	0.051	0.9	3.6
P1062N-B13	B	16.2	2.1	2.3	2.7	0.56	0.040	0.8	3.6
P1062N-B14	B	16.8	2.1	2.6	2.9	0.60	0.061	1.0	3.6
P1062N-B15	B	16.6	2.3	2.5	2.8	0.60	0.050	1.5	3.7
P1062N-B16	B	17.0	2.4	2.6	2.9	0.59	0.051	1.1	3.8
P1062N-B17	B	16.3	2.4	2.4	2.9	0.59	0.061	1.5	3.7
P1062N-B1-PF1	B	15.6	2.2	2.2	2.6	0.53	0.040	1.1	3.6
P1062N-B1-PF2	B	17.1	2.3	2.7	2.8	0.64	0.051	1.0	3.8
P1062N-B1-PF3	B	17.5	2.3	2.6	3.2	0.63	0.051	1.0	3.8
P1062N-B1-PF4	B	16.6	2.2	2.6	2.7	0.62	0.051	1.1	3.6
P1062N-B1-PF5	B	16.7	2.3	2.5	2.8	0.60	0.051	1.6	3.7
P1062N-B1-PF6	B	17.1	2.3	2.6	2.9	0.60	0.051	1.5	3.7
P1062N-B1-PF7	B	15.6	2.2	2.2	2.5	0.61	0.030	1.1	3.5
P1062N-B1-S1	S	16.5	2.2	1.9	3.7	0.45	0.031	1.0	3.7

Table F.2: Pilot Peak sample compositions (Nb to Zr)
Type X=rock, B=soil, S=saprolite

Sample Name	Type	Nb ppm	P ₂ O ₅ %	Rb ppm	SiO ₂ %	Sr ppm	Th ppm	TiO ₂ %	Y ppm	Zr ppm
P2280-X1	X	15.7	0.087	73	72.5	697	6.4	0.26	9.8	129
P2280-X2	X	13.6	0.071	75	73.2	684	9.1	0.21	9.6	117
P2280-X3	X	17.9	0.106	89	73.0	637	13.3	0.28	11.2	132
P2280-X4	X	15.6	0.079	69	73.6	660	6.5	0.25	8.6	136
P2280-X5	X	10.0	0.052	72	78.2	546	7.1	0.16	7.4	112
P2280-X6	X	13.0	0.055	62	70.3	859	9.2	0.23	8.4	94
P2280-X7	X	15.0	0.076	80	70.9	709	4.5	0.24	8.1	116
P2280-X8	X	15.6	0.084	66	73.4	632	7.0	0.24	8.4	119
P2280-X9	X	13.3	0.057	59	70.4	857	8.6	0.24	8.3	103
P2280-X10	X	15.6	0.076	75	73.3	641	5.6	0.23	7.7	122
P2280-X11	X	15.4	0.085	68	73.4	642	7.5	0.25	10.1	130
P2280-X12	X	15.0	0.087	71	73.6	641	5.8	0.24	8.9	130
P2280-X13	X	14.6	0.092	84	72.0	677	6.8	0.23	8.8	123
P2280-X14	X	15.9	0.081	69	74.7	563	6.4	0.22	8.7	123
P2280-X15	X	13.9	0.103	68	72.7	668	4.9	0.23	7.7	125
P2280-X16	X	13.8	0.083	68	74.3	638	5.8	0.23	8.5	135
P2280-X17	X	11.6	0.090	65	75.7	612	9.2	0.19	7.9	106
P2280-X18	X	14.4	0.078	66	74.4	631	6.5	0.24	8.9	134
P2280-X19	X	13.8	0.083	92	71.2	722	5.0	0.24	10.4	127
P2280-X20	X	14.3	0.085	70	73.6	633	7.5	0.24	8.0	123
P2280-X21	X	11.6	0.064	72	74.3	724	8.2	0.17	7.7	75
P2280-X22	X	15.8	0.132	68	73.1	650	5.7	0.25	9.6	131
P2280-X23	X	13.6	0.089	103	75.7	477	3.6	0.24	8.1	123
P2280-X24	X	15.8	0.085	72	72.7	683	7.4	0.26	10.5	128
P2280-X25	X	14.2	0.078	66	74.0	625	7.5	0.23	8.7	122
P2280-X26	X	24.9	0.054	196	76.1	168	1.2	0.05	10.3	36
P2280-X27	X	15.2	0.073	81	71.9	697	5.7	0.24	9.0	119
P2280-X28	X	15.2	0.082	76	72.3	672	6.5	0.24	10.0	119
P2280-X29	X	17.7	0.120	164	70.2	681	9.1	0.31	11.1	72
P2280-X30	X	15.0	0.097	101	76.6	444	5.3	0.23	9.6	123
P2280-X31	X	11.4	0.098	67	73.6	697	8.2	0.19	7.3	111
P2280-X32	X	14.6	0.080	95	71.0	703	4.9	0.22	9.0	116
P2280-X33	X	14.0	0.073	71	74.7	587	7.6	0.21	7.7	113
P2280-X34	X	16.5	0.078	68	74.1	586	5.9	0.25	8.6	131
P2280-X35	X	15.7	0.079	76	72.2	683	5.9	0.24	8.0	114
P2280-X36	X	14.4	0.073	76	73.8	628	8.7	0.23	7.2	124
P2280-X37	X	16.3	0.093	74	73.7	603	8.2	0.24	7.9	120
P2280-X38	X	14.0	0.094	90	72.5	653	6.3	0.22	9.5	120
P2280-X39	X	15.1	0.091	74	72.3	688	6.4	0.26	8.6	130
P2280-X40	X	14.3	0.079	90	71.4	721	7.5	0.23	8.5	112
P2090-X1	X	13.7	0.080	60	74.6	640	6.9	0.24	8.4	135
P2090-X2	X	14.5	0.072	61	74.7	640	5.9	0.24	9.4	122
P2090-X3	X	8.5	0.074	114	70.1	804	2.8	0.15	8.7	104
P2090-X4	X	14.4	0.081	76	72.7	674	5.0	0.24	9.2	125
P2090-X5	X	14.6	0.080	57	74.1	654	7.2	0.24	9.3	129
P2090-X6	X	15.3	0.084	68	73.5	637	7.0	0.23	8.9	121
P2090-X7	X	13.8	0.077	70	74.4	628	6.4	0.24	10.0	124

Sample Name	Type	Nb ppm	P ₂ O ₅ %	Rb ppm	SiO ₂ %	Sr ppm	Th ppm	TiO ₂ %	Y ppm	Zr ppm
P2090-X8	X	14.6	0.099	69	73.7	651	5.0	0.24	9.1	127
P2090-X9	X	14.5	0.079	81	72.9	677	6.1	0.25	10.1	134
P2090-X10	X	12.1	0.072	78	74.9	639	8.9	0.20	8.6	119
P2090-X11	X	13.9	0.072	68	71.2	815	10.2	0.25	7.9	102
P2090-X12	X	12.6	0.100	76	71.8	736	5.8	0.23	7.3	122
P2090-X13	X	11.1	0.097	57	76.3	623	5.7	0.22	8.4	139
P2090-X14	X	11.3	0.088	84	72.2	722	4.5	0.20	9.3	114
P2090-X15	X	12.0	0.080	81	73.0	689	5.0	0.22	9.4	122
P2090-X16	X	15.3	0.088	82	72.0	622	3.8	0.23	8.7	125
P2090-X17	X	15.4	0.110	72	72.1	681	5.2	0.27	8.8	127
P2090-X18	X	14.4	0.081	64	73.5	650	5.0	0.25	7.9	131
P2090-X19	X	12.7	0.085	67	73.6	666	6.0	0.23	8.0	119
P2090-X20	X	13.7	0.075	71	72.9	678	4.3	0.23	7.8	122
P2090-X21	X	15.5	0.080	69	72.7	636	5.4	0.25	8.0	115
P2090-X22	X	13.6	0.094	67	72.8	686	5.4	0.25	9.3	129
P2090-X23	X	5.5	0.067	112	66.7	178	-1.4	0.04	7.2	14
P2090-X24	X	18.2	0.104	117	72.5	576	15.6	0.29	13.2	126
P2090-X25	X	15.9	0.078	68	72.2	713	6.9	0.25	9.1	132
P2090-X26	X	15.7	0.075	106	74.4	435	3.9	0.13	11.3	52
P2090-X27	X	12.6	0.089	74	72.2	701	3.8	0.23	8.5	115
P2090-X28	X	15.7	0.108	66	73.0	661	5.0	0.25	8.2	125
P2090-X29	X	26.7	0.068	81	73.7	502	9.8	0.25	16.2	124
P2090-X30	X	13.1	0.082	72	72.3	713	4.4	0.23	8.5	118
P2090-X31	X	13.1	0.083	62	74.0	633	5.8	0.23	7.4	123
P2090-X32	X	14.6	0.085	69	73.6	634	6.2	0.24	8.2	120
P2090-X33	X	5.7	0.057	179	71.6	151	0.3	0.03	11.1	8
P2090-X34	X	12.8	0.073	76	72.6	695	6.1	0.23	8.3	117
P2090-X35	X	14.0	0.077	72	73.4	663	6.4	0.23	8.3	118
P2090-X36	X	12.0	0.084	70	73.0	706	4.6	0.23	8.9	130
P2090-X37	X	13.9	0.077	70	71.8	721	5.1	0.27	9.4	126
P2090-X38	X	11.9	0.072	65	74.3	770	4.4	0.19	8.8	94
P2090-X39	X	13.7	0.084	60	74.0	652	5.5	0.26	7.5	131
P2090-X40	X	11.7	0.077	79	72.6	716	4.3	0.19	9.0	118
P1850-X1	X	12.8	0.061	92	74.0	656	13.9	0.17	8.9	104
P1850-X2	X	12.6	0.072	69	73.9	658	7.5	0.24	8.9	140
P1850-X3	X	10.2	0.069	63	73.1	710	6.7	0.21	8.4	137
P1850-X4	X	10.4	0.074	75	73.9	693	8.1	0.19	9.4	130
P1850-X5	X	10.9	0.081	70	72.2	747	5.2	0.22	8.8	130
P1850-X6	X	12.9	0.080	65	73.3	652	8.2	0.22	8.5	132
P1850-X7	X	12.0	0.066	74	74.0	672	7.4	0.24	9.1	130
P1850-X8	X	11.3	0.068	69	73.2	714	6.0	0.23	9.0	133
P1850-X9	X	22.7	0.059	114	72.9	370	10.3	0.21	14.0	91
P1850-X10	X	11.4	0.073	54	73.6	684	7.5	0.21	9.2	131
P1850-X11	X	25.2	0.090	117	69.1	674	17.0	0.33	13.1	83
P1850-X12	X	12.3	0.069	57	76.3	583	7.5	0.22	7.6	132
P1850-X13	X	15.8	0.188	70	75.6	512	17.0	0.30	19.7	311
P1850-X14	X	9.6	0.077	53	77.6	568	6.1	0.17	7.4	133
P1850-X15	X	11.6	0.082	64	75.2	628	7.3	0.22	7.6	129
P1850-X16	X	13.7	0.059	106	75.8	549	9.9	0.17	12.2	93
P1850-X17	X	18.0	0.063	114	73.1	556	17.2	0.22	10.9	79

Sample Name	Type	Nb ppm	P ₂ O ₅ %	Rb ppm	SiO ₂ %	Sr ppm	Th ppm	TiO ₂ %	Y ppm	Zr ppm
P1850-X18	X	12.7	0.076	67	74.7	644	8.2	0.23	9.0	132
P1850-X19	X	8.9	0.052	103	76.2	554	9.9	0.12	8.0	83
P1850-X20	X	12.7	0.064	66	73.2	676	8.7	0.24	10.9	129
P1850-X21	X	10.6	0.071	69	75.5	620	5.7	0.21	7.7	124
P1850-X22	X	13.7	0.074	77	74.9	613	9.3	0.24	9.1	142
P1850-X23	X	11.9	0.072	77	74.7	622	6.2	0.22	8.1	127
P1850-X24	X	13.0	0.093	68	72.0	701	6.2	0.25	7.9	124
P1850-X25	X	11.4	0.073	59	77.4	558	7.5	0.20	8.3	136
P1850-X26	X	14.0	0.072	65	74.0	642	7.8	0.23	9.0	140
P1850-X27	X	12.9	0.122	79	72.4	697	6.2	0.23	10.4	131
P1850-X28	X	9.7	0.059	80	77.0	567	10.5	0.14	7.7	80
P1850-X29	X	22.3	0.078	138	74.0	553	28.6	0.26	14.7	113
P1850-X30	X	13.4	0.086	67	75.0	627	4.2	0.21	8.4	126
P1850-X31	X	13.9	0.058	84	73.9	433	6.3	0.16	13.3	98
P1850-X32	X	11.7	0.079	71	76.0	596	6.6	0.22	8.5	135
P1850-X33	X	13.4	0.125	72	71.8	701	6.6	0.26	10.4	142
P1850-X34	X	14.2	0.078	72	74.2	626	6.5	0.24	8.4	129
P1850-X35	X	12.5	0.066	81	72.1	722	7.5	0.23	8.8	142
P1850-X36	X	11.9	0.107	74	72.9	660	6.8	0.22	9.0	132
P1850-X37	X	12.0	0.065	78	73.2	665	6.1	0.22	8.0	125
P1850-X38	X	14.1	0.069	61	74.3	627	6.2	0.25	8.7	127
P1850-X39	X	13.8	0.084	74	71.3	724	6.1	0.24	8.7	126
P1850-X40	X	16.5	0.065	94	71.6	518	10.0	0.22	12.1	158
P1706-X1	X	6.3	0.055	77	76.0	687	4.0	0.10	6.3	101
P1706-X2	X	16.5	0.079	69	73.3	678	7.2	0.24	9.7	128
P1706-X3	X	14.1	0.126	55	76.2	609	9.1	0.21	7.9	141
P1706-X4	X	14.3	0.100	62	74.7	650	10.5	0.22	9.2	139
P1706-X5	X	13.3	0.078	61	74.1	678	7.5	0.22	8.1	138
P1706-X6	X	12.3	0.067	56	75.2	651	8.3	0.20	6.9	128
P1706-X7	X	16.0	0.088	85	71.8	728	6.7	0.21	9.1	124
P1706-X8	X	16.8	0.063	71	73.5	658	8.1	0.24	9.3	131
P1706-X9	X	11.8	0.057	69	80.2	510	11.3	0.18	6.8	106
P1706-X11	X	12.6	0.123	52	76.9	593	7.3	0.21	7.4	140
P1706-X12	X	14.8	0.094	63	75.8	600	7.6	0.24	9.0	143
P1706-X13	X	5.4	0.065	101	74.1	726	3.6	0.09	6.9	91
P1706-X14	X	11.6	0.058	83	73.5	695	6.8	0.19	7.6	122
P1706-X15	X	14.0	0.089	82	71.9	724	6.7	0.22	8.5	129
P1706-X16	X	13.9	0.155	69	74.7	633	5.8	0.22	7.7	131
P1706-X17	X	10.0	0.046	111	75.6	293	2.1	0.08	16.1	47
P1706-X18	X	10.4	0.108	74	74.6	679	9.6	0.17	7.7	114
P1706-X19	X	11.1	0.074	76	78.0	566	11.6	0.18	8.4	102
P1706-X20	X	13.9	0.083	64	74.3	647	6.7	0.24	8.7	136
P1706-X21	X	13.9	0.073	76	73.4	686	7.3	0.23	8.4	131
P1706-X22	X	13.9	0.071	70	73.0	682	7.3	0.23	8.4	132
P1706-X23	X	13.1	0.065	61	75.0	635	6.5	0.21	8.1	128
P1706-X24	X	12.9	0.079	78	73.5	687	7.4	0.20	8.9	120
P1706-X25	X	13.5	0.079	68	73.8	664	7.8	0.23	7.9	130
P1706-X26	X	13.4	0.088	119	74.6	403	1.1	0.13	12.7	80
P1706-X28	X	12.8	0.054	67	74.9	662	7.3	0.12	7.8	131
P1706-X29	X	10.0	0.071	81	73.6	628	6.9	0.21	12.8	97

Sample Name	Type	Nb ppm	P ₂ O ₅ %	Rb ppm	SiO ₂ %	Sr ppm	Th ppm	TiO ₂ %	Y ppm	Zr ppm
P1706-X30	X	15.9	0.060	70	74.2	707	6.8	0.14	10.5	128
P1706-X31	X	15.5	0.071	64	72.0	700	7.6	0.24	8.8	142
P1706-X32	X	12.5	0.077	66	72.1	669	6.5	0.27	7.6	127
P1706-X33	X	14.2	0.074	67	73.6	636	6.8	0.21	8.1	129
P1706-X34	X	15.3	0.068	69	74.5	664	8.1	0.22	7.9	136
P1706-X27	X	21.5	0.074	113	73.4	329	5.2	0.24	17.8	79
P1706-X35	X	14.6	0.093	55	74.9	631	9.8	0.22	8.1	146
P1706-X36	X	13.4	0.085	66	73.9	668	6.3	0.21	9.1	140
P1706-X37	X	6.8	0.057	89	75.5	593	18.9	0.09	9.8	141
P1706-X38	X	14.3	0.079	81	72.5	699	5.8	0.23	9.1	126
P1706-X39	X	13.4	0.075	77	72.3	707	7.9	0.22	8.5	122
P1706-X40	X	16.4	0.079	66	72.1	695	9.0	0.25	8.2	131
P1480-X1	X	14.8	0.061	84	71.1	758	5.7	0.21	9.4	121
P1480-X2	X	14.2	0.069	73	71.7	747	8.1	0.23	9.1	134
P1480-X3	X	14.7	0.070	95	72.3	665	5.0	0.21	11.8	117
P1480-X4	X	13.9	0.070	83	72.6	711	7.9	0.22	9.2	131
P1480-X5	X	12.8	0.063	55	75.0	626	7.5	0.21	8.3	135
P1480-X6	X	15.4	0.072	101	73.9	449	5.1	0.15	26.2	75
P1480-X7	X	12.6	0.065	67	73.5	689	6.1	0.22	9.3	125
P1480-X8	X	13.3	0.063	59	74.3	685	6.4	0.22	7.9	127
P1480-X9	X	11.0	0.048	67	74.8	668	6.4	0.18	8.6	112
P1480-X10	X	15.6	0.065	65	73.7	654	9.7	0.25	9.6	150
P1480-X11	X	14.8	0.098	55	75.2	642	8.1	0.25	8.1	141
P1480-X12	X	13.4	0.066	71	73.7	715	7.8	0.23	8.9	127
P1480-X13	X	12.9	0.073	57	73.8	706	7.3	0.24	7.9	136
P1480-X14	X	13.0	0.130	69	70.4	821	9.6	0.24	8.2	140
P1480-X15	X	13.4	0.084	64	73.2	734	5.8	0.24	7.9	136
P1480-X16	X	16.2	0.073	69	71.9	746	8.9	0.30	8.8	142
P1480-X17	X	14.8	0.080	52	74.7	669	7.1	0.26	8.1	147
P1480-X18	X	14.4	0.078	60	74.4	682	10.6	0.26	8.1	151
P1480-X19	X	13.3	0.078	62	72.3	759	8.7	0.25	8.3	144
P1480-X20	X	13.4	0.075	59	72.5	767	7.8	0.25	8.4	141
P1480-X21	X	12.9	0.072	59	74.3	689	8.5	0.23	7.9	141
P1480-X22	X	13.2	0.092	65	77.7	546	5.7	0.21	7.8	112
P1480-X23	X	16.1	0.063	189	78.7	60	6.9	0.27	8.5	151
P1480-X24	X	16.9	0.081	73	73.0	668	8.3	0.25	10.4	133
P1480-X25	X	16.0	0.070	138	73.7	525	8.6	0.23	9.0	138
P1480-X26	X	12.6	0.070	65	72.0	782	6.9	0.22	7.4	133
P1480-X27	X	13.7	0.076	56	72.3	763	7.8	0.24	8.3	137
P1480-X28	X	14.8	0.079	77	71.6	728	8.2	0.25	8.7	133
P1480-X29	X	17.1	0.082	78	73.6	639	5.9	0.25	9.5	125
P1480-X30	X	13.8	0.073	65	74.1	654	7.7	0.24	9.1	133
P1480-X31	X	11.6	0.065	81	73.3	699	6.9	0.20	8.4	116
P1480-X32	X	5.6	0.058	118	77.1	438	5.1	0.08	10.9	68
P1480-X33	X	9.4	0.066	84	73.2	715	8.4	0.16	9.6	103
P1480-X34	X	12.4	0.073	62	75.2	619	7.1	0.22	7.7	138
P1480-X35	X	13.9	0.064	84	72.1	691	6.4	0.22	8.4	120
P1480-X36	X	14.1	0.062	86	74.7	599	7.2	0.22	11.0	123
P1480-X37	X	13.1	0.067	71	73.0	682	5.5	0.22	8.4	132
P1480-X38	X	11.4	0.064	103	71.7	736	6.8	0.20	8.4	104

Sample Name	Type	Nb ppm	P ₂ O ₅ %	Rb ppm	SiO ₂ %	Sr ppm	Th ppm	TiO ₂ %	Y ppm	Zr ppm
P1480-X39	X	13.6	0.064	88	75.5	398	2.2	0.14	10.8	68
P1480-X40	X	14.0	0.077	60	73.9	691	7.4	0.24	8.4	138
P1270-X1	X	17.0	0.071	69	74.3	596	8.2	0.21	10.1	127
P1270-X2	X	12.8	0.072	94	72.4	665	7.0	0.18	9.7	117
P1270-X3	X	16.1	0.071	65	74.9	595	7.6	0.23	9.6	138
P1270-X4	X	16.5	0.064	65	75.0	608	7.5	0.22	8.9	135
P1270-X5	X	14.0	0.067	77	73.3	681	7.3	0.20	10.1	118
P1270-X6	X	17.5	0.061	80	72.5	674	6.4	0.24	8.9	124
P1270-X7	X	15.6	0.071	88	73.3	656	7.1	0.22	9.4	119
P1270-X8	X	21.7	0.067	164	75.6	374	4.5	0.13	16.7	81
P1270-X9	X	18.5	0.047	152	76.4	36	4.4	0.04	34.4	49
P1270-X10	X	12.1	0.057	102	72.4	699	4.9	0.17	8.4	105
P1270-X11	X	14.2	0.072	86	72.0	695	6.5	0.20	9.5	121
P1270-X12	X	12.5	0.070	95	71.7	714	7.2	0.19	9.3	116
P1270-X13	X	17.0	0.066	67	73.9	627	7.1	0.23	9.4	126
P1270-X14	X	17.5	0.066	77	73.8	638	5.6	0.23	9.4	128
P1270-X15	X	16.5	0.073	64	74.8	606	8.2	0.24	8.9	138
P1270-X16	X	15.2	0.075	79	71.6	719	6.3	0.23	9.5	123
P1270-X17	X	15.2	0.065	67	74.3	627	6.9	0.22	8.5	127
P1270-X18	X	19.8	0.048	177	76.0	22	2.7	0.04	22.8	34
P1270-X19	X	13.9	0.069	73	73.4	657	8.0	0.21	8.6	127
P1270-X20	X	14.0	0.063	55	75.0	629	6.6	0.20	7.9	127
P1270-X21	X	15.5	0.074	73	72.2	685	5.4	0.23	9.1	134
P1270-X22	X	15.1	0.068	78	73.9	623	6.5	0.21	9.2	131
P1270-X23	X	13.8	0.075	65	74.1	636	5.9	0.21	8.7	129
P1270-X24	X	14.1	0.054	60	75.0	598	7.4	0.22	8.1	138
P1270-X25	X	15.6	0.078	76	72.8	656	9.0	0.23	8.7	132
P1270-X26	X	15.0	0.063	73	72.7	660	7.6	0.21	8.6	129
P1270-X27	X	14.6	0.076	73	73.5	648	6.6	0.20	8.3	118
P1270-X28	X	16.1	0.149	77	73.3	627	7.1	0.23	9.1	126
P1270-X29	X	16.0	0.086	64	74.0	612	8.6	0.24	9.3	136
P1270-X30	X	16.6	0.075	94	71.5	672	8.4	0.21	9.2	123
P1270-X31	X	14.4	0.067	81	71.7	692	5.7	0.19	9.8	123
P1270-X32	X	16.4	0.074	86	72.1	662	7.0	0.22	9.8	125
P1270-X33	X	16.1	0.069	64	74.4	616	9.1	0.23	9.0	134
P1270-X34	X	17.9	0.070	69	75.4	583	7.1	0.24	9.5	129
P1270-X35	X	12.4	0.041	193	74.9	45	1.7	0.04	25.9	30
P1270-X36	X	13.6	0.066	61	75.3	609	9.1	0.21	7.7	149
P1270-X37	X	20.5	0.055	93	71.0	683	18.7	0.32	8.5	96
P1270-X38	X	13.0	0.055	60	76.2	580	6.8	0.19	7.6	132
P1270-X39	X	15.4	0.066	72	72.5	664	8.1	0.22	8.9	117
P1270-X40	X	17.3	0.072	72	72.9	644	7.1	0.23	9.8	132
P1062-X1	X	13.3	0.066	81	72.6	703	9.2	0.20	8.2	121
P1062-X2	X	15.6	0.067	70	73.9	663	12.0	0.23	9.4	126
P1062-X3	X	11.8	0.060	80	74.5	662	7.7	0.17	9.3	114
P1062-X4	X	14.6	0.060	65	73.2	695	7.7	0.21	9.1	126
P1062-X5	X	15.7	0.071	73	74.0	660	11.6	0.23	9.4	133
P1062-X6	X	15.3	0.064	73	72.6	703	8.5	0.23	9.1	127
P1062-X7	X	17.0	0.068	67	73.9	647	9.2	0.25	8.6	134

Sample Name	Type	Nb ppm	P ₂ O ₅ %	Rb ppm	SiO ₂ %	Sr ppm	Th ppm	TiO ₂ %	Y ppm	Zr ppm
P1062-X8	X	15.8	0.084	60	75.1	612	11.1	0.24	9.2	145
P1062-X9	X	15.6	0.079	71	73.5	667	11.2	0.23	10.1	149
P1062-X10	X	15.2	0.071	73	73.7	669	10.7	0.23	9.7	135
P1062-X11	X	13.3	0.074	73	72.7	712	7.3	0.21	9.1	121
P1062-X12	X	14.1	0.069	69	75.7	605	7.2	0.22	8.8	137
P1062-X13	X	13.4	0.068	72	72.8	686	6.7	0.22	7.7	119
P1062-X14	X	13.9	0.079	74	72.3	703	8.4	0.20	8.5	127
P1062-X15	X	15.0	0.077	69	76.3	531	7.4	0.22	9.2	147
P1062-X16	X	15.6	0.082	69	73.0	680	7.3	0.23	9.9	142
P1062-X17	X	15.8	0.081	71	74.0	636	9.7	0.24	9.6	135
P1062-X18	X	13.6	0.066	77	73.2	680	5.8	0.20	9.1	127
P1062-X19	X	15.0	0.067	75	72.9	675	6.6	0.23	8.5	129
P1062-X20	X	15.8	0.077	67	72.3	691	7.2	0.24	9.1	135
P1062-X21	X	12.4	0.056	92	73.7	594	4.4	0.15	11.3	101
P1062-X22	X	14.0	0.062	72	73.1	670	7.4	0.23	8.2	122
P1062-X23	X	15.7	0.068	65	74.2	637	8.8	0.24	7.9	139
P1062-X24	X	15.8	0.076	65	74.1	651	7.1	0.23	8.8	134
P1062-X25	X	13.6	0.065	76	71.9	734	7.9	0.21	7.7	122
P1062-X26	X	12.2	0.063	72	73.8	674	7.2	0.19	7.9	133
P1062-X27	X	16.3	0.074	67	74.1	632	7.8	0.24	9.2	142
P1062-X28	X	14.3	0.071	68	72.9	695	6.6	0.21	8.9	124
P1062-X29	X	14.0	0.071	80	72.0	718	7.3	0.22	8.9	128
P1062-X30	X	16.0	0.068	73	73.4	651	7.1	0.25	9.8	139
P1062-X31	X	14.8	0.076	65	76.0	585	8.6	0.23	9.4	142
P1062-X32	X	15.2	0.085	78	73.1	568	6.4	0.23	8.3	130
P1062-X33	X	12.2	0.068	69	73.6	683	6.8	0.18	8.4	120
P1062-X34	X	12.5	0.065	65	74.2	658	7.0	0.20	7.7	124
P1062-X35	X	14.2	0.065	70	73.4	674	5.7	0.22	8.2	123
P1062-X36	X	12.8	0.062	73	73.8	669	6.4	0.20	7.8	118
P1062-X37	X	14.7	0.064	62	72.7	707	7.6	0.22	8.1	121
P1062-X38	X	14.9	0.070	65	74.2	650	7.7	0.23	8.9	139
P1062-X39	X	13.7	0.065	74	74.5	599	7.3	0.22	8.0	120
P1062-X40	X	13.3	0.067	72	73.9	655	6.3	0.22	8.0	131
P2283S-B2	B	16.1	0.082	87	72.2	557	6.7	0.32	9.1	147
P2283S-B3	B	14.5	0.095	95	72.9	562	5.4	0.28	9.4	138
P2283S-B4	B	15.4	0.107	84	73.3	532	6.5	0.31	9.4	138
P2283S-B5	B	15.5	0.089	82	72.8	567	6.1	0.29	9.3	144
P2283S-B6	B	15.6	0.104	82	73.2	558	5.9	0.29	9.6	141
P2283S-B7	B	14.8	0.104	85	72.5	577	6.5	0.29	9.5	138
P2283S-B8	B	15.9	0.119	88	71.5	597	5.9	0.30	9.7	133
P2283S-B9	B	15.9	0.120	84	72.0	590	6.5	0.30	9.8	135
P2283S-B10	B	17.6	0.101	88	71.9	552	6.6	0.34	9.9	143
P2283S-B11	B	14.2	0.087	83	74.0	541	7.9	0.27	9.6	136
P2283S-B12	B	15.6	0.092	87	72.7	571	6.5	0.28	8.8	141
P2283S-B13	B	14.2	0.118	84	73.1	567	6.1	0.27	8.7	129
P2283S-B14	B	16.4	0.096	89	71.5	571	8.0	0.32	10.0	142
P2283S-B15	B	15.7	0.094	78	73.6	554	4.9	0.28	8.5	142
P2283S-B16	B	14.8	0.093	75	74.6	532	6.1	0.28	8.8	142
P2283S-B17	B	16.4	0.114	84	72.4	571	6.4	0.32	9.6	141
P2283S-B1-PF1	B	14.3	0.098	80	73.8	550	5.9	0.27	8.6	138

Sample Name	Type	Nb ppm	P ₂ O ₅ %	Rb ppm	SiO ₂ %	Sr ppm	Th ppm	TiO ₂ %	Y ppm	Zr ppm
P2283S-B1-PF2	B	17.8	0.103	91	70.4	603	5.9	0.34	9.7	143
P2283S-B1-PF3	B	15.8	0.088	87	72.2	579	5.6	0.29	9.5	138
P2283S-B1-PF4	B	15.3	0.091	80	73.9	542	7.3	0.28	9.1	136
P2283S-B1-PF5	B	14.8	0.086	84	74.1	527	4.5	0.28	10.2	142
P2283S-B1-PF6	B	14.3	0.083	75	75.1	505	6.5	0.28	9.1	141
P2283S-B1-PF7	B	16.7	0.089	87	72.2	555	7.0	0.33	9.6	146
P2281N-B2	B	18.3	0.139	85	71.2	556	7.6	0.36	11.0	141
P2281N-B3	B	16.0	0.124	83	72.9	540	7.7	0.32	9.7	145
P2281N-B4	B	15.8	0.128	81	73.6	530	7.5	0.30	9.6	129
P2281N-B5	B	17.0	0.156	93	70.7	573	8.4	0.35	10.5	142
P2281N-B6	B	16.9	0.156	91	71.4	562	7.6	0.34	9.9	145
P2281N-B7	B	14.1	0.148	83	72.9	555	6.2	0.30	9.2	138
P2281N-B8	B	16.4	0.135	86	72.4	528	5.3	0.34	10.0	139
P2281N-B9	B	17.0	0.140	88	71.9	535	8.9	0.34	10.3	140
P2281N-B10	B	15.8	0.132	81	73.4	518	4.3	0.31	9.7	147
P2281N-B11	B	17.0	0.156	88	72.1	527	8.7	0.36	10.1	140
P2281N-B12	B	14.7	0.138	81	74.6	497	6.6	0.30	9.4	129
P2281N-B13	B	16.0	0.144	85	72.4	527	7.7	0.33	9.6	138
P2281N-B14	B	14.0	0.102	78	74.3	533	6.1	0.27	9.0	138
P2281N-B15	B	18.0	0.119	87	71.3	559	6.7	0.35	9.7	138
P2281N-B16	B	16.3	0.132	86	71.8	553	10.3	0.32	10.0	143
P2281N-B17	B	17.3	0.121	86	71.5	555	9.0	0.35	10.3	144
P2281N-B1-PF1	B	16.5	0.153	89	71.6	568	8.4	0.33	9.8	138
P2281N-B1-PF2	B	15.6	0.133	83	73.1	528	6.4	0.31	9.5	130
P2281N-B1-PF3	B	17.2	0.145	87	71.4	553	7.8	0.35	10.0	141
P2281N-B1-PF4	B	15.8	0.135	85	72.5	536	7.8	0.32	10.2	145
P2281N-B1-PF5	B	17.4	0.151	84	72.5	505	7.4	0.34	10.0	140
P2281N-B1-PF6	B	15.2	0.108	80	75.1	473	4.9	0.24	8.6	121
P2281N-B1-PF7	B	16.6	0.100	75	74.5	498	6.1	0.25	9.0	121
P2090-B2	B	15.1	0.150	86	71.3	582	6.3	0.35	10.3	141
P2090-B3	B	12.8	0.123	70	76.1	479	6.1	0.31	9.6	140
P2090-B4	B	15.0	0.143	79	72.2	565	5.4	0.35	10.8	142
P2090-B5	B	15.0	0.140	77	72.9	515	6.0	0.38	10.1	137
P2090-B6	B	13.3	0.132	76	74.2	518	5.5	0.32	9.6	141
P2090-B7	B	13.9	0.153	78	73.0	561	6.6	0.34	10.5	137
P2090-B8	B	13.7	0.137	76	74.0	520	6.8	0.33	10.0	138
P2090-B9	B	14.5	0.140	76	73.2	544	5.9	0.33	9.8	139
P2090-B10	B	13.6	0.126	80	73.8	531	5.7	0.31	9.7	135
P2090-B11	B	14.2	0.134	80	72.5	547	5.5	0.36	10.0	143
P2090-B12	B	13.6	0.122	72	74.7	514	4.9	0.32	9.0	141
P2090-B13	B	12.8	0.138	79	73.8	545	7.0	0.32	9.4	127
P2090-B14	B	12.9	0.127	78	74.1	534	5.4	0.31	9.8	132
P2090-B15	B	13.2	0.132	75	74.7	510	5.3	0.31	9.3	138
P2090-B16	B	14.4	0.134	77	74.1	510	5.7	0.34	9.5	135
P2090-B17	B	12.3	0.121	79	74.3	542	3.4	0.29	9.1	133
P2090-B1PF1	B	13.0	0.130	76	74.8	515	5.6	0.29	9.6	129
P2090-B1PF2	B	14.3	0.129	76	74.2	524	7.3	0.34	9.9	138
P2090-B1PF3	B	15.5	0.128	79	72.3	551	6.2	0.37	9.9	145
P2090-B1PF4	B	12.8	0.101	77	74.3	557	6.3	0.28	9.1	133

Sample Name	Type	Nb ppm	P ₂ O ₅ %	Rb ppm	SiO ₂ %	Sr ppm	Th ppm	TiO ₂ %	Y ppm	Zr ppm
P2090-B1PF5	B	14.9	0.100	81	71.8	588	6.4	0.34	10.1	135
P2090-B1PF6	B	14.1	0.087	85	72.4	588	5.9	0.30	9.6	137
P2090-B1PF7	S	15.4	0.074	84	72.8	659	6.4	0.26	8.5	121
P2090-B1PF8	S	10.8	0.071	106	70.6	776	1.1	0.18	8.0	108
P1850-B2	B	15.5	0.082	99	73.0	497	6.6	0.22	12.2	105
P1850-B3	B	16.8	0.073	101	73.8	441	6.9	0.20	14.3	102
P1850-B4	B	16.2	0.071	95	73.0	510	6.7	0.23	11.5	115
P1850-B5	B	13.9	0.063	83	73.5	563	6.7	0.24	10.5	121
P1850-B6	B	15.9	0.075	94	71.7	603	7.3	0.30	10.5	132
P1850-B7	B	16.7	0.088	101	72.9	467	5.6	0.22	12.6	109
P1850-B8	B	16.5	0.080	102	73.1	455	6.1	0.22	12.7	106
P1850-B9	B	12.4	0.061	87	72.7	638	6.6	0.23	8.8	126
P1850-B10	B	14.4	0.066	84	73.0	608	8.4	0.27	9.5	130
P1850-B11	B	16.1	0.090	91	73.4	509	6.1	0.24	11.6	122
P1850-B12	B	15.6	0.088	99	72.8	500	6.9	0.22	12.4	108
P1850-B13	B	15.2	0.072	84	73.4	554	7.3	0.26	10.7	133
P1850-B14	B	15.9	0.073	90	72.0	612	7.0	0.30	10.6	143
P1850-B15	B	14.0	0.061	85	73.3	583	6.4	0.25	9.4	121
P1850-B16	B	14.1	0.067	85	74.3	530	6.8	0.23	10.9	126
P1850-B17	B	13.9	0.081	87	74.4	523	6.9	0.21	10.8	119
P1850-B1PF1	B	15.2	0.075	89	73.2	533	5.6	0.23	10.3	116
P1850-B1PF2	B	15.8	0.068	86	73.2	546	7.4	0.25	10.4	123
P1850-B1PF3	B	14.2	0.060	89	73.3	550	6.8	0.22	9.9	118
P1850-B1PF4	B	13.1	0.060	88	73.8	544	7.5	0.21	9.4	116
P1850-B1PF5	S	14.7	0.059	86	72.4	623	5.5	0.25	9.2	123
P1850-B1PF6	S	16.3	0.058	78	72.2	616	7.4	0.28	10.0	134
P1850-B1PF7	S	15.1	0.056	74	71.4	679	8.2	0.27	9.0	141
P1706-B2	B	15.1	0.085	72	72.9	670	6.7	0.26	9.7	138
P1706-B3	B	14.7	0.071	66	73.2	676	8.3	0.24	9.1	131
P1706-B4	B	16.9	0.073	80	71.8	672	10.1	0.30	11.7	141
P1706-B5	B	14.7	0.077	75	73.3	650	8.4	0.25	10.3	137
P1706-B6	B	13.6	0.072	80	74.0	640	9.0	0.23	10.1	130
P1706-B7	B	15.7	0.069	83	71.5	692	8.4	0.28	9.9	133
P1706-B8	B	16.1	0.079	75	72.0	676	12.2	0.29	10.6	138
P1706-B9	B	15.9	0.073	77	72.7	656	10.7	0.28	10.7	137
P1706-B10	B	14.5	0.075	76	73.5	642	9.4	0.25	10.5	132
P1706-B11	B	14.4	0.078	81	72.4	675	7.4	0.25	10.3	135
P1706-B12	B	15.8	0.075	72	72.8	661	10.0	0.27	10.0	137
P1706-B13	B	14.1	0.070	71	73.0	661	8.7	0.25	9.8	130
P1706-B14	B	16.3	0.079	77	72.5	662	10.1	0.28	10.8	137
P1706-B15	B	14.4	0.081	79	72.3	666	8.8	0.27	10.5	133
P1706-B16	B	14.7	0.069	85	72.0	665	11.1	0.27	10.0	129
P1706-B17	B	13.9	0.068	80	73.8	635	9.4	0.24	10.1	133
P1706-B1PF1	B	15.1	0.090	77	73.1	646	10.3	0.26	11.1	140
P1706-B1PF2	B	14.1	0.077	79	74.0	634	8.9	0.24	11.0	131
P1706-B1PF3	B	17.4	0.091	79	71.6	658	11.4	0.30	12.1	147
P1706-B1PF4	B	16.9	0.089	85	71.3	678	12.7	0.30	11.7	147
P1706-B1PF5	B	17.3	0.073	78	71.8	677	11.9	0.29	10.5	152
P1706-B1PF6	S	12.6	0.069	72	73.5	689	7.4	0.19	8.9	135

Sample Name	Type	Nb ppm	P ₂ O ₅ %	Rb ppm	SiO ₂ %	Sr ppm	Th ppm	TiO ₂ %	Y ppm	Zr ppm
P1706-B1PF7	S	13.6	0.067	76	74.7	641	9.5	0.21	9.0	125
P1485N-B2	B	16.5	0.077	85	72.7	535	8.1	0.34	11.2	155
P1485N-B3	B	17.3	0.073	91	71.3	561	7.6	0.35	11.6	149
P1485N-B4	B	14.6	0.069	84	73.6	521	6.9	0.30	10.9	146
P1485N-B5	B	16.9	0.074	96	71.6	546	7.1	0.34	12.6	158
P1485N-B6	B	15.6	0.072	85	73.1	532	9.6	0.32	11.3	152
P1485N-B7	B	17.3	0.072	86	72.0	588	8.0	0.32	11.3	148
P1485N-B8	B	16.3	0.064	87	72.2	566	6.9	0.33	11.4	147
P1485N-B9	B	16.5	0.066	88	72.0	565	7.2	0.32	10.8	150
P1485N-B10	B	16.1	0.063	83	72.4	613	6.4	0.29	9.7	135
P1485N-B11	B	15.0	0.069	87	73.0	554	8.1	0.30	11.1	145
P1485N-B12	B	15.7	0.065	85	72.2	574	7.6	0.32	11.0	148
P1485N-B13	B	17.0	0.071	87	71.9	559	10.2	0.34	11.2	156
P1485N-B14	B	14.2	0.064	81	73.6	550	8.1	0.29	10.7	148
P1485N-B15	B	16.8	0.071	93	70.8	607	7.8	0.34	11.4	145
P1485N-B16	B	15.5	0.075	90	72.0	563	8.5	0.32	11.4	149
P1485N-B17	B	14.6	0.075	82	73.7	539	7.6	0.29	10.8	149
P1485N-B1PF1	B	15.2	0.071	81	73.5	547	7.9	0.30	10.4	143
P1485N-B1PF2	B	15.4	0.069	87	72.4	565	6.7	0.31	10.8	148
P1485N-B1PF3	B	15.5	0.069	86	72.7	545	7.9	0.32	11.2	153
P1485N-B1PF4	S	14.7	0.041	85	73.3	605	7.2	0.24	8.6	135
P1485N-B1PF5	S	13.8	0.041	92	75.2	513	6.6	0.22	8.1	135
P1485N-B1PF6	S	13.4	0.041	84	73.6	610	5.8	0.22	7.9	123
P1471S-B2	B	13.4	0.075	77	74.6	565	6.4	0.24	10.4	133
P1471S-B3	B	15.1	0.092	83	72.5	631	8.7	0.26	10.8	125
P1471S-B4	B	14.4	0.082	80	73.2	596	6.8	0.26	10.8	138
P1471S-B5	B	14.8	0.091	85	73.0	572	6.5	0.29	11.5	144
P1471S-B6	B	15.5	0.091	76	74.3	563	8.9	0.27	11.1	151
P1471S-B7	B	14.9	0.077	79	73.6	580	7.9	0.28	10.9	144
P1471S-B8	B	13.5	0.076	79	74.3	579	10.0	0.25	10.6	138
P1471S-B9	B	14.2	0.090	79	73.5	573	7.4	0.28	11.2	138
P1471S-B10	B	14.1	0.088	81	73.1	592	7.8	0.26	11.0	135
P1471S-B11	B	13.8	0.088	80	73.7	543	7.3	0.26	11.0	143
P1471S-B12	B	14.9	0.079	79	73.4	591	8.9	0.27	12.3	144
P1471S-B13	B	14.5	0.085	76	72.8	596	8.8	0.29	11.2	143
P1471S-B14	B	14.7	0.068	76	73.4	591	7.8	0.27	10.6	138
P1471S-B15	B	12.5	0.074	79	73.9	587	8.0	0.24	11.1	140
P1471S-B16	B	14.0	0.093	80	73.9	558	8.3	0.27	11.1	136
P1471S-B17	B	14.6	0.094	78	74.3	529	9.8	0.27	11.3	140
P1471S-B1-PF1	B	13.1	0.086	76	74.3	561	8.8	0.26	10.9	143
P1471S-B1-PF2	B	14.0	0.088	81	73.2	583	7.4	0.26	11.4	151
P1471S-B1-PF3	B	12.8	0.084	83	73.5	577	7.6	0.26	10.5	144
P1471S-B1-PF4	B	17.8	0.096	137	67.7	486	6.9	0.34	13.3	165
P1471S-B1-PF5	B	15.9	0.076	129	70.3	469	9.2	0.29	12.0	158
P1471S-B1-PF6	B	13.9	0.057	146	72.7	370	7.6	0.23	9.6	145
P1471S-B1-PF7	S	14.8	0.049	84	74.4	540	10.0	0.25	9.4	127
P1277S-B2	B	10.9	0.057	68	75.1	614	6.8	0.18	8.4	121
P1277S-B3	B	14.2	0.059	74	73.6	631	7.3	0.22	9.5	130

Sample Name	Type	Nb ppm	P ₂ O ₅ %	Rb ppm	SiO ₂ %	Sr ppm	Th ppm	TiO ₂ %	Y ppm	Zr ppm
P1277S-B4	B	13.8	0.060	71	74.8	605	9.0	0.22	9.4	143
P1277S-B5	B	12.6	0.062	70	74.3	616	7.4	0.21	9.0	132
P1277S-B6	B	10.6	0.068	66	75.6	595	5.3	0.16	8.2	121
P1277S-B7	B	11.5	0.063	65	75.2	613	6.7	0.17	8.2	118
P1277S-B8	B	12.8	0.060	68	75.1	595	6.2	0.21	9.6	141
P1277S-B9	B	12.0	0.061	70	74.9	600	8.4	0.19	9.0	126
P1277S-B10	B	11.8	0.072	69	74.7	605	6.9	0.19	8.8	127
P1277S-B11	B	12.7	0.066	68	74.8	604	7.3	0.20	9.6	130
P1277S-B12	B	11.9	0.056	69	76.1	571	7.5	0.20	9.6	130
P1277S-B13	B	15.7	0.055	71	74.2	598	8.9	0.24	9.4	138
P1277S-B14	B	11.9	0.060	72	75.3	593	8.3	0.19	9.6	134
P1277S-B15	B	12.2	0.060	66	74.9	608	7.4	0.19	9.1	125
P1277S-B16	B	11.7	0.059	87	74.9	585	5.8	0.20	9.3	128
P1277S-B17	B	15.0	0.055	70	74.9	585	9.2	0.23	9.8	145
P1277S-B1-PF1	B	11.5	0.062	71	74.5	632	6.0	0.18	8.7	122
P1277S-B1-PF2	B	12.6	0.059	71	74.4	614	7.5	0.21	10.0	133
P1277S-B1-PF3	B	13.1	0.058	63	75.7	574	7.7	0.21	9.4	135
P1277S-B1-PF4	B	15.2	0.054	72	74.2	603	8.0	0.23	9.3	134
P1277S-B1-PF5	B	17.0	0.059	72	73.0	635	7.2	0.25	9.7	144
P1277S-B1-PF6	B	16.4	0.053	71	73.7	618	7.4	0.23	9.5	130
P1277S-B1-PF7	B	15.0	0.058	82	72.9	654	5.8	0.21	9.3	123
P1277S-B1-PF8	S	16.6	0.049	68	74.0	613	8.0	0.23	9.5	128
P1264N-B2	B	14.7	0.082	72	74.0	591	7.5	0.24	10.0	121
P1264N-B3	B	15.2	0.074	81	73.4	597	7.9	0.24	10.3	135
P1264N-B4	B	13.9	0.070	77	73.4	618	5.6	0.22	9.2	121
P1264N-B5	B	13.5	0.074	78	73.4	606	6.6	0.21	9.6	122
P1264N-B6	B	12.1	0.071	71	75.3	576	6.7	0.20	8.7	121
P1264N-B7	B	14.0	0.079	80	73.1	612	9.1	0.24	10.7	124
P1264N-B8	B	15.7	0.084	73	73.8	577	8.5	0.25	9.8	129
P1264N-B9	B	16.5	0.084	76	72.2	619	7.2	0.26	10.2	134
P1264N-B10	B	17.7	0.078	78	73.6	622	10.4	0.24	10.6	135
P1264N-B11	B	14.9	0.089	78	71.6	594	7.9	0.29	9.6	128
P1264N-B12	B	13.1	0.080	80	73.1	595	7.9	0.23	10.2	122
P1264N-B13	B	14.7	0.083	74	74.2	589	9.3	0.23	10.7	130
P1264N-B14	B	14.5	0.081	82	72.7	619	8.3	0.24	9.6	124
P1264N-B15	B	16.7	0.092	74	72.6	602	10.3	0.27	10.8	130
P1264N-B16	B	14.6	0.081	74	73.2	606	7.8	0.24	10.5	128
P1264N-B17	B	15.1	0.087	75	72.8	601	10.4	0.25	9.9	125
P1264N-B1PF1	B	15.2	0.093	74	72.6	626	9.1	0.25	10.2	125
P1264N-B1PF2	B	16.4	0.088	73	72.6	615	9.9	0.26	10.5	134
P1264N-B1PF3	B	15.4	0.080	72	73.3	597	9.6	0.25	10.0	129
P1264N-B1PF4	B	15.6	0.074	74	72.6	625	10.0	0.25	9.9	131
P1264N-B1PF5	B	14.9	0.065	77	73.4	612	11.1	0.24	9.4	123
P1264N-B1PF6	B	19.0	0.073	83	71.5	636	14.2	0.29	10.0	132
P1264N-B1PF7	B	19.2	0.069	83	71.6	625	15.0	0.30	9.3	124
P1264N-B1PF8	S	10.6	0.042	85	77.0	504	9.7	0.16	6.6	87
P1264N-B1PF9	S	16.1	0.051	87	72.7	623	18.5	0.24	8.0	105
P1264N-B1PF10	S	13.7	0.045	86	74.1	575	15.0	0.21	7.5	111
P1264N-B1PF11	S	11.5	0.048	76	76.3	587	13.2	0.17	6.9	85

Sample Name	Type	Nb ppm	P ₂ O ₅ %	Rb ppm	SiO ₂ %	Sr ppm	Th ppm	TiO ₂ %	Y ppm	Zr ppm
P1062S-B2	B	23.3	0.062	96	71.0	588	8.9	0.41	13.9	171
P1062S-B3	B	20.6	0.061	91	71.4	582	11.2	0.38	13.1	167
P1062S-B4	B	18.1	0.060	85	73.4	562	8.3	0.32	11.5	163
P1062S-B5	B	18.8	0.065	82	72.3	599	8.7	0.33	11.1	153
P1062S-B6	B	17.6	0.072	86	73.8	432	7.5	0.27	9.3	142
P1062S-B7	B	17.6	0.059	89	71.7	632	7.2	0.29	11.9	145
P1062S-B8	B	20.8	0.059	93	71.8	588	10.2	0.35	12.6	164
P1062S-B9	B	16.9	0.055	79	73.1	605	6.0	0.29	10.7	151
P1062S-B10	B	21.4	0.056	88	71.5	589	11.1	0.37	13.5	162
P1062S-B11	B	23.4	0.062	94	71.1	584	10.7	0.39	13.6	173
P1062S-B12	B	18.4	0.053	87	73.5	550	10.3	0.31	11.3	154
P1062S-B13	B	21.7	0.063	90	71.2	604	9.4	0.37	13.0	169
P1062S-B14	B	17.6	0.071	78	72.8	631	8.7	0.28	10.9	147
P1062S-B15	B	16.3	0.063	76	73.6	598	7.9	0.27	10.6	144
P1062S-B16	B	18.9	0.060	83	72.5	604	8.6	0.32	12.0	157
P1062S-B17	B	15.4	0.065	78	73.3	643	7.1	0.22	10.0	134
P1062S-B1-PF1	B	20.1	0.060	88	71.9	592	10.5	0.37	13.4	169
P1062S-B1-PF2	B	21.8	0.061	95	71.0	606	10.7	0.38	14.0	167
P1062S-B1-PF3	B	24.2	0.060	100	70.5	586	11.3	0.43	14.0	173
P1062S-B1-PF4	B	28.2	0.066	113	67.6	578	10.9	0.49	17.2	169
P1062S-B1-PF5	B	27.4	0.066	108	68.3	564	12.2	0.47	16.2	170
P1062S-B1-PF6	B	30.7	0.069	111	66.7	555	10.5	0.53	17.8	173
P1062S-B1-PF7	B	30.8	0.071	107	66.0	548	14.0	0.53	17.2	172
P1062S-B1-PF8	B	31.4	0.068	108	65.9	538	14.2	0.56	17.9	176
P1062N-B2	B	21.3	0.058	93	70.5	607	7.3	0.40	12.7	162
P1062N-B3	B	21.7	0.062	94	70.1	599	9.1	0.43	14.0	166
P1062N-B4	B	22.3	0.062	95	69.8	606	10.4	0.44	13.6	164
P1062N-B5	B	17.8	0.057	90	72.2	586	8.5	0.33	12.2	155
P1062N-B6	B	20.2	0.060	89	71.5	573	8.7	0.39	11.8	165
P1062N-B7	B	21.8	0.069	93	70.3	612	8.0	0.40	13.1	158
P1062N-B8	B	21.3	0.067	92	70.2	599	8.7	0.42	12.9	158
P1062N-B9	B	19.9	0.056	91	71.8	570	8.0	0.37	13.2	156
P1062N-B10	B	20.6	0.079	95	69.9	602	8.7	0.43	13.4	167
P1062N-B11	B	18.1	0.058	87	71.4	594	5.9	0.36	11.9	154
P1062N-B12	B	21.3	0.063	92	71.3	550	8.1	0.43	14.3	169
P1062N-B13	B	19.8	0.057	85	72.1	565	8.6	0.36	10.5	161
P1062N-B14	B	21.6	0.061	95	70.8	562	8.1	0.43	13.7	164
P1062N-B15	B	20.5	0.065	92	71.0	585	6.5	0.40	12.4	159
P1062N-B16	B	21.0	0.075	92	70.2	607	8.2	0.41	13.4	164
P1062N-B17	B	19.3	0.094	87	71.2	588	5.7	0.38	12.2	151
P1062N-B1-PF1	B	18.0	0.058	83	72.8	565	9.0	0.36	13.2	162
P1062N-B1-PF2	B	21.5	0.058	95	70.1	599	8.3	0.43	13.6	167
P1062N-B1-PF3	B	20.9	0.060	98	69.3	618	8.5	0.43	13.9	166
P1062N-B1-PF4	B	21.4	0.060	93	71.1	565	9.9	0.43	13.2	168
P1062N-B1-PF5	B	20.1	0.060	91	70.8	588	9.0	0.41	13.9	162
P1062N-B1-PF6	B	20.6	0.059	91	70.3	607	8.2	0.40	12.7	161
P1062N-B1-PF7	B	17.8	0.056	74	73.0	579	6.1	0.30	10.3	153
P1062N-B1-S1	S	15.1	0.067	87	71.3	696	6.4	0.23	8.9	125

Table F.3: Tailholt Mountain sample compositions (Al to Na)
 Type X=rock, B=soil, S=saprolite

Sample Name	Type	Al ₂ O ₃ %	CaO %	Fe ₂ O ₃ %	K ₂ O %	MgO %	MnO %	Mo ppm	Na ₂ O %
T2364-X1	X	14.9	1.6	0.8	3.0	0.20	0.040	1.5	4.0
T2364-X2	X	14.9	1.4	0.9	4.0	0.21	0.040	1.3	3.6
T2364-X3	X	13.5	1.3	0.5	3.8	0.16	0.020	1.4	3.2
T2364-X4	X	14.9	1.4	1.0	3.3	0.27	0.040	1.6	3.7
T2364-X5	X	15.0	1.3	1.0	4.3	0.21	0.060	1.4	3.5
T2364-X6	X	14.6	0.8	0.6	1.3	0.04	0.180	1.1	5.7
T2364-X7	X	14.8	1.2	0.7	4.3	0.19	0.030	1.6	3.5
T2364-X8	X	14.4	1.4	1.0	3.4	0.26	0.050	1.4	3.7
T2364-X9	X	15.0	0.3	0.3	7.6	0.03	0.020	1.7	2.6
T2364-X10	X	14.8	1.6	0.9	3.0	0.23	0.050	1.5	3.9
T2364-X11	X	14.3	0.1	0.3	9.3	0.04	0.010	1.7	1.2
T2364-X12	X	14.7	0.3	0.7	5.3	0.04	0.121	1.7	3.1
T2364-X13	X	14.9	0.5	0.7	4.6	0.05	0.181	1.6	3.6
T2364-X14	X	14.3	0.5	0.6	4.3	0.05	0.071	1.4	3.6
T2364-X15	X	14.4	0.1	0.2	10.1	0.01	0.010	1.6	1.2
T2364-X16	X	14.5	0.7	0.4	3.9	0.05	0.010	1.4	3.7
T2364-X17	X	14.8	0.7	0.4	4.9	0.05	0.010	1.4	3.7
T2364-X18	X	14.4	0.2	0.3	8.4	0.02	0.030	1.8	2.3
T2364-X19	X	14.1	1.2	0.9	3.6	0.24	0.040	1.4	3.4
T2364-X20	X	13.9	0.5	0.7	4.3	0.03	0.171	1.3	3.7
T2364-X21	X	14.1	0.7	0.6	2.0	0.06	0.059	1.3	4.5
T2364-X22	X	14.3	0.1	0.2	10.3	0.00	0.010	1.4	1.2
T2364-X23	X	14.6	0.7	0.7	2.2	0.06	0.040	1.5	4.4
T2364-X24	X	14.1	0.5	0.7	3.7	0.07	0.161	1.6	3.5
T2364-X25	X	13.8	1.3	0.8	3.3	0.22	0.040	1.5	3.4
T2364-X26	X	15.0	1.4	0.9	3.4	0.24	0.041	1.9	3.8
T2364-X27	X	15.5	0.7	0.7	3.1	0.07	0.080	1.3	4.5
T2364-X28	X	14.9	0.8	0.5	4.3	0.08	0.040	1.4	3.6
T2364-X29	X	15.2	0.8	0.4	4.5	0.08	0.020	1.6	3.5
T2364-X30	X	14.2	0.6	0.6	3.7	0.07	0.040	14.8	3.6
T2364-X31	X	15.2	0.1	0.5	8.4	0.07	0.010	1.3	1.4
T2364-X32	X	14.6	0.2	0.3	8.3	0.01	0.020	1.5	2.4
T2364-X33	X	15.0	0.9	0.6	1.8	0.05	0.060	1.1	5.0
T2364-X34	X	14.4	0.6	0.5	4.8	0.03	0.040	1.8	4.0
T2364-X35	X	14.6	1.3	0.9	3.7	0.22	0.040	1.4	3.4
T2364-X36	X	14.9	0.2	0.5	3.2	0.14	0.050	1.6	3.7
T2364-X37	X	15.8	1.5	1.1	3.8	0.25	0.052	1.5	3.8
T2364-X38	X	14.4	1.4	0.9	3.3	0.18	0.041	1.8	3.6
T2364-X39	X	16.7	0.5	0.8	3.6	0.11	0.111	1.6	4.8
T2364-X40	X	14.7	0.5	0.8	4.0	0.03	0.121	1.6	3.8
T2073-X1	X	14.8	1.8	1.3	3.5	0.29	0.040	1.4	3.9
T2073-X2	X	14.8	1.7	1.2	3.8	0.26	0.030	1.7	3.7
T2073-X3	X	15.2	1.8	1.3	3.6	0.29	0.040	1.4	4.0
T2073-X4	X	14.8	1.9	1.2	3.4	0.24	0.030	1.1	3.8
T2073-X5	X	15.0	1.8	1.3	3.6	0.26	0.030	1.4	3.9
T2073-X6	X	14.7	1.7	1.2	3.7	0.22	0.030	1.1	3.6
T2073-X7	X	15.3	1.9	1.1	3.7	0.25	0.030	1.3	4.0

Sample Name	Type	Al ₂ O ₃ %	CaO %	Fe ₂ O ₃ %	K ₂ O %	MgO %	MnO %	Mo ppm	Na ₂ O %
T2073-X8	X	15.2	1.9	1.3	3.3	0.25	0.030	1.1	3.9
T2073-X9	X	14.6	1.7	1.2	3.7	0.29	0.030	1.0	3.7
T2073-X10	X	14.5	1.9	1.1	3.1	0.26	0.030	1.4	3.9
T2073-X11	X	14.2	0.7	1.0	3.0	0.19	0.030	1.0	3.9
T2073-X12	X	14.1	1.7	1.2	3.1	0.23	0.040	1.4	3.8
T2073-X13	X	14.0	1.9	1.3	2.7	0.28	0.030	1.3	3.8
T2073-X14	X	14.3	1.8	1.2	3.1	0.24	0.030	1.6	3.7
T2073-X15	X	15.4	2.0	1.6	2.9	0.33	0.040	1.2	4.1
T2073-X16	X	14.6	1.9	1.2	2.9	0.28	0.040	1.5	4.0
T2073-X17	X	15.0	1.8	1.1	3.5	0.27	0.040	1.4	3.9
T2073-X18	X	14.6	1.9	1.1	2.9	0.24	0.020	1.3	4.1
T2073-X20	X	14.1	1.7	1.2	3.3	0.26	0.030	1.6	3.8
T2073-X21	X	14.1	1.6	1.3	3.4	0.31	0.030	1.3	3.6
T2073-X22	X	14.3	1.6	1.3	4.0	0.26	0.030	1.3	3.5
T2073-X23	X	14.9	1.9	1.3	3.5	0.28	0.040	1.6	3.8
T2073-X24	X	14.6	1.8	1.4	2.9	0.29	0.041	1.2	4.0
T2073-X25	X	14.0	1.7	1.2	3.3	0.30	0.040	1.2	3.6
T2073-X26	X	14.0	1.7	1.2	3.3	0.24	0.030	1.4	3.7
T2073-X27	X	14.6	1.7	1.1	3.9	0.24	0.030	1.5	3.7
T2073-X28	X	14.8	1.7	1.2	4.0	0.24	0.030	1.4	3.7
T2073-X29	X	14.3	1.7	1.0	3.7	0.21	0.030	1.6	3.7
T2073-X30	X	15.1	1.6	1.3	3.9	0.27	0.030	1.3	3.7
T2073-X31	X	14.5	1.7	1.3	3.2	0.25	0.030	1.3	3.7
T2073-X32	X	14.7	1.7	1.3	3.5	0.26	0.030	1.3	3.8
T2073-X33	X	15.5	1.6	1.6	3.5	0.32	0.041	1.3	4.0
T2073-X34	X	15.1	1.7	1.2	3.6	0.24	0.030	1.6	3.9
T2073-X35	X	14.4	1.7	1.2	3.0	0.23	0.030	1.4	3.9
T2073-X36	X	14.7	1.9	1.2	3.3	0.27	0.030	1.3	3.9
T2073-X37	X	14.7	1.8	1.2	3.4	0.28	0.030	0.9	3.9
T2073-X38	X	14.3	1.8	1.2	3.1	0.28	0.040	1.5	3.9
T2073-X39	X	13.9	1.4	1.3	3.1	0.19	0.020	1.3	3.6
T2073-X40	X	14.9	1.6	1.3	4.1	0.26	0.030	1.4	3.7
T1755-X1	X	14.2	0.9	0.3	3.7	0.06	0.010	1.5	3.7
T1755-X2	X	15.3	0.3	0.7	5.2	0.12	0.061	1.4	2.1
T1755-X3	X	14.3	1.3	1.1	3.5	0.19	0.030	1.4	3.8
T1755-X4	X	14.3	1.0	1.0	3.3	0.10	0.030	1.4	3.9
T1755-X5	X	14.9	1.5	1.3	3.4	0.21	0.040	1.4	4.1
T1755-X6	X	14.4	1.4	0.9	3.7	0.16	0.030	0.8	3.8
T1755-X7	X	14.7	1.4	1.1	3.6	0.19	0.030	1.4	3.9
T1755-X8	X	14.7	1.4	1.2	3.5	0.20	0.030	0.8	3.9
T1755-X9	X	13.9	0.3	0.3	6.0	0.04	0.010	1.7	2.8
T1755-X10	X	13.6	0.7	0.4	3.9	0.11	0.010	1.5	2.5
T1755-X11	X	8.5	0.1	0.5	1.6	0.01	0.010	1.5	0.2
T1755-X12	X	5.0	0.0	0.3	0.8	0.03	0.010	1.8	0.1
T1755-X13	X	8.5	0.1	0.4	2.1	0.01	0.010	1.7	0.3
T1755-X14	X	9.6	0.0	0.2	2.2	0.00	0.000	1.5	0.1
T1755-X15	X	5.0	0.1	0.4	1.0	0.02	0.030	1.7	0.2
T1755-X16	X	12.6	0.1	0.5	3.1	0.05	0.010	1.6	0.2
T1755-X17	X	8.7	0.1	0.4	2.2	0.02	0.010	1.9	0.5
T1755-X18	X	7.7	0.2	0.5	1.4	0.00	0.020	1.6	0.1

Sample Name	Type	Al ₂ O ₃ %	CaO %	Fe ₂ O ₃ %	K ₂ O %	MgO %	MnO %	Mo ppm	Na ₂ O %
T1755-X19	X	13.5	0.1	0.4	3.2	0.07	0.010	1.1	0.2
T1755-X20	X	12.4	0.1	0.4	3.0	0.03	0.010	1.6	0.2
T1755-X21	X	12.2	0.1	0.2	2.7	0.03	0.000	1.4	0.1
T1755-X22	X	15.2	0.0	0.9	3.9	0.09	0.020	1.3	0.2
T1755-X23	X	14.5	0.1	0.3	3.3	0.06	0.000	1.0	0.2
T1755-X24	X	15.3	0.1	1.2	3.6	0.04	0.041	1.1	0.2
T1755-X25	X	14.3	0.1	0.7	3.3	0.03	0.030	1.0	0.2
T1755-X26	X	15.2	0.1	1.6	3.2	0.05	0.010	1.4	0.1
T1755-X27	X	11.6	0.1	0.8	2.8	0.03	0.021	1.4	0.4
T1755-X28	X	13.6	0.1	0.7	3.0	0.07	0.010	1.8	0.1
T1755-X29	X	7.9	0.0	0.2	1.8	-0.01	0.010	1.6	0.2
T1755-X30	X	7.5	0.1	0.5	1.2	0.01	0.020	2.0	0.2
T1755-X31	X	14.7	0.1	1.2	3.1	0.03	0.020	1.3	0.1
T1755-X32	X	14.3	0.1	0.6	3.3	0.07	0.040	1.4	0.3
T1755-X33	X	9.1	0.1	0.4	2.0	0.00	0.000	1.5	0.1
T1755-X34	X	12.4	0.1	0.7	2.7	0.03	0.050	1.5	0.2
T1755-X35	X	11.0	0.1	0.4	2.4	0.02	0.010	1.5	0.2
T1755-X36	X	14.6	1.2	1.1	3.6	0.18	0.030	1.1	3.8
T1755-X37	X	14.1	0.5	0.4	6.5	0.05	0.071	1.1	2.3
T1755-X38	X	15.0	0.9	1.0	4.8	0.12	0.160	1.2	3.6
T1755-X39	X	14.2	1.2	1.3	3.5	0.20	0.040	1.1	3.7
T1755-X40	X	8.5	0.0	0.3	1.6	0.00	0.010	1.4	0.1
T1508-X1	X	14.9	1.5	1.0	3.5	0.22	0.030	1.3	3.9
T1508-X2	X	14.7	1.6	1.0	3.5	0.22	0.030	1.4	3.8
T1508-X3	X	15.2	1.6	0.9	3.8	0.21	0.030	1.5	4.0
T1508-X4	X	15.1	1.6	1.1	3.7	0.21	0.030	1.6	4.0
T1508-X5	X	15.4	1.4	1.0	4.0	0.21	0.030	1.5	4.0
T1508-X6	X	14.0	0.3	0.5	4.1	0.11	0.020	1.3	3.6
T1508-X7	X	12.6	0.1	0.5	4.2	0.09	0.020	1.3	3.0
T1508-X8	X	14.0	1.5	1.0	3.4	0.21	0.030	1.3	3.6
T1508-X9	X	15.2	1.7	1.0	3.4	0.22	0.030	1.3	4.2
T1508-X10	X	15.0	1.7	1.2	3.4	0.26	0.030	1.0	4.1
T1508-X11	X	14.2	1.5	1.1	3.4	0.23	0.030	1.4	3.8
T1508-X12	X	14.6	1.4	1.2	3.6	0.24	0.040	1.4	3.9
T1508-X13	X	14.8	1.4	1.2	3.7	0.25	0.030	1.1	3.9
T1508-X14	X	14.9	1.5	1.1	3.4	0.23	0.040	1.3	4.0
T1508-X15	X	15.0	1.6	1.3	3.9	0.28	0.040	1.0	3.8
T1508-X16	X	14.6	1.6	1.2	3.2	0.25	0.040	1.4	3.9
T1508-X17	X	14.5	1.3	1.3	3.2	0.25	0.040	1.1	4.0
T1508-X18	X	14.2	1.5	1.0	3.4	0.21	0.030	1.3	3.8
T1508-X19	X	14.7	1.4	1.0	3.5	0.21	0.030	1.5	3.9
T1508-X20	X	15.0	1.2	1.1	3.3	0.22	0.030	1.1	4.2
T1508-X21	X	14.3	1.4	1.2	3.1	0.25	0.040	1.5	3.9
T1508-X22	X	14.5	1.4	1.2	3.3	0.23	0.050	1.4	4.0
T1508-X23	X	14.6	1.6	1.1	3.2	0.24	0.040	1.2	4.0
T1508-X24	X	15.0	1.5	1.0	3.3	0.22	0.040	1.4	4.0
T1508-X25	X	2.1	0.2	0.2	0.6	0.00	0.010	1.6	0.0
T1508-X26	X	14.4	0.1	0.8	3.8	0.19	0.111	1.4	3.5
T1508-X27	X	14.1	0.1	1.0	2.7	0.19	0.100	1.5	3.9
T1508-X28	X	15.0	0.9	0.9	4.1	0.21	0.020	0.9	2.8

Sample Name	Type	Al ₂ O ₃ %	CaO %	Fe ₂ O ₃ %	K ₂ O %	MgO %	MnO %	Mo ppm	Na ₂ O %
T1508-X29	X	16.1	1.0	1.1	4.5	0.25	0.030	1.5	3.4
T1508-X30	X	14.5	0.3	1.0	3.3	0.16	0.040	1.3	4.0
T1508-X31	X	14.7	0.2	0.9	3.3	0.17	0.030	1.5	4.2
T1508-X32	X	14.7	0.2	0.9	3.3	0.17	0.030	1.3	4.2
T1508-X33	X	14.7	0.3	0.9	3.1	0.19	0.040	1.3	4.2
T1508-X34	X	14.5	1.5	1.1	3.7	0.21	0.030	1.6	3.7
T1508-X35	X	14.8	1.6	1.1	3.5	0.23	0.040	0.3	3.9
T1508-X36	X	15.0	1.6	1.2	3.1	0.24	0.040	1.1	4.2
T1508-X37	X	14.8	1.6	1.2	3.5	0.22	0.030	0.9	3.9
T1508-X38	X	14.6	1.6	1.2	3.4	0.25	0.050	1.4	3.9
T1508-X39	X	14.5	1.7	1.2	3.1	0.25	0.040	1.0	4.0
T1508-X40	X	14.6	1.5	1.2	3.6	0.25	0.040	1.1	3.8
T1294-X1	X	14.4	1.5	0.8	3.3	0.11	0.030	1.6	4.0
T1294-X2	X	15.5	1.6	0.5	4.4	0.08	0.020	1.4	4.2
T1294-X3	X	14.9	1.2	0.6	4.5	0.11	0.020	1.3	2.9
T1294-X4	X	14.3	1.3	0.7	3.6	0.13	0.020	1.2	3.4
T1294-X5	X	14.7	0.3	0.9	3.8	0.15	0.030	1.3	3.9
T1294-X6	X	14.1	0.9	1.0	3.6	0.16	0.030	1.5	3.7
T1294-X7	X	14.8	1.7	0.8	3.5	0.12	0.030	1.4	4.1
T1294-X8	X	14.9	1.4	0.7	3.8	0.13	0.030	1.6	3.9
T1294-X9	X	15.4	1.5	0.7	4.0	0.11	0.020	1.6	4.1
T1294-X10	X	15.4	1.4	0.6	5.2	0.10	0.020	1.6	3.7
T1294-X11	X	14.8	0.8	1.1	3.7	0.17	0.041	1.5	3.9
T1294-X12	X	14.6	0.4	1.0	3.0	0.17	0.030	1.5	4.4
T1294-X13	X	14.8	1.0	1.0	3.7	0.14	0.030	1.6	3.9
T1294-X14	X	14.8	0.7	1.0	3.8	0.15	0.040	1.8	4.0
T1294-X15	X	14.6	1.3	0.9	3.9	0.14	0.030	1.4	3.6
T1294-X16	X	14.5	1.5	1.2	3.4	0.18	0.041	1.3	3.8
T1294-X17	X	13.8	0.5	0.4	4.5	0.04	0.110	1.5	3.4
T1294-X18	X	15.1	0.3	1.0	3.3	0.19	0.041	1.4	4.0
T1294-X19	X	14.9	0.6	1.0	3.6	0.15	0.050	1.4	4.1
T1294-X20	X	15.2	0.7	1.0	3.7	0.18	0.040	1.2	4.0
T1294-X21	X	14.3	0.8	1.0	3.8	0.16	0.030	1.2	3.5
T1294-X22	X	14.0	0.3	1.1	3.5	0.18	0.040	1.2	3.7
T1294-X23	X	14.5	1.1	0.9	4.0	0.17	0.030	1.5	3.2
T1294-X24	X	15.9	0.7	0.9	4.7	0.18	0.030	1.2	3.5
T1294-X25	X	14.5	1.3	0.7	3.8	0.11	0.020	1.5	3.6
T1294-X26	X	15.1	1.2	0.7	3.6	0.15	0.021	1.5	3.0
T1294-X27	X	14.7	1.1	1.0	4.3	0.17	0.040	1.4	3.2
T1294-X28	X	14.5	1.5	1.0	3.6	0.15	0.020	1.8	3.7
T1294-X29	X	14.7	1.5	1.6	3.6	0.21	0.030	1.3	3.7
T1294-X30	X	14.5	1.1	0.7	3.9	0.12	0.020	1.2	3.7
T1294-X31	X	14.5	1.3	0.8	3.5	0.13	0.020	1.3	3.9
T1294-X32	X	14.5	0.6	1.0	3.7	0.16	0.030	1.6	3.9
T1294-X33	X	14.7	0.3	0.9	3.7	0.15	0.020	1.4	4.0
T1294-X34	X	14.9	0.6	1.1	4.4	0.21	0.040	0.8	2.9
T1294-X35	X	14.6	0.2	1.1	3.1	0.21	0.020	1.5	4.0
T1294-X36	X	14.5	1.4	1.2	3.5	0.18	0.040	0.9	3.8
T1294-X37	X	14.4	1.5	1.0	3.5	0.16	0.030	1.1	3.8
T1294-X38	X	14.9	1.6	1.3	3.3	0.22	0.040	1.1	3.8

Sample Name	Type	Al ₂ O ₃ %	CaO %	Fe ₂ O ₃ %	K ₂ O %	MgO %	MnO %	Mo ppm	Na ₂ O %
T1294-X39	X	15.0	1.6	0.8	4.1	0.13	0.030	1.8	3.9
T1294-X40	X	14.4	1.5	1.1	3.6	0.19	0.040	1.3	3.8
T1084-X1	X	14.7	1.5	0.9	3.7	0.15	0.030	1.4	3.9
T1084-X2	X	13.8	1.4	0.8	3.4	0.13	0.030	1.5	3.8
T1084-X3	X	15.0	1.5	1.0	3.9	0.16	0.030	1.4	3.9
T1084-X4	X	14.4	1.4	0.8	3.6	0.14	0.030	1.3	3.8
T1084-X5	X	14.5	1.4	1.1	3.5	0.20	0.040	1.6	3.8
T1084-X6	X	14.5	1.3	0.8	3.9	0.14	0.030	1.3	3.9
T1084-X7	X	15.3	1.6	0.7	4.0	0.13	0.030	1.5	4.0
T1084-X8	X	14.2	1.6	0.9	3.2	0.14	0.030	1.1	4.0
T1084-X9	X	14.0	1.6	1.0	3.0	0.16	0.040	1.5	3.9
T1084-X10	X	14.0	1.4	0.9	3.4	0.17	0.030	1.2	3.8
T1084-X11	X	14.5	1.6	1.1	3.6	0.18	0.041	2.0	3.9
T1084-X12	X	14.8	1.7	1.2	3.2	0.21	0.040	0.9	4.1
T1084-X13	X	14.3	0.2	0.6	3.1	0.18	0.030	1.3	3.8
T1084-X14	X	14.5	1.4	1.0	3.7	0.17	0.030	1.5	3.8
T1084-X15	X	14.5	1.4	1.1	3.6	0.17	0.030	1.3	3.9
T1084-X16	X	14.6	1.5	1.2	3.6	0.21	0.041	1.6	3.9
T1084-X17	X	13.9	1.3	1.0	4.0	0.15	0.030	0.9	3.5
T1084-X18	X	14.2	1.4	1.1	3.5	0.18	0.040	1.0	3.7
T1084-X19	X	14.5	1.2	1.4	3.6	0.21	0.050	1.0	3.8
T1084-X20	X	14.1	1.1	1.2	3.0	0.18	0.040	1.3	3.8
T1084-X21	X	14.2	1.2	1.0	3.5	0.17	0.030	0.9	3.8
T1084-X22	X	14.5	1.3	1.0	3.3	0.18	0.040	1.0	4.0
T1084-X23	X	14.8	1.4	0.9	4.0	0.14	0.030	1.5	4.0
T1084-X24	X	14.0	0.8	0.9	3.7	0.15	0.030	1.2	3.6
T1084-X25	X	14.7	0.7	0.7	4.0	0.13	0.030	1.3	3.8
T1084-X26	X	14.5	1.1	1.2	3.9	0.20	0.040	1.1	3.8
T1084-X27	X	14.3	1.3	1.0	3.7	0.17	0.030	1.3	3.7
T1084-X28	X	14.8	0.6	1.0	3.5	0.20	0.030	1.1	3.9
T1084-X29	X	13.9	0.7	1.0	3.4	0.16	0.040	1.3	3.6
T1084-X30	X	13.4	1.2	1.0	3.8	0.15	0.030	1.1	3.4
T1084-X31	X	14.5	1.2	0.8	3.5	0.10	0.101	1.3	4.1
T1084-X32	X	14.9	1.4	1.1	3.4	0.18	0.040	0.9	4.1
T1084-X33	X	14.7	1.0	0.9	3.8	0.15	0.030	1.2	4.0
T1084-X34	X	14.3	1.0	1.0	3.7	0.17	0.030	1.3	3.8
T1084-X35	X	15.0	0.8	1.2	3.8	0.20	0.040	1.2	4.0
T1084-X36	X	15.3	0.8	1.0	4.4	0.15	0.030	1.4	3.7
T1084-X37	X	14.9	1.3	1.0	3.8	0.18	0.030	1.1	4.0
T1084-X38	X	14.9	0.9	1.0	3.7	0.18	0.030	1.0	3.9
T1084-X39	X	14.4	1.3	1.1	3.4	0.18	0.030	1.6	4.1
T1084-X40	X	14.1	0.9	1.0	4.1	0.17	0.040	1.1	3.6
T2364-B2	B	16.6	1.3	1.5	3.3	0.50	0.071	2.0	3.4
T2364-B3	B	16.2	1.3	1.6	3.1	0.42	0.081	1.7	3.4
T2364-B4	B	15.7	1.2	1.6	3.4	0.39	0.091	1.8	3.0
T2364-B5	B	15.6	1.1	1.5	3.2	0.41	0.081	1.8	3.0
T2364-B6	B	16.5	1.5	1.5	3.2	0.39	0.071	1.7	3.8
T2364-B7	B	15.6	1.2	1.3	3.8	0.33	0.061	1.5	3.2
T2364-B8	B	15.9	1.4	1.4	3.0	0.37	0.071	1.7	3.6

Sample Name	Type	Al ₂ O ₃ %	CaO %	Fe ₂ O ₃ %	K ₂ O %	MgO %	MnO %	Mo ppm	Na ₂ O %
T2364-B9	B	15.9	1.2	1.6	3.3	0.43	0.061	2.3	3.1
T2364-B10	B	15.2	1.2	1.4	3.4	0.39	0.061	2.1	3.1
T2364-B11	B	15.8	1.0	1.3	3.7	0.51	0.051	1.8	2.7
T2364-B12	B	15.6	1.4	1.0	3.5	0.27	0.040	2.0	3.7
T2364-B13	B	16.2	1.3	1.5	3.9	0.36	0.051	1.8	3.3
T2364-B14	B	16.0	1.2	1.5	3.4	0.41	0.061	2.0	3.2
T2364-B15	B	16.3	1.3	1.5	3.6	0.42	0.081	1.2	3.4
T2364-B16	B	14.9	1.1	1.3	4.0	0.30	0.061	1.7	3.0
T2364-B17	B	15.7	1.3	1.4	3.4	0.38	0.081	1.3	3.3
T2364-B1-PF1	B	16.1	1.2	1.5	3.9	0.38	0.071	2.5	3.2
T2364-B1-PF2	B	17.0	1.3	1.8	3.4	0.47	0.092	1.5	3.4
T2364-B1-PF3	B	16.8	1.3	1.6	3.4	0.43	0.061	2.1	3.4
T2364-B1-PF4	S	15.1	1.2	1.0	3.5	0.26	0.040	1.7	3.0
T2364-B1-PF5	S	15.8	1.3	1.0	3.9	0.28	0.041	1.5	3.3
T2364-B1-PF6	S	15.6	1.4	1.0	3.4	0.28	0.040	2.1	3.6
T2073-B2	B	15.6	1.7	1.4	3.4	0.29	0.040	0.6	3.8
T2073-B3	B	15.5	1.9	1.5	3.3	0.33	0.051	1.5	3.8
T2073-B4	B	15.2	1.8	1.4	3.4	0.28	0.040	1.7	3.7
T2073-B5	B	14.8	1.8	1.4	3.5	0.29	0.050	1.5	3.6
T2073-B6	B	15.9	1.6	1.4	3.8	0.26	0.040	1.7	3.8
T2073-B7	B	14.9	1.7	1.4	3.3	0.29	0.040	0.9	3.5
T2073-B8	B	14.7	1.8	1.5	2.9	0.31	0.051	1.5	3.6
T2073-B9	B	15.0	1.8	1.4	3.4	0.29	0.050	1.1	3.6
T2073-B10	B	14.5	1.4	1.3	3.7	0.25	0.041	1.7	3.3
T2073-B11	B	15.5	1.7	1.4	3.3	0.28	0.040	1.1	3.7
T2073-B12	B	15.2	1.8	1.6	3.0	0.34	0.051	1.7	3.8
T2073-B13	B	16.0	2.0	1.7	3.2	0.36	0.051	0.7	3.9
T2073-B14	B	15.1	1.7	1.5	3.2	0.31	0.050	1.3	3.6
T2073-B15	B	15.7	1.6	1.7	3.3	0.35	0.051	1.7	3.7
T2073-B16	B	14.9	1.6	1.5	3.4	0.30	0.050	1.1	3.5
T2073-B17	B	15.6	1.6	1.6	3.4	0.33	0.051	1.7	3.7
T2073-B1-PF1	B	14.9	1.7	1.4	3.3	0.32	0.051	1.8	3.6
T2073-B1-PF2	B	15.7	1.8	1.5	3.5	0.34	0.050	0.7	3.7
T2073-B1-PF3	B	15.2	1.7	1.5	3.1	0.33	0.051	1.1	3.7
T2073-B1-PF4	B	14.5	1.0	1.0	3.3	0.15	0.030	1.8	3.5
T2073-B1-PF5	S	15.0	1.0	1.0	3.6	0.15	0.020	1.7	3.6
T2073-B1-PF6	S	14.6	1.1	1.2	3.1	0.19	0.020	1.1	3.6
T1755-B2	B	15.2	1.1	1.5	3.3	0.19	0.050	1.0	3.7
T1755-B3	B	14.4	1.0	1.1	3.5	0.14	0.040	1.5	3.4
T1755-B4	B	15.5	1.1	1.3	3.5	0.20	0.071	1.0	3.2
T1755-B5	B	16.2	1.3	1.4	3.6	0.24	0.071	1.6	3.7
T1755-B6	B	15.1	0.9	1.1	3.6	0.14	0.041	1.3	3.3
T1755-B7	B	15.8	1.1	1.3	3.6	0.22	0.081	0.8	3.0
T1755-B8	B	15.9	1.2	1.4	3.5	0.23	0.071	0.8	3.6
T1755-B9	B	14.9	1.2	1.3	3.4	0.20	0.061	1.3	3.7
T1755-B10	B	15.0	1.2	1.2	3.4	0.18	0.051	1.0	3.5
T1755-B11	B	16.5	1.2	1.4	3.5	0.24	0.040	1.5	3.5
T1755-B12	B	16.0	1.3	1.5	3.5	0.25	0.081	1.5	3.6
T1755-B13	B	15.2	1.2	1.3	3.5	0.22	0.070	1.5	3.5

Sample Name	Type	Al ₂ O ₃ %	CaO %	Fe ₂ O ₃ %	K ₂ O %	MgO %	MnO %	Mo ppm	Na ₂ O %
T1755-B14	B	15.8	1.3	1.4	3.4	0.24	0.061	1.5	3.6
T1755-B15	B	14.6	1.1	1.2	3.4	0.20	0.040	1.8	3.7
T1755-B16	B	16.7	1.3	1.6	3.5	0.27	0.081	1.1	3.6
T1755-B17	B	16.1	1.3	1.5	3.6	0.26	0.091	2.1	3.8
T1755-B1-PF1	B	15.2	1.0	1.2	3.5	0.17	0.060	1.5	3.3
T1755-B1-PF2	B	16.1	0.9	1.3	3.5	0.21	0.041	1.3	2.8
T1755-B1-PF3	S	17.9	0.2	1.8	3.9	0.20	0.020	1.3	0.5
T1755-B1-PF4	S	16.4	0.2	2.0	3.5	0.16	0.010	1.5	0.5
T1755-B1-PF5	S	16.9	0.2	2.0	3.4	0.16	0.010	1.3	0.5
T1755-B1-PF6	S	15.1	0.2	1.4	3.4	0.13	0.010	1.3	0.5
T1508-B2	B	15.7	1.4	1.4	3.4	0.31	0.041	0.9	4.0
T1508-B3	B	15.7	1.3	1.5	3.5	0.33	0.061	1.1	3.9
T1508-B4	B	14.8	1.2	1.2	3.5	0.28	0.051	1.7	3.8
T1508-B5	B	15.4	1.1	1.3	3.4	0.26	0.030	1.1	4.0
T1508-B6	B	15.5	1.4	1.4	3.6	0.31	0.071	2.1	3.8
T1508-B7	B	14.8	1.4	1.2	3.6	0.24	0.030	1.1	3.8
T1508-B8	B	15.4	1.1	1.4	3.4	0.33	0.050	2.1	3.7
T1508-B9	B	15.1	1.4	1.2	3.4	0.28	0.041	1.3	4.0
T1508-B10	B	14.7	1.4	1.3	3.3	0.28	0.061	1.7	3.8
T1508-B11	B	15.2	1.3	1.3	3.7	0.27	0.050	1.1	3.8
T1508-B12	B	15.2	1.2	1.2	3.8	0.25	0.051	0.9	3.7
T1508-B13	B	15.5	1.3	1.4	3.5	0.30	0.051	1.5	3.9
T1508-B14	B	15.4	1.4	1.3	3.3	0.28	0.061	1.3	3.8
T1508-B15	B	16.4	1.4	1.6	3.6	0.34	0.052	1.1	4.0
T1508-B16	B	15.4	1.3	1.4	3.5	0.31	0.061	2.1	3.8
T1508-B17	B	15.4	1.3	1.5	3.5	0.31	0.082	1.7	3.9
T1508-B1-PF1	B	15.2	1.3	1.4	3.4	0.36	0.091	1.3	3.7
T1508-B1-PF2	B	15.0	1.3	1.3	3.5	0.29	0.061	1.7	3.7
T1508-B1-PF3	B	15.1	1.0	1.2	3.6	0.29	0.020	1.3	3.5
T1508-B1-PF4	B	15.1	1.1	1.3	3.4	0.35	0.020	1.5	3.5
T1508-B1-PF5	B	15.3	1.1	1.3	3.4	0.38	0.020	1.3	3.4
T1508-B1-PF6	B	14.6	1.0	1.1	3.5	0.29	0.030	1.9	3.4
T1508-B1-PF7	B	15.6	1.2	1.3	3.6	0.33	0.030	1.7	3.7
T1508-B1-PF8	B	15.2	1.1	1.2	3.5	0.28	0.020	1.9	3.7
T1294-B2	B	15.4	1.5	1.5	3.4	0.24	0.050	1.2	4.0
T1294-B3	B	14.7	1.5	1.1	3.5	0.16	0.040	1.5	3.9
T1294-B4	B	14.5	1.5	1.2	3.4	0.21	0.061	1.4	3.8
T1294-B5	B	15.1	1.6	1.4	3.5	0.22	0.050	1.4	4.0
T1294-B6	B	15.2	1.6	1.2	3.4	0.20	0.050	1.4	4.1
T1294-B7	B	14.7	1.5	1.1	3.4	0.17	0.040	1.4	4.0
T1294-B8	B	14.8	1.4	1.2	3.5	0.21	0.050	1.2	3.9
T1294-B9	B	14.9	1.5	1.5	3.4	0.24	0.070	1.4	3.9
T1294-B10	B	14.5	1.4	1.1	3.5	0.18	0.040	0.7	3.8
T1294-B11	B	15.0	1.5	1.4	3.5	0.22	0.050	1.2	3.9
T1294-B12	B	14.8	1.6	1.2	3.2	0.18	0.040	0.8	4.0
T1294-B13	B	14.6	1.5	1.2	3.5	0.20	0.040	1.4	3.8
T1294-B14	B	14.1	1.4	1.0	3.4	0.16	0.040	1.2	3.8
T1294-B15	B	14.9	1.5	1.3	3.5	0.21	0.051	1.5	3.9
T1294-B16	B	14.5	1.4	1.3	3.4	0.21	0.050	1.0	3.8

Sample Name	Type	Al ₂ O ₃ %	CaO %	Fe ₂ O ₃ %	K ₂ O %	MgO %	MnO %	Mo ppm	Na ₂ O %
T1294-B17	B	14.9	1.5	1.3	3.6	0.20	0.051	1.0	3.9
T1294-B1-PF1	B	14.2	1.4	1.1	3.2	0.17	0.040	1.0	3.8
T1294-B1-PF2	B	14.2	1.4	1.2	3.4	0.19	0.050	0.8	3.7
T1294-B1-PF3	B	14.7	1.4	1.4	3.4	0.22	0.050	1.4	3.9
T1294-B1-PF4	B	14.6	1.4	1.2	3.5	0.18	0.040	1.2	3.9
T1294-B1-PF5	B	15.3	1.5	1.4	3.4	0.23	0.040	1.2	4.0
T1294-B1-PF6	B	14.9	1.6	1.5	3.3	0.23	0.040	1.0	4.0
T1294-B1-PF7	B	14.0	1.6	1.1	3.1	0.16	0.030	1.5	3.9
T1294-B1-PF8	B	14.5	1.7	1.3	3.1	0.20	0.040	1.0	4.1
T1084-B2	B	14.5	1.2	1.0	3.6	0.16	0.030	1.4	3.9
T1084-B3	B	14.9	1.3	1.0	3.7	0.17	0.030	1.4	3.9
T1084-B4	B	15.2	1.2	1.4	3.7	0.23	0.051	1.3	3.8
T1084-B5	B	14.9	1.3	1.2	3.6	0.21	0.051	1.3	3.9
T1084-B6	B	15.0	1.3	1.3	3.5	0.22	0.041	1.0	3.9
T1084-B7	B	15.2	1.4	1.3	3.7	0.22	0.051	1.6	3.9
T1084-B8	B	14.9	1.4	1.4	3.5	0.24	0.071	1.1	3.8
T1084-B10	B	14.9	1.3	1.3	3.7	0.22	0.061	1.1	3.8
T1084-B9	B	15.0	1.4	1.4	3.6	0.24	0.061	1.0	3.8
T1084-B11	B	14.9	1.3	1.3	3.6	0.22	0.060	1.3	3.8
T1084-B12	B	14.6	1.3	1.1	3.8	0.20	0.061	1.4	3.8
T1084-B13	B	14.8	1.2	1.3	3.6	0.22	0.060	1.1	3.8
T1084-B14	B	14.8	1.3	1.3	3.4	0.24	0.060	1.1	3.7
T1084-B15	B	14.8	1.3	1.3	3.7	0.24	0.071	1.6	3.7
T1084-B16	B	14.9	1.3	1.4	3.4	0.24	0.061	1.6	3.8
T1084-B17	B	15.2	1.3	1.3	3.6	0.22	0.060	1.4	3.9
T1084-B1-PF1	B	14.8	1.2	1.2	3.5	0.20	0.051	1.1	3.8
T1084-B1-PF2	B	15.3	1.2	1.4	3.9	0.24	0.061	1.4	3.7
T1084-B1-PF3	B	15.2	1.3	1.5	3.6	0.25	0.061	1.1	3.8
T1084-B1-PF4	B	14.8	1.3	1.3	3.5	0.23	0.061	1.4	3.8
T1084-B1-PF5	B	14.7	1.1	1.2	3.7	0.21	0.051	1.7	3.6
T1084-B1-PF6	B	15.3	1.2	1.3	3.8	0.22	0.051	1.7	3.8
T1084-B1-PF7	B	15.0	1.2	1.2	3.9	0.20	0.051	1.0	3.8
T1084-B1-PF8	B	14.7	1.3	1.5	3.4	0.26	0.061	1.4	3.7

Table F.4: Tailholt Mountain sample compositions (Nb to Zr)
 Type X=rock, B=soil, S=saprolite

Sample Name	Type	Nb ppm	P ₂ O ₅ %	Rb ppm	SiO ₂ %	Sr ppm	Th ppm	TiO ₂ %	Y ppm	Zr ppm
T2364-X1	X	10.8	0.054	91	75.3	368	4.5	0.08	8.1	50
T2364-X2	X	11.4	0.061	114	74.8	362	2.0	0.09	9.8	52
T2364-X3	X	8.7	0.059	107	77.4	354	3.0	0.07	8.9	52
T2364-X4	X	12.6	0.066	106	75.3	347	2.5	0.10	12.2	48
T2364-X5	X	12.1	0.074	126	74.4	366	1.1	0.09	9.8	48
T2364-X6	X	15.1	0.062	72	76.7	32	5.8	0.04	23.8	45
T2364-X7	X	9.9	0.057	118	75.1	359	1.8	0.07	8.6	38
T2364-X8	X	11.8	0.067	107	75.7	364	3.5	0.10	9.5	49
T2364-X9	X	11.3	0.066	256	74.0	28	-0.1	0.03	11.6	12
T2364-X10	X	12.5	0.093	96	75.3	366	3.5	0.09	10.4	51
T2364-X11	X	9.8	0.068	272	74.7	83	-0.5	0.03	10.8	13
T2364-X12	X	17.8	0.078	217	75.6	34	-1.1	0.03	9.5	20
T2364-X13	X	15.9	0.075	193	75.5	33	-0.1	0.04	15.0	32
T2364-X14	X	13.9	0.077	148	76.4	17	1.9	0.04	18.6	25
T2364-X15	X	4.9	0.070	279	73.9	82	-0.9	0.03	9.5	11
T2364-X16	X	10.9	0.079	114	76.5	113	0.3	0.05	10.5	9
T2364-X17	X	8.4	0.078	132	75.4	130	-1.1	0.05	12.1	9
T2364-X18	X	5.6	0.077	243	74.3	75	-1.2	0.04	9.3	10
T2364-X19	X	10.6	0.060	107	76.4	367	4.1	0.09	8.5	53
T2364-X20	X	9.9	0.073	136	76.6	25	0.9	0.03	14.3	25
T2364-X21	X	17.0	0.069	90	77.8	18	4.2	0.04	22.4	29
T2364-X22	X	4.8	0.079	289	73.8	49	-1.4	0.03	9.6	14
T2364-X23	X	18.8	0.083	93	77.1	24	4.3	0.04	21.9	21
T2364-X24	X	13.4	0.061	129	77.1	64	1.4	0.04	13.5	29
T2364-X25	X	11.9	0.060	103	77.0	320	2.6	0.09	11.3	45
T2364-X26	X	11.6	0.059	107	75.1	365	2.7	0.09	7.7	45
T2364-X27	X	14.7	0.057	120	75.3	67	1.6	0.04	10.4	31
T2364-X28	X	14.9	0.131	144	75.5	102	-1.1	0.05	12.3	22
T2364-X29	X	14.8	0.148	143	75.4	114	0.1	0.04	10.8	17
T2364-X30	X	16.1	0.105	140	77.0	39	4.4	0.05	6.5	13
T2364-X31	X	15.6	0.060	269	74.2	74	-1.0	0.04	8.9	12
T2364-X32	X	7.7	0.083	250	74.0	24	-0.7	0.03	11.8	13
T2364-X33	X	22.9	0.081	74	76.4	30	5.4	0.05	23.9	28
T2364-X34	X	12.8	0.075	148	75.5	26	0.4	0.04	11.2	14
T2364-X35	X	12.1	0.058	109	75.6	345	3.7	0.09	8.8	50
T2364-X36	X	10.6	0.039	115	77.2	235	3.0	0.09	7.2	48
T2364-X37	X	13.8	0.068	115	73.5	366	3.2	0.11	10.0	47
T2364-X38	X	10.3	0.062	97	76.1	342	1.4	0.08	9.4	51
T2364-X39	X	14.9	0.061	144	73.1	71	-0.7	0.05	13.5	27
T2364-X40	X	13.7	0.068	135	75.9	25	1.5	0.03	14.1	27
T2073-X1	X	14.3	0.043	95	74.2	421	10.2	0.14	9.1	75
T2073-X2	X	13.6	0.047	101	74.3	424	7.4	0.13	11.7	76
T2073-X3	X	14.9	0.051	100	73.6	437	6.4	0.14	12.4	75
T2073-X4	X	13.1	0.042	91	74.5	455	8.0	0.14	9.3	85
T2073-X5	X	14.2	0.048	96	73.9	430	6.6	0.15	10.8	80
T2073-X6	X	12.8	0.041	100	74.6	441	10.1	0.14	11.8	84
T2073-X7	X	12.5	0.049	95	73.6	435	8.2	0.13	10.8	73

Sample Name	Type	Nb ppm	P ₂ O ₅ %	Rb ppm	SiO ₂ %	Sr ppm	Th ppm	TiO ₂ %	Y ppm	Zr ppm
T2073-X8	X	14.4	0.069	109	74.0	447	9.6	0.15	10.2	88
T2073-X9	X	14.4	0.048	101	74.7	407	8.4	0.14	13.8	82
T2073-X10	X	13.4	0.043	86	75.0	422	7.4	0.13	10.4	91
T2073-X11	X	15.1	0.047	100	76.8	328	7.5	0.14	9.7	91
T2073-X12	X	14.2	0.053	89	75.8	390	8.5	0.13	11.7	79
T2073-X13	X	15.9	0.056	83	75.8	395	8.9	0.15	9.4	89
T2073-X14	X	13.1	0.065	86	75.5	404	6.9	0.13	9.4	84
T2073-X15	X	15.8	0.067	91	73.3	430	7.9	0.17	11.6	87
T2073-X16	X	13.6	0.048	86	74.9	414	7.1	0.14	13.3	74
T2073-X17	X	13.2	0.049	97	74.1	428	6.3	0.14	9.4	81
T2073-X18	X	12.4	0.055	83	75.0	416	5.4	0.13	9.8	83
T2073-X20	X	13.3	0.050	94	75.4	398	6.1	0.14	10.4	79
T2073-X21	X	15.0	0.076	99	75.4	382	7.1	0.15	10.1	83
T2073-X22	X	13.4	0.048	110	74.8	413	4.9	0.15	10.2	80
T2073-X23	X	13.9	0.072	100	74.1	430	6.3	0.15	11.4	80
T2073-X24	X	15.7	0.049	90	74.9	398	7.4	0.16	9.6	90
T2073-X25	X	13.5	0.050	92	75.6	401	7.0	0.14	12.9	91
T2073-X26	X	14.2	0.051	95	75.7	389	6.6	0.14	10.0	85
T2073-X27	X	13.1	0.043	102	74.5	423	5.9	0.13	9.2	74
T2073-X28	X	13.1	0.050	104	74.2	426	6.6	0.13	10.4	79
T2073-X29	X	11.4	0.054	101	75.2	405	6.0	0.13	10.0	78
T2073-X30	X	13.2	0.043	104	73.9	422	5.0	0.14	10.8	81
T2073-X31	X	13.9	0.049	92	75.2	397	7.7	0.15	8.6	84
T2073-X32	X	13.3	0.045	98	74.6	411	6.6	0.15	9.4	84
T2073-X33	X	16.3	0.074	105	73.2	407	6.3	0.17	10.7	76
T2073-X34	X	13.0	0.045	98	74.1	423	6.9	0.13	9.3	77
T2073-X35	X	13.1	0.049	87	75.3	403	9.0	0.14	10.0	89
T2073-X36	X	13.1	0.049	91	74.6	421	9.6	0.14	18.5	81
T2073-X37	X	14.2	0.047	95	74.5	418	7.7	0.14	22.6	83
T2073-X38	X	14.2	0.044	87	75.1	407	9.6	0.14	11.0	90
T2073-X39	X	14.8	0.111	87	76.1	346	8.5	0.15	10.1	94
T2073-X40	X	14.5	0.075	107	74.0	418	7.8	0.14	10.4	83
T1755-X1	X	10.0	0.056	117	76.9	257	1.4	0.06	9.7	38
T1755-X2	X	34.9	0.042	217	76.1	102	2.1	0.10	14.3	39
T1755-X3	X	14.6	0.049	116	75.5	347	4.6	0.12	12.1	73
T1755-X4	X	15.7	0.055	114	76.3	280	6.2	0.11	12.3	74
T1755-X5	X	16.9	0.061	117	74.3	355	5.5	0.12	17.8	76
T1755-X6	X	13.7	0.063	114	75.5	336	4.5	0.10	13.8	76
T1755-X7	X	14.3	0.059	113	74.9	365	6.1	0.12	13.6	82
T1755-X8	X	16.4	0.061	115	74.8	353	5.3	0.13	12.2	80
T1755-X9	X	16.4	0.056	232	76.5	49	-0.1	0.04	10.3	7
T1755-X10	X	21.7	0.036	137	78.6	198	1.0	0.10	10.7	42
T1755-X11	X	8.3	0.034	56	89.1	107	3.3	0.07	8.2	45
T1755-X12	X	4.5	0.027	41	93.7	43	1.3	0.04	3.7	18
T1755-X13	X	10.1	0.030	91	88.6	101	0.2	0.06	8.2	33
T1755-X14	X	11.8	0.034	76	87.7	131	2.5	0.09	10.1	53
T1755-X15	X	6.9	0.034	42	93.2	72	1.9	0.06	6.3	35
T1755-X16	X	15.2	0.039	96	83.3	165	4.3	0.11	9.7	69
T1755-X17	X	10.4	0.031	84	87.9	124	2.2	0.07	7.6	40
T1755-X18	X	8.5	0.033	51	90.0	95	2.4	0.07	9.1	37

Sample Name	Type	Nb ppm	P ₂ O ₅ %	Rb ppm	SiO ₂ %	Sr ppm	Th ppm	TiO ₂ %	Y ppm	Zr ppm
T1755-X19	X	13.8	0.039	109	82.4	146	5.9	0.10	11.3	62
T1755-X20	X	12.6	0.035	99	83.9	125	3.8	0.10	10.3	55
T1755-X21	X	13.5	0.044	84	84.5	128	4.9	0.11	13.5	61
T1755-X22	X	23.1	0.040	160	79.5	107	4.0	0.11	14.7	49
T1755-X23	X	18.1	0.036	107	81.5	147	6.9	0.13	16.1	82
T1755-X24	X	16.2	0.044	129	79.4	119	3.4	0.10	17.7	60
T1755-X25	X	16.9	0.043	112	81.3	159	4.2	0.11	13.1	65
T1755-X26	X	17.7	0.063	106	79.5	170	4.5	0.13	12.7	78
T1755-X27	X	15.5	0.044	104	84.3	116	2.7	0.09	12.1	50
T1755-X28	X	16.6	0.043	126	82.3	126	3.9	0.10	12.2	69
T1755-X29	X	8.3	0.031	78	89.8	78	1.1	0.05	5.7	25
T1755-X30	X	8.0	0.031	55	90.4	110	2.7	0.06	7.3	33
T1755-X31	X	19.1	0.050	109	80.5	121	4.7	0.11	17.3	65
T1755-X32	X	16.8	0.034	105	81.1	111	0.9	0.11	13.8	52
T1755-X33	X	8.7	0.033	68	88.3	113	2.2	0.07	7.3	47
T1755-X34	X	15.3	0.041	87	83.7	127	4.8	0.11	9.3	63
T1755-X35	X	12.8	0.040	78	85.8	133	3.5	0.09	10.5	59
T1755-X36	X	17.1	0.046	122	75.3	318	4.9	0.12	13.0	68
T1755-X37	X	18.7	0.068	241	76.1	138	1.6	0.05	13.4	26
T1755-X38	X	25.0	0.081	247	74.2	228	3.2	0.10	17.8	53
T1755-X39	X	17.3	0.055	121	75.6	330	4.8	0.13	11.6	75
T1755-X40	X	9.5	0.035	60	89.4	126	2.2	0.07	7.2	41
T1508-X1	X	14.7	0.058	122	74.7	382	5.5	0.12	13.4	69
T1508-X2	X	13.6	0.067	116	74.9	389	5.2	0.12	14.4	72
T1508-X3	X	13.8	0.051	122	74.1	394	5.2	0.11	15.7	63
T1508-X4	X	14.7	0.051	133	74.2	390	4.8	0.12	13.0	72
T1508-X5	X	14.6	0.066	136	73.7	401	4.4	0.12	12.9	71
T1508-X6	X	11.2	0.044	146	77.4	123	2.1	0.06	10.7	42
T1508-X7	X	10.4	0.047	139	79.4	89	3.0	0.06	18.1	50
T1508-X8	X	14.1	0.054	108	76.1	338	4.3	0.12	19.2	75
T1508-X9	X	14.5	0.049	119	74.0	398	4.4	0.12	15.8	67
T1508-X10	X	15.6	0.057	118	74.2	394	4.4	0.13	15.3	76
T1508-X11	X	14.1	0.045	120	75.7	369	3.0	0.12	11.7	75
T1508-X12	X	15.3	0.059	125	74.9	374	4.5	0.13	13.1	72
T1508-X13	X	15.9	0.054	126	74.6	377	4.2	0.13	14.9	76
T1508-X14	X	15.5	0.061	121	74.7	388	4.2	0.12	17.5	77
T1508-X15	X	17.0	0.085	136	73.9	400	5.9	0.14	14.7	83
T1508-X16	X	15.6	0.076	114	75.0	376	4.0	0.13	14.2	69
T1508-X17	X	16.3	0.062	117	75.1	360	6.9	0.14	12.3	78
T1508-X18	X	14.3	0.061	116	75.8	356	4.4	0.12	12.5	68
T1508-X19	X	15.5	0.095	126	75.0	372	4.5	0.12	13.3	68
T1508-X20	X	16.4	0.074	120	74.7	343	5.4	0.13	20.4	77
T1508-X21	X	16.1	0.063	116	75.7	358	6.2	0.13	12.1	83
T1508-X22	X	15.2	0.086	121	75.2	354	6.5	0.13	11.5	72
T1508-X23	X	15.2	0.054	113	75.1	364	5.6	0.12	15.1	72
T1508-X24	X	15.1	0.046	108	74.7	372	4.8	0.12	15.9	71
T1508-X25	X	8.8	0.108	45	96.8	7	0.2	0.04	4.9	8
T1508-X26	X	13.6	0.036	161	77.0	109	5.8	0.10	8.9	82
T1508-X27	X	17.7	0.045	122	77.7	170	4.9	0.12	10.9	71
T1508-X28	X	22.0	0.044	141	75.9	221	4.6	0.12	18.8	44

Sample Name	Type	Nb ppm	P ₂ O ₅ %	Rb ppm	SiO ₂ %	Sr ppm	Th ppm	TiO ₂ %	Y ppm	Zr ppm
T1508-X29	X	21.6	0.042	148	73.4	275	6.2	0.14	17.2	46
T1508-X30	X	16.4	0.042	121	76.6	208	6.4	0.12	13.9	72
T1508-X31	X	16.8	0.040	149	76.5	179	5.8	0.11	13.0	67
T1508-X32	X	17.5	0.040	113	76.4	167	7.8	0.11	11.8	71
T1508-X33	X	13.6	0.047	130	76.6	371	5.3	0.13	11.1	67
T1508-X34	X	15.6	0.047	119	75.2	381	3.2	0.12	11.7	74
T1508-X35	X	14.7	0.072	126	74.8	380	6.7	0.12	44.9	70
T1508-X36	X	16.7	0.087	120	74.4	380	5.3	0.13	11.8	73
T1508-X37	X	16.1	0.065	123	74.5	377	7.0	0.13	15.6	82
T1508-X38	X	15.2	0.061	118	74.9	379	6.4	0.13	13.9	72
T1508-X39	X	15.6	0.050	112	75.0	373	6.1	0.13	17.4	74
T1508-X40	X	15.9	0.066	126	74.9	368	7.1	0.14	16.1	80
T1294-X1	X	12.6	0.061	107	75.7	349	4.7	0.09	13.3	64
T1294-X2	X	8.6	0.048	126	73.6	398	2.8	0.07	12.2	56
T1294-X3	X	16.8	0.047	131	75.7	299	3.2	0.10	18.0	52
T1294-X4	X	14.9	0.048	114	76.4	312	3.3	0.10	11.1	58
T1294-X5	X	14.5	0.037	141	76.1	260	4.5	0.10	11.8	64
T1294-X6	X	13.8	0.044	119	76.4	331	5.6	0.11	8.9	75
T1294-X7	X	11.8	0.106	110	74.8	378	3.6	0.09	15.5	62
T1294-X8	X	12.5	0.056	117	75.0	353	5.4	0.09	13.1	70
T1294-X9	X	10.8	0.063	119	74.1	397	3.3	0.09	8.4	64
T1294-X10	X	9.2	0.051	139	73.5	405	1.3	0.08	14.8	50
T1294-X11	X	16.3	0.054	143	75.3	320	5.2	0.11	14.6	65
T1294-X12	X	18.9	0.046	145	76.2	235	4.9	0.11	13.3	65
T1294-X13	X	15.0	0.059	121	75.2	306	1.8	0.10	11.2	51
T1294-X14	X	15.4	0.058	129	75.3	317	4.8	0.11	14.0	69
T1294-X15	X	16.0	0.045	124	75.4	327	5.5	0.11	14.5	52
T1294-X16	X	17.0	0.095	116	75.2	348	4.0	0.12	16.2	63
T1294-X17	X	19.4	0.059	194	77.2	103	0.4	0.04	10.2	17
T1294-X18	X	14.0	0.042	126	75.8	210	3.8	0.10	11.3	62
T1294-X19	X	15.1	0.059	125	75.4	318	3.9	0.11	11.3	76
T1294-X20	X	15.6	0.048	124	75.2	293	4.1	0.11	9.8	64
T1294-X21	X	17.0	0.042	125	76.3	287	4.6	0.12	17.2	58
T1294-X22	X	13.9	0.044	134	77.1	227	5.6	0.11	8.4	63
T1294-X23	X	18.2	0.046	126	75.9	317	4.4	0.12	18.0	57
T1294-X24	X	17.3	0.060	153	73.9	306	5.4	0.11	23.4	46
T1294-X25	X	13.1	0.146	122	75.9	263	2.6	0.09	14.8	39
T1294-X26	X	22.0	0.043	123	76.1	242	3.0	0.13	15.0	42
T1294-X27	X	18.7	0.074	156	75.3	268	2.6	0.12	13.3	52
T1294-X28	X	15.6	0.084	115	75.3	340	2.9	0.11	13.9	60
T1294-X29	X	21.9	0.157	126	74.3	347	5.8	0.16	16.7	65
T1294-X30	X	15.2	0.064	129	75.8	248	3.8	0.09	22.8	36
T1294-X31	X	13.7	0.063	112	75.7	289	2.8	0.09	19.1	51
T1294-X32	X	15.1	0.047	124	76.0	293	3.7	0.12	13.5	61
T1294-X33	X	15.4	0.044	132	76.1	237	4.2	0.10	10.9	62
T1294-X34	X	20.3	0.049	163	75.8	251	4.1	0.14	28.3	57
T1294-X35	X	13.4	0.051	156	76.7	182	4.9	0.10	9.7	66
T1294-X36	X	16.2	0.066	121	75.1	350	4.9	0.13	8.9	61
T1294-X37	X	14.3	0.065	116	75.4	358	4.4	0.11	9.2	72
T1294-X38	X	21.1	0.066	119	74.6	331	4.8	0.15	12.8	67

Sample Name	Type	Nb ppm	P ₂ O ₅ %	Rb ppm	SiO ₂ %	Sr ppm	Th ppm	TiO ₂ %	Y ppm	Zr ppm
T1294-X39	X	12.1	0.056	122	74.4	381	4.0	0.09	13.1	51
T1294-X40	X	16.0	0.060	117	75.2	355	5.4	0.12	11.6	69
T1084-X1	X	14.1	0.067	113	74.9	365	3.8	0.10	9.7	64
T1084-X2	X	13.6	0.062	109	76.4	330	3.5	0.09	13.7	57
T1084-X3	X	15.5	0.061	122	74.3	363	5.9	0.11	15.9	69
T1084-X4	X	13.7	0.050	111	75.6	346	4.1	0.09	20.4	58
T1084-X5	X	17.6	0.071	114	75.2	338	4.0	0.12	10.4	61
T1084-X6	X	14.3	0.058	120	75.2	337	4.6	0.10	16.5	57
T1084-X7	X	12.4	0.048	116	74.0	409	4.0	0.08	12.6	61
T1084-X8	X	14.1	0.054	102	75.6	354	3.6	0.10	22.9	68
T1084-X9	X	16.5	0.048	104	76.2	341	5.6	0.11	11.7	62
T1084-X10	X	15.7	0.055	112	76.1	323	2.9	0.10	18.6	57
T1084-X11	X	16.8	0.058	115	74.9	360	5.2	0.11	11.4	61
T1084-X12	X	19.2	0.057	110	74.6	349	3.5	0.13	27.3	62
T1084-X13	X	20.4	0.085	142	77.7	146	7.0	0.10	11.0	50
T1084-X14	X	15.3	0.052	120	75.2	350	5.0	0.11	11.0	61
T1084-X15	X	15.5	0.055	116	75.1	354	3.7	0.11	15.4	66
T1084-X16	X	18.1	0.077	117	74.7	352	5.1	0.13	15.9	64
T1084-X17	X	15.2	0.073	125	76.0	336	6.8	0.10	13.4	68
T1084-X18	X	16.5	0.050	111	75.7	355	4.6	0.11	21.5	65
T1084-X19	X	20.5	0.066	122	75.0	328	6.2	0.14	18.3	59
T1084-X20	X	20.0	0.059	105	76.5	305	6.0	0.12	10.7	57
T1084-X21	X	16.1	0.068	117	75.9	323	3.5	0.11	19.0	60
T1084-X22	X	16.5	0.052	113	75.4	338	4.3	0.11	14.7	63
T1084-X23	X	13.4	0.054	129	74.6	371	2.2	0.10	9.7	58
T1084-X24	X	17.2	0.120	130	76.6	252	5.4	0.10	18.5	71
T1084-X25	X	16.0	0.060	131	75.8	261	4.6	0.10	18.0	59
T1084-X26	X	17.6	0.054	130	75.0	329	3.6	0.12	19.5	66
T1084-X27	X	17.1	0.059	121	75.6	338	5.0	0.11	13.3	66
T1084-X28	X	16.6	0.055	131	75.7	231	2.7	0.11	19.1	72
T1084-X29	X	16.0	0.054	124	77.1	272	14.1	0.10	13.2	67
T1084-X30	X	15.3	0.063	121	76.9	314	4.9	0.10	20.0	62
T1084-X31	X	27.1	0.115	256	75.5	259	3.9	0.08	14.7	52
T1084-X32	X	17.6	0.054	117	74.6	357	4.3	0.12	18.0	64
T1084-X33	X	15.3	0.068	134	75.2	329	4.2	0.10	20.8	56
T1084-X34	X	15.6	0.062	123	75.9	314	4.0	0.11	13.5	57
T1084-X35	X	18.5	0.054	127	74.8	315	4.3	0.12	14.9	58
T1084-X36	X	17.5	0.058	135	74.5	305	4.7	0.11	17.1	57
T1084-X37	X	17.3	0.044	126	74.6	351	3.9	0.11	14.4	58
T1084-X38	X	18.8	0.064	123	75.2	303	4.6	0.11	17.1	68
T1084-X39	X	16.0	0.047	113	75.4	339	4.0	0.11	16.6	59
T1084-X40	X	15.6	0.059	140	76.0	305	3.5	0.11	16.7	52
T2364-B2	B	14.0	0.107	106	73.0	332	2.8	0.17	8.3	64
T2364-B3	B	14.1	0.086	102	73.6	297	3.1	0.19	10.0	72
T2364-B4	B	12.4	0.079	107	74.3	293	3.5	0.19	11.9	73
T2364-B5	B	12.6	0.075	103	74.7	285	2.7	0.18	10.1	70
T2364-B6	B	14.7	0.094	106	72.7	375	3.8	0.15	9.7	63
T2364-B7	B	12.4	0.085	113	74.3	337	2.5	0.14	7.3	62
T2364-B8	B	13.3	0.098	100	73.9	344	5.0	0.15	8.6	68

Sample Name	Type	Nb ppm	P ₂ O ₅ %	Rb ppm	SiO ₂ %	Sr ppm	Th ppm	TiO ₂ %	Y ppm	Zr ppm
T2364-B9	B	12.9	0.073	105	74.2	290	3.5	0.18	9.1	64
T2364-B10	B	13.3	0.071	106	75.0	296	2.5	0.16	9.1	66
T2364-B11	B	13.6	0.063	114	74.7	264	3.0	0.13	8.4	55
T2364-B12	B	10.7	0.066	100	74.4	352	3.4	0.11	8.4	50
T2364-B13	B	14.0	0.076	119	73.3	331	2.0	0.15	9.2	57
T2364-B14	B	13.5	0.074	108	74.0	299	3.0	0.18	11.7	64
T2364-B15	B	13.6	0.083	113	73.1	325	2.0	0.17	10.3	68
T2364-B16	B	12.2	0.073	116	75.1	313	2.2	0.14	10.5	60
T2364-B17	B	13.9	0.077	111	74.0	319	3.3	0.16	8.7	65
T2364-B1-PF1	B	13.0	0.078	117	73.5	331	2.8	0.17	8.2	63
T2364-B1-PF2	B	15.1	0.077	113	72.3	320	3.5	0.20	8.5	73
T2364-B1-PF3	B	13.6	0.070	110	72.7	330	1.4	0.18	8.6	62
T2364-B1-PF4	S	14.9	0.063	105	75.8	294	2.6	0.11	9.3	47
T2364-B1-PF5	S	14.2	0.060	116	74.2	337	3.0	0.11	7.2	48
T2364-B1-PF6	S	12.3	0.062	103	74.5	358	3.1	0.10	8.4	49
T2073-B2	B	14.8	0.080	96	73.4	404	6.5	0.16	9.7	84
T2073-B3	B	15.7	0.090	98	73.4	406	4.6	0.18	12.3	90
T2073-B4	B	14.7	0.066	94	74.0	402	5.3	0.17	11.3	85
T2073-B5	B	14.4	0.073	96	74.4	405	5.9	0.17	11.1	89
T2073-B6	B	15.1	0.073	106	73.1	397	8.2	0.16	11.9	82
T2073-B7	B	14.7	0.069	96	74.6	381	6.8	0.16	13.7	93
T2073-B8	B	15.4	0.072	89	74.8	381	6.9	0.17	12.0	90
T2073-B9	B	15.5	0.080	101	74.1	403	7.3	0.17	11.3	87
T2073-B10	B	13.7	0.062	101	75.3	365	5.9	0.15	10.4	85
T2073-B11	B	15.3	0.065	99	73.8	388	5.4	0.17	11.5	86
T2073-B12	B	16.4	0.074	90	74.0	385	5.6	0.19	11.2	87
T2073-B13	B	16.7	0.092	98	72.5	416	7.8	0.19	12.9	93
T2073-B14	B	15.7	0.072	99	74.2	387	7.0	0.18	10.9	87
T2073-B15	B	16.7	0.074	102	73.3	375	6.2	0.20	14.1	93
T2073-B16	B	13.8	0.070	97	74.6	377	7.9	0.17	11.1	93
T2073-B17	B	15.4	0.083	100	73.4	378	6.9	0.19	11.2	87
T2073-B1-PF1	B	14.4	0.090	96	74.4	380	7.4	0.17	10.6	92
T2073-B1-PF2	B	15.7	0.079	101	73.2	399	5.0	0.18	11.3	95
T2073-B1-PF3	B	15.8	0.075	95	74.2	372	8.8	0.18	11.3	87
T2073-B1-PF4	B	13.8	0.065	108	76.3	305	5.4	0.12	11.3	81
T2073-B1-PF5	S	15.0	0.064	104	75.4	341	5.2	0.14	9.3	82
T2073-B1-PF6	S	15.2	0.063	98	76.0	329	7.7	0.15	11.1	86
T1755-B2	B	17.7	0.052	121	74.7	296	4.4	0.14	14.4	80
T1755-B3	B	14.9	0.049	123	76.2	285	4.4	0.12	13.7	72
T1755-B4	B	17.9	0.059	125	74.9	278	4.4	0.15	14.5	75
T1755-B5	B	18.6	0.054	131	73.3	315	5.8	0.16	12.2	79
T1755-B6	B	17.1	0.051	119	75.6	270	4.4	0.13	14.4	73
T1755-B7	B	18.2	0.050	123	74.8	273	5.4	0.15	12.1	81
T1755-B8	B	18.8	0.057	127	73.8	301	3.6	0.16	16.1	86
T1755-B9	B	15.9	0.051	119	75.1	299	4.5	0.14	13.9	73
T1755-B10	B	16.2	0.051	124	75.4	296	5.6	0.13	11.6	77
T1755-B11	B	19.7	0.048	130	73.4	311	4.4	0.16	12.8	82
T1755-B12	B	19.5	0.053	127	73.6	304	4.2	0.16	13.8	82
T1755-B13	B	17.8	0.050	125	74.9	302	3.6	0.15	13.9	75

Sample Name	Type	Nb ppm	P ₂ O ₅ %	Rb ppm	SiO ₂ %	Sr ppm	Th ppm	TiO ₂ %	Y ppm	Zr ppm
T1755-B14	B	18.5	0.051	124	74.2	297	4.3	0.15	12.4	81
T1755-B15	B	19.6	0.051	129	75.6	295	5.8	0.12	13.0	66
T1755-B16	B	20.7	0.054	129	72.8	306	6.1	0.18	13.6	82
T1755-B17	B	19.3	0.060	132	73.2	311	5.0	0.17	15.1	76
T1755-B1-PF1	B	17.8	0.058	120	75.3	272	4.4	0.14	12.4	80
T1755-B1-PF2	B	18.8	0.048	121	74.9	255	4.9	0.15	12.1	85
T1755-B1-PF3	S	20.7	0.047	118	75.2	148	6.6	0.16	11.3	93
T1755-B1-PF4	S	18.4	0.048	107	77.0	141	5.5	0.14	10.4	86
T1755-B1-PF5	S	19.2	0.049	105	76.6	145	4.5	0.15	11.2	89
T1755-B1-PF6	S	17.6	0.042	105	79.1	111	3.4	0.11	12.4	59
T1508-B2	B	17.6	0.061	120	73.5	326	5.5	0.16	14.9	72
T1508-B3	B	18.7	0.065	127	73.6	309	4.5	0.16	14.4	74
T1508-B4	B	15.5	0.057	121	75.0	295	5.4	0.14	14.1	71
T1508-B5	B	20.0	0.054	120	74.4	297	6.1	0.15	18.3	80
T1508-B6	B	18.3	0.060	125	73.6	330	4.3	0.16	15.3	75
T1508-B7	B	16.0	0.057	120	74.7	338	4.9	0.12	11.3	70
T1508-B8	B	18.6	0.058	127	74.3	287	3.4	0.17	11.5	78
T1508-B9	B	16.3	0.056	123	74.4	310	4.7	0.14	13.0	80
T1508-B10	B	17.0	0.058	116	74.9	320	4.8	0.15	12.5	73
T1508-B11	B	16.9	0.065	127	74.2	322	5.9	0.16	14.4	75
T1508-B12	B	15.7	0.056	130	74.4	307	4.6	0.14	14.2	75
T1508-B13	B	19.7	0.062	133	73.9	270	3.4	0.15	16.9	67
T1508-B14	B	15.8	0.063	116	74.2	322	4.2	0.15	14.4	75
T1508-B15	B	18.8	0.070	124	72.4	317	5.1	0.19	16.4	77
T1508-B16	B	16.7	0.069	127	74.1	300	5.5	0.17	12.6	76
T1508-B17	B	19.1	0.064	132	73.8	278	3.9	0.17	16.3	82
T1508-B1-PF1	B	17.0	0.075	125	74.2	301	5.7	0.17	13.0	78
T1508-B1-PF2	B	16.5	0.063	125	74.7	300	5.6	0.16	17.6	75
T1508-B1-PF3	B	16.8	0.051	128	75.1	288	4.5	0.14	11.7	77
T1508-B1-PF4	B	17.7	0.051	125	75.0	284	3.2	0.15	13.0	79
T1508-B1-PF5	B	17.1	0.054	126	74.9	279	2.5	0.15	17.1	73
T1508-B1-PF6	B	15.2	0.051	120	75.8	283	4.1	0.13	10.7	67
T1508-B1-PF7	B	17.6	0.048	124	74.1	294	6.0	0.14	15.9	68
T1508-B1-PF8	B	15.6	0.046	117	74.8	291	5.4	0.12	9.6	70
T1294-B2	B	19.0	0.068	120	73.8	351	4.9	0.16	15.7	68
T1294-B3	B	15.1	0.056	114	75.0	359	4.7	0.12	12.9	70
T1294-B4	B	17.1	0.068	118	75.1	346	2.6	0.14	12.7	72
T1294-B5	B	19.6	0.063	119	74.0	361	5.2	0.15	16.6	68
T1294-B6	B	16.9	0.063	117	74.0	367	3.4	0.14	10.3	67
T1294-B7	B	14.8	0.059	115	75.0	357	3.1	0.12	12.6	64
T1294-B8	B	16.7	0.068	118	74.7	348	2.3	0.14	19.6	66
T1294-B9	B	19.8	0.069	121	74.2	352	3.5	0.16	15.9	70
T1294-B10	B	14.5	0.061	116	75.2	348	3.1	0.12	12.4	73
T1294-B11	B	18.1	0.072	121	74.1	355	4.6	0.16	15.9	73
T1294-B12	B	16.0	0.063	110	74.7	366	4.7	0.13	17.3	73
T1294-B13	B	16.0	0.066	118	74.9	349	3.3	0.13	13.9	70
T1294-B14	B	13.2	0.062	110	76.0	344	4.5	0.11	12.8	66
T1294-B15	B	17.1	0.063	118	74.4	349	3.4	0.14	14.2	65
T1294-B16	B	17.3	0.065	116	75.0	342	4.0	0.15	14.3	69

Sample Name	Type	Nb ppm	P ₂ O ₅ %	Rb ppm	SiO ₂ %	Sr ppm	Th ppm	TiO ₂ %	Y ppm	Zr ppm
T1294-B17	B	18.0	0.063	119	74.3	358	5.6	0.14	14.2	72
T1294-B1-PF1	B	14.5	0.058	109	75.9	332	2.8	0.13	11.1	75
T1294-B1-PF2	B	16.5	0.057	114	75.8	338	4.6	0.13	14.3	69
T1294-B1-PF3	B	16.8	0.062	117	74.8	342	5.4	0.15	15.4	72
T1294-B1-PF4	B	15.5	0.065	115	75.0	349	3.7	0.13	14.2	70
T1294-B1-PF5	B	18.1	0.062	121	73.8	358	4.1	0.16	11.8	73
T1294-B1-PF6	B	18.9	0.056	116	74.3	359	4.6	0.15	15.4	76
T1294-B1-PF7	B	14.8	0.048	103	75.8	362	5.2	0.11	14.8	75
T1294-B1-PF8	B	17.3	0.049	104	74.9	371	4.2	0.13	15.7	80
T1084-B2	B	14.6	0.054	118	75.4	296	2.2	0.12	14.3	63
T1084-B3	B	14.3	0.062	120	74.9	315	3.2	0.12	11.6	66
T1084-B4	B	17.7	0.061	129	74.1	308	4.1	0.15	16.6	74
T1084-B5	B	16.1	0.071	122	74.6	309	3.9	0.15	19.1	73
T1084-B6	B	17.5	0.064	122	74.4	306	4.3	0.16	18.5	75
T1084-B7	B	16.0	0.068	126	74.1	313	4.4	0.15	14.2	70
T1084-B8	B	17.2	0.070	123	74.5	301	3.8	0.17	16.2	74
T1084-B10	B	15.8	0.076	124	74.6	302	4.7	0.15	20.9	77
T1084-B9	B	16.6	0.068	125	74.4	305	5.4	0.17	15.8	78
T1084-B11	B	16.0	0.073	124	74.6	301	3.5	0.15	13.0	68
T1084-B12	B	13.8	0.082	121	74.9	306	4.6	0.14	14.8	71
T1084-B13	B	16.6	0.082	126	74.8	291	2.8	0.15	15.7	69
T1084-B14	B	16.7	0.061	122	74.9	292	4.8	0.16	16.0	73
T1084-B15	B	16.5	0.074	124	74.6	308	4.0	0.16	14.0	77
T1084-B16	B	17.2	0.067	119	74.6	296	3.4	0.17	18.7	74
T1084-B17	B	16.6	0.068	125	74.2	306	4.9	0.15	14.3	71
T1084-B1-PF1	B	15.9	0.062	122	75.0	297	3.2	0.14	13.8	71
T1084-B1-PF2	B	17.7	0.066	130	73.9	307	4.3	0.17	15.0	73
T1084-B1-PF3	B	18.5	0.066	128	74.1	300	3.2	0.17	16.6	79
T1084-B1-PF4	B	17.1	0.071	121	74.7	296	3.5	0.16	17.4	75
T1084-B1-PF5	B	16.4	0.057	126	75.2	290	3.8	0.15	12.0	71
T1084-B1-PF6	B	17.3	0.066	129	74.1	298	3.6	0.16	12.9	67
T1084-B1-PF7	B	15.7	0.061	127	74.5	301	2.3	0.14	17.2	71
T1084-B1-PF8	B	18.0	0.065	123	74.9	285	3.5	0.17	13.4	75